

THE FLORIDA STATE UNIVERSITY
COLLEGE OF ARTS AND SCIENCES

COLD NUCLEAR MATTER EFFECTS ON $J/\psi \rightarrow e^+e^-$ AND $\psi' \rightarrow e^+e^-$
PRODUCTION IN $d + \text{Au}$ COLLISIONS AT 200 GEV

By

D. MCGLINCHEY

A Dissertation submitted to the
Department of Physics
in partial fulfillment of the
requirements for the degree of
Doctor of Philosophy

Degree Awarded:
Fall Semester, 2012

D. McGlinchey defended this dissertation on October 22, 2012.

The members of the supervisory committee were:

Anthony Frawley
Professor Directing Dissertation

Paul Eugenio
Professor Co-Directing Dissertation

Munir Humayun
University Representative

Simon Capstick
Committee Member

Todd Adams
Committee Member

The Graduate School has verified and approved the above-named committee members, and certifies that the dissertation has been approved in accordance with the university requirements.

To my family, without whom I would not be where I am today.

ACKNOWLEDGMENTS

While it would take far too long to thank all the people who have helped make this work possible, I'd like to take the opportunity to acknowledge a few who have not only helped me along the way, but have made my last few years a true joy. To everyone I don't mention, my apologies and my thanks.

Many thanks to my advisor, Tony Frawley, for being not only a great scientist, but also a great advisor. Your grasp of physics, and your willingness to answer any question at any time, has guided me throughout the last five years. On top of that, your curiosity and enthusiasm for understanding any and every problem constantly inspires me. It has been a pleasure to work with you.

To the many friends I've made here at FSU, thank you. To Andrew and Liz, I would never have gotten through classes without you. To Tim and Jess for being great roommates. To everyone in NRB for Momo's Friday's. To Jeff, Anthony, and Michelle for getting me out of NRB, whether it be for lunch, a round of golf, or an FSU football game.

To everyone on PHENIX, thank you for always making me feel welcome. Thank you to all the new found friends who have made owl shifts a blast. A special thanks to Alex and Cesar for all your help with my analysis, it wouldn't have gone nearly as well without you.

Finally, to my family. There is no way any of this could have been done without you. Thank you for your unfailing support and encouragement, it has meant more than I can possibly express. To Chelsey, thank you for always being there for me, and especially for putting up with me these last few months. I love you.

TABLE OF CONTENTS

| | |
|---|-----------|
| List of Tables | ix |
| List of Figures | xii |
| List of Abbreviations | xxiii |
| Abstract | xxiv |
| 1 Overview | 1 |
| 2 Quantum Chromodynamics | 3 |
| 2.1 QCD in Nuclear Matter - Cold Nuclear Matter Effects | 6 |
| 2.1.1 Nuclear Shadowing | 6 |
| 2.1.2 Gluon Saturation | 10 |
| 2.1.3 Cronin Effect | 11 |
| 2.1.4 Radiative Energy Loss | 11 |
| 2.2 A New Phase of QCD - The Quark Gluon Plasma | 12 |
| 2.2.1 Quark Scaling of Elliptic Flow | 14 |
| 2.2.2 Near-perfect Fluidity of the Medium Produced in Au+Au Collisions | 15 |
| 2.2.3 Suppression of High- p_T Hadrons in Au+Au Collisions | 15 |
| 3 Charmonia and the J/ψ | 17 |
| 3.1 Production Mechanism | 19 |
| 3.1.1 Feeddown to J/ψ from higher mass charmonium states | 22 |
| 3.2 Charmonia as a Probe of Hot Nuclear Matter | 22 |
| 3.2.1 SPS $A + A$ Results | 23 |
| 3.2.2 RHIC Au+Au Results | 24 |
| 3.2.2.1 The RHIC J/ψ Puzzle. | 24 |
| 3.2.2.2 Low Energy RHIC Results | 25 |
| 3.2.3 Recent Results from the LHC | 26 |
| 3.2.4 Bringing all the Energies Together | 27 |
| 3.3 Cold Nuclear Matter Effects | 28 |
| 3.3.1 Results from the Low Energy Fixed Target Experiments | 29 |
| 3.3.2 Previous RHIC Results | 32 |
| 3.4 Motivation - Tying it all Together | 32 |

| | | |
|----------|--|-----------|
| 4 | Experiment | 35 |
| 4.1 | RHIC | 35 |
| 4.2 | The Pioneering High Energy Nuclear Interaction eXperiment (PHENIX) | 36 |
| 4.2.1 | Global Detectors | 36 |
| 4.2.2 | Central Spectrometers | 38 |
| 4.2.2.1 | Drift Chamber. | 38 |
| 4.2.2.2 | Pad Chambers. | 39 |
| 4.2.2.3 | Ring Imaging Cherenkov Detector. | 40 |
| 4.2.2.4 | Electromagnetic Calorimeter. | 40 |
| 4.2.3 | Muon Spectrometers | 42 |
| 4.2.4 | Data Acquisition and Triggering | 43 |
| 4.2.5 | Centrality Determination | 44 |
| 4.2.6 | Electron Identification in the Central Arms | 45 |
| 4.3 | Data Selection | 46 |
| 5 | J/ψ Analysis | 48 |
| 5.1 | J/ψ Signal Extraction | 48 |
| 5.1.1 | Correlated e^+e^- Signal extraction | 48 |
| 5.1.2 | Estimation of the Correlated Background and Losses Due to the Radiative Tail in the J/ψ Mass Distribution | 50 |
| 5.2 | Detector Acceptance and Efficiency Corrections | 53 |
| 5.2.1 | J/ψ Acceptance \times Reconstruction Efficiency | 53 |
| 5.2.2 | J/ψ Trigger Efficiency | 57 |
| 5.2.3 | J/ψ Embedding Efficiency | 61 |
| 5.3 | Results | 61 |
| 5.3.1 | J/ψ Invariant Yield | 63 |
| 5.3.2 | Calculation of the $J/\psi \langle p_T^2 \rangle$ | 64 |
| 5.3.3 | J/ψ Nuclear Modification Factor | 69 |
| 6 | ψ' Analysis | 72 |
| 6.1 | Simulations | 72 |
| 6.1.1 | ψ' and J/ψ Simulations | 73 |
| 6.1.2 | Drell-Yan Simulations | 73 |
| 6.1.3 | Pythia Heavy Flavor Simulations | 74 |
| 6.1.4 | MC@NLO Heavy Flavor Simulations | 74 |
| 6.2 | Efficiency Corrections | 74 |
| 6.2.1 | Acceptance Calculation | 75 |
| 6.2.2 | Trigger Efficiency Determination | 76 |
| 6.3 | Determining the Raw ψ' to J/ψ ratio | 77 |
| 6.3.1 | Determining the Raw Invariant Mass Distribution | 77 |
| 6.3.2 | Fitting the Invariant Mass Distributions | 78 |
| 6.3.3 | Testing against the $p+p \psi'/(J/\psi)$ ratio | 85 |
| 6.4 | Relative modification | 87 |
| 6.5 | $\psi' R_{dAu}$ | 87 |

| | |
|---|------------|
| 7 Discussion of Results and Comparison with Theory | 89 |
| 7.1 $J/\psi \langle p_T^2 \rangle$ | 89 |
| 7.2 The J/ψ Nuclear Modification Factor | 90 |
| 7.2.1 Models of the Rapidity Dependent Modification | 93 |
| 7.2.2 Models of the Transverse Momentum Dependent Modification | 96 |
| 7.3 ψ' Production in $d+Au$ collisions | 101 |
| 7.4 Correcting the $J/\psi R_{dAu}$ for Feed-down Effects | 103 |
| 7.5 Geometric Dependence of the $J/\psi R_{dAu}$ | 107 |
| 8 Investigating the Geometric Dependence of the $J/\psi R_{dAu}$ | 110 |
| 8.1 Modeling the Nuclear Modification | 110 |
| 8.2 $d+Au$ Glauber Model | 111 |
| 8.3 Nuclear Shadowing Parametrization 1 | 115 |
| 8.4 Nuclear Shadowing Parametrization 2 | 120 |
| 8.5 Discussion | 122 |
| 8.5.1 Comparison with the p_T dependence of R_{dAu} | 125 |
| 9 Calculating the CNM Baseline in Au+Au collisions | 129 |
| 9.1 Modeling of $R_{AA}(CNM)$ | 129 |
| 9.2 Hot Nuclear Matter Effects | 135 |
| 10 Summary and Outlook | 138 |
| Appendix A Calibration of the EMCal Track Matching Variables | 140 |
| A.1 emcsdphi_e | 140 |
| A.2 emcsdz_e | 145 |
| Appendix B Calibration of the Dep Variable | 151 |
| Appendix C Derivation of the Statistical Uncertainty on $\langle p_T^2 \rangle$ | 158 |
| Appendix D Pythia Configurations | 160 |
| D.1 J/ψ Pythia Configuration | 160 |
| D.2 ψ' Pythia Configuration | 160 |
| D.3 Heavy Flavor Pythia Configuration | 161 |
| D.4 DY Pythia Configuration | 162 |
| Appendix E Fitting in the $\psi' \rightarrow e^+e^-$ Analysis | 164 |
| E.1 Fit Function | 164 |
| E.2 Alternate Fit Results | 166 |
| Appendix F Additional Figures | 172 |
| F.1 Single electron trigger efficiency | 172 |
| F.2 Invariant Mass Spectra in Different Centrality Bins | 180 |

| | |
|--|------------|
| Appendix G Tables | 184 |
| G.1 J/ψ Yield Values | 184 |
| G.2 J/ψ Acceptance x Reconstruction Efficiency Values | 188 |
| G.3 J/ψ Trigger Efficiencies | 189 |
| G.4 J/ψ Inv. Yield Values | 190 |
| G.5 $R_{AA}(CNM)$ Values | 194 |
| References | 196 |
| Biographical Sketch | 203 |

LIST OF TABLES

| | | |
|-----|--|----|
| 2.1 | The four fundamental forces and their effective strengths relative to gravity. | 3 |
| 2.2 | The Standard Model particles [48]. | 4 |
| 3.1 | Properties of various charmonia states. For the χ_{ci} states, r_0 and T_D are given for the spin averaged χ_c state. | 18 |
| 4.1 | RHIC running periods with collision species, collision energy, and delivered luminosity to all experiments. | 37 |
| 4.2 | Characterization of the collision centrality for d +Au collisions along with the correction factor c (see text for details). | 44 |
| 4.3 | Information on the data sample used in this analysis. | 47 |
| 5.1 | The fit parameters used to determine ϵ_{cont} and ϵ_{rad} | 51 |
| 5.2 | A summary of the systematic uncertainties on the $J/\psi \rightarrow e^+e^-$ invariant yield and their associated types for each observable. | 63 |
| 5.3 | The J/ψ invariant yield as a function of rapidity for 0-100% centrality integrated d +Au collisions and as a function of centrality. | 64 |
| 5.4 | The $J/\psi \langle p_T^2 \rangle$ correction factors, k , for $p+p$ and d +Au collisions. | 67 |
| 5.5 | The $J/\psi \langle p_T^2 \rangle$ results for $p+p$ and d +Au collisions where the first quoted uncertainty corresponds to the type A uncertainties and the second corresponds to the type B uncertainties. | 68 |
| 5.6 | The J/ψ nuclear modification factor, $R_{d\text{Au}}$, as a function of rapidity for each centrality bin and for 0-100% centrality integrated d +Au collisions. | 69 |
| 5.7 | The J/ψ modification factor, R_{CP} , as a function of rapidity for each centrality bin. | 71 |
| 6.1 | Number of simulated electron pairs for J/ψ 's, ψ' 's, open charm, open bottom and DY. The number of pairs accepted into the central arms is dependent on the rungroup, but an approximate number is given in the third column. | 72 |

| | | |
|-----|---|-----|
| 6.2 | The $A \times \epsilon_{\text{eID}}$ for the ψ' and J/ψ , as well as the J/ψ to ψ' ratio for each rungroup. The total shown in the bottom row is a weighted average based on the number of analyzed MB events in each rungroup given in Table 4.3 | 76 |
| 6.3 | The ϵ_{ERT} for the ψ' and J/ψ , as well as the J/ψ to ψ' ratio for each rungroup. The total shown in the bottom row is a weighted average based on the number of analyzed MB events in each rungroup given in Table 4.3 | 76 |
| 6.4 | The rungroup and p_T averaged $A \times \epsilon_{\text{eID}}$ and ϵ_{ERT} for each mass distribution. | 78 |
| 6.5 | Results for $N_{\psi'}/N_{J/\psi}$ from different fitting schemes. | 81 |
| 6.6 | Comparing the χ^2 values from fits where $N_{\psi'}/N_{J/\psi}$ is left free (χ^2_{free}) to those where it is fixed to the $p+p$ value. In the case where $N_{\psi'}/N_{J/\psi}$ is fixed to the $p+p$ value, all other parameters are refitted. | 86 |
| 6.7 | The ψ' to J/ψ ratio. | 87 |
| 6.8 | The relative modification between the ψ' and the J/ψ | 87 |
| 6.9 | The ψ' $R_{d\text{Au}}$ | 88 |
| 7.1 | Compilation of the values used to calculate the proper time spent in the nucleus by the J/ψ (or $c\bar{c}$ precursor). | 104 |
| 8.1 | Average centrality values calculated from the Glauber model. | 115 |
| A.1 | emcsdphi_e recalibration parameters. | 144 |
| A.2 | emcsdz_e recalibration parameters. | 150 |
| B.1 | Dep recalibration parameters for each sector. For Dep, the parameters are the same for both $\alpha < 0$ and $\alpha > 0$ | 155 |
| G.1 | J/ψ counts for each rungroup and $-0.5 < y < -0.1$ | 185 |
| G.2 | J/ψ counts for each rungroup and $-0.1 < y < 0.1$ | 186 |
| G.3 | J/ψ counts for each rungroup and $0.1 < y < 0.5$ | 187 |
| G.4 | The J/ψ Acceptance x Reconstruction Efficiency for each rungroup. | 188 |
| G.5 | J/ψ Acceptance x Reconstruction Efficiency for each rungroup. | 188 |
| G.6 | J/ψ Trigger Efficiency for each rungroup. | 189 |
| G.7 | J/ψ yield values summed over rungroups for $-0.5 < y < -0.1$ | 191 |
| G.8 | J/ψ yield values summed over rungroups for $-0.1 < y < 0.1$ | 192 |

| | | |
|------|---|-----|
| G.9 | J/ψ yield values summed over rungroups for $0.1 < y < 0.5$. | 193 |
| G.10 | J/ψ $R_{AA}(CNM)$ values as a function of N_{part} calculated based on a step function nuclear shadowing given by Equation 8.14 using globally fit values of $R = 2.40$ fm and $d = 0.12$ fm and σ_{abs} values shown in Figure 8.6. | 194 |
| G.11 | J/ψ $R_{AA}/R_{AA}(CNM)$ values as a function of N_{part} as described in Section 9.2.195 | |

LIST OF FIGURES

| | | |
|------|---|----|
| 2.1 | The strong coupling constant, α_s , as a function of the energy scale, Q [49]. | 5 |
| 2.2 | An example of a parton distribution function for the quarks and gluons at $Q^2 = 10 \text{ GeV}^2$ from the CTEQ collaboration [97] | 7 |
| 2.3 | A purely schematic example of the modification of the parton distribution function in nuclei. | 8 |
| 2.4 | nPDF modifications for a Pb nucleus from EPS09 [63] (solid black lines) for the valence quark (R_V^{Pb}), sea quark (R_S^{Pb}) and gluon (R_G^{Pb}) distributions at LO(Top) and NLO(Bottom) compared to other nPDF sets. | 9 |
| 2.5 | A schematic picture of the evolution of proton parton density with x and Q^2 | 11 |
| 2.6 | A schematic view of the phase diagram for QCD matter. | 12 |
| 2.7 | The energy density and three times the pressure normalized to $1/T^4$ as a function of temperature from LQCD [47]. The vertical lines indicate the transition region ($180 < T [\text{MeV}] < 200$) between normal nuclear matter and a deconfined QGP. | 13 |
| 2.8 | (a) v_2 vs p_T , (b) v_2 vs KE_T , (c) v_2/n_q vs p_T and (d) v_2/n_q vs KE_T for identified particle species obtained in minimum bias Au+Au collisions at $\sqrt{s_{NN}} = 200 \text{ GeV}$ [12]. | 14 |
| 2.9 | The p_T dependence of v_2 through v_5 [22]. The curves are calculations from ideal hydrodynamics (a), viscous hydrodynamics with $\eta/s = 0.08$ (b) and $\eta/s = 0.16$ (c) [99]. | 15 |
| 2.10 | (a) A cartoon of jet production in a hot medium. (b) Comparison of the two particle azimuthal distributions for $p+p$, $d+\text{Au}$, and $\text{Au}+\text{Au}$ collisions at $\sqrt{s_{NN}} = 200 \text{ GeV}$ [9]. | 16 |
| 3.1 | Spectrum of the charmonia states which are stable under strong decays and their dominant decay modes. | 18 |

| | | |
|------|--|----|
| 3.2 | Representative Feynman diagrams which contribute to the production of 3S_1 quarkonia states via color-singlet channels at order α_s^3 (a), α_s^4 (b,c,d) and α_s^5 (e,f) and via color-octet channels at order α_s^3 (g,h). Figure taken from [51]. | 21 |
| 3.3 | The inclusive J/ψ p_T distributions at $ y < 0.35$ and $1.2 < y < 2.4$ measured by PHENIX [20]. Included are predictions based on CSM [85], CEM [69], NRQCD [53], and B -meson decay based on FONLL calculations [54]. | 21 |
| 3.4 | A cartoon picture of a $c\bar{c}$ in the vacuum (a) compared to in a QGP medium (b). | 22 |
| 3.5 | (Left) The ratio of the J/ψ production cross section to the Drell-Yan production cross section in the range $2.9 < M [\text{GeV}/c^2] < 4.5$ in $\sqrt{s_{NN}} = 20$ GeV S+U collisions as measured by the NA38 Collaboration [6].(Right) The ratio of the J/ψ production cross section to the Drell-Yan production cross section in the range $2.9 < M [\text{GeV}/c^2] < 4.5$ in $\sqrt{s_{NN}} = 17$ GeV Pb+Pb collisions as measured by the NA50 Collaboration [34]. | 24 |
| 3.6 | (Left) The $J/\psi R_{AA}$ measured by PHENIX at $\sqrt{s_{NN}} = 200$ GeV [21]. (Right) The $J/\psi R_{AA}$ in $1.2 < y < 2.2$ measured by PHENIX in $\sqrt{s_{NN}} = 39, 62.4,$ and 200 GeV Au+Au collisions [23] | 25 |
| 3.7 | (a) The inclusive $J/\psi R_{AA}$ as a function of N_{part} measured by the ALICE collaboration in $\sqrt{s_{NN}} = 2.76$ TeV Pb+Pb collisions [110].(b) The prompt $J/\psi R_{AA}$ as a function of N_{part} for $6.5 < p_T < 30$ GeV/c as measured by the CMS collaboration in $\sqrt{s_{NN}} = 2.76$ TeV Pb+Pb collisions [2]. | 26 |
| 3.8 | Compilation of results on the $J/\psi R_{AA}$ from the SPS [6, 34, 42], RHIC [23, 11, 21] and the LHC [110]. | 27 |
| 3.9 | The nuclear shadowing of the gluon distribution in Au taken from EPS09 for LO(Left) and NLO(Right). | 29 |
| 3.10 | Compilation of the x_F dependence of the α parameter (described in the text) for J/ψ production from low energy fixed target experiments [43]. | 30 |
| 3.11 | The J/ψ nuclear breakup cross section as a function of x_F (Left) and \sqrt{s} (Right) extracted from data collected by NA3, NA50, E866 and HERA-B [87]. | 31 |
| 3.12 | (Left) x_F dependence of the α parameter for both J/ψ and ψ' production in $p+A$ collisions measured by E866 [86]. (Right) The ratio of ψ' production to J/ψ production in $p+A$ measured by NA50 [35] collisions as a function of L | 31 |
| 3.13 | The $J/\psi R_{d\text{Au}}$ at $\sqrt{s_{NN}} = 200$ GeV measured by the PHENIX experiment from data collected in 2003 [13]. The curves represent calculations including nuclear shadowing and nuclear breakup, where the breakup cross section is fitted to the data. | 33 |

| | | |
|------|--|----|
| 3.14 | The anomalous suppression of J/ψ production in In+In [42] (circles) and Pb+Pb (triangles) corrected for CNM effects using the measured J/ψ production in 400 GeV $p+A$ collisions [35] (a) and the 158 GeV $p+A$ collisions [43](b). | 33 |
| 4.1 | An aerial photograph of the RHIC complex. This picture was taken before the recent installation of EBIS. | 36 |
| 4.2 | PHENIX detector configuration for 2008. The Left plot shows a beam view of the Central Arm detectors while the Right plot shows a side view detailing the muon arms. | 38 |
| 4.3 | (Left)Layout of the DC wire position within one sector. (Right)A top view schematic diagram of the wire configuration. | 39 |
| 4.4 | The pad and pixel geometry in the PC. A cell defined by three pixels is at the center of the right picture. | 39 |
| 4.5 | A cutaway view of one arm of the RICH detector. | 40 |
| 4.6 | Schematic view of a Pb-scintillator module. | 41 |
| 4.7 | Schematic view of a Pb-glass supermodule. | 42 |
| 4.8 | A schematic diagram of the data acquisition system. | 43 |
| 4.9 | Nucleon nucleon collision (N_{coll}) distributions for each centrality bin obtained using a Glauber model for $d+\text{Au}$ collisions described in the text.. | 45 |
| 4.10 | The number of electrons per scaled MB trigger versus run number for each EMcal sector. | 47 |
| 5.1 | Invariant mass distribution of unlike-sign (filled circles) and like-sign (filled boxes) dielectron pairs in central $d+\text{Au}$ collisions, integrated over p_T and rapidity. Dashed vertical lines represent the mass range used to determine the correlated e^+e^- yield. | 49 |
| 5.2 | Correlated dielectron invariant mass distribution for minimum bias $d+\text{Au}$ collisions. The line shapes are those used to extract the continuum and radiative tail contributions to the correlated e^+e^- yield in the mass range $2.8 < M_{ee} [\text{GeV}/c^2] < 3.3$. The apparent structure in the continuum line shape is due to statistical fluctuations in the simulations. | 52 |
| 5.3 | A comparison of the ϕ distributions between data (Red) and simulations (blue) for the first rungroup. | 53 |
| 5.4 | The J/ψ acceptance \times electron ID efficiency as a function of transverse momentum for each rungroup and each rapidity bin used in the analysis. | 55 |

| | | |
|------|--|----|
| 5.5 | The eID efficiency in simulations compared with measured electrons from Dalitz decays [20]. | 56 |
| 5.6 | The reconstructed p_T distributions for a given generated p_T range, as well as the full reconstructed p_T distribution. | 57 |
| 5.7 | The ratio of the number of J/ψ 's reconstructed within a given p_T range to the number of J/ψ 's generated in that p_T range for each rapidity and p_T bin used in the analysis. | 58 |
| 5.8 | The single electron trigger efficiency for each SM in the EMCAL in the first rungroup. Each panel represents the single electron trigger efficiency as a function of electron momentum for a given sector (Y-axis of the figure) and SM (X-axis of the figure). The data is represented by the blue points and the red curve represents the error function fit to the measured data described in the text. | 59 |
| 5.9 | The single electron trigger efficiency for each SM in the RICH in the first rungroup. Each panel represents the single electron trigger efficiency as a function of electron momentum for a given sector (Y-axis of the figure) and SM (X-axis of the figure). The data is represented by the red points and the blue line represents the fit to the measured data described in the text. | 60 |
| 5.10 | The J/ψ ERT efficiency for each rungroup in the 3 rapidity bins used in this analysis. | 62 |
| 5.11 | The J/ψ invariant yield as a function of transverse momentum for 0-100% centrality integrated d +Au collisions at $ y < 0.35$. The type C systematic uncertainty for each distribution is given as a percentage in the legend. | 65 |
| 5.12 | The J/ψ invariant yield as a function of transverse momentum for each centrality at $ y < 0.35$. The type C systematic uncertainty for each distribution is given as a percentage in the legend. | 66 |
| 5.13 | Results of modified Kaplan fits to midrapidity $p+p$ (Left) and midrapidity 0-100% d +Au (Right). | 67 |
| 5.14 | Results of modified Kaplan fits to midrapidity d +Au collisions for each centrality. | 68 |
| 5.15 | The J/ψ nuclear modification factor, $R_{d\text{Au}}$, as a function of transverse momentum for 0-100% centrality integrated d +Au collisions at $ y < 0.35$ | 70 |
| 5.16 | The J/ψ nuclear modification factor, $R_{d\text{Au}}$, as a function of transverse momentum for a) central, b) midcentral, c) midperipheral, and d) peripheral events at $ y < 0.35$ | 71 |
| 6.1 | The ZVTX for all events in analyzed runs, along with a Gaussian fit to the distribution. | 73 |

| | | |
|------|--|----|
| 6.2 | A comparison of dielectron mass spectra from open charm and open bottom generated using MC@NLO, PYTHIA, and FONLL. The PYTHIA simulations with MSEL=1 (described in Section 6.1.3) are arbitrarily normalized to the FONLL calculations for plotting and comparison purposes only. | 75 |
| 6.3 | Plot of the 0-88% invariant mass distribution for unlike-sign and like-sign (Left) and like-sign subtracted (Right). | 77 |
| 6.4 | A comparison of fits to the 0-88% d +Au mass spectrum with the J/ψ internal radiation fraction constrained to $9\pm 5\%$ (Left) and fitted to the data (Right), giving a value of 36%. The fits gives an overall χ^2/NDF of 3.98(Left) and 1.26(Right). | 80 |
| 6.5 | (Left) Result of fit to the 60-88% d +Au mass distribution. (Right) The same fit, with all bins with negative counts explicitly rejected from the fitting algorithm. When the negative bins are rejected in the right plot, it creates a plotting artifact where the fit (black line) goes to 0 at the boundaries of each negative bin. | 81 |
| 6.6 | Fits to the 0-20% d +Au invariant mass distribution for the Best case (Left) and Case 1 (Right). | 83 |
| 6.7 | Fits to the 20-40% d +Au invariant mass distribution for the Best case (Left) and Case 1 (Right). | 83 |
| 6.8 | Fits to the 40-60% d +Au invariant mass distribution for the Best case (Left) and Case 1 (Right). | 84 |
| 6.9 | Fits to the 60-88% d +Au invariant mass distribution for the Best case (Left) and Case 1 (Right). | 84 |
| 6.10 | Fits to the 0-88% d +Au invariant mass distribution for the Best case (Left) and Case 1 (Right). | 85 |
| 6.11 | Fits to the d +Au invariant mass spectrum in 4 centrality bins using the Best fitting scheme and fixing the $\psi'/(J/\psi)$ ratio to the $p+p$ value. | 86 |
| 6.12 | The ψ' $R_{d\text{Au}}$ at $ y < 0.35$ as a function of N_{coll} | 88 |
| 7.1 | The difference between $\langle p_T^2 \rangle$ in d +Au and $p+p$ as a function of N_{coll} at each rapidity. The uncertainties in the $\langle p_T^2 \rangle_{pp}$ are shown as boxes at $\Delta \langle p_T^2 \rangle = 0$ [10]. | 90 |
| 7.2 | The $\Delta \langle p_T^2 \rangle$ calculated for $0 \leq p_T [\text{GeV}/c] \leq 5$ as a function of N_{part} for $p+p$ [10], d +Au [10], Cu+Cu [14], and Au+Au [11] collisions at $\sqrt{s_{NN}} = 200$ GeV. For clarity the d +Au points at backward and forward rapidity have been shifted by $\pm 10\%$ in N_{part} | 91 |

| | | |
|------|---|-----|
| 7.3 | The J/ψ nuclear modification factor, $R_{d\text{Au}}$, as a function of rapidity for 0-100% centrality integrated $d+\text{Au}$ collisions. Curves are model calculations detailed in Section 7.2.1. [19] | 92 |
| 7.4 | The J/ψ nuclear modification factors, $R_{d\text{Au}}$ (Left) and R_{CP} (Right), as a function of rapidity for each centrality. | 93 |
| 7.5 | The J/ψ nuclear modification factor, $R_{d\text{Au}}$, as a function of transverse momentum for a) backward rapidity, b) midrapidity, and c) forward rapidity 0-100% centrality integrated $d+\text{Au}$ collisions. Curves are model calculations detailed in Section 7.2.2. [10] | 94 |
| 7.6 | The 0-100% centrality integrated $R_{d\text{Au}}$ as a function of p_T at all rapidities. The Type C systematic uncertainty for each distribution is given as a percentage in the legend. [10] | 95 |
| 7.7 | The J/ψ nuclear modification factor, $R_{d\text{Au}}$, as a function of transverse momentum for a) central, b) midcentral, c) midperipheral, and d) peripheral events at $-2.2 < y < -1.2$. Curves are calculations by Ferreiro et al. [67] discussed in Section 7.2.2. [10] | 96 |
| 7.8 | The J/ψ nuclear modification factor, $R_{d\text{Au}}$, as a function of transverse momentum for a) central, b) midcentral, c) midperipheral, and d) peripheral events at (Left) $ y < 0.35$ and (Right) $1.2 < y < 2.4$. Curves are calculations by Ferreiro et al. [67] discussed in Section 7.2.2. [10] | 97 |
| 7.9 | The J/ψ nuclear modification factor $R_{d\text{Au}}$ central (a), $R_{d\text{Au}}$ peripheral (b) and R_{CP} central (c). Curves are model calculations detailed in Section 7.2.1. [19] | 98 |
| 7.10 | The J/ψ $R_{d\text{Au}}$, as a function of p_T momentum for midrapidity 0-100% centrality integrated $d+\text{Au}$ collisions. The curves are theoretical calculations from [102] described in the text. [10] | 101 |
| 7.11 | The J/ψ $R_{d\text{Au}}$ as a function of transverse momentum for a) backward rapidity, b) midrapidity, and c) forward rapidity 0-100% centrality integrated $d+\text{Au}$ collisions. Curves are model calculations from [79] detailed in Section 7.2.2. | 102 |
| 7.12 | The ψ' and J/ψ $R_{d\text{Au}}$ at $ y < 0.35$ as a function of N_{coll} . | 103 |
| 7.13 | The relative modification of the ψ' to J/ψ in $d+\text{Au}$ ad $ y < 0.35$ as a function of time spent in the nucleus. | 104 |
| 7.14 | The modification in $d+\text{Au}$ collisions of direct production for different charmonia states as a function of the binding energy. These are integrated over all centrality. | 106 |
| 7.15 | A comparison between the inclusive J/ψ $R_{d\text{Au}}$, and the J/ψ $R_{d\text{Au}}$ corrected for ψ' feed-down, $R_{d\text{Au}}(J/\psi + \chi_c \rightarrow J/\psi)$ as a function of N_{coll} . | 106 |

| | | |
|------|--|-----|
| 7.16 | The r_T distributions for each of the four PHENIX centrality bins along with the $\Lambda(r_T)$ distribution. The distributions are all re-normalized to a maximum of 1 for a clearer comparison. [19] | 107 |
| 7.17 | The J/ψ nuclear modification factors R_{CP} vs $R_{d\text{Au}}$ for experimental data compared with three geometric dependencies of the nuclear modification (curves). [19] | 109 |
| 8.1 | Distribution of the gluon modification vs p_T obtained from EPS09 by using the x_2 and Q^2 values obtained from a NLO calculation (NLO) and from Equations 8.3 and 8.4 ($2 \rightarrow 1$ kinematics). Each panel corresponds to a different cut on the rapidity of the J/ψ , as indicated. | 112 |
| 8.2 | Distribution of the gluon modification vs rapidity obtained from EPS09 by using the x_2 and Q^2 values obtained from a NLO calculation (NLO) and from Equations 8.3 and 8.4 ($2 \rightarrow 1$ kinematics). Each panel corresponds to a different cut on the p_T of the J/ψ , as indicated. | 113 |
| 8.3 | Resulting optimum σ_{abs} and n values for different Glauber parameter sets. | 116 |
| 8.4 | The $\bar{\chi}^2$ contours for $y \leq 0$ where σ_{abs} and n are optimized separately at each rapidity. [90] | 118 |
| 8.5 | The $\bar{\chi}^2$ contours for $y > 0$ where σ_{abs} and n are optimized separately at each rapidity. [90] | 119 |
| 8.6 | The optimum values and uncertainties on σ_{abs} as a function of rapidity obtained from the fits described in Section 8.3 and Section 8.4. For clarification purposes the individual fits at each rapidity are slightly offset. [90] | 120 |
| 8.7 | The gluon modification as a function of r_T for the best fit R and d parameters (solid red line), along with the modifications from all combinations of R and d within $\Delta\bar{\chi}^2 = 2.3$ (thin blue lines). The modification from the best fit global analysis of $\Lambda^n(r_T)$ ($n = 15$) is shown by the solid orange line. The impact parameter dependence of the recently released EPS09s is given by the dashed magenta line [74]. [90] | 121 |
| 8.8 | Comparison to the data of the fits using a global R and d in Equation 8.14. The dashed curves represent the uncertainty in σ_{abs} only. | 123 |
| 8.9 | The $\bar{\chi}^2$ contours obtained from the global fits of R and d using Equation 8.14. [90] | 124 |
| 8.10 | The optimum σ_{abs} values with 1 standard deviation uncertainties extracted using the thickness dependent modification compared with σ_{abs} values calculated using a saturated parametrization of the dipole cross section [82]. | 125 |

| | | |
|------|---|-----|
| 8.11 | The $R_{d\text{Au}}$ values integrated over the rapidity acceptance of the three PHENIX spectrometers. The solid curves are obtained by combining the fits from the 12 rapidity bins as described in the text. The dashed curves show the uncertainty band arising from the fit uncertainties for the σ_{abs} values. | 126 |
| 8.12 | The $R_{d\text{Au}}$ versus p_T for backward rapidity, calculated from the best fits to the centrality dependence of the d+Au data in finer rapidity bins, as explained in the text. | 127 |
| 8.13 | The $R_{d\text{Au}}$ versus p_T for midrapidity (Left), and forward rapidity (Right), calculated from the best fits to the centrality dependence of the d+Au data in finer rapidity bins, as explained in the text. | 128 |
| 9.1 | (Top) The calculated $R_{AA}(CNM)$ for mid and forward rapidity, as described in the text. (Bottom) The measured $J/\psi R_{AA}$ at mid [11] and forward [21] rapidities in Au+Au collisions at $\sqrt{s_{NN}} = 200$ GeV. | 131 |
| 9.2 | The calculated $J/\psi R_{AA}(CNM)$ considering nuclear shadowing only (a), nuclear breakup only (b), and the combination of the two effects (c). | 132 |
| 9.3 | Comparison of the p_T dependence of $R_{AA}(CNM)$ calculated using Equation 8.14 with the measured R_{AA} [11] at midrapidity. | 133 |
| 9.4 | (Top) The experimental R_{AA} vs centrality divided by the calculated $R_{AA}(CNM)$. To the extent that CNM effects can be factorized from hot matter effects, the modifications shown in this plot should show the effects of hot nuclear matter on J/ψ production. (Bottom) The ratio of $R_{AA}/R_{AA}(CNM)$ at forward to mid rapidity, where the Type C systematic uncertainty on the ratio is represented by a box at $y=1$ | 135 |
| 9.5 | A comparison of the calculate $R_{AA}/R_{AA}(CNM)$ for $y = 0$ at RHIC and the SPS [51] as a function of the particle production. The global scale uncertainty on the $y = 0$ RHIC calculation is represented by the red box at $R_{AA}/R_{AA}(CNM) = 1$ | 136 |
| A.1 | Fits of the mean values of emcdphi as a function of zed for EMCAL sector 1 $\alpha > 0$ | 141 |
| A.2 | Fits of the σ values of emcdphi as a function of zed for EMCAL sector 1 $\alpha < 0$ | 141 |
| A.3 | Fits to the p_T dependence of the mean and σ parameters of emcdphi for EMCAL sector 1 $\alpha < 0$ | 142 |
| A.4 | Recalibrated emcsdphi_e for each sector of the EMCAL (blue is alpha<0 & red is alpha>0) | 143 |
| A.5 | Mean (Left) and σ (Right) values for the emcsdphi_e distributions (blue is alpha<0 & red is alpha>0) | 144 |

| | | |
|------|---|-----|
| A.6 | Fit of the mean values as a function of theta for EMCAL sector 0 and alpha<0. Fit function is $m0 + m1 * \tan(\theta - \pi/2)$ | 146 |
| A.7 | Fit of sigma values as a function of theta for EMCAL sector 0 and alpha<0. Fit function is $s0 * \cos(\theta - \pi/2) + s1$ | 147 |
| A.8 | Fit of parameters as a function of momentum for EMCAL sector 0 and alpha<0. Fit function is $p0 + \frac{p1}{p_T} + \frac{p2}{p_T^2}$ | 148 |
| A.9 | Recalibrated emcsdz_e for each EMCAL sector (blue is alpha<0 & red is alpha>0) | 149 |
| A.10 | Mean (Left) and σ (Right) values for the emcsdz_e distributions (blue is alpha<0 & red is alpha>0) | 150 |
| B.1 | Dalitz electron mass spectrum. | 151 |
| B.2 | E/p distributions from Dalitz electron pairs for EMCAL Sector 3. | 152 |
| B.3 | Fits to the mean of the E/p distributions as a function of momentum for each EMCAL sector. | 153 |
| B.4 | Fits to the mean of the E/p distributions as a function of momentum for each EMCAL sector. | 154 |
| B.5 | Mean of the calibrated Dep distributions as a function of momentum for each EMCAL sector. | 156 |
| B.6 | Width of the calibrated Dep distributions as a function of momentum for each EMCAL sector. | 157 |
| E.1 | Fits to the d +Au invariant mass spectrum in 4 centrality bins using the Best fitting scheme with an overlay where the $\psi'/(J/\psi)$ ratio is set to the $p+p$ value. | 166 |
| E.2 | Fits to the d +Au invariant mass spectrum in 4 centrality bins using the Case 1 fitting scheme. | 167 |
| E.3 | Fits to the d +Au invariant mass spectrum in 4 centrality bins using the Case 2 fitting scheme. | 167 |
| E.4 | Fits to the d +Au invariant mass spectrum in 4 centrality bins using the Case 3 fitting scheme. | 168 |
| E.5 | Fits to the d +Au invariant mass spectrum in 4 centrality bins using the Case 4 fitting scheme. | 168 |
| E.6 | Fits to the d +Au invariant mass spectrum in 4 centrality bins using the Case 5 fitting scheme. | 169 |

| | | |
|------|--|-----|
| E.7 | Fits to the d +Au invariant mass spectrum in 4 centrality bins using the Case 6 fitting scheme. | 169 |
| E.8 | Fits to the d +Au invariant mass spectrum in 4 centrality bins using the Case 7 fitting scheme. | 170 |
| E.9 | Fits to the d +Au invariant mass spectrum in 4 centrality bins using the Case 8 fitting scheme. | 170 |
| E.10 | Fits to the d +Au invariant mass spectrum in 4 centrality bins using the Case 9 fitting scheme. | 171 |
| E.11 | Fits to the d +Au invariant mass spectrum in 4 centrality bins using the Case 10 fitting scheme. | 171 |
| F.1 | (color online) EMCAL SM efficiencies for rungroup 0 where the blue points are the data and the red lines the fit. | 172 |
| F.2 | (color online) RICH SM efficiencies for rungroup 0 where the red points are the data and the blue lines the fit. | 173 |
| F.3 | (color online) EMCAL SM efficiencies for rungroup 1 where the blue points are the data and the red lines the fit. | 174 |
| F.4 | (color online) RICH SM efficiencies for rungroup 1 where the red points are the data and the blue lines the fit. | 175 |
| F.5 | (color online) EMCAL SM efficiencies for rungroup 2 where the blue points are the data and the red lines the fit. | 176 |
| F.6 | (color online) RICH SM efficiencies for rungroup 2 where the red points are the data and the blue lines the fit. | 177 |
| F.7 | (color online) EMCAL SM efficiencies for rungroup 3 where the blue points are the data and the red lines the fit. | 178 |
| F.8 | (color online) RICH SM efficiencies for rungroup 3 where the red points are the data and the blue lines the fit. | 179 |
| F.9 | Plot of the 0-20% invariant mass distributions for unlike-sign and like-sign (Top) and like-sign subtracted (Bottom). | 180 |
| F.10 | Plot of the 20-40% invariant mass distributions for unlike-sign and like-sign (Top) and like-sign subtracted (Bottom). | 181 |
| F.11 | Plot of the 40-60% invariant mass distributions for unlike-sign and like-sign (Top) and like-sign subtracted (Bottom). | 182 |

F.12 Plot of the 60-88% invariant mass distributions for unlike-sign and like-sign
(Top) and like-sign subtracted (Bottom). 183

LIST OF ABBREVIATIONS

- QGP - Quark Gluon Plasma
CNM - Cold Nuclear Matter
RHIC - Relativistic Heavy Ion Collider
PHENIX - Pioneering High-Energy Nuclear Interaction eXperiment
BNL - Brookhaven National Lab
SPS - The Super Proton Synchrotron
SLAC - Stanford Linear Accelerator
QCD - Quantum Chromodynamics
SM - Standard Model
QED - Quantum Electrodynamics
LHC - Large Hadron Collider
PDF - Parton Distribution Function
DIS - Deep Inelastic Scattering
DY - Drell-Yan
nPDF - Nuclear Parton Distribution Function
CGC - Color Glass Condensate
LQCD - Lattice QCD
CSM - Color Singlet Model
CEM - Color Evaporation Model
NRQCD - Non Relativistic QCD
FONLL - Fixed Order Next Leading Log
NLO - Next-to-Leading Order
BBC - Beam-Beam Counter
ZVTX - z vertex
DC - Drift Chamber
PC - Pad Chamber
RICH - Ring Imaging Cherenkov Detector
EMCal - Electromagnetic Calorimeter
SM - SuperModule
NBD - Negative Binomial Distribution
ERT - Electron RICH Trigger
MB - Minimum Bias
eID - electron Identification
 NN - nucleon-nucleon
HNM - Hot Nuclear Matter

ABSTRACT

Mesons composed of heavy quark-antiquark pairs, known as quarkonia, provide the only direct probe of the screening length in the deconfined state of quarks and gluons, known as the quark gluon plasma (QGP), which is believed to be produced in high energy heavy ion collisions. However, the observation of suppression of quarkonia production in heavy ion collisions at high energies is complicated by the modification of quarkonia production in normal nuclear matter. Measuring the modification of quarkonia production due to the effects of normal nuclear matter, often termed cold nuclear matter (CNM) effects, provides a critical baseline for understanding the properties of the QGP.

CNM effects on quarkonia production are also interesting in their own right, and can be measured independently in proton-nucleus ($p+A$) collisions. The modification of quarkonia production in $p+A$ collisions provides insight into quarkonia production mechanisms unavailable through the study of proton-proton collisions alone. The study of quarkonia production in $p+A$ collisions over a wide range of kinematic variables can also provide constraints on the modification of parton distribution functions in nuclei.

In order to quantify the CNM effects present at the Relativistic Heavy Ion Collider (RHIC), the PHENIX experiment has recorded data on $d+\text{Au}$ collisions at $\sqrt{s_{NN}} = 200 \text{ GeV}$. The analysis of $J/\psi \rightarrow e^+e^-$ and $\psi' \rightarrow e^+e^-$ production from that data set is presented here. Both J/ψ and ψ' production are found to be suppressed in $d+\text{Au}$ relative to $p+p$ collisions, with the suppression increasing for collisions with small impact parameters. The ψ' production is found to be much more suppressed than J/ψ production, a result which is unexpected based on measurements at lower collision energy and present theoretical pictures.

A parametrization of the J/ψ modification measured by PHENIX in terms of two CNM effects is also presented. One is the nuclear breakup of the forming quarkonium state through collisions with nucleons during the $d+\text{Au}$ collision. The other is the modification of the gluon distribution in the Au nucleus. It is found that the two effects can be separated due to the very different impact parameter dependencies. A strongly non-linear geometric dependence on the modification of the gluon distribution function is observed, with the modification found to be concentrated near the center of the Au nucleus. This parametrization is also used to estimate the modification of J/ψ production in $\text{Au}+\text{Au}$ collisions due to CNM effects. This modification is compared to PHENIX measurements of J/ψ production in $\text{Au}+\text{Au}$ collisions. Suppression of J/ψ production in $\text{Au}+\text{Au}$ collisions beyond CNM effects is observed. This excess suppression is interpreted as suppression of J/ψ production due to the formation of a QGP.

CHAPTER 1

OVERVIEW

On November 11, 1974 the J/ψ meson was discovered independently by groups at the Brookhaven National Laboratory (BNL) [44] and the Stanford Linear Accelerator (SLAC) [46] lead by Burton Richter and Samuel Ting respectively. This discovery confirmed the existence of the predicted charm quark and ushered in a series of rapid shifts in the understanding of high-energy physics, now termed the “November Revolution”. For the discovery, Richter and Ting were awarded the 1976 Nobel Prize in Physics.

The J/ψ , along with the other $c\bar{c}$ bound states that make up the charmonium family, continues to be of strong theoretical and experimental interest, particularly in the field of heavy ion physics. In 1986 Matsui and Satz predicted that the suppression of J/ψ production in heavy ion collisions would be a clear signature of the formation of a new state of matter, the quark gluon plasma (QGP) [89]. While suppression of J/ψ production in heavy ion collisions has been observed at the CERN SPS [6, 34, 42], RHIC [11, 21, 23], and the LHC [2, 110], spanning three orders of magnitude in collision energy, a clear understanding has not yet emerged.

This dissertation presents measurements of J/ψ and ψ' production into the dielectron decay channel in $d+\text{Au}$ collisions at $\sqrt{s_{NN}} = 200$ GeV performed by the PHENIX collaboration at the Relativistic Heavy Ion Collider (RHIC) at BNL. This work sheds further light on the production of charmonia in nuclear targets and is a critical step towards understanding properties of the QGP medium produced in $\text{Au}+\text{Au}$ collisions at RHIC.

Also presented in this dissertation are the results of an effort to parametrize the measured modification of the J/ψ production in $d+\text{Au}$ collisions to gain insight into the geometric dependence of its modification within a Au nucleus. This parametrization is then used to calculate the cold nuclear matter baseline for J/ψ production in $\text{Au}+\text{Au}$ collisions so that the hot nuclear matter effects may be separated.

The organization of this dissertation is as follows: Chapter 2 gives a short introduction to quantum chromodynamics (QCD) to give the reader some background and introduce terms and concepts that will be used throughout this dissertation. Chapter 3 includes an introduction to the charmonium family, with a focus on the J/ψ meson, and its relevance to heavy ion physics. A summary of the current experimental and theoretical understanding of J/ψ production in heavy ion physics will also be given. Chapter 4 gives a detailed overview of the PHENIX detector used in collecting the data on which the analysis is based. Chapter 5 details the analysis and results of $J/\psi \rightarrow e^+e^-$ production in $d+\text{Au}$ collisions at $\sqrt{s_{NN}} = 200$

GeV. Chapter 6 details the analysis and results of $\psi' \rightarrow e^+e^-$ production in $d+\text{Au}$ collisions at $\sqrt{s_{NN}} = 200$ GeV. Chapter 7 discusses the implications of the measured J/ψ and ψ' results as well as comparisons with theoretical predictions. Chapter 8 will present the modeling and parametrization of the J/ψ nuclear modification factor and discuss the implications of the model. In Chapter 9 the calculation of the cold nuclear matter baseline for J/ψ modification in $\text{Au}+\text{Au}$ collisions will be presented and compared with PHENIX measurements of the modification of J/ψ production in $\text{Au}+\text{Au}$ collisions. Finally, Chapter 10 will summarize the conclusions drawn from the results presented in this dissertation, and present a path forward for a greater understanding of quarkonia production in heavy ion collisions.

CHAPTER 2

QUANTUM CHROMODYNAMICS

Before delving into quantum chromodynamics (QCD), it is perhaps appropriate to first take a step back and remind ourselves of the larger framework of the Standard Model (SM) of which QCD is only a part.

Table 2.1: The four fundamental forces and their effective strengths relative to gravity.

| Force | Current Theory | Relative Strength | Range [m] | Mediators |
|-----------------|-------------------------------|-------------------|------------|---------------------|
| strong | Quantum Chromodynamics (QCD) | 10^{38} | 10^{-15} | gluon (g) |
| electromagnetic | Quantum Electrodynamics (QED) | 10^{36} | ∞ | photon (γ) |
| weak | Electroweak Theory | 10^{25} | 10^{-18} | Z^0, W^+, W^- |
| gravity | General Relativity (GR) | 1 | ∞ | graviton |

The SM as we know it today has evolved over many years, beginning with the unification of the electromagnetic and weak forces in the late 1960's. The current evolution of the SM includes four fundamental forces, listed in Table 2.1, and 17 fundamental particles, listed in Table 2.2.

The SM is built open the framework of group theory, and the overall symmetries of the SM are given by the combined group $SU(3) \otimes SU(2) \otimes U(1)$. Each group corresponds to the symmetries of one of the three forces considered within the framework of the SM ¹. QED is represented by the $U(1)$ group, the weak interaction by $SU(2)$, and QCD by $SU(3)$. Each force is mediated by a number of spin-1 gauge bosons. QED is mediated by a single (the photon), the weak interaction has three mediating bosons (The W^\pm and Z bosons), and there are 8 mediating bosons for QCD (the gluons). These gauge bosons interact with the 12 fermions, which are further broken down into 3 generations of 4 fermions, including 2 leptons (ex. e, ν_e) and 2 quarks (ex. d, u) each. The final SM particle, potentially discovered recently at the LHC [55, 3], is the Higgs boson. The Higgs, if confirmed, is responsible for the masses of the other massive elementary particles through the breaking of electroweak symmetry [75].

¹while gravity is known to be the fourth fundamental force, it is not included within the SM framework

Table 2.2: The Standard Model particles [48].

| Name | Symbol | Charge | Spin | Rest Mass [MeV/c ²] |
|------------------|------------|---------|------|---|
| Leptons | | | | |
| electron | e | -1 | 1/2 | 0.511 |
| e -neutrino | ν_e | 0 | 1/2 | $< 2.2 \times 10^{-3}$ |
| muon | μ | -1 | 1/2 | 105.66 |
| μ -neutrino | ν_μ | 0 | 1/2 | < 0.17 |
| tau | τ | -1 | 1/2 | 1776.82 ± 0.16 |
| τ -neutrino | ν_τ | 0 | 1/2 | < 15.5 |
| Quarks | | | | |
| up | u | 2/3 | 1/2 | 1.7-3.3 |
| down | d | -1/3 | 1/2 | 4.1-5.8 |
| strange | s | 2/3 | 1/2 | 101^{+29}_{-21} |
| charm | c | -1/3 | 1/2 | $(1.27^{+0.07}_{-0.09}) \times 10^3$ |
| top | t | 2/3 | 1/2 | $(172.0 \pm 0.9 \pm 1.3) \times 10^3$ |
| bottom | b | -1/3 | 1/2 | $(4.19^{+0.18}_{-0.06}) \times 10^3$ |
| Gauge Bosons | | | | |
| photon | γ | 0 | 1 | 0 |
| gluon | g | 0 | 1 | 0 |
| W -boson | W^\pm | ± 1 | 1 | 80.4×10^3 |
| Z -boson | Z^0 | 0 | 1 | 91.2×10^3 |
| Higgs | H^0 | 0 | 1 | $(125.3 \pm 0.4 \pm 0.5) \times 10^3$ [55] $(126.0 \pm 0.4 \pm 0.4) \times 10^3$ [3] |

Calculations within the SM have been remarkably successful at making precise predictions which have been confirmed experimentally. It is one of the most rigorously tested theories in physics and has held up remarkably well to years of experimental testing.

When dealing with the strong force, the most relevant force at the high energies provided by hadron-hadron collisions at RHIC, we turn to QCD. Quantum chromodynamics introduces an additional quantum number to the SM and is governed by the $SU(3)$ symmetry group. This new quantum number, labeled color, can take three values referred to as red (r), green (g), and blue (b), in an analogy to the three colors in optics. Like the electric charge in QED, each color has an opposite, “negative” value, carried by the antiquarks, referred to as anti-red (\bar{r}), anti-green (\bar{g}), and anti-blue (\bar{b}).

Unlike QED, QCD is a non-abelian gauge theory, meaning that the force carrying gluon itself carries color. The gluon can be thought of as carrying both color and anti-color, creating 8 different color-states of the gluon. These states are said to be color-octet states, and they can be defined as

$$g_i = \lambda_i \begin{pmatrix} rr & r\bar{b} & r\bar{g} \\ b\bar{r} & bb & b\bar{g} \\ g\bar{r} & g\bar{b} & gg \end{pmatrix}, \quad (2.1)$$

where $i = 1, 2, \dots, 8$ and λ_i are the Gell-Mann matrices. The Gell-Man matrices are traceless,

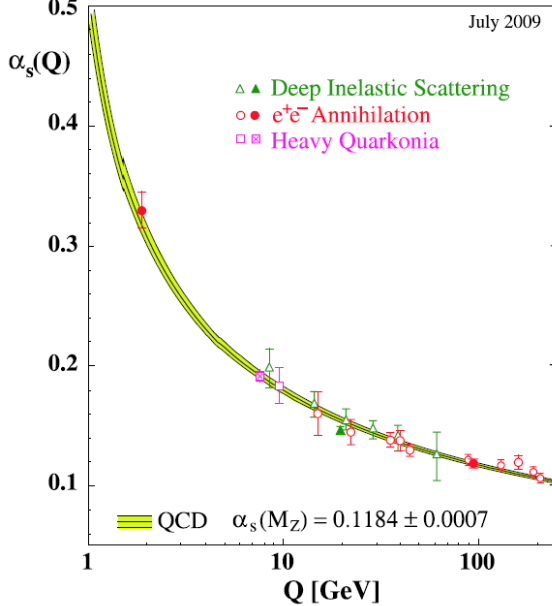


Figure 2.1: The strong coupling constant, α_s , as a function of the energy scale, Q [49].

thus disallowing the color neutral state for the gluon. The colored property of the gluon allows it to interact with itself, which has two very important consequences for QCD. The self-interaction of the gluon gives rise to both **confinement** and **asymptotic freedom**.

In QED the electric field diminishes with distance, allowing, for example, electrons to be separated from nuclei. However, due to the self interaction of the gluons, as two quarks separate the force between them grows proportionally to the distance between them. As a quark-antiquark ($q\bar{q}$) pair, for instance, separates it becomes energetically favorable at some distance to create a new $q\bar{q}$ pair out of the vacuum and the original $q\bar{q}$ pair now becomes two independent $q\bar{q}$ pairs. This mechanism is responsible for the lack of experimental observation of free quarks as well as the color neutral property of hadrons, and is known as confinement. Color neutrality arises, in the simplest form, from two different arrangements of quarks and antiquarks. The hadron can consist of a quark and antiquark pair where one quark carries a color and the other carries the corresponding anti-color (ex. $r\bar{r}$, $g\bar{g}$, $b\bar{b}$), giving rise to mesons. Alternatively the hadron can consist of three quarks or anti-quarks where each quark carries a different color (ex. rgb , $\bar{r}\bar{g}\bar{b}$). Hadrons consisting of three quarks are known as baryons. Color neutrality can also arise from combinations of quarks and gluons, or even arrangements of gluons with no valence quarks. These arrangements are known as exotic mesons, and experiments are actively searching for their signatures.

The self interaction of the gluon also has a significant effect on the screening of the bare quark color. In QED, charged pairs from the vacuum screen the bare electric charge, causing the observed charge to diminish. As one probes closer to the electron, a greater charge is seen because fewer charged pairs are affecting the observation. In QCD, $q\bar{q}$ pairs serve the same role, providing a screening effect on the bare color charge. However, the color-carrying

gluon in turn creates an *antiscreening* effect, which ends up dominating the screening coming from $q\bar{q}$ pairs. This means that the strong force actually gets weaker the closer one gets to a bare charge, which is called asymptotic freedom. This is directly manifested in the running of the strong coupling constant, α_s , as seen in Figure 2.1, where α_s represents the strength of the QCD force as a function of the energy scale. Consequently, if one gets sufficiently close, as in hard collisions where the energy transfer is large, the quarks can be thought of as moving freely, allowing perturbative calculations to be performed. The running of α_s provides this scale, usually denoted as Λ_{QCD} ², above which perturbative calculations should be valid.

2.1 QCD in Nuclear Matter - Cold Nuclear Matter Effects

In order to fully understand the results of any observables in heavy ion collision, in particular results from hard probes, effects due to normal nuclear matter must first be understood. It is known that the production of hard probes is modified from $p+p$ collisions when the production occurs in a nuclear target. These effects are collectively referred to as Cold Nuclear Matter (CNM) effects (or sometimes initial state effects).

The generally accepted CNM effects are:

Nuclear Shadowing: Modification of the parton distribution functions within a nucleus.

Gluon Saturation: Saturation of the gluon distribution function.

Radiative Energy Loss: Modification of the momentum fraction of partons due to multiple soft scatterings.

Cronin Effect: Broadening of the transverse momentum distribution due to multiple scattering of incident partons.

These effects are discussed in greater detail below.

2.1.1 Nuclear Shadowing

When performing perturbative calculations in QCD, it is generally assumed that calculations of cross sections for a hard process can be factorized into a product of parton density probability functions and a perturbatively calculable hard scattering cross section. The parton density probability functions are given by parton distribution functions (PDF's), which describe the probability density of quarks and gluons inside a free proton as a function of their longitudinal momentum fraction, x , and energy scale, Q^2 . An example PDF for an energy transfer of $Q^2 = 10 \text{ GeV}^2$ (roughly the scale relevant for J/ψ production) is shown in Figure 2.2. These PDF's are phenomenological parametrization of data taken mostly from deep inelastic scattering (DIS) experiments and Drell-Yan (DY) production. Both DIS and DY studies directly probe only the quark and antiquark distributions, while the gluon distribution is probed only indirectly. This leads to a larger uncertainty on the gluon distribution compared to those for the quarks (See [97] for a discussion of the uncertainties

² $\Lambda_{QCD} \approx 220 \text{ MeV}$.

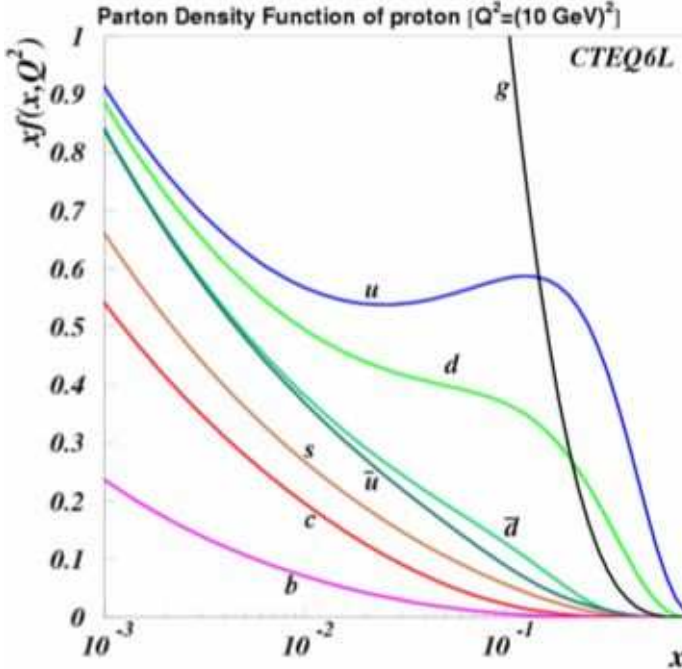


Figure 2.2: An example of a parton distribution function for the quarks and gluons at $Q^2 = 10 \text{ GeV}^2$ from the CTEQ collaboration [97]

on the CTEQ6 PDF). This is important, as the gluon distribution dominates hard scattering processes in the high energy collisions at RHIC.

Investigations of the parton distribution functions extracted from nuclear DIS experiments [45] found that the PDF's were modified for protons bound in a nucleus, leading to the development of nuclear parton distribution functions (nPDF's). The modification of the PDF's is typically quantified by the ratio

$$R_i^A(x, Q^2) = \frac{f_i^A(x, Q^2)}{f_i(x, Q^2)}, \quad (2.2)$$

where $f_i(x, Q^2)$ is the free proton PDF for parton flavor i , $f_i^A(x, Q^2)$ is the PDF for parton flavor i of a proton bound in nucleus A . Interesting structure is observed in the ratio, a purely schematic example of which is shown in Figure 2.3. The modification is generally broken into four regions, labeled as:

Shadowing refers to the low- x ($x \lesssim 0.03$) region where $R_i^A(x, Q^2) < 1$, signifying a decrease in the number of partons when compared to the free proton case. In the case of the gluon distribution, where this effect is largest, it is believed to be caused by fusion of gluons into a single, higher- x gluon, due to the greater density of gluons present in the nucleus.

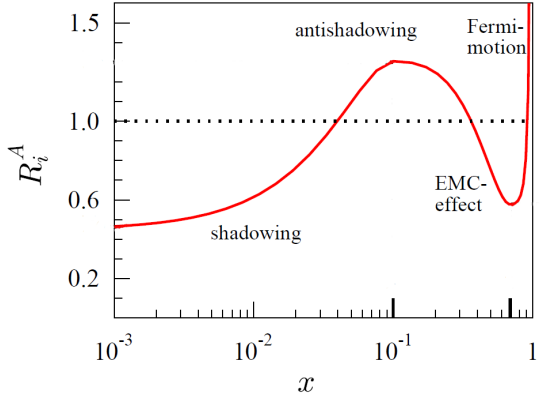


Figure 2.3: A purely schematic example of the modification of the parton distribution function in nuclei.

Anti-shadowing refers to the intermediate x region ($0.03 \lesssim x \lesssim 0.3$) where $R_i^A(x, Q^2) > 1$. In the case of the gluon distribution, this is believed to be caused by the fusion of low- x gluons, creating an excess in this region and a deficit in the lower x region.

EMC Region refers to the higher x region ($0.3 \lesssim x \lesssim 0.7$) where $R_i^A(x, Q^2) < 1$ and is named after the experiment which discovered this phenomenon in DIS experiments with nuclei [45]. No strong consensus has been reached as to the cause of this suppression. For a recent review, see [95].

Fermi-motion refers to the highest x region where $R_i^A(x, Q^2) > 1$ due to Fermi motion of the nucleons in the nucleus.

The nPDF modification in general is also sometimes referred to as shadowing, which can lead to some confusion. Here, the phenomenon of the modification of the PDF's will be referred to as nuclear shadowing, while shadowing alone (or the shadowing region) will refer to low- x suppression of the parton distribution.

As in the free proton case, it is assumed that the nPDF's can be factorized from the perturbative calculation of a hard scattering process. While factorization has proven to be very successful in the free proton case, there is some concern that factorization of the nPDF is less rigorous due to the possibility of multiple scatterings with different nucleons. However, this effect should be included in the nPDF's through the parametrization of the available data. In the nPDF case $l+A$ DIS measurements and DY dilepton production in $p+A$ collisions form the bulk of the data used in the parametrization of nPDF's. There are a number of parametrizations, referred to as nPDF sets, available. These include nDSg [58], EKS98 [65] and EPS09 [63]. EPS09 is the most common currently used nPDF set, as it provides not only the best fit to the available data (which also includes π^0 production data in $p+p$ and $d+Au$ collisions at RHIC), but an estimate of the uncertainty in the distributions. An example of the nPDF distributions from EPS09 is shown in Figure 2.4, along with a comparison to previous nPDF sets. While the valence and sea quark distributions are well constrained by the data, there is a large uncertainty in the gluon distribution, which is

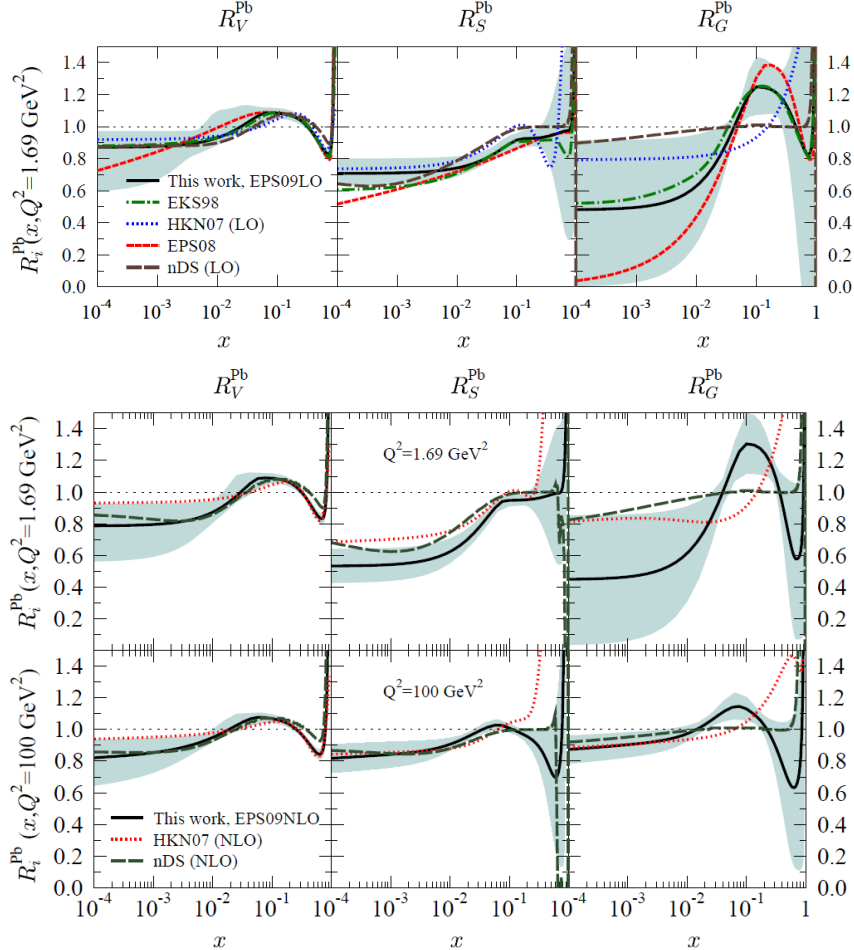


Figure 2.4: nPDF modifications for a Pb nucleus from EPS09 [63] (solid black lines) for the valence quark (R_V^{Pb}), sea quark (R_S^{Pb}) and gluon (R_G^{Pb}) distributions at LO(Top) and NLO(Bottom) compared to other nPDF sets.

alleviated somewhat only for very high Q^2 at NLO. As in the free proton case, the majority of the available data does not provide direct constraints on the gluon distributions. The main sources of constraint on the gluon distribution come from DIS measurements through the scale evolution of the sea quarks due to gluons, and also the RHIC π^0 results which provides the most direct constraint, although with large uncertainties on the data.

The nPDF modification is determined from data integrated over all impact parameters, and so contain no direct information on the centrality (impact parameter) dependence of the modification. In general, when nuclear shadowing is compared to data as a function of centrality, the centrality dependence must be introduced outside the nPDF framework. Recently, Helenius *et al* [74] have introduced an impact parameter nPDF set based on EPS09, which they refer to as EPS09s. This presents new and interesting opportunities to test the geometric dependence of nuclear shadowing.

2.1.2 Gluon Saturation

As shown in Figure 2.2, as one goes to smaller values of the longitudinal momentum fraction, x , (alternatively higher momentum transfer Q^2) the density of gluons begins to quickly dominate that of the quarks. At some scale, known as the saturation scale, Q_s , the density of gluons per unit transverse area becomes so large that individual gluons begin to overlap and can no longer be resolved. This evolution, along with the evolution of Q_s , is shown schematically in Figure 2.5. This leads to a saturation of the gluon distribution where non-linear corrections to the normal evolution equations dominate. If the saturation scale is large compared to the perturbative scale ($Q_s \gg \Lambda_{QCD}$), then weak coupling techniques can be employed. This led to the development of an effective field theory known as the Color Glass Condensate (CGC), which attempts to explain the small- x behavior of QCD [72, 92].

While initial state energy loss and the Cronin effect describe inherently different physical phenomena, nuclear shadowing and gluon saturation are not so clearly separated. While it is not entirely clear, gluon saturation and nuclear shadowing are likely two different interpretations of the same physical phenomenon. Both essentially deal with the modification of the x and Q^2 dependence of parton distributions. In the gluon saturation picture this is interpreted as arising from coherent interactions of gluons above some scale, while nuclear shadowing assumes the nucleus is simply a collection of bound nucleons and parametrizes the collective modification.

One limitation of the CGC framework is that it is naturally limited in its range of applicability through the saturation scale Q_s . Calculations indicate that this approach is valid for low- p_T process at forward rapidity at RHIC, where the x values probed are typically small, however it breaks down near midrapidity. At the LHC, however, the CGC should be applicable over a much wider range of rapidity and p_T due to the significant increase in collision energies, and thus decrease in x , achieved.

Unambiguous confirmation of the gluon saturation picture is elusive. While many calculations performed within the CGC framework are in good agreement with experimental data, there are a number of competing pictures (such as nuclear shadowing) which are in equally good agreement, and in many instances applicable over a wider kinematic range. Although no clear signature of the CGC has yet been found, this is still a very active area of both theoretical and experimental interest. The future upgrades program for PHENIX,

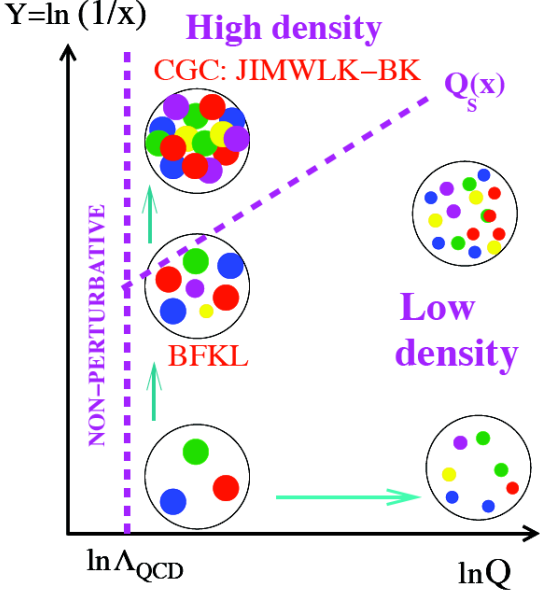


Figure 2.5: A schematic picture of the evolution of proton parton density with x and Q^2 .

called sPHENIX, includes a forward physics program with one of it's main goals searching for clear signatures of the CGC [101].

2.1.3 Cronin Effect

In 1974, modification of the transverse momentum, p_T , distributions of particles in $p+A$ collisions compared to scaled $p+p$ collisions was observed [56]. This modification, termed the Cronin effect, is typically attributed to multiple elastic scattering of the incoming parton before undergoing a hard collision. When observing the ratio of the production cross section for particles in $p+A$ relative to the scaled $p+p$ reference, this effect manifests itself as a suppression at low- p_T followed by a compensating excess at intermediate p_T with the ratio returning to 1 at high- p_T .

2.1.4 Radiative Energy Loss

Radiative energy loss is due to radiation, or exchange, of gluons with the medium. This can come in two flavors, initial state energy loss and final state energy loss. The main difference being what is radiating the gluons. In initial state energy loss the incoming parton radiates gluons as it traverses the medium, before the hard scatter process occurs. This decreases the incoming parton x , effectively causing a shift in the parton distribution relative to $p+p$ collisions. In final state energy loss, it is the outgoing particle, either a quark, gluon, or meson, which radiates energy as it traverses the medium. This also effectively decreases the x of the outgoing particle. For a recent review of radiative energy loss, see [40].

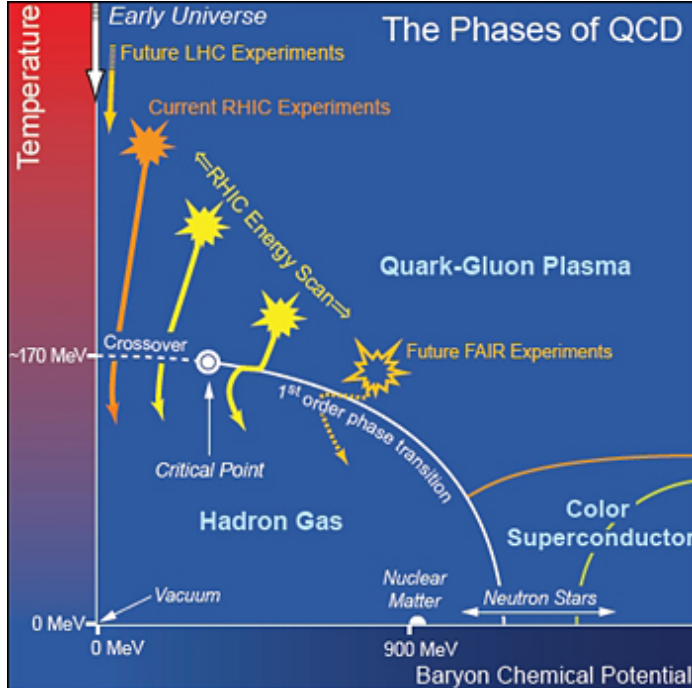


Figure 2.6: A schematic view of the phase diagram for QCD matter.

2.2 A New Phase of QCD - The Quark Gluon Plasma

The main goal of the heavy ion physics program is to map out the high temperature low baryon chemical potential region of QCD matter through collisions of heavy ions at high energies. A schematic view of the QCD phase diagram is shown in Figure 2.6. If the temperature or net baryon density is high enough, QCD suggests that a transition should occur from normal nuclear matter, where quarks and gluons are confined in hadrons, to a new state of matter where the quarks and gluons are deconfined. Analogous to electric plasmas, the abundance of color charge creates a Debye screening effect which limits the interaction length of the strong force, allowing the deconfinement of the quarks and gluons. This is discussed further in Section 3.2. This state of deconfined quarks and gluons is called the quark gluon plasma (QGP). It is expected that the universe would have existed in a QGP state with zero net baryon density during the first few microseconds after the Big Bang and it is possible that neutron stars, which have a low temperature but high net baryon number, might contain a QGP at their core. The QGP is a naturally interesting target for scientific study.

The transition between quark confinement and deconfinement is a non-perturbative process, and normal perturbative QCD approaches are no longer valid. To perform calculations in this regime Lattice QCD (LQCD) is used. In LQCD numerical non-perturbative QCD calculations are performed on a discrete grid of space time points. In the limit of infinitely small lattice spacings this approach regains continuum QCD. Practically, this approach is computationally limited, as increasingly small lattice spacing requires increasingly intensive

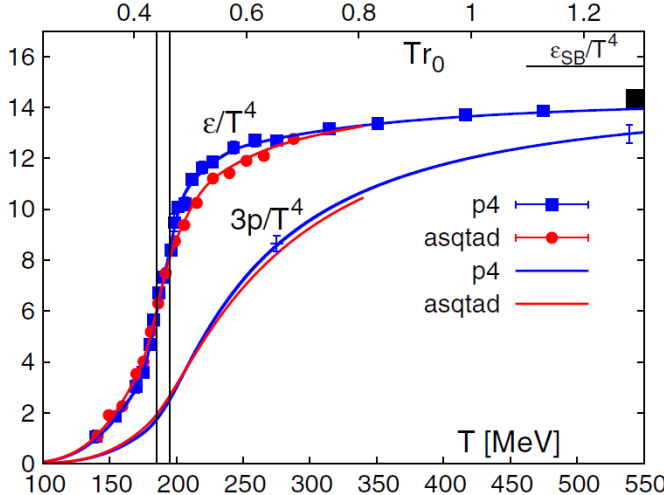


Figure 2.7: The energy density and three times the pressure normalized to $1/T^4$ as a function of temperature from LQCD [47]. The vertical lines indicate the transition region ($180 < T [\text{MeV}] < 200$) between normal nuclear matter and a deconfined QGP.

numerical calculations. LQCD has been critical in making tests of QCD for scales where $\alpha_s \simeq 1$. In principal, LQCD has 6 input parameters, α_s and the 5 quark masses (m_u , m_d , m_s , m_c , m_b)³. One advantage of LQCD is the ability to “easily” vary the quark masses and observe the systematic dependence of results, for example the mass of the pion, on the input quark masses. This can help constrain our understanding of the bare quark masses. For a more in-depth introduction to LQCD, see [73].

Lattice QCD calculations predict that the transition to a QGP should occur at a critical temperature of $T_c \approx 170$ MeV for 0 net baryon density. This transition is indicated by a large change in the energy density as a function of temperature, as shown in Figure 2.7 [47]. These calculations are performed in (2+1) flavor QCD with a physical strange quark mass (m_s) and 2 degenerate up and down quark masses which are taken to be $\frac{1}{10}m_s$. Measurements of the initial temperature at RHIC through direct photons gives an initial temperature of $T \approx 300$ MeV [17], approximately $1.7T_c$, indicating a likely transition to a QGP at RHIC energies. The higher energies achieved in Pb+Pb collisions at the LHC yield temperatures $\approx 30\%$ higher than those at RHIC under the conservative estimate that the formation time is the same at both energies [93].

While deconfinement of quarks and gluons has not been directly observed in collisions at RHIC, there are a number of experimental signatures which indicate the likelihood of QGP production at RHIC. Three of these signatures are discussed below.

³The top quark is excluded in LQCD, as its lifetime is too short to form bound states.

2.2.1 Quark Scaling of Elliptic Flow

In Au+Au collisions at RHIC it was found that there was a significant anisotropy of produced particles relative to the plane of the Au+Au reaction. This anisotropy is related to the shape of the initial interaction region. As the two Au nuclei collide, the most likely scenario is some modest amount of overlap between the nuclei. This creates an almond shaped interaction region leading to an asymmetric pressure gradient. For collisions of identical nuclei, the particle density at an angle ϕ at midrapidity can be described by an expansion of the form

$$\frac{d^2N}{d\phi dp_T} = \frac{N_0}{2\pi} (1 + \sum_n 2v_n(p_T) \cos [n(\phi - \Psi_{plane})]), \quad (2.3)$$

where Ψ_{plane} is the angle of the reaction plane, and v_n are the Fourier coefficients, the second of which, v_2 measures the elliptic flow.

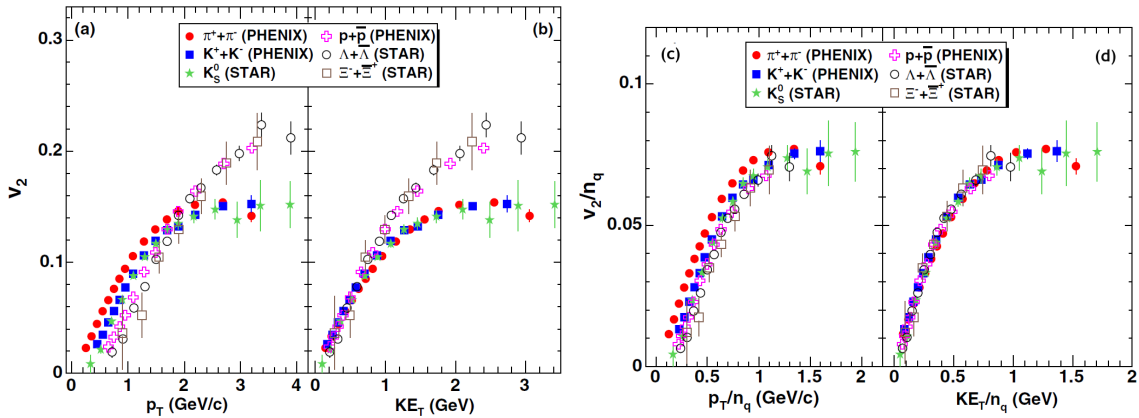


Figure 2.8: (a) v_2 vs p_T , (b) v_2 vs KE_T , (c) v_2/n_q vs p_T and (d) v_2/n_q vs KE_T for identified particle species obtained in minimum bias Au+Au collisions at $\sqrt{s_{NN}} = 200$ GeV [12].

The v_2 for identified hadrons in Au+Au collisions at RHIC [12] as a function of p_T is shown in Figure 2.8(a). It was found that plotting the v_2 as a function of the transverse kinetic energy (KE_T), which takes into account relativistic effects, produced a similar scaling for all mesons, and a separate scaling for baryons, as shown in Figure 2.8(b). The similarity between the v_2 vs KE_T for all particles at $p_T \lesssim 1$ GeV/ c suggests evidence of some universal scaling. Dividing v_2 and KE_T by the number of constituent quarks, n_q ($n_q = 3$ for baryons, $n_q = 2$ for mesons), as shown in Figure 2.8(d), results in good scaling over the measured KE_T range. This behavior suggests that for the bulk of produced particles the relevant degrees of freedom are partonic, as one would expect within a QGP, rather than hadronic.

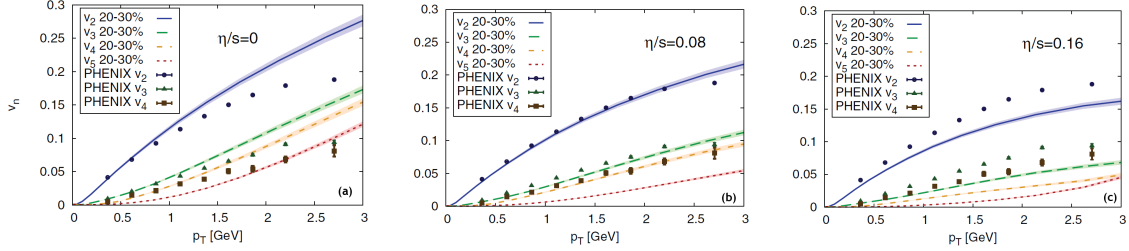


Figure 2.9: The p_T dependence of v_2 through v_5 [22]. The curves are calculations from ideal hydrodynamics (a), viscous hydrodynamics with $\eta/s = 0.08$ (b) and $\eta/s = 0.16$ (c) [99].

2.2.2 Near-perfect Fluidity of the Medium Produced in Au+Au Collisions

The elliptic flow of measured particles, as discussed in Section 2.2.1, also gave rise to the understanding that the produced medium at RHIC flows like a near-perfect fluid. The large v_2 observed at RHIC was a surprise. It was assumed that because α_s gets weaker at higher energies the produced medium would be weakly coupled, essentially a partonic gas. But the large measured v_2 indicated a strongly coupled medium. The strength and shape of the v_2 is well described by ideal hydrodynamics with a vanishing value for the viscosity to entropy density ratio, η/s . This ratio is estimated to be the smallest value for any known fluid.

Increases in the understanding of the initial state, as well as increases in the sophistication of the hydrodynamic calculations continue to indicate a small value for η/s . A recent calculation [88] which attempts to include many of the model and experimental uncertainties gives a value of

$$\frac{\eta}{s} = 0.1 \pm 0.1(\text{theory}) \pm 0.08(\text{experiment}). \quad (2.4)$$

With the increased understanding of the initial state has come the realization that not only is v_2 large and important, but the higher order harmonics such as v_3 , v_4 , and v_5 , which come from fluctuations in the initial state, play a significant role and can be used to help constrain η/s . The p_T dependence of v_2 , v_3 , v_4 , and v_5 in Au+Au collisions at RHIC is shown in Figure 2.9. Also shown in Figure 2.9 are three hydrodynamic calculations with different assumed values for η/s [99]. While not a fit to the data, $\eta/s = 0.08$ provides a good description of the available data.

2.2.3 Suppression of High- p_T Hadrons in Au+Au Collisions

The angular correlation of high- p_T hadrons has been measured by both the STAR [9] and PHENIX [27, 28, 26] collaborations for $p+p$, $d+\text{Au}$ and Au+Au collisions at $\sqrt{s_{NN}} = 200$ GeV. In [9], when measuring the angular correlation, the trigger particle is required to have $4 < p_{T,\text{trig}} [\text{GeV}/c] < 6$. The angular correlation relative to the trigger particle is then measured for all associated particles with $2 < p_{T,\text{assoc}} [\text{GeV}/c] < p_{T,\text{trig}}$ in the same event. The angular correlations in $p+p$, $d+\text{Au}$ and Au+Au after subtraction of the underlying

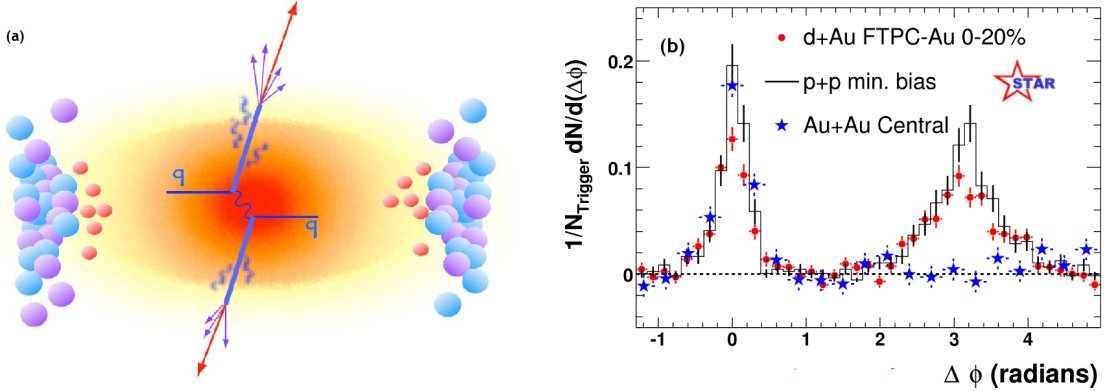


Figure 2.10: (a) A cartoon of jet production in a hot medium. (b) Comparison of the two particle azimuthal distributions for $p+p$, $d+\text{Au}$, and $\text{Au}+\text{Au}$ collisions at $\sqrt{s_{NN}} = 200$ GeV [9].

background are shown in Figure 2.10(b) [9]. In $p+p$ and $d+\text{Au}$ collisions two peaks are observed, the first centered at $\Delta\phi \approx 0$ and the second centered at $\Delta\phi \approx \pi$. The peaks are interpreted as being due to hadrons from back to back jets. The hadronization of the jets will create a cone of particles centered around the original parton direction.

In $\text{Au}+\text{Au}$ collisions, however, a complete suppression of the away-side ($\Delta\phi \approx \pi$) peak is observed. This is indicative of the suppression of the jet in the produced medium. As the partons traverse the QGP medium, energy will be lost through interactions with the intense color field. Or, if the jet hardonizes while still inside the medium, the momentum distribution of the produced hadrons will also be modified by the presence of the color field through which they must propagate. A simple cartoon is shown in Figure 2.10(a). It is difficult to interpret the results shown in Figure 2.10(b) without the presence of an *extremely* dense colored medium, such as the QGP.

CHAPTER 3

CHARMONIA AND THE J/ψ

The J/ψ , a meson constructed from a charm anti-charm ($c\bar{c}$) quark pair with a mass of 3.096 GeV/ c^2 , was discovered in 1974 by groups at both BNL [44] and SLAC [46]. This was the first member of the charmonium family, those mesons constructed from a $c\bar{c}$ pair, to be discovered. Just 10 days later a second resonance with a mass of 3.695 GeV/ c^2 was discovered at SLAC [4], designated the ψ' . Since 1974 a number of further $c\bar{c}$ mesons have been discovered (see Figure 3.1), with experimental interest in the spectrum continuing today.

Since the charm quark carries the majority of the mass of the charmonium mesons ($2m_c \approx 2.6$ GeV) the meson can be described, to a good approximation, by a model of a nonrelativistic quark anti-quark pair. This allows for the treatment of charmonium using a potential coupled with the Schrodinger equation. An approximation of the charmonium potential can be written as

$$V(r) = \sigma r - \frac{\alpha}{r}, \quad (3.1)$$

where r is the separation of the $q\bar{q}$ pair. The potential contains a Coloumb-like term and a linear term, which models the confinement. This potential is known as the ‘‘Cornell potential’’ [60, 61], and using the input parameters $m_c = 1.25$ GeV, $\sqrt{\sigma} = 0.445$ GeV and $\alpha = \pi/12$ the masses of the charmonium states can be calculated, as well as the average radius, r_0 . The masses calculated in this manner agree with the experimental observations to better than 1% [98], and are shown along with the radii in Table 3.1 ¹.

Analogous to the hydrogen atom, the charmonia states can be described by their orbital angular momentum, L , the total spin of the $c\bar{c}$ pair, S , the total angular momentum, J , and the radial excitation n_r where $n_r = 0$ corresponds to the ground state. The quantum numbers for the states are customarily encoded in the form $(n_r + 1)^{(2S+1)} L_J$. For example, the J/ψ is designated as 1^3S_1 while the ψ' is designated 2^3S_1 . The charmonium spectrum for those mesons which are stable under strong decays, namely those which have a mass below the $D\bar{D}$ threshold of 3.73 GeV/ c^2 , are shown in Figure 3.1 along with their quantum numbers and prominent decay modes. Further information for each of the charmonia states, including the binding energy and approximate radius, can be found in Table 3.1.

The J/ψ meson is of particular interest experimentally. The fact that it has $J^{PC} = 1^{--}$ allows direct l^+l^- decays, which are easy to detect experimentally. On top of that, the OZI

¹The three χ_{ci} states are often written as the spin averaged state χ_c , with a radius from potential models of 0.72 fm

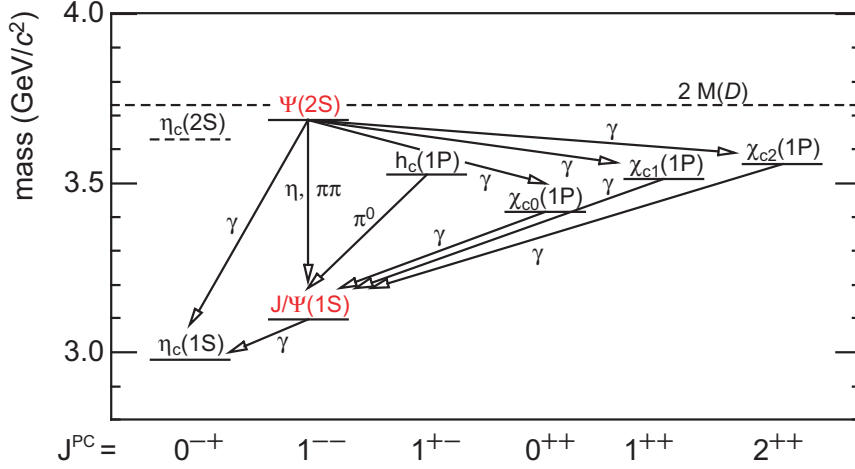


Figure 3.1: Spectrum of the charmonia states which are stable under strong decays and their dominant decay modes.

Table 3.1: Properties of various charmonia states. For the χ_{ci} states, r_0 and T_D are given for the spin averaged χ_c state.

| state | η_c | J/ψ | χ_{c0} | χ_{c1} | χ_{c2} | ψ' |
|--------------------|----------|----------|-------------|-------------|-------------|----------|
| $n_r^{2S+1}L_J$ | 1^1S_0 | 1^3S_1 | $1^{-1}P_0$ | 1^1P_1 | 1^3P_2 | 2^3S_1 |
| J^{PC} | 0^-+ | 1^{--} | 0^{++} | 1^{++} | 2^{++} | 1^{--} |
| Mass [GeV/ c^2] | 2.98 | 3.10 | 3.42 | 3.51 | 3.56 | 3.69 |
| ΔE [GeV] | 0.75 | 0.64 | 0.32 | 0.22 | 0.18 | 0.05 |
| r_0 [fm] | | 0.50 | | 0.72 | | 0.90 |
| T_D | | | $1.2T_c$ | $\leq T_c$ | $\leq T_c$ | |

rule strongly suppresses the hadronic decays of the J/ψ , giving a relatively large branching fraction to dileptons, with $B(J/\psi \rightarrow e^+e^-) = (5.94 \pm 0.06)\%$ and $B(J/\psi \rightarrow \mu^+\mu^-) = (5.93 \pm 0.06)\%$ [48]. The suppression of hadronic decays through the OZI rule also gives the J/ψ its characteristically narrow width of 92.9 ± 2.8 keV [48]. The relatively large branching fraction to dieleptons along with its narrow width make the J/ψ an ideal probe experimentally.

The remainder of this chapter is dedicated to giving a brief introduction to recent theoretical and experimental results on charmonia production, in particular the J/ψ and ψ' states, to provide motivation for the analysis detailed in this work, as well as to give the reader context for interpreting the results presented here. For a more in-depth review of quarkonia, the general term for heavy quark anti-quark mesons, see [51].

3.1 Production Mechanism

Despite almost 40 years since the discovery of the J/ψ , a concrete understanding of the production mechanism for hadroproduction of charmonia states is still evolving. The production of charmonia states is often thought of as occurring in two stages, governed by different time scales. First, the $c\bar{c}$ pair is created, which is a short distance process on scales of order $1/m_c$ and therefore can be calculated perturbatively. The evolution of the $c\bar{c}$ into a physical meson, however, involves long distance scales on the order $1/m_c v$, where v is the typical velocity of the c or \bar{c} in the charmonia rest frame ($v^2 \approx 0.3$ for the J/ψ [51]), and therefore involves non-perturbative processes. Provided the two scales are well separated ($1/m_c v \gg 1/m_c$), then it is likely that the two processes can be factorized. This is the assumption made in the majority of theories used to describe charmonia production. Three of the most prevalent theories, the color-singlet model (CSM), the color-evaporation model (CEM), and nonrelativistic QCD (NRQCD) are discussed briefly below.

In the color-singlet model [62], the $c\bar{c}$ pair that evolves into the charmonia meson is assumed to be in the color-singlet state with the same spin and angular momentum quantum numbers as the charmonia state. The CSM was successful at predicting the production cross sections at lower energies [100], however at higher energies it was found that large corrections appear at next-to-leading order (NLO) and next-to-next-to-leading order (NNLO) in α_s , the strong coupling constant. This brings into question the convergence of the perturbative expansion in α_s . Furthermore, the CSM contains known infrared divergences in the χ_c production and decay processes.

In the color-evaporation model [70], it is assumed that every $c\bar{c}$ pair created with a mass less than that for producing a pair of open-heavy flavor (D or \bar{D}) mesons evolves into a charmonium meson, where the color of the $c\bar{c}$ pair is neutralized by soft gluon emission. The probability that a $c\bar{c}$ pair will evolve into a specific charmonium meson is taken to be energy, momentum and process independent, and is fixed by comparison to measured total cross sections.

NRQCD [50] is an effective field theory of QCD where the quark and anti-quark are treated nonrelativistically. The theory reproduces the dynamics of full QCD for scales $m_Q v$ and smaller where m_Q is the mass of the heavy quark, Q . In this approach the inclusive cross section for direct production of a quarkonia state, H , is written as a sum of terms, each of which factors into a product of the cross section for producing a $Q\bar{Q}$ pair multiplied

by the NRQCD matrix elements,

$$\sigma(H) = \sum_n \sigma_n(\Lambda) \langle \mathcal{O}_n^H(\Lambda) \rangle. \quad (3.2)$$

Here Λ is the ultraviolet cutoff of the effective theory, n represents a given color, spin, and angular momentum state. $\sigma_n(\Lambda)$ is the cross section for producing a $Q\bar{Q}$ pair in the given state n , and is therefore the short distance piece which can be calculated perturbatively. $\langle \mathcal{O}_n^H(\Lambda) \rangle$ is the NRQCD matrix element for transitioning from the $Q\bar{Q}$ state to the quarkonia state, H [51]. In principle then, one must sum over an infinite number of the nonperturbative long distance NRQCD matrix elements. Typically, however, these are arranged in powers of the quark velocity, v , and truncated at a given order of v , yielding a double expansion in terms of α_s and v . Assuming the validity of the perturbative nature of the $Q\bar{Q}$ cross section and the universality of the matrix elements, along with the truncation at a given order of v , NRQCD is the most comprehensive of the models presented here, as well as the most sound theoretically. For instance, if one retains only the color-singlet states in Equation 3.2 and truncates at leading order in v , CSM is reproduced.

In NRQCD, not only are the color-singlet states considered, but also the color-octet states. In the color-octet case the $Q\bar{Q}$ state neutralizes its color by the emission of soft gluons, as in the CEM case, which then allow the $Q\bar{Q}$ to evolve into a colorless quarkonia state with the appropriate quantum numbers. In addition to the color-octet state, processes of higher order in α_s should also be taken into account. It has generally been found that, while the overall cross section does not change significantly with the inclusion of processes of higher order in α_s , the differential cross section in p_T can be greatly affected [51].

At RHIC (and LHC) energies, the gluon distribution dominates within the proton. Therefore charmonia production, already a lower x process, proceeds through gluon fusion or gluon fragmentation. At the higher energies provided at RHIC, formation processes other than the leading order color-singlet production could begin to dominate. A selection of Feynman diagrams for charmonia production at LO (α_s^3), NLO, and NNLO via color-singlet and color-octet processes are shown in Figure 3.2.

Predictions for the p_T dependence of J/ψ production at RHIC based on CSM, CEM, and NRQCD are compared with inclusive J/ψ measurements by PHENIX [20] in Figure 3.3. Both the CEM and NRQCD calculations provide good descriptions of the data over the p_T range calculated. The CSM calculations however disagree with the data strongly, showing a cross section which falls much more rapidly with p_T than is seen in the data. It should be mentioned that none of the calculations shown in Figure 3.3 take the B -meson feeddown into account. According to the Fixed Order plus Next-to-Leading Logarithms (FONLL) calculations, B -meson feeddown accounts for $\approx 2\%$ of the inclusive J/ψ yield at 1 GeV/ c and $\approx 20\%$ at 7.5 GeV/ c in the midrapidity region [51].

One observable, not discussed here, which provides additional constraints on production models is the charmonia polarization. At RHIC energies, both NRQCD and NLO CSM calculations of the J/ψ polarization are in agreement with the PHENIX data [18]. However, tension remains between NRQCD calculations and CDF data taken at $\sqrt{s} = 1.8$ TeV. For a more detailed discussion, see [51].

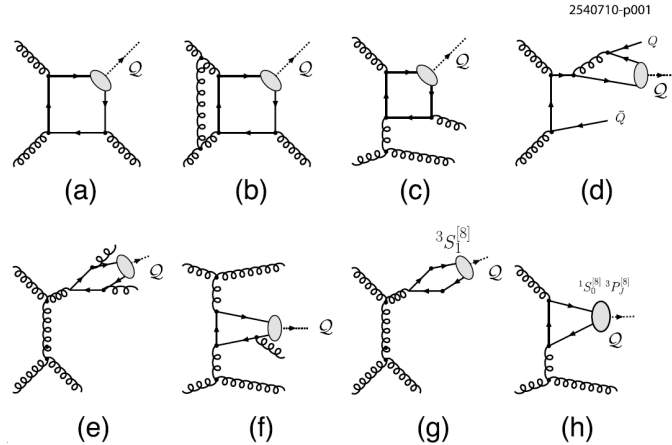


Figure 3.2: Representative Feynman diagrams which contribute to the production of 3S_1 quarkonia states via color-singlet channels at order α_s^3 (a), α_s^4 (b,c,d) and α_s^5 (e,f) and via color-octet channels at order α_s^3 (g,h). Figure taken from [51].

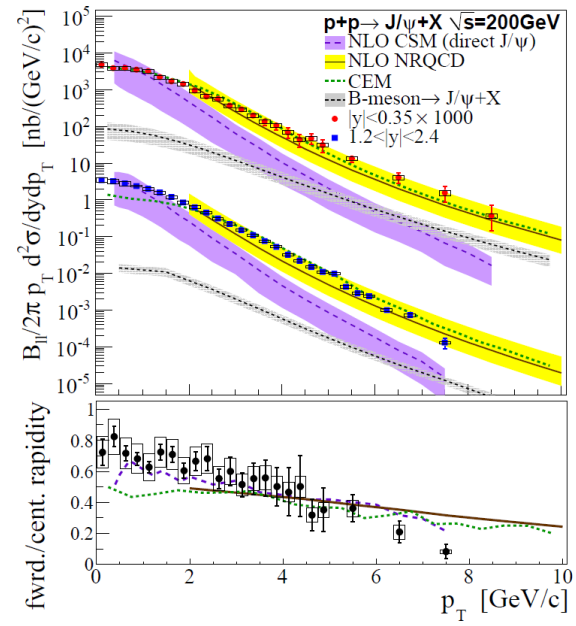


Figure 3.3: The inclusive J/ψ p_T distributions at $|y| < 0.35$ and $1.2 < y < 2.4$ measured by PHENIX [20]. Included are predictions based on CSM [85], CEM [69], NRQCD [53], and B -meson decay based on FONLL calculations [54].

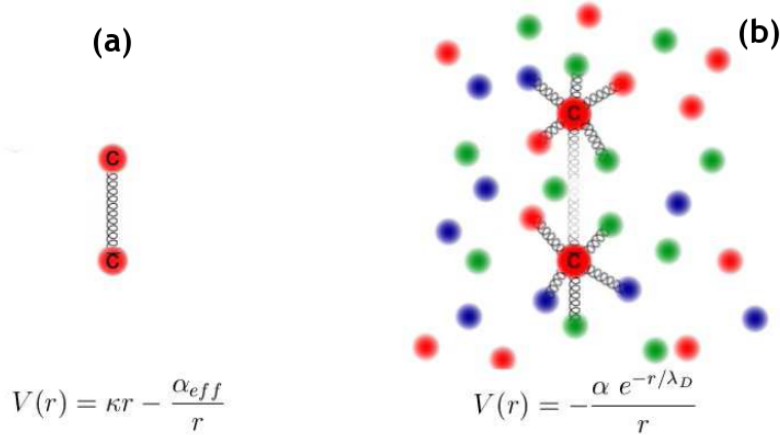


Figure 3.4: A cartoon picture of a $c\bar{c}$ in the vacuum (a) compared to in a QGP medium (b).

3.1.1 Feeddown to J/ψ from higher mass charmonium states

When measuring the modification of the production of J/ψ 's through the dilepton channel in either a nuclear environment or a hot nuclear medium, as discussed in the remainder of this chapter, it is important to consider the feeddown from higher mass charmonia resonances. Measurements of J/ψ , ψ' , and χ_c production in $p+p$ collisions at RHIC [20] suggest that $(9.7 \pm 2.4)\%$ and $(32 \pm 9)\%$ of observed J/ψ 's in the dielectron channel come from ψ' and χ_c decays respectively. The results at $\sqrt{s} = 200$ GeV are in good agreement with the world averages for these feeddown fractions of $(8.1 \pm 0.3)\%$ and $(25 \pm 5)\%$ for ψ' and χ_c decays respectively [66]. This suggests that direct J/ψ production accounts for only $\approx 60\%$ of observed J/ψ 's.

3.2 Charmonia as a Probe of Hot Nuclear Matter

In 1986 Matsui and Satz [89] predicted that “ J/ψ suppression in nuclear collisions should provide an unambiguous signature of quark-gluon plasma formation.” The presence of deconfined quarks and gluons should create a Debye screening of the color charge. If the radius of the J/ψ is larger than the screening radius, it would lead to a clear dissociation of the J/ψ . This can be thought of as a dominance of short range interactions in the QGP over long range interactions, shown pictorially in Figure 3.4. Over the intervening years the suppression of J/ψ production in heavy ion collisions has been observed over a wide range of collision energies from $\sqrt{s_{NN}} = 17$ GeV to $\sqrt{s_{NN}} = 2.76$ TeV. However, the suppression of J/ψ production in heavy ion collisions has not been the smoking gun it was hoped to be due to a number of complications.

Debye screening occurs in a medium of charged particles when the interaction between particles is modified (reduced or canceled) due to the presence of surrounding charged particles. This is well known in electromagnetic plasmas, and the effect is easily translated to

color charge. The screening length, called the Debye radius (λ_D) in lowest order perturbative QCD is given by [111]

$$\lambda_D(T) = \sqrt{\frac{2}{9\pi\alpha}} \frac{1}{T}, \quad (3.3)$$

where α is the coefficient of the Coloumbic term in the charmonia potential (Equation 3.1).

For a simple estimate, it is expected that in a QGP the linear term of the potential disappears and a screening factor modifies the Coloumb term. This gives a potential of the form

$$V(r) = -\frac{\alpha}{r} e^{-r/\lambda_D(T)}. \quad (3.4)$$

Using the modified potential it is estimated that the J/ψ would become dissociated for $T \approx 1.2T_c$, where T_c is the critical temperature for forming a QGP [89].

Over the intervening years more detailed calculations have been performed in LQCD and potential models on the spectral functions of charmonium in a QGP. While the work is ongoing (see [51] for a recent review), a range on the dissociation temperature, T_D , is given for the charmonia states in Table 3.1.

It has also been theorized that there are effects of the QGP which could actually *enhance* J/ψ production, known as recombination or coalescence. Recombination comes in two forms. The first is simply the combination of a random c and \bar{c} during hadronization. These $c\bar{c}$ pairs are not necessarily created during the same hard scattering nor do they require any initial correlation. In the simplest picture, if a c and \bar{c} are near each other in phase space during hardonisation they have some probability of forming a charmonium bound state. This effect should therefore produce a number of J/ψ 's which scales as roughly $N_{J/\psi} \sim N_{c\bar{c}}/N_h$ where N_h represents the number of light hadrons and $N_{c\bar{c}}$ is the total number of produced $c\bar{c}$ pairs. A hallmark of this effect is that it increases drastically with centrality and collision energy (since more charm quarks are produced), and in extreme cases can cause an enhancement in the J/ψ production relative to $p+p$ collisions. The second possibility is that $c\bar{c}$ pairs created in the same hard process, but which did not form a charmonium bound state, may retain some correlation. At hadronization, if they are in the right phase space, they then have a probability of recombining into a charmonium bound state. This process is essentially independent of $N_{c\bar{c}}$ and can produce a similar effect at widely different collision energies, even though there may be a large increase in $N_{c\bar{c}}$. For recent calculations of J/ψ production in Au+Au collisions including coalescence, see [112, 113]

3.2.1 SPS $A + A$ Results

J/ψ production has been measured at the CERN SPS in fixed target S+U, Pb+Pb and In+In collisions at $\sqrt{s_{NN}} = 20, 17$, and 17 GeV respectively [6, 34, 42]. The results showed for the first time the suppression of the J/ψ production cross section ($\sigma_{J/\psi}$) relative to the Drell-Yan cross section (σ_{DY}). The high mass Drell-Yan cross section was used as a baseline because it should not be strongly modified in the medium, unlike the J/ψ , and instead should scale simply as the number of nucleon-nucleon collisions. This suppression was believed to be the first evidence of deconfinement and the formation of a QGP [7]. However, other factors such as the large crossing time of the nuclei at the lower energies,

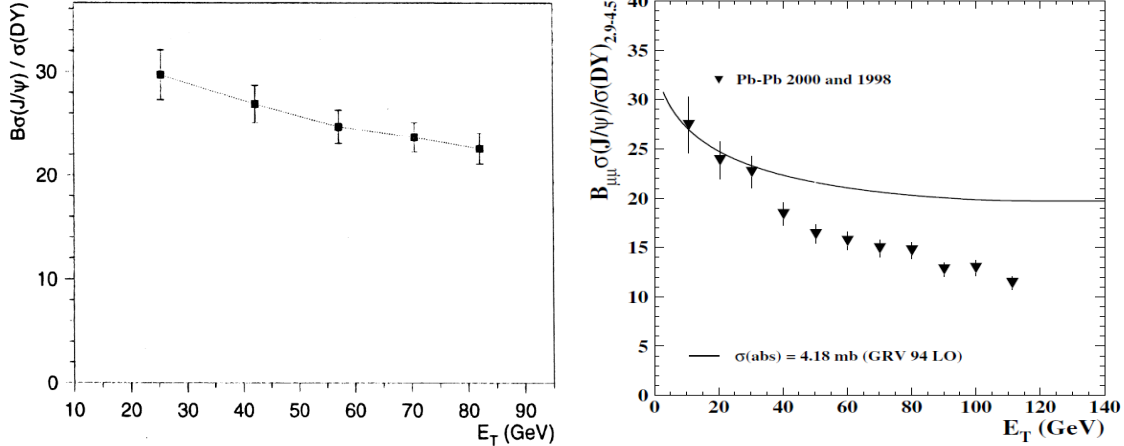


Figure 3.5: (Left) The ratio of the J/ψ production cross section to the Drell-Yan production cross section in the range $2.9 < M [\text{GeV}/c^2] < 4.5$ in $\sqrt{s_{NN}} = 20 \text{ GeV}$ S+U collisions as measured by the NA38 Collaboration [6]. (Right) The ratio of the J/ψ production cross section to the Drell-Yan production cross section in the range $2.9 < M [\text{GeV}/c^2] < 4.5$ in $\sqrt{s_{NN}} = 17 \text{ GeV}$ Pb+Pb collisions as measured by the NA50 Collaboration [34].

anti-shadowing, and the normal nuclear absorption of J/ψ 's (discussed later) makes the claim less straightforward.

3.2.2 RHIC Au+Au Results

The PHENIX experiment at RHIC has measured J/ψ production in Au+Au collisions at $\sqrt{s_{NN}} = 39$ [23], 62 [23], and 200 GeV [11, 21] and in Cu+Cu collisions at $\sqrt{s_{NN}} = 200$ GeV [14]. A substantial suppression of J/ψ production in $A + A$ collisions relative to $p+p$ collisions is observed, where the suppression is quantified as the nuclear modification factor R_{AB} for an $A + B$ collision. R_{AB} is given by

$$R_{AB} = \frac{d\sigma_{J/\psi}^{AB}/dy}{\langle N_{\text{coll}} \rangle d\sigma_{J/\psi}^{pp}/dy}, \quad (3.5)$$

where $d\sigma_{J/\psi}^{AB}/dy$ is the differential J/ψ production cross section in $A + B$ collisions, $d\sigma_{J/\psi}^{pp}/dy$ is the differential J/ψ production cross section in $p+p$ collisions, and $\langle N_{\text{coll}} \rangle$ is the mean number of nucleon-nucleon collisions in the given centrality bin. In the ratio R_{AB} J/ψ production is assumed to scale with the number of hard process (or binary (N_{coll}) scaling), in which case $R_{AB} = 1$. Any deviation from N_{coll} scaling will yield $R_{AB} > 1$ for an enhancement in J/ψ production relative to $p+p$ collisions, or $R_{AB} < 1$ for a suppression of J/ψ production relative to $p+p$ collisions.

3.2.2.1 The RHIC J/ψ Puzzle. The nuclear modification factor, R_{AA} , for J/ψ production in Au+Au collisions at $\sqrt{s_{NN}} = 200 \text{ GeV}$ [21] as a function of the number of

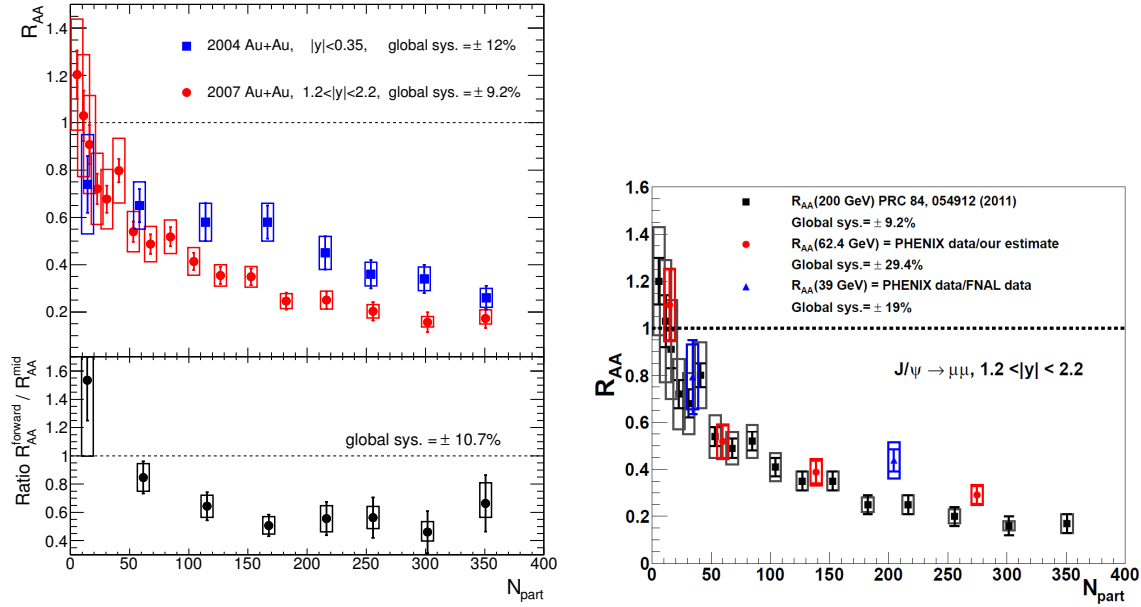


Figure 3.6: (Left) The J/ψ R_{AA} measured by PHENIX at $\sqrt{s_{NN}} = 200$ GeV [21]. (Right) The J/ψ R_{AA} in $1.2 < |y| < 2.2$ measured by PHENIX in $\sqrt{s_{NN}} = 39, 62.4$, and 200 GeV Au+Au collisions [23]

participant nucleons (N_{part}) is shown in Figure 3.6. The R_{AA} in Figure 3.6 is shown in two different rapidity regions, where rapidity (y) is the relativistic velocity along the beam direction given by

$$y = \frac{1}{2} \ln \frac{E + p_z}{E - p_z}, \quad (3.6)$$

where E is the energy of the particle and p_z is the momentum of the particle along the beam direction. In general, rapidity is used in collider experiments because the addition of rapidity maintains Lorentz invariance.

There are two striking features of Figure 3.6. The first is the strong trend of increasing suppression with increasing N_{part} , with $R_{AA} \approx 0.3$ for the most central (largest N_{part}) collisions. This is evidence that J/ψ production is strongly suppressed in Au+Au collisions relative to $p+p$ collisions at RHIC, a finding which is not unexpected based on the results from the SPS. The second feature, which came as a surprise, is the larger suppression at forward rapidity ($1.2 < |y| < 2.2$) compared to midrapidity ($|y| < 0.35$). Simple energy density arguments imply that the energy density is greater at $|y| < 0.35$, and therefore the J/ψ suppression would be expected to be *larger* than at $1.2 < |y| < 2.2$.

3.2.2.2 Low Energy RHIC Results. The J/ψ R_{AA} has also been measured at 39 & 62 GeV. The results are shown as a function of N_{part} in Figure 3.6. It is striking that the observed suppression of J/ψ production as a function of N_{part} is similar, not only at 39 and 62 GeV, but at 200 GeV as well.

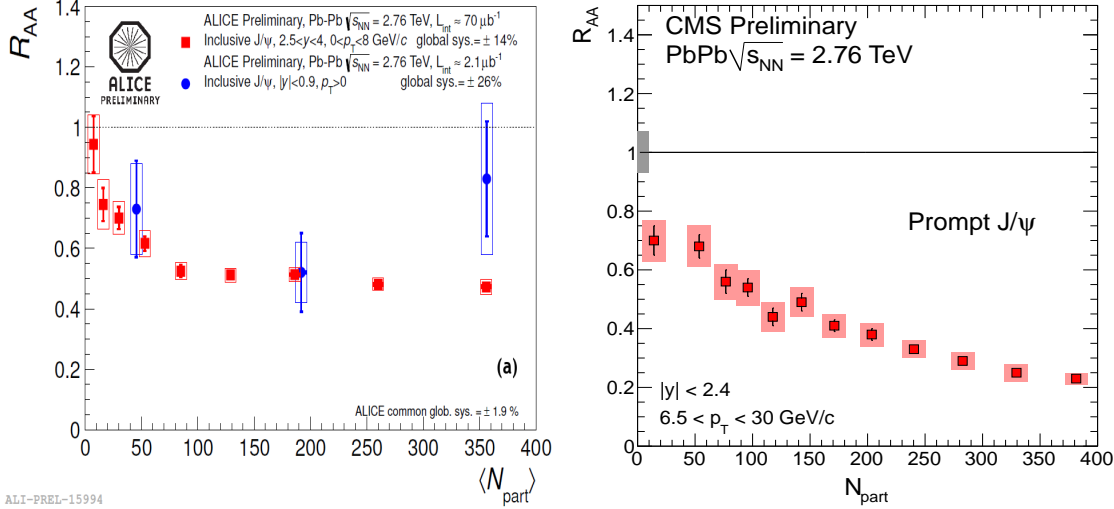


Figure 3.7: (a) The inclusive J/ψ R_{AA} as a function of N_{part} measured by the ALICE collaboration in $\sqrt{s_{NN}} = 2.76 \text{ TeV}$ Pb+Pb collisions [110].(b) The prompt J/ψ R_{AA} as a function of N_{part} for $6.5 < p_T < 30 \text{ GeV}/c$ as measured by the CMS collaboration in $\sqrt{s_{NN}} = 2.76 \text{ TeV}$ Pb+Pb collisions [2].

3.2.3 Recent Results from the LHC

Preliminary measurements of J/ψ production in Pb+Pb and $p+p$ collisions at $\sqrt{s_{NN}} = 2.76 \text{ TeV}$ have been made by CMS [2] and ALICE [110], two of the experiments located at the LHC. The results for the J/ψ R_{AA} as a function of N_{part} are shown in Figure 3.7.

The ALICE measurement is for inclusive J/ψ production measured in two rapidity regions. $J/\psi \rightarrow \mu^+ \mu^-$ production is measured at far forward rapidity, covering the range $2.5 < y < 4$ for $0 < p_T < 8 \text{ GeV}/c$, while $J/\psi \rightarrow e^+ e^-$ production is measured around midrapidity, covering the range $|y| < 0.9$ for $p_T > 0 \text{ GeV}/c$. The inclusive data contain all produced J/ψ 's, including those from $B \rightarrow J/\psi + X$ decays. At forward rapidity the N_{part} dependence falls rapidly up to $N_{part} \approx 75$ then remains flat at $R_{AA} \approx 0.5$. This is in contrast to the RHIC forward rapidity results which show increasing suppression all the way to $N_{part} \approx 250$, where $R_{AA} \approx 0.2$. In the midrapidity region the R_{AA} seems to follow the trend of the forward rapidity results up to the most central collisions, where the midrapidity R_{AA} is larger than that observed at forward rapidity, although this observation is tempered by the large statistical and systematic uncertainties in the data. The factor of ~ 2 higher R_{AA} at the higher LHC energies could be an indication of J/ψ recombination.

The CMS measurement, on the other hand measures prompt J/ψ production over the rapidity interval $|y| < 2.4$ and a J/ψ p_T range of $6.5 < p_T < 30 \text{ GeV}/c$. Prompt J/ψ production includes direct production of J/ψ 's as well as feeddown from higher charmonium states (ψ' , χ_c) but excludes the J/ψ 's from B meson decays. The prompt J/ψ 's measured by CMS show a much stronger suppression with increasing N_{part} than that seen by ALICE. However a direct comparison is meaningless, as the J/ψ 's are measured over different rapidity and p_T intervals.

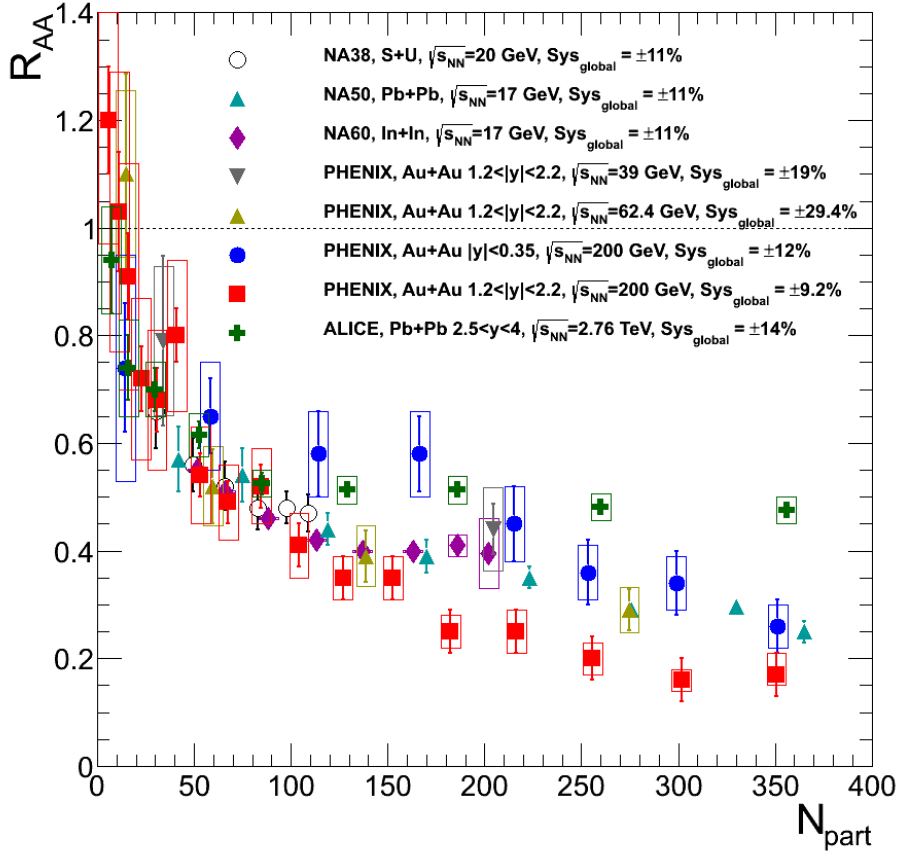


Figure 3.8: Compilation of results on the J/ψ R_{AA} from the SPS [6, 34, 42], RHIC [23, 11, 21] and the LHC [110].

The p_T dependence of J/ψ suppression has been measured by both CMS [2] and ALICE [110] as well. Both experiments find increasing suppression with increasing p_T , covering the range $0 < p_T [\text{GeV}/c] < 30$ between the two experiments. This is the opposite to what was found at RHIC [21], where the suppression was found to be a maximum at low- p_T , with decreasing suppression observed with increasing p_T . This is likely evidence of coalescence, which should propagate the low- p_T part of the J/ψ distribution with coalesced J/ψ 's.

3.2.4 Bringing all the Energies Together

A compilation of the measured J/ψ suppression in $A + A$ collisions spanning an energy range $\sqrt{s_{NN}} = 17 \text{ GeV} - 2.76 \text{ TeV}$ is shown in Figure 3.8. The evolution of the suppression with N_{part} appears to be similar at all energies out to $N_{\text{part}} \sim 100$, at which point the ALICE data flattens while the other energies continue to show a decreasing R_{AA} . At the highest N_{part} the forward rapidity PHENIX data at $\sqrt{s_{NN}} = 200 \text{ GeV}$ shows the greatest suppression ($R_{AA} \sim 0.2$), while the ALICE data at $\sqrt{s_{NN}} = 2.76 \text{ TeV}$ shows the least suppression

($R_{AA} \sim 0.5$). This is contrary to what is expected based on the simple assumptions of J/ψ dissociation. The least suppression should occur at the lowest collision energies, where the Debye screening radius in the medium is largest, while the greatest suppression should occur at the highest collision energies, where the Debye screening radius in the medium should be smallest. It should be cautioned that the energy densities vary greatly between the different collision energies, which can affect the interpretation of the similarities and differences.

What could be the cause of this effect? There are two possibilities (likely a combination of the two) which may be able to explain these results. The first is J/ψ recombination. While not yet proven, recombination could provide a mechanism through which the suppression at lower energies could be greater than at higher energies. At lower energies the direct suppression of J/ψ 's may be “small”, and since there are few produced $c\bar{c}$ pairs, the effect of recombination should also be small. As you increase the collision energy the direct suppression should increase, but the effect of recombination should also increase, providing an enhancement factor that could compensate for the larger direct suppression. It may be that this produces the similar suppression at RHIC and the SPS, while at the LHC the effect of recombination may begin to dominate the direct suppression, causing a decrease in the overall suppression compared to RHIC.

The second possibility to consider is CNM effects. These effects are known to be different at different energies, and in particular they are known to be greater at lower collision energies than at higher collision energies. The CNM effects on J/ψ production are discussed in the following section.

3.3 Cold Nuclear Matter Effects

As discussed in Section 2.1, there are a number of effects which modify the production of charmonia in A+A collisions which are not due to the production of a QGP. This section briefly focuses on these effects, some of which were discussed in Section 2.1, as they apply to the modification of charmonia production in heavy ion collisions. We start by reviewing what has been learned from previous $p+A$ measurements.

In high energy collisions, such as those achieved at RHIC, charmonia production occurs mainly through gluon fusion. When talking about nuclear shadowing the relevant distribution is that of the gluons. However, this is precisely where the nPDF modification is least constrained. The nuclear modification taken from EPS09, and the corresponding uncertainty, for $Q^2 = 9$ GeV ($\approx M_{J/\psi}^2$) is shown in Figure 3.9. There is an obvious improvement when moving from LO to NLO, however the high- x , EMC, region is very poorly constrained in both cases.

One very important CNM effect on charmonia production, not discussed in Section 2.1, is nuclear breakup. As the charmonia (or perhaps the $c\bar{c}$ precursor) traverses the remainder of the nucleus after its creation, a collision of sufficient energy with nucleons will break up the charmonia into a pair of light charmed-mesons. This is often referred to as a final-state effect (not to be confused with the final-state effects due to a QGP). The nuclear breakup, also sometimes referred to as nuclear absorption in the literature, is often parametrized through a breakup (or absorption) cross section. Little theoretical guidance currently exists

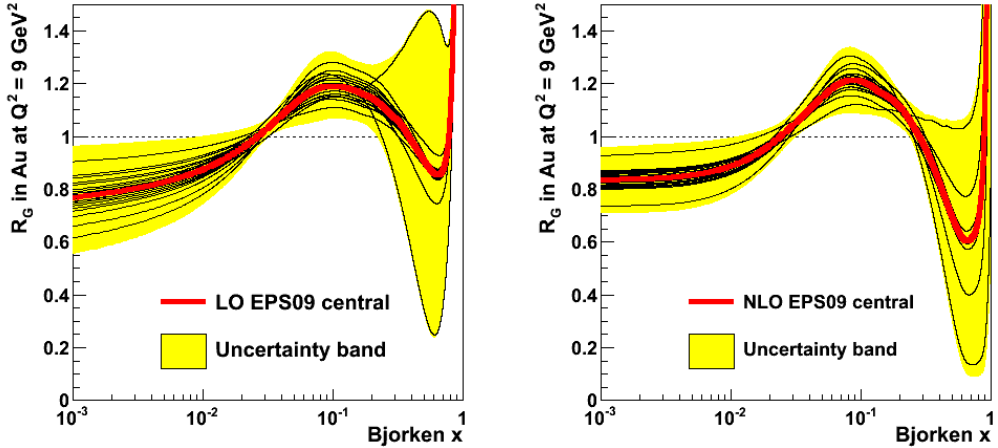


Figure 3.9: The nuclear shadowing of the gluon distribution in Au taken from EPS09 for LO(Left) and NLO(Right).

on the exact nature of this effect. Due to the lack of theoretical guidance the breakup cross section is often quoted as an *effective* breakup cross section, since it could include the effects of other physics.

There have been a number of recent calculations for J/ψ production in d +Au collisions at RHIC within the CGC framework [81, 80, 59, 79] as well as for the upcoming p +Pb run at the LHC. At RHIC, the saturation scale is likely only valid for J/ψ production at forward rapidity and low- p_T [79], while at the LHC it should be valid over a much broader kinematic region due to the larger collision energies. Results of calculations within the CGC framework on J/ψ production in d +Au collisions at RHIC will be discussed further in Section 7 in the context of the results presented in this dissertation.

There are a number of models that calculate the effects of energy loss on J/ψ production. This can take the form of initial state energy loss of the incoming gluon only [102], or both initial and final state energy loss [39]. Calculations indicate that energy loss on J/ψ production in p +A collisions is most important in the forward rapidity region [39]. In this region the incoming parton and the J/ψ must traverse the full extent of the Au nucleus, and therefore the likelihood of exchanging gluons with the medium is the largest.

3.3.1 Results from the Low Energy Fixed Target Experiments

An extensive study of J/ψ , and to a lesser extent ψ' , production in p +A collisions has been carried out at CERN, FNAL and DESY [5, 32, 33, 35, 43, 86, 8] covering the center of mass energy range $\sqrt{s} \approx 17 - 42$ GeV. At lower energies the modification of the J/ψ production in p +A collisions compared to p + p collisions is assumed to follow a power law

$$\sigma_{pA} = \sigma_{pp} A^\alpha \quad (3.7)$$

where the parameter α characterizes the nuclear dependence. If the production scales with the number of binary collisions then $\alpha = 1$ and no modification is observed. A value

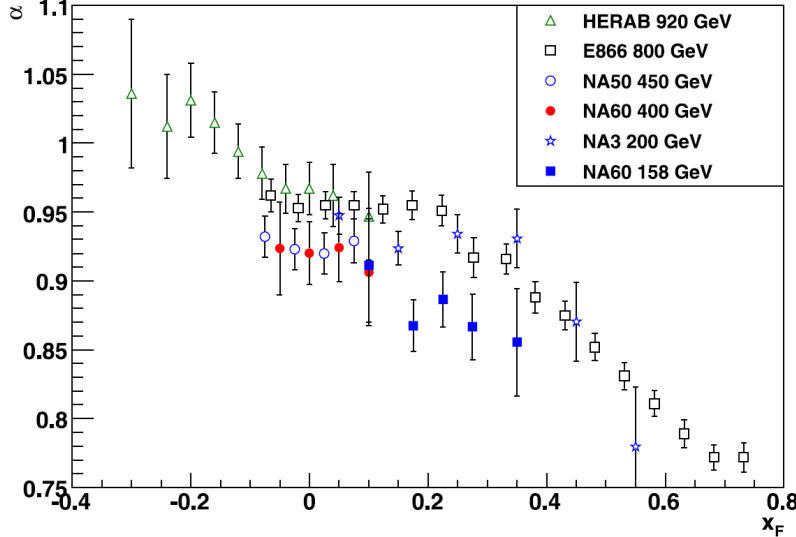


Figure 3.10: Compilation of the x_F dependence of the α parameter (described in the text) for J/ψ production from low energy fixed target experiments [43].

of $\alpha < 1$ indicates a suppression of J/ψ production in $p+A$ collisions compared to $p+p$ collisions, while $\alpha > 1$ indicates an enhancement in the production in $p+A$ compared to the expectation from $p+p$.

The Feynman- x (x_F) dependence of α from the fixed target experiments is shown in Figure 3.10. Feynman- x is given by

$$x_F = x_1 - x_2, \quad (3.8)$$

where x_1 and x_2 are the x values in the projectile and target respectively. Large values of x_F can be thought of as forward rapidity, while $x_F = 0$ maps to $y = 0$. Two clear trends emerge. First, suppression of J/ψ production in $p+A$ collisions relative to $p+p$ collisions is observed. Second, the suppression appears to increase with *decreasing* energy, and increase with increasing x_F .

The observed increase in suppression with decreasing energy has been interpreted [87] as an increase in the nuclear breakup at lower energies. The extracted nuclear breakup cross section, σ_{abs} , as a function of \sqrt{s} at $y = 0$ ($x_F = 0$) is shown in Figure 3.11. The large increase observed in the breakup cross section at low energy can possibly be understood as a consequence of the formation time of the J/ψ . At low energies the time spent by the J/ψ traversing the nucleus is large. This may allow the J/ψ to fully form, causing a higher probability for collisions with nuclei. At higher energies, however the $c\bar{c}$ pair may not fully evolve into a J/ψ while traversing the nucleus, which could indicate a smaller breakup cross section due to the smaller physical size of the $c\bar{c}$ pair.

The same formation time argument may also be the explanation for the results observed by E866 [86], shown in Figure 3.12, which indicate a greater suppression of the (larger) ψ' compared to the (smaller) J/ψ near $x_F \approx 0$, and a similar suppression of the J/ψ and ψ' for $x_F > 0$. The NA50 collaboration [33, 35] has also measured both J/ψ and ψ' production

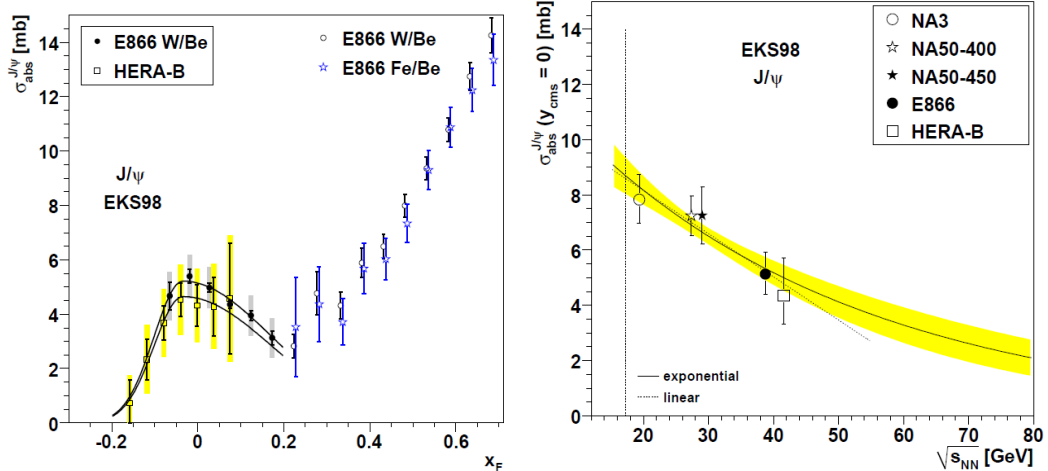


Figure 3.11: The J/ψ nuclear breakup cross section as a function of x_F (Left) and \sqrt{s} (Right) extracted from data collected by NA3, NA50, E866 and HERA-B [87].

in $p+A$ collisions, shown in Figure 3.12, which indicate that the ψ' is more suppressed than the J/ψ for longer average distances of nuclear matter crossed by the charmonium states on their way out of the nucleus, L . This will be discussed further in the context of the results presented in this dissertation in Chapter 7.

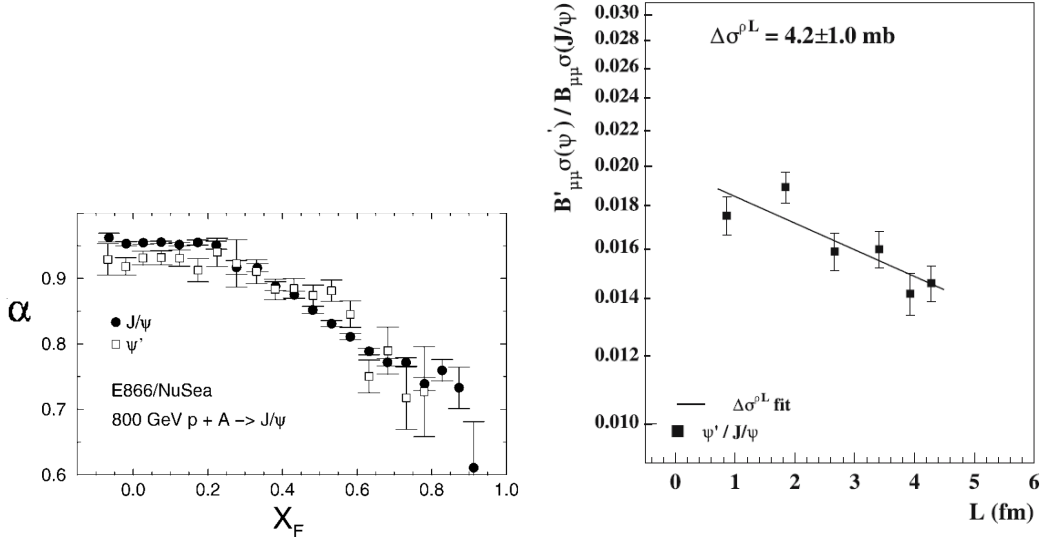


Figure 3.12: (Left) x_F dependence of the α parameter for both J/ψ and ψ' production in $p+A$ collisions measured by E866 [86]. (Right) The ratio of ψ' production to J/ψ production in $p+A$ measured by NA50 [35] collisions as a function of L .

The large increase in σ_{abs} at forward x_F , shown in Figure 3.11, is also striking. While the increase may be due to formation time effects, as the evolving $c\bar{c}$ will spend longer traversing the nucleus at forward x_F , it seems unlikely that this fully explains the magnitude of the change observed at forward x_F . It is possible that this increase is due to energy loss, which should be greater at forward x_F .

3.3.2 Previous RHIC Results

The PHENIX experiment has previously published results on J/ψ production in $d+\text{Au}$ collisions at $\sqrt{s_{NN}} = 200$ GeV based on data taken in 2003 [13]. In [13] the results are presented in terms of the nuclear modification factor $R_{d\text{Au}}$, calculated by

$$R_{d\text{Au}} = \frac{1}{\langle N_{coll} \rangle} \frac{dN_{J/\psi}^{d+\text{Au}}/dy}{dN_{J/\psi}^{p+p}/dy}, \quad (3.9)$$

where $dN_{J/\psi}^{d+\text{Au}}/dy$ is the J/ψ invariant yield measured in $d+\text{Au}$ collisions, $dN_{J/\psi}^{p+p}/dy$ is the J/ψ invariant yield measured in $p+p$ collisions in the same rapidity bin, and $\langle N_{coll} \rangle$ is the average number of binary nucleon-nucleon collisions. As for the parameter α , $R_{d\text{Au}} = 1$ indicates no modification of J/ψ production in $d+\text{Au}$ relative to $p+p$ collisions, $R_{d\text{Au}} < 1$ indicates a suppression of J/ψ production in $d+\text{Au}$ collisions relative to $p+p$ collisions, and $R_{d\text{Au}} > 1$ indicates a suppression of J/ψ production in $d+\text{Au}$ collisions relative to $p+p$ collisions. The 2003 PHENIX results for the $J/\psi R_{d\text{Au}}$ are plotted as a function of rapidity for minimum bias (centrality integrated) collisions in Figure 3.13. The data show a trend of increasing suppression with increasing rapidity, although the statistical and systematic uncertainties are too large to make a strong statement about the level of the effect.

Also included in Figure 3.13 are calculations which include nuclear shadowing, taken from the EKS98 nPDF set, and nuclear breakup, where the breakup cross section is assumed to be independent of rapidity and is fitted to the data. The best fit breakup cross section is found to be $\sigma_{\text{breakup}} = 2.8^{+2.3}_{-2.1}$, which is consistent with predictions based on the energy dependence of the breakup extracted from lower energy results [87], albeit with large uncertainties.

3.4 Motivation - Tying it all Together

As detailed above, CNM effects on J/ψ production are large. A detailed understanding of the CNM effects on J/ψ production is necessary to interpret the observed suppression of J/ψ production in $\text{Au}+\text{Au}$ collisions at RHIC, which in turn is needed to investigate key properties of the QGP. High quality J/ψ production measurements in $d+\text{Au}$ collisions at RHIC can address this, and help constrain properties of the J/ψ production mechanism, the modification of parton distribution functions in nuclei, and the Cronin effect.

To give some historical context of the importance of understanding and measuring the CNM baseline for J/ψ production, Figure 3.14 shows the measured/expected J/ψ yield from $\text{In}+\text{In}$ and $\text{Pb}+\text{Pb}$ collisions at 158 GeV measured at the SPS, after correcting for the CNM baseline. The left plot of Figure 3.14 shows the correction using $p+A$ data taken at 400 GeV, a factor of ~ 2.5 times the energy at which the J/ψ production in $A+A$ collisions

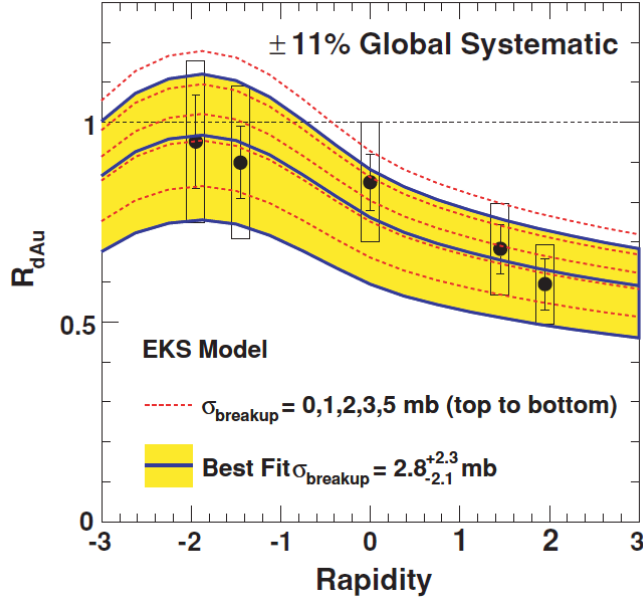


Figure 3.13: The J/ψ $R_{d\text{Au}}$ at $\sqrt{s_{NN}} = 200$ GeV measured by the PHENIX experiment from data collected in 2003 [13]. The curves represent calculations including nuclear shadowing and nuclear breakup, where the breakup cross section is fitted to the data.

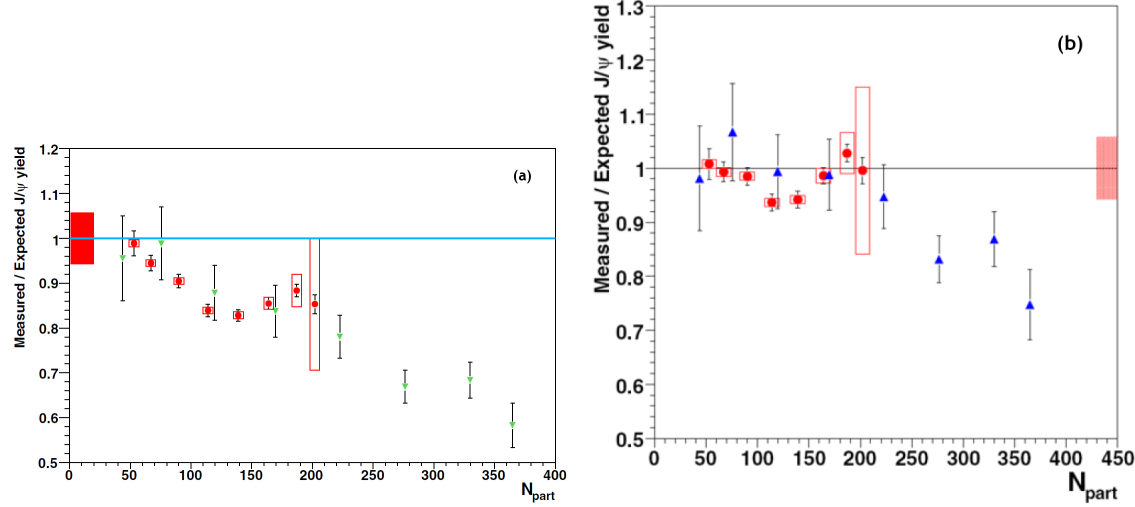


Figure 3.14: The anomalous suppression of J/ψ production in In+In [42] (circles) and Pb+Pb (triangles) corrected for CNM effects using the measured J/ψ production in 400 GeV $p+A$ collisions [35] (a) and the 158 GeV $p+A$ collisions [43](b).

was measured. It was assumed that the CNM effects would not vary greatly with collision energy. Using this baseline, suppression is observed for $N_{\text{part}} > 75$, and reaches 0.55 for central collisions. The right plot of Figure 3.14 shows the correction using $p + A$ data taken at 158 GeV, the same energy as the $A + A$ data. In this case suppression is not seen until $N_{\text{part}} > 200$ and reaches only 0.75 for central collisions, leading to a drastically different conclusion. This illustrates how important measuring and understanding the CNM baseline truly is.

The previous measurements in $d + \text{Au}$ collisions at RHIC, based on data collected in 2003, include large statistical and systematic uncertainties which make it impossible to extract detailed information about the rapidity, p_T , and centrality dependence of cold nuclear matter effects. The $d + \text{Au}$ data set collected by PHENIX in 2008 provides more than a factor of 10 increase in the integrated luminosity available for J/ψ production studies. This increase in the statistical precision also allows for the measurement of ψ' production for the first time in $d + \text{Au}$ collisions at RHIC.

The remainder of this dissertation presents the analysis of $J/\psi \rightarrow e^+e^-$ and $\psi' \rightarrow e^+e^-$ production data in $d + \text{Au}$ collisions at $\sqrt{s_{NN}} = 200$ GeV as measured by the PHENIX detector. The implications of these results will be discussed, as well as a parametrization of the $d + \text{Au}$ data for use in quantifying the CNM baseline on J/ψ production in $\text{Au} + \text{Au}$ collisions.

CHAPTER 4

EXPERIMENT

4.1 RHIC

The Relativistic Heavy Ion Collider (RHIC) is a superconducting hadron collider located at Brookhaven National Lab (BNL) in Upton, NY. It consists of two concentric collider rings with 0.6 km radii which allow the collisions of polarized and unpolarized protons up to $\sqrt{s} = 500$ GeV, as well as heavy ions (ex. Cu, Au) over a large range in collision energy ($\sqrt{s_{NN}} = 7.7 - 200$ GeV). Collisions are delivered to 6 interaction regions spread around the ring, four of which are occupied by the experiments PHENIX, STAR, PHOBOS, and BRAHMS. The PHOBOS and BRAHMS detectors completed data taking in 2006, as planned, leaving PHENIX and STAR as the two active experiments currently taking data at RHIC. An overhead view of the RHIC complex can be seen in Figure 4.1.

RHIC typically operates for roughly 5-6 months during the winter/spring of each year. The convention at RHIC is to label these running periods as “Run” followed by a number which is increased consecutively since RHIC operations began. Fortunately, since RHIC operations began in 2000, this number generally corresponds to the year in which the data were taken, for example, Run 8 contains data taken in the winter/spring of 2008. Each Run contains collisions from one or more colliding species (ex. $p+p$, $d+Au$, $Au+Au$) with different collision energies. A detailed list of the collision species, collision energies, and delivered luminosity in each Run to date can be found in Table 4.1. The work presented here uses $d+Au$ data collected by the PHENIX experiment in 2008.

Heavy ions are accelerated to the full $\sqrt{s_{NN}} = 200$ GeV collision energy through the following process, detailed for Gold ions (Au)

1. The Electron Beam Ion Source accelerates heavy ions up to 2 MeV/u, stripping 32 electrons from the Au nucleus.
2. The ions are then transferred to the Tandem-to-Booster Line, which transports them under vacuum to the next accelerator.
3. The Booster Synchrotron then accelerates the Au ions to 100 MeV/u, stripping another 45 electrons for a total charge $Q = +77$.
4. The ions are then transferred to the Alternating Gradient Synchrotron which strips the remaining 2 electrons and accelerates the Au ions to 8.86 GeV/u.



Figure 4.1: An aerial photograph of the RHIC complex. This picture was taken before the recent installation of EBIS.

5. The ions are then transferred through the AGS-to-RHIC line to their final destination, the RHIC, where they are accelerated up to the desired collision energy.

4.2 The Pioneering High Energy Nuclear Interaction eXperiment (PHENIX)

The PHENIX detector [25] consists of multiple detectors organized into four separate spectrometers, built with the intent to measure properties of leptons, hadrons and photons with good momentum and energy resolution over a wide range of collision energies and species. Two spectrometers at mid rapidity are optimized for detecting electrons, hadrons and photons, while two spectrometers at forward and backward rapidity are optimized for detecting muons. Two beam-beam counters measure event time and position along the beam axis for global event characterization. A schematic view of the various detector subsystems can be seen in Figure 4.2.

4.2.1 Global Detectors

PHENIX includes two beam-beam counters (BBC's) located on either side of the interaction region at $3 < |\eta| < 3.9$ and covering $\Delta\phi = 2\pi$ [36], where η is the pseudorapidity

Table 4.1: RHIC running periods with collision species, collision energy, and delivered luminosity to all experiments.

| Dates | Designation | Colliding Species | $\sqrt{s_{NN}}$ [GeV] | Delivered Luminosity |
|--------------|-------------|-------------------|-----------------------|-------------------------|
| 3/00 - 9/00 | Run 1 | Au+Au | 130 | $20 \mu\text{b}^{-1}$ |
| 5/01 - 1/02 | Run 2 | Au+Au | 200 | $258 \mu\text{b}^{-1}$ |
| | | Au+Au | 19.6 | $0.4 \mu\text{b}^{-1}$ |
| | | p+p | 200 | 1.4 pb^{-1} |
| 12/02 - 5/03 | Run 3 | d+Au | 200 | 73 nb^{-1} |
| | | p+p | 200 | 5.5 pb^{-1} |
| 11/03 - 5/04 | Run 4 | Au+Au | 200 | 3.53 nb^{-1} |
| | | Au+Au | 62.4 | $67 \mu\text{b}^{-1}$ |
| | | p+p | 200 | 7.1 pb^{-1} |
| 11/04 - 6/05 | Run 5 | Cu+Cu | 200 | 42.1 nb^{-1} |
| | | Cu+Cu | 62.4 | 1.5 nb^{-1} |
| | | Cu+Cu | 22.4 | 0.02 nb^{-1} |
| | | p+p | 200 | 29.5 pb^{-1} |
| 2/06 - 6/06 | Run 6 | p+p | 200 | 88.6 pb^{-1} |
| | | p+p | 62.4 | 1.05 pb^{-1} |
| 2/07 - 6/07 | Run 7 | Au+Au | 200 | 7.25 nb^{-1} |
| 11/07 - 3/08 | Run 8 | d+Au | 200 | 437 nb^{-1} |
| | | p+p | 200 | 38.4 pb^{-1} |
| 2/09 - 7/09 | Run 9 | p+p | 500 | 110.4 pb^{-1} |
| | | p+p | 200 | 114 pb^{-1} |
| 12/09 - 6/10 | Run 10 | Au+Au | 200 | 10.3 nb^{-1} |
| | | Au+Au | 62.4 | 0.544 nb^{-1} |
| | | Au+Au | 39 | 0.206 nb^{-1} |
| | | Au+Au | 7.7 | $2.1 \mu\text{b}^{-1}$ |
| | | Au+Au | 11.5 | $4.7 \mu\text{b}^{-1}$ |
| 1/11 - 7/11 | Run 11 | p+p | 500 | 166 pb^{-1} |
| | | Au+Au | 19.6 | $33.2 \mu\text{b}^{-1}$ |
| | | Au+Au | 200 | 9.79 nb^{-1} |
| | | Au+Au | 27 | $63.1 \mu\text{b}^{-1}$ |

defined as

$$\eta = \frac{1}{2} \ln \frac{|\vec{p}| + p_z}{|\vec{p}| - p_z} = -\ln \tan \frac{\theta}{2}. \quad (4.1)$$

Here θ is the angle measured from the beam axis (z -axis). Pseudorapidity is often used in high energy experiments as a measure of the polar angle, and will be used throughout this work. For massless particles $\eta = y$. The BBC's provide collision vertex positioning along the beam axis (ZVTX) as well as a collision trigger.

Each BBC consists of 64 photomultiplier tubes (PMT's) mounted on a 3 cm quartz radiator. It has an inner radius of 10 cm, which provides 1 cm of clearance from the beam pipe, and an outer radius of 30 cm. The timing and pulse height of each BBC element are read out in real time for each beam crossing using time-to-voltage converters and flash ADC's.

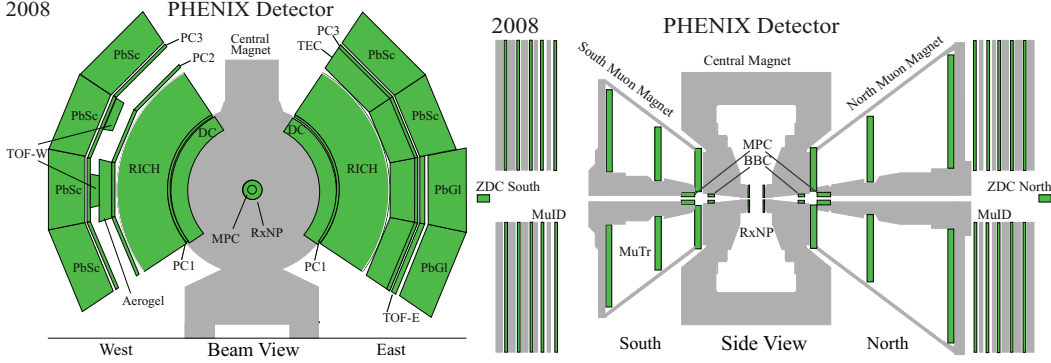


Figure 4.2: PHENIX detector configuration for 2008. The Left plot shows a beam view of the Central Arm detectors while the Right plot shows a side view detailing the muon arms.

4.2.2 Central Spectrometers

The two PHENIX central arms are located at midrapidity, with each arm covering $|\eta| < 0.35$ and $\Delta\phi = \frac{\pi}{2}$, where ϕ is the azimuthal angle. Each arm includes a number of detector subsystems to handle tracking, particle identification, and calorimetry. All subsystems are used in coincidence to make measurements of the properties of electrons, photons and charged hadrons. A layout of the various subsystems installed during the 2008 run can be seen in Figure 4.2.

The important detector subsystems for electron analyses are those used for tracking (DC, PC) and particle identification (RICH, EMCal). These subsystems are described in detail below.

4.2.2.1 Drift Chamber. The Drift Chamber (DC) [24] consists of two gas wire chambers, one located in each arm, and is used to measure particle trajectories in the $r - \phi$ plane with the primary goals of measuring the particles transverse momentum (p_T) and providing an anchoring point for the tracking.

The DC is the innermost subsystem in the central arms, 2 m from the z -axis, placing them in a residual magnetic field of 0.6 kG. Each DC is cylindrical in design and covers 2 m along the beam direction and is 0.4 m thick, with the DC located in the West arm being a mirror image of that located in the East arm. A gas mixture of 50% Ar and 50% Ethane is used in each of the detectors.

Each detector is divided into 20 equal sectors covering 4.5° in ϕ . Each sector contains six types of wire modules stacked radially and labeled X1, U1, V1, X2, U2, V2, respectively from the inside out. The X wires run parallel to the beam to perform precise $r - \phi$ measurements while the U and V wires are set at small angles of about 6° relative to the X wires to provide information about the z position of the track. A diagram of the wire layout in each sector is shown in Figure 4.3. In total, the DC consists of 6500 anode wires leading to 13,000 readout channels, with a measured single wire resolution of $165 \mu\text{m}$ and a spatial resolution of 2mm.

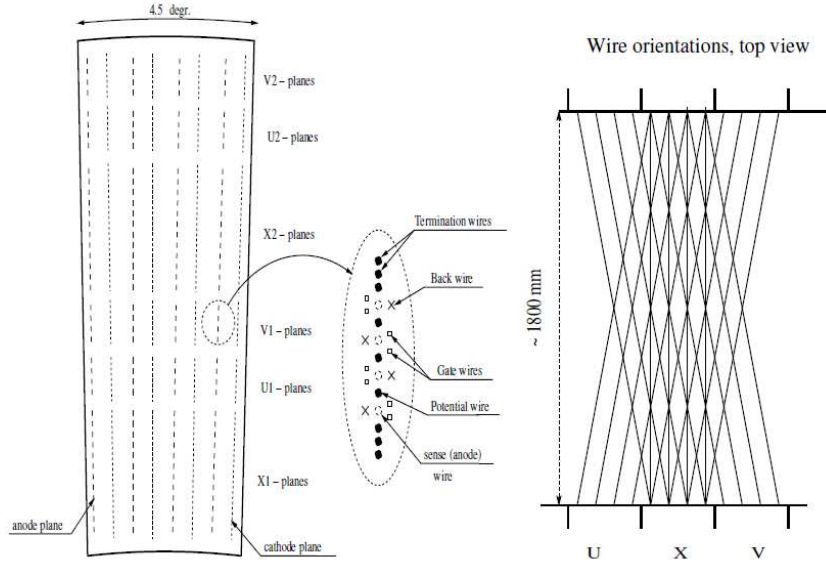


Figure 4.3: (Left) Layout of the DC wire position within one sector. (Right) A top view schematic diagram of the wire configuration.

4.2.2.2 Pad Chambers. The Pad Chambers (PC) [24] are multiwire proportional chambers which consists of three separate layers of detectors measuring precise hit positions and making up the bulk of the PHENIX tracking system. The innermost layer, PC1, is located in both the East and West arms immediately outside the DC, providing a measurement of the z position at the back plane of the DC. The second layer, PC2, is located behind the RICH in the West arm only. The outer layer, PC3, is located just inside the EMCAL in both arms and provides a second point on the straight line trajectories of the tracks through the detector, outside of the magnetic field.

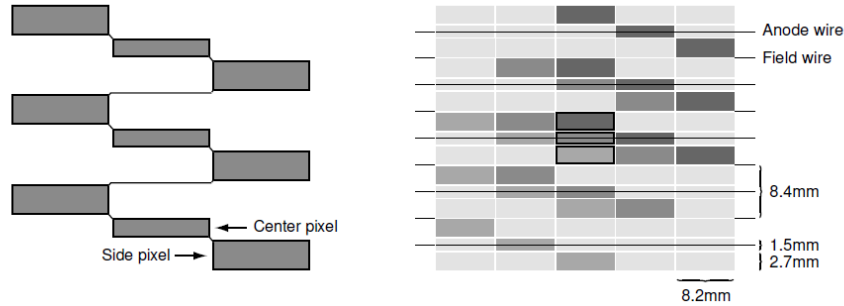


Figure 4.4: The pad and pixel geometry in the PC. A cell defined by three pixels is at the center of the right picture.

Each detector consists of a single plane of anode and field wires lying in a gas volume

between two cathode planes. The inner cathode plane is solid, while the outer is segmented to provide pixelated hit information. Three pixels are tied together into a cell, where each pixel is required to measure the charge from an avalanche to form a valid hit. A schematic of the pixel and cell geometry is shown in Figure 4.4. In PC1, These cells are segmented into $8.4 \times 8.4 \text{ mm}^2$ yielding a z position resolution of $\pm 1.7 \text{ mm}$. The same angular resolution is used in PC2 and PC3 (cells in PC3 are therefore 4 times larger as they are twice as far from the interaction region).

4.2.2.3 Ring Imaging Cherenkov Detector. The Ring Imaging Cherenkov (RICH) detector [30] is located immediately behind PC1, and provides the primary electron identification in PHENIX, in conjunction with the EMCal. The RICH consists of two identical detectors located in each arm and provides e/π discrimination below the pion Cherenkov threshold of $4.65 \text{ GeV}/c$ in the CO_2 gas used in the detectors.

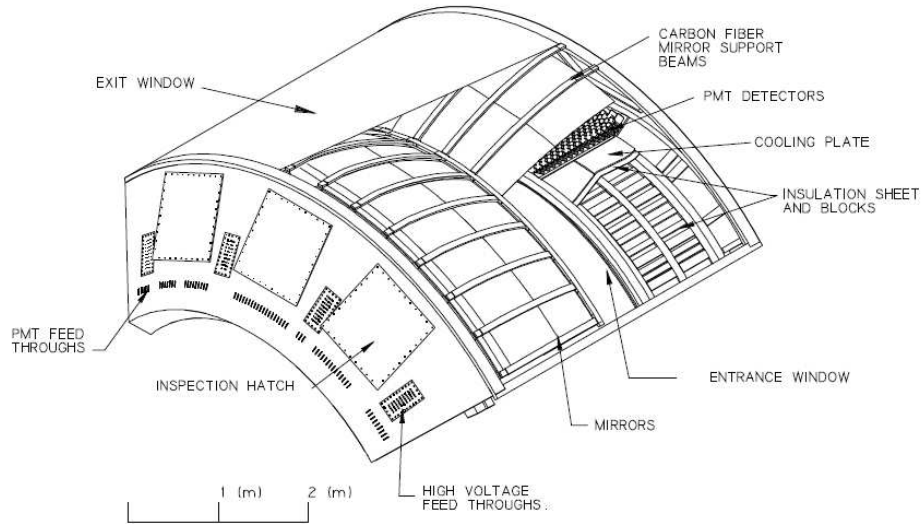


Figure 4.5: A cutaway view of one arm of the RICH detector.

Each RICH detector has a volume of 40 m^3 and consists of a gas volume, a set of spherical mirrors, and an array of photomultiplier tubes (PMT's). A cut away view of one of the two RICH detectors is shown in Figure 4.5. In each arm, 48 composite mirror panels form two intersecting spherical surfaces with a total reflective area of 20 m^2 . Two arrays of 1280 phototubes are located on either side of the entrance window to measure the reflected Cherenkov light. Each set of phototubes are arranged into modules of 32 PMT's. Each module contains two staggered rows of 16 phototubes to provide a tightly packed array.

4.2.2.4 Electromagnetic Calorimeter. The Electromagnetic Calorimeter (EMCal) [37] is the outermost subsystem in the central arms and is designed primarily to measure the energies and positions of photons and electrons. It also plays a key role in the identification of electrons as well as providing triggering for rare events. Two different EMCal designs were utilized, with 6 sectors based on a Pb-scintillator (PbSc) design, and

2 based on a Pb-glass (PbGl) design. The two different designs were chosen deliberately as each provides advantages and disadvantages, for instance the PbGl has a better energy resolution, while the PbSc has better linearity and timing. When used in combination these two designs provide an internal cross check on the data. The two setups are described separately below.

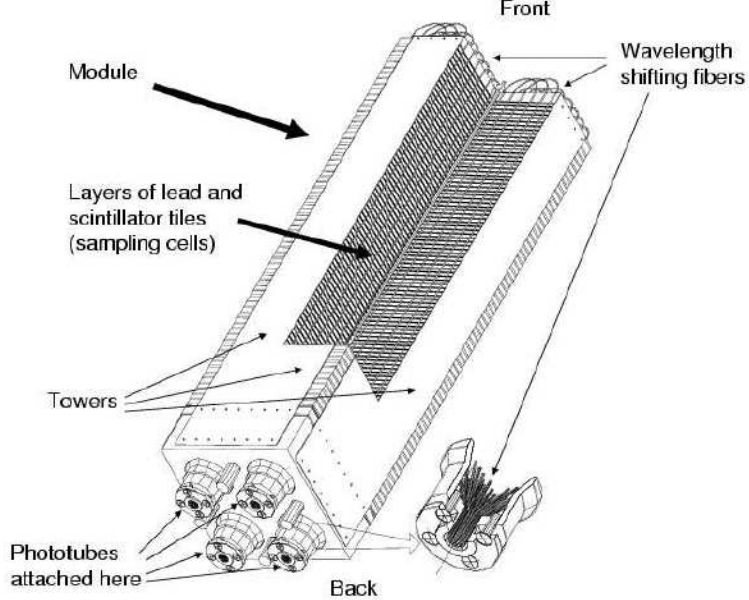


Figure 4.6: Schematic view of a Pb-scintillator module.

The PbSc is a sampling calorimeter consisting of alternating layers of Pb and scintillator. A tower consists of 66 sampling layers containing 0.15 cm of Pb and 0.4 cm of scintillator. Thirty-six longitudinally penetrating wavelength shifting fibers optically connect the cells to PMT's mounted to the back of the tower. Four towers are mechanically grouped into modules as shown in Figure 4.6. Thirty-six Modules are further grouped together in supermodules (SM), and 18 supermodules grouped into $2 \times 4 \text{ m}^2$ sectors. Four PbSc sectors are mounted on the West arm, while 2 are mounted on the upper half of the East arm, as shown in Figure 4.2. The energy resolution of the PbSc was measured to be

$$\frac{\sigma(E)}{E} = \frac{8.1\%}{\sqrt{E [\text{GeV}]}} \oplus 2.1\%, \quad (4.2)$$

using test beams at U71, the AGS, and the SPS.

The PbGl is a Cherenkov calorimeter using a Pb-glass crystal. The light is collected using PMT's mounted to the back of the crystal tower. Each of the two PbGl sectors, located on the lower East central arm, contains 192 supermodules. Each SM contains a 6×4 array of PbGl modules, as seen in Figure 4.7. Each module is 4 cm \times 4 cm at the front

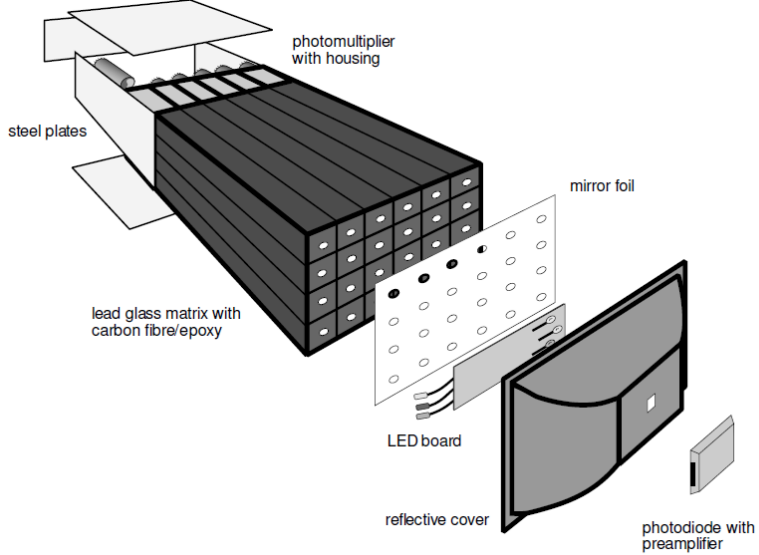


Figure 4.7: Schematic view of a Pb-glass supermodule.

end and 40 cm long. The energy resolution was measured using test beams to be

$$\frac{\sigma(E)}{E} = \frac{[5.9 \pm 0.1]\%}{\sqrt{E \text{ [GeV]}}} \oplus [0.8 \pm 0.1]\%. \quad (4.3)$$

The PbGl towers used in PHENIX were previously used in the WA98 experiment at CERN.

4.2.3 Muon Spectrometers

The PHENIX muon arms [31] cover $1.2 < |\eta| < 2.2$ and $\Delta\phi = 2\pi$ and are designed to detect muons with good momentum resolution and muon identification at forward and backward rapidities. Each arm consists of a tracking system (muon tracker) in a radial magnetic field followed by a stack of absorber and low resolution tracking layers (muon identifier). The layout of the muon arms, as well as their relationship to the central arms is shown in Figure 4.2.

The muon tracker (MuTr) consists of three stations of cathode-strip tracking chambers mounted inside the conical north and south muon magnets. Each station consists of multiple orientations of cathode strips and readout planes to provide a position resolution of $\sim 100 \mu\text{m}$.

The muon identifier (MuID) consists of four layers of steel absorbers that are 10, 10, 20, 20 cm thick, respectively, interspersed with the MuID panels. The MuID panels are made up of two layers of Iarocci tubes alternately aligned vertically and horizontally. A muon produced at the collision vertex must have an energy of at least 1.9 GeV to reach the MuID and an energy of at least 2.7 GeV to completely penetrate through all four layers of the MuID. The probability of a 4 GeV pion reaching the final layer of the MuID is $\sim 3\%$, providing excellent pion rejection.

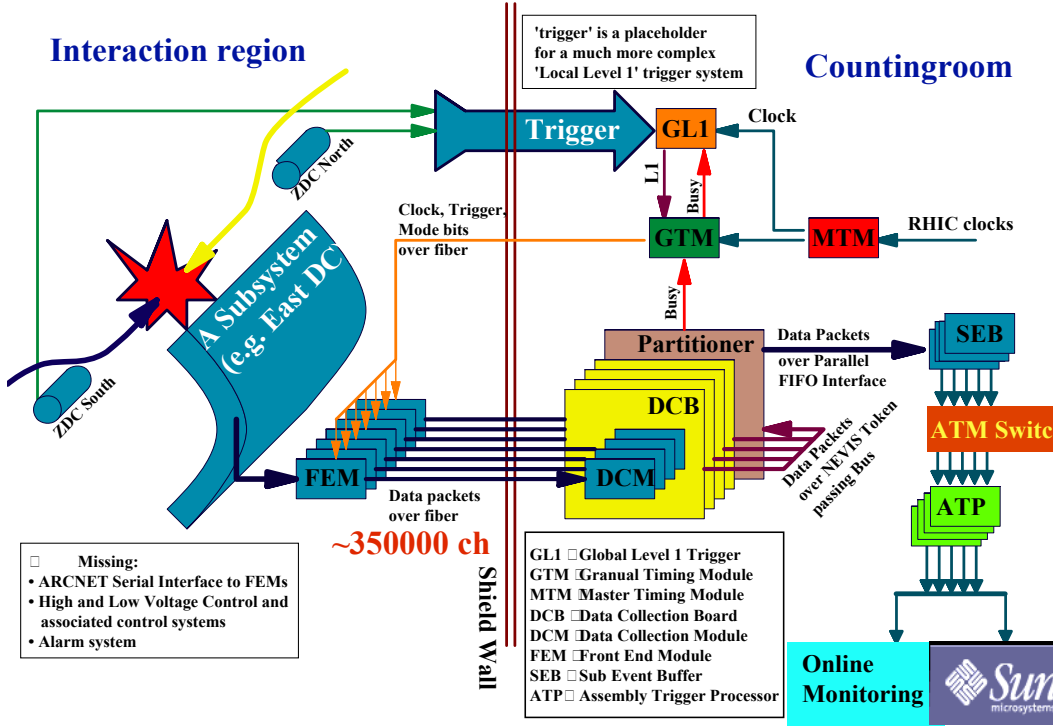


Figure 4.8: A schematic diagram of the data acquisition system.

4.2.4 Data Acquisition and Triggering

Both the event rate and event size are large at RHIC, and therefore a system which can make decisions event by event and select events containing rare signals is necessary. The online data acquisition system (DAQ) [29] collects the signals from the various subsystems and then processes the event acceptance decision based on various triggers. A general schematic of the PHENIX DAQ system is shown in Figure 4.8 and described below.

Front End Modules (FEM) on each subsystem process signals from the various detector electronics for every beam crossing. The FEM's provide a data buffer of 40 beam crossings in order to allow for the time necessary to make Level-1 (LVL1) trigger decisions. After a LVL1 trigger decision is made, the information from the FEM's is transferred via fiber optic cables to Data Collection Modules (DCM) located outside of the PHENIX interaction region. The DCM's format and zero suppress the data and provide data packets to the Event Builder (EvB), which processes the event.

The LVL1 trigger provides event rejection sufficient to reduce the data to a rate manageable to the DAQ. It consists of two systems. The Local Level-1 (LL1) communicates directly with specific subsystems such as the BBC, EMCAL, and RICH, providing triggering decisions based on subsystem trigger output. This information is passed to the Global

Level-1 (GL1) which combines the data from the LL1 to produce a trigger decision.

In the 2008 d +Au data a LL1 minimum bias (MB) collision trigger was defined to require at least one hit in each of the two BBC's within a collision ZVTX of ± 30 cm. Collisions in that range see the full geometric acceptance of the central arms. This MB trigger selection covers $88 \pm 4\%$ of the total d +Au inelastic cross section of 2260 mb [109]. The data sample used in this analysis requires the minimum bias trigger to be in coincidence with an additional LL1 trigger. This is a single electron EMCAL RICH trigger (ERT), which requires a minimum energy deposited in any 2×2 group of EMCAL supermodules, plus an associated hit in the RICH. Two thresholds on the minimum EMCAL energy were used, 600 MeV and 800 MeV, each for roughly half of the data sample.

4.2.5 Centrality Determination

Table 4.2: Characterization of the collision centrality for d +Au collisions along with the correction factor c (see text for details).

| Centrality | $\langle N_{\text{coll}} \rangle$ | c | $c/\langle N_{\text{coll}} \rangle$ |
|------------|-----------------------------------|-------------------|-------------------------------------|
| 0-20 % | 15.1 ± 1.0 | 0.94 ± 0.01 | 0.062 ± 0.003 |
| 20-40 % | 10.2 ± 0.7 | 1.000 ± 0.006 | 0.098 ± 0.004 |
| 40-60 % | 6.6 ± 0.4 | 1.03 ± 0.02 | 0.157 ± 0.008 |
| 60-88 % | 3.2 ± 0.2 | 1.03 ± 0.06 | 0.33 ± 0.02 |
| 0-100 % | 7.6 ± 0.4 | 0.889 ± 0.001 | 0.117 ± 0.004 |

The centrality, which is related to the impact parameter, b , of the d +Au collision is determined using the total charge deposited in the BBC that is located at negative rapidity (Au-going direction). The centrality is defined as a percentage of the total charge distribution referenced to the greatest charge, *i.e.* 0-20% refers to the 20% of the total charge distribution with the greatest charge. On average the 0-20% centrality corresponds to collisions with the smallest b .

For each centrality bin the mean number of nucleon-nucleon collisions ($\langle N_{\text{coll}} \rangle$) is determined using a Glauber calculation [91] combined with a simulation of the BBC response. For each binary collision, the response in the BBC located at negative rapidity is assumed to be described by a negative binomial distribution (NBD), modified at low multiplicity by the BBC trigger efficiency. The parameters for the NBD distribution are fitted to real data distributions of the BBC response in a region where the MB trigger efficiency is nearly 100%. The BBC trigger efficiency can then be parametrized by comparing the NBD distribution with the measured BBC distribution at low multiplicity. The resulting $\langle N_{\text{coll}} \rangle$ values for the centrality categories used in this analysis are shown in Table 4.2. The N_{coll} distributions within each centrality bin are shown in Figure 4.9. There is a significant overlap between the N_{coll} distributions for different centralities.

Also shown in Table 4.2 is the correction factor c , which accounts for the correlation between the detection of a J/ψ in the final state and an increase in the total charge collected in the BBC [13]. This correlation affects both the minimum bias trigger efficiency and the determination of the centrality of a given collision. The correction factors for each centrality

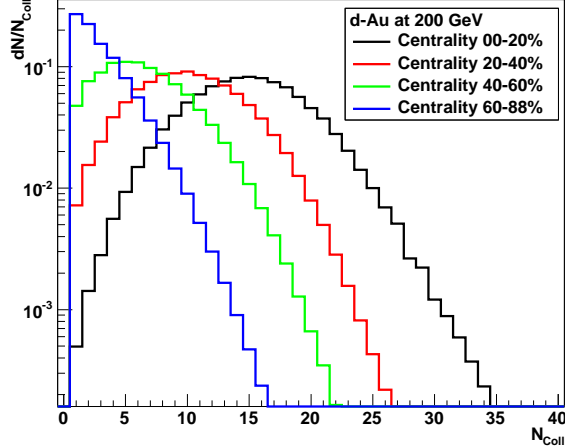


Figure 4.9: Nucleon nucleon collision (N_{coll}) distributions for each centrality bin obtained using a Glauber model for $d+\text{Au}$ collisions described in the text..

bin are obtained within the same Glauber framework as the $\langle N_{\text{coll}} \rangle$ values by assuming that one of the N binary collisions produces a charge in the BBC that is characteristic of a hard scattering process (the remaining $N-1$ binary collisions maintain a BBC charge distribution characteristic of soft scattering processes). The increase in the BBC charge from a hard process is tuned using real data.

Since both c and $\langle N_{\text{coll}} \rangle$ are calculated in the same Glauber framework there are correlations between their uncertainties. These correlations are removed in the ratio of $c/\langle N_{\text{coll}} \rangle$, which occurs in the calculation of $R_{d\text{Au}}$. The resulting values and uncertainties are given in the third column of Table 4.2. The correction factor for 0-100% centrality contains an additional factor to extrapolate the measured yield, which covers only 88% of all $d+\text{Au}$ collisions, to 100% of the $d+\text{Au}$ inelastic cross section, essentially correcting for the efficiency of the BBC trigger. This correction is again determined within the Glauber framework using the parametrization of the BBC trigger efficiency.

4.2.6 Electron Identification in the Central Arms

In the PHENIX central arms, charged particle tracks are defined from hits in the DC and PC. Electron candidates are selected by associating tracks with energy deposited in the EMCAL and rings in the RICH. Electron candidates are required to have a RICH ring associated with the track, the center of which is required to be < 5 cm from the track projection at the RICH. A RICH ring requires at least two phototube hits within a radius of $3.4 < R[\text{cm}] < 8.4$, as well as a value of χ^2 , which describes the circularity of the RICH ring, per photoelectron of < 20 . An association of a track with a cluster in the EMCAL of $\pm 4\sigma$ is also required, where σ characterizes the distribution of displacements after correction for the momentum dependence and geometric effects. The calibration of these signalized track matching parameters can be found in Appendix A.

After the requirement of an associated RICH ring, the most powerful discriminator of electron tracks is the ratio of the tracks energy to its momentum, E/p . For the electron momenta used in J/ψ analysis ($p > 150$ MeV) the electron can be considered massless and therefore the expected value for electron tracks is $E/p = 1$. Hadrons, on the other hand, rarely deposit a large fraction of their energy in the EMCAL. An electron track is required to have an energy to momentum ratio $> -2.5\sigma$ from the expected value, where σ again characterizes the momentum dependent width of the E/p peak that arises from the momentum and energy resolution of the detector. The calibration of this momentum dependent width can be found in Appendix B.

4.3 Data Selection

The $d+\text{Au}$ running period is broken down into individual “physics” runs, of which there were a few for each fill of d and Au bunches injected into RHIC. The $d+\text{Au}$ running period consisted of ≈ 850 analyzable “physics” runs, selected based on the overall detector and accelerator performance. These must then be further selected based on detector performance criteria specific for electron analysis.

Runs were tested based on the electron yield normalized to the number of MB triggers. For this sample a tighter electron identification cut requiring a unique match between hits in the DC and PC1 and the track was used to further reject contamination from hadrons. The electron yield in each run was checked separately in each sector of the EMCAL to separate geometric dependencies. The resulting electron yield in each EMCAL sector as a function of run number is shown in Figure 4.10.

A number of features in the observed ratios are notable. First, the group of runs showing larger than average electron yields, 251420-251633, are converter runs. In these runs a thin layer of Copper of a known radiation length is wrapped around the beam pipe to induce $\gamma \rightarrow e^+e^-$ conversions to give a cross check for single electron analysis. These are good runs and thus were not rejected on the basis of their electron yield. Second, for EMCAL sector 4 there is a drop in electron yield after run 249391. This drop is due to an issue in PC1, where a large segment was lost during the run. Since this drop does not seem clean, indeed the yield fluctuates up and down drastically, runs 249370-249447 where this fluctuation occurred were cut from the analysis. There is also a drop in the electron yield in EMCAL sector 6 after run 252968.

Because of the failure in PC1 and the change in the ERT trigger threshold, the data set was divided into four ranges, shown as the color samples in Figure 4.10. Details on each of the rungroups can be found in Table 4.3. The individual runs were checked separately for each set by determining the mean and width of the electron yield per MB trigger. Runs were rejected if the ratio was $> 4\sigma$ from the mean in at least three of the EMCAL sectors.

Runs were also rejected if the ratio of the number of MB triggers found in the reconstructed data files to that recorded in the DAQ was < 0.95 or > 1.05 . This insures that no file segments were lost or corrupted during the reconstruction of the data.

A total of 39 runs were rejected from this process, corresponding to a loss of 2.6% of the MB events. The final data sample analyzed corresponds to 141.6B MB events, for a total integrated luminosity of 62.7 nb^{-1} (assuming a $d+\text{Au}$ cross section of 2260 mb).

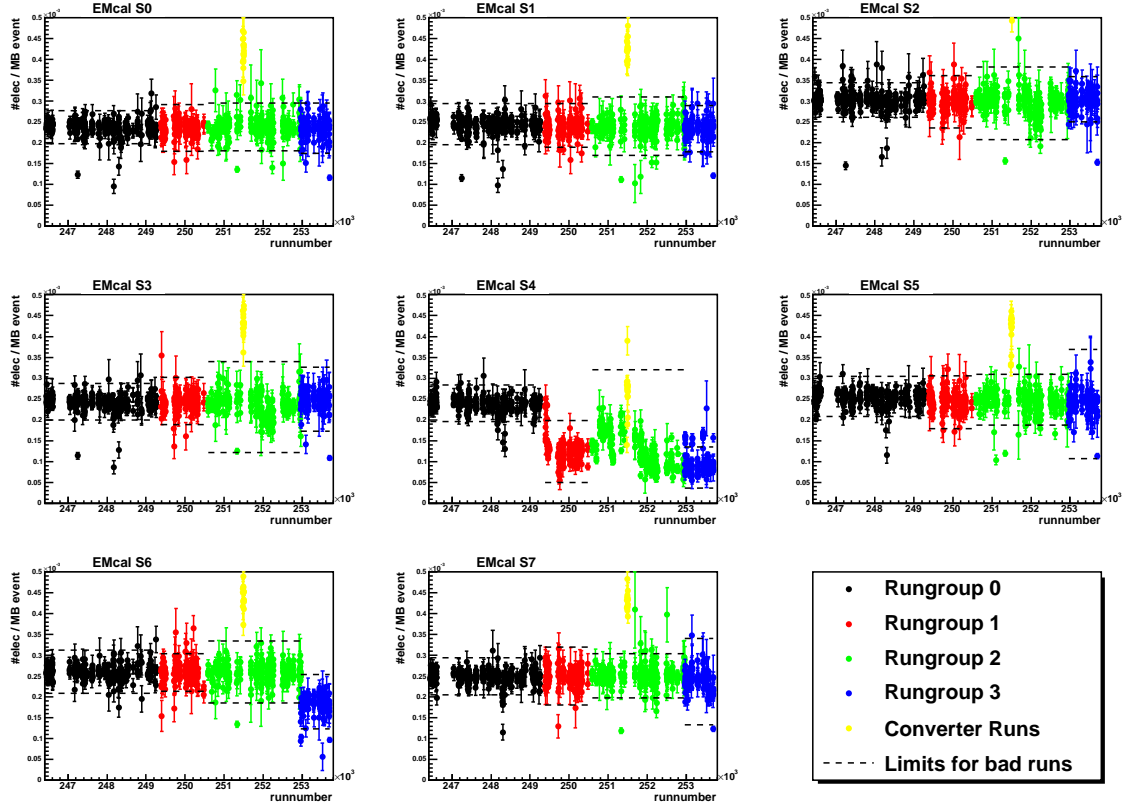


Figure 4.10: The number of electrons per scaled MB trigger versus run number for each EMcal sector.

Table 4.3: Information on the data sample used in this analysis.

| Rungroup | Run Range | ERT Trigger Threshold | # Good Runs | Analyzed MB events [$\times 10^9$] |
|----------|-----------------|-----------------------|-------------|--------------------------------------|
| 0 | 246444 → 249259 | 600 MeV | 299 | 29.0 |
| 1 | 249391 → 250484 | 600 MeV | 136 | 19.6 |
| 2 | 250593 → 252968 | 800 MeV | 276 | 65.0 |
| 3 | 252969 → 253701 | 800 MeV | 96 | 28.0 |
| Total | 246444 → 253701 | | 807 | 141.6 |

CHAPTER 5

J/ψ ANALYSIS

This chapter details the analysis methods, and presents the results, of the measurement of the $J/\psi \rightarrow e^+e^-$ production in the PHENIX central arms from $d+\text{Au}$ collision data taken in 2008. The final data sample used in the analysis was detailed in Section 4.3. The extraction of the measured $J/\psi \rightarrow e^+e^-$ yield is detailed in Section 5.1. The calculation of the detector efficiencies is detailed in Section 5.2. The results of this analysis are presented in Section 5.3, and discussed in conjunction with the $J/\psi \rightarrow \mu^+\mu^-$ analysis in Chapter 7.

5.1 J/ψ Signal Extraction

The J/ψ yield is measured in the central arms using the invariant mass spectrum of all e^+e^- pairs. This procedure is detailed in Section 5.1.1. The determination of the continuum correlated background under the J/ψ peak is detailed in Section 5.1.2.

5.1.1 Correlated e^+e^- Signal extraction

The invariant mass spectrum is calculated for all dielectron pairs in which at least one of the electrons fired the ERT trigger. This selection is necessary to match the conditions under which the J/ψ trigger efficiency is calculated (see Section 5.2.2). The invariant mass spectrum is determined separately for all unlike-sign and like-sign electron tracks in a given event, and then summed over all events. An example dielectron mass spectrum is shown in Figure 5.1 for 0-20% central collisions.

In a given bin of p_T , rapidity, and collision centrality, the correlated e^+e^- yield ($N_{e^+e^-}$) is determined by counting, over a fixed mass window of $2.8 < M_{ee} [\text{GeV}/c^2] < 3.3$, the number of unlike-sign dielectrons (fg), after the subtraction of the like-sign dielectrons (bg). The like-sign dielectron pairs arise by random association, and are therefore a measure of the combinatorial background within the unlike-sign dielectron distribution. This method assumes that the acceptance is the same for e^+ and e^- , which is true to better than 1% in the J/ψ mass region. Where yields are large, the statistical uncertainties on fg and bg are assumed to be Gaussian, therefore the statistical uncertainty on $N_{e^+e^-}$ is given by $\sigma_{N_{e^+e^-}} = \sqrt{fg + bg}$.

At high- p_T , where statistics are limited, this assumption no longer holds. Both $N_{e^+e^-}$ and its uncertainty are then determined assuming fg and bg follow Poisson statistics, where

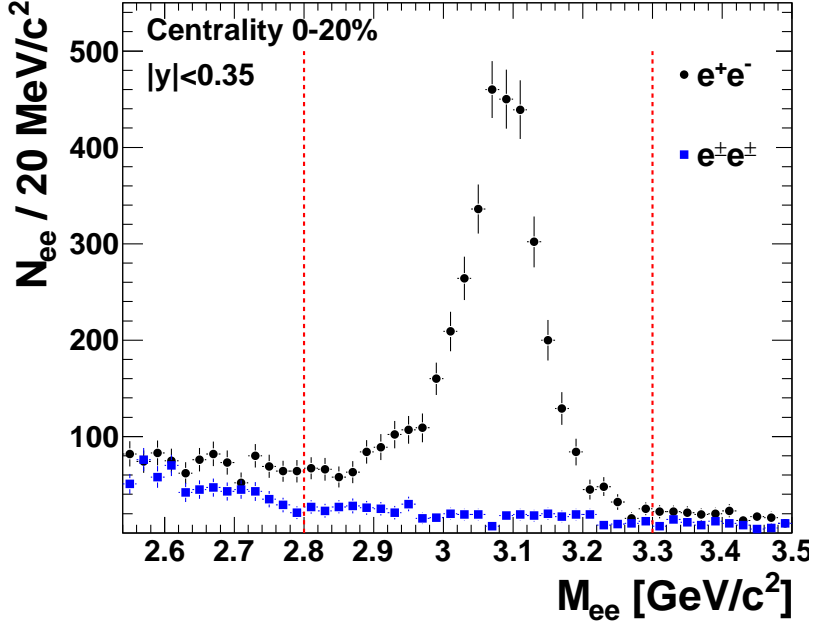


Figure 5.1: Invariant mass distribution of unlike-sign (filled circles) and like-sign (filled boxes) dielectron pairs in central $d+Au$ collisions, integrated over p_T and rapidity. Dashed vertical lines represent the mass range used to determine the correlated e^+e^- yield.

the probability of ν counts is given by

$$P(\nu) = e^{-\mu} \frac{\mu^\nu}{\nu!}, \quad (5.1)$$

where μ is the expected average counts ($\bar{\nu} = \mu$). The probability distribution for $N_{e^+e^-}$ is then given by a folding of two Poisson distributions. The correlated signal $s = \mu_f - \mu_b$ is

$$P(s, \mu_b) = \frac{\mu_b^{bg}}{bg!} \frac{\mu_b^{fg}}{fg!} e^{-2\mu_b} \left(1 + \frac{s}{\mu_b}\right)^{fg} e^{-s}. \quad (5.2)$$

The term $\left(1 + \frac{s}{\mu_b}\right)^{fg}$ is expanded:

$$\left(1 + \frac{s}{\mu_b}\right)^{fg} = \sum_{k=0}^{fg} \frac{fg!}{(fg-k)!k!} \left(\frac{s}{\mu_b}\right)^k, \quad (5.3)$$

which gives

$$P(s, \mu_b) = \sum_{k=0}^{fg} \frac{\mu_b^{bg+fg-k} e^{-2\mu_b}}{bg!(fg-k)!} \frac{s^k e^{-s}}{k!}. \quad (5.4)$$

Assuming no negative signal, the expression is summed over μ_b from 0 to ∞ using the normalization of the Gamma distribution

$$\int_0^\infty dx x^{p-1} e^{-bx} = \frac{(p-1)!}{b^p} \quad (5.5)$$

and $b = 2$, $p - 1 = bg + fg - k$. The final probability distribution is given by

$$P(s) = \sum_{k=0}^{fg} \frac{(bg + fg - k)!}{bg!(fg - k)!} \frac{1}{2} \left(\frac{1}{2}\right)^{bg+fg-k} \frac{s^k e^{-s}}{k!}, \quad (5.6)$$

which is used to determine the correlated dielectron signal, $N_{e^+e^-} = \langle s \rangle_P$. The statistical uncertainty is then taken as the standard deviation of $P(s)$, which is asymmetric in s .

A correlated e^+e^- yield in the mass window $2.8 < M_{ee} [\text{GeV}/c^2] < 3.3$ of approximately 8600 is obtained across all p_T and collision centralities. The detailed breakdown of fg and bg yields in each rapidity, centrality and p_T bin can be found in Appendix G.1.

5.1.2 Estimation of the Correlated Background and Losses Due to the Radiative Tail in the J/ψ Mass Distribution

When using the like-sign subtraction method detailed above, there remains a background of correlated e^+e^- pairs in the J/ψ mass region. This background comes mainly from open heavy flavor decays and Drell-Yan pairs, and must be separated from the J/ψ signal of interest. Counting the dielectron signal over a fixed mass window also causes an underestimate of the J/ψ yield due to the fraction of the J/ψ line shape that falls outside the mass window of choice. Both of these effects are quantified by using simulated line shapes fitted to the real data invariant mass distribution.

J/ψ and ψ' particles with uniform distributions in p_T ($0 < p_T [\text{GeV}/c] < 12$) and rapidity ($|y| < 0.35$) are decayed to e^+e^- and the external radiation effects are evaluated using a GEANT-3 based model of the PHENIX detector (described in Section 5.2.1). While a uniform distribution in p_T is unrealistic, the J/ψ rapidity distribution is roughly constant within $|y| < 0.35$. When used here, the J/ψ and ψ' line shapes will be compared to p_T integrated data as a function of invariant mass only, with a mass resolution fitted to the data, and therefore the effect of using a uniform p_T distribution is negligible.

The line shape for J/ψ radiative decays ($J/\psi \rightarrow e^+e^-\gamma$), also called internal radiation, is based on calculations of the mass distribution from QED [104] convoluted with the detector resolution and is given by

$$P(m) = \frac{\alpha}{\pi} \frac{2m}{(M_{J/\psi}^2 - m^2)} \left(1 + \frac{m^4}{M_{J/\psi}^4}\right) \left(\ln \frac{1+r}{1-r} - r\right), \quad (5.7)$$

where $r = \sqrt{1 - 4m_e^2/m^2}$, $\alpha = 1/137$ is the fine structure constant, m_e is the electron mass, and $M_{J/\psi}$ is the PDG value of the J/ψ mass. The fraction of J/ψ 's resulting from radiative decays is given by [104]

$$C_{\text{hard}} = \frac{\alpha}{2\pi} \left[4 \ln \frac{M_{J/\psi}}{2E_{\min}} \left(\ln \frac{M_{J/\psi}^2}{m_e^2} - 1 \right) - 3 \ln \frac{M_{J/\psi}^2}{m_e^2} - \frac{2}{3}\pi^2 + \frac{11}{2} \right], \quad (5.8)$$

Table 5.1: The fit parameters used to determine ϵ_{cont} and ϵ_{rad} .

| Parameter | Fit value |
|--|-----------------------------|
| Dielectron Yield from $D\bar{D}$ | 16130.2 ± 0.000116377 |
| Ratio of Dielectron Yield from $B\bar{B}/D\bar{D}$ | $0.031769 \pm 4.5697e-06$ |
| Dielectron Yield from DY | 161.924 ± 0.00859529 |
| J/ψ yield | 8589.59 ± 0.000116377 |
| $\psi'/J/\psi$ ratio | $0.0139667 \pm 1.39549e-06$ |
| Additional Mass Resolution [GeV] | $0.0016668 \pm 7.98756e-09$ |
| C_{hard} | $0.0517743 \pm 2.57646e-06$ |
| Mass Scale | 0.995137 ± 0.000108142 |
| Additional Mass Scale of Internal Radiation | $0.950444 \pm 7.74139e-07$ |

where E_{\min} is the minimum energy of the photon. For a minimum photon energy $E_{\min} = 100$ MeV, roughly 14.7% of the observed J/ψ spectrum comes from radiative decays ($C_{\text{hard}} \approx 0.147$). This is in good agreement with measurements by E760 which give a value of $14.7 \pm 2.2\%$ [41]. C_{hard} is left as a fit parameter in the fitting routine described below.

The heavy flavor background comes mainly from leptonic decays of correlated $D\bar{D}$ and $B\bar{B}$. The decays $D(B) \rightarrow e^+ + X$ and $\bar{D}(\bar{B}) \rightarrow e^- + X$ create a correlated dielectron signal over a broad mass range. The line shapes from these processes are simulated using PYTHIA [103]. The decay electrons from PYTHIA are then run through the GEANT simulation of the PHENIX detector to evaluate the external radiation effects. These line shapes are generated assuming $p + p$ collisions, and no corrections for CNM effects (i.e. application of nPDF modifications) are applied to the distributions. The CNM effects on these distributions are assumed to be small and roughly constant over the narrow mass window of the J/ψ due to the x values probed. No suppression of heavy flavor production has been observed in $d+\text{Au}$ collisions, and any suppression, if it exists, is assumed to not significantly effect the overall line shapes.

The line shapes are then fitted to the p_T and collision centrality integrated invariant mass spectrum over the mass range $2 < M_{ee} [\text{GeV}/c^2] < 8$. Here only the p_T and centrality integrated invariant mass spectrum is fitted, due to a lack of statistics in many of the individual rapidity and p_T bins used. The continuum contribution is assumed to be roughly constant with p_T and centrality. Since these contributions in the J/ψ region are relatively small (< 7%) any p_T or centrality dependence is likely a small effect. The normalizations on the J/ψ , ψ' , correlated heavy flavor, and DY are free to vary independently, along with an overall mass shift, an additional overall mass resolution parameter, and the factor C_{hard} , which fixes the ratio of direct $J/\psi \rightarrow e^+e^-$ decays to J/ψ radiative decays. The line shape for the J/ψ radiative decay is also allowed a mass shift independent of the other line shapes. The resulting fit parameters are shown in Table 5.1. The best fit is shown in the quarkonium mass region in Figure 5.2, where the continuum line shape is the combination of correlated e^+e^- pairs from $D\bar{D}$, $B\bar{B}$, and DY decays, and the J/ψ and ψ' line shapes are the combinations of the line shapes from both internal and external radiation effects.

Within the mass window $2.8 < M_{ee} [\text{GeV}/c^2] < 3.3$ the correlated continuum contribution (ϵ_{cont}) is found to be $6.6 \pm 0.2\%$ and the fraction of the J/ψ line shape contained within

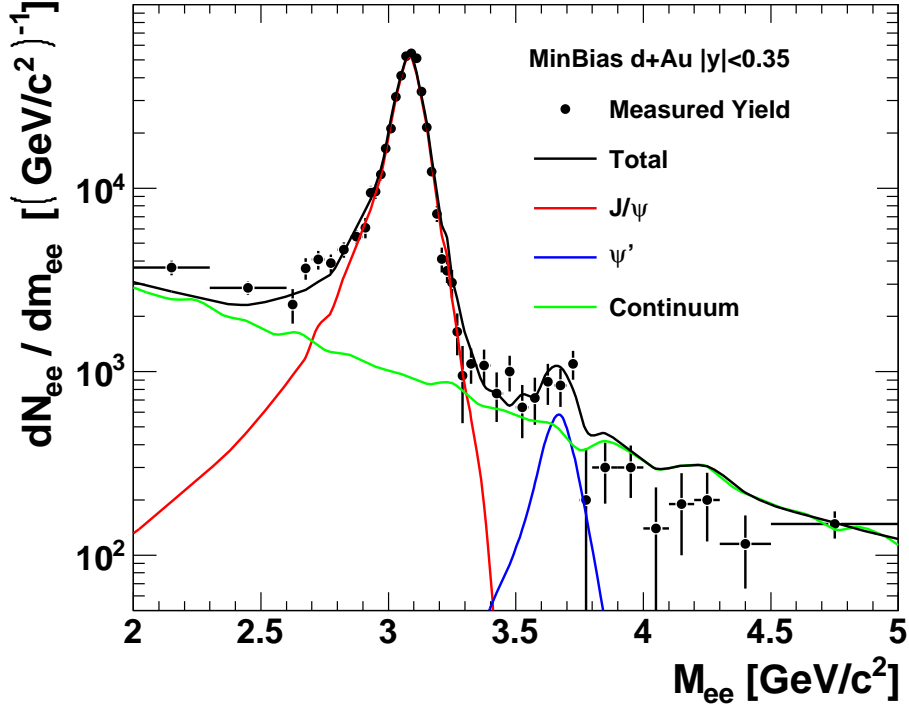


Figure 5.2: Correlated dielectron invariant mass distribution for minimum bias $d+Au$ collisions. The line shapes are those used to extract the continuum and radiative tail contributions to the correlated e^+e^- yield in the mass range $2.8 < M_{ee} [\text{GeV}/c^2] < 3.3$. The apparent structure in the continuum line shape is due to statistical fluctuations in the simulations.

the mass window (ϵ_{rad}) to be $94.3 \pm 0.2\%$. As ϵ_{cont} and ϵ_{rad} are not fit parameters, their uncertainties are complicated combinations of the uncertainties on all the fit parameters. To provide a direct method for sampling the uncertainty on ϵ_{cont} and ϵ_{rad} , the data points were randomly varied within their Type A systematic uncertainties and re-fitted. This procedure was repeated 1000 times, calculating ϵ_{cont} and ϵ_{rad} separately for each iteration. The widths of the ϵ_{cont} and ϵ_{rad} distributions from this procedure are taken as the uncertainties on ϵ_{cont} and ϵ_{rad} .

The disagreement between the fit and the data in the $3.7 < M_{ee} [\text{GeV}/c^2] < 4.5$ mass range is likely due to the inability of the $D\bar{D}$ and $B\bar{B}$ line shapes to match the shape of the data at higher mass. However, when varying the data points within their Type A uncertainties, it was found that large changes in the ratio of the $D\bar{D}$ to $B\bar{B}$ contributions produced only small changes in the total continuum contribution in the J/ψ mass region. The effect of these variations are included in the uncertainty on ϵ_{cont} and ϵ_{rad} .

5.2 Detector Acceptance and Efficiency Corrections

The raw J/ψ yields from Section 5.1 must be corrected for detector effects. The geometric efficiency of the detector as well as the J/ψ reconstruction efficiency is described in Section 5.2.1. The effect of the ERT trigger on the J/ψ yield is described in Section 5.2.2.

5.2.1 J/ψ Acceptance \times Reconstruction Efficiency

The J/ψ acceptance and reconstruction efficiency is investigated using a GEANT-3 [1] based Monte Carlo model of the PHENIX detector. To provide the most accuracy, dead and malfunctioning channels in the DC, PC1, RICH, and the EMCal are investigated using QA data taken during the Run. Channels which are found to be dead or malfunctioning in the data are masked in the simulation. This is done separately for each of the four rungroups described in Section 4.3, as the performance of the detector changed over the course of the Run.

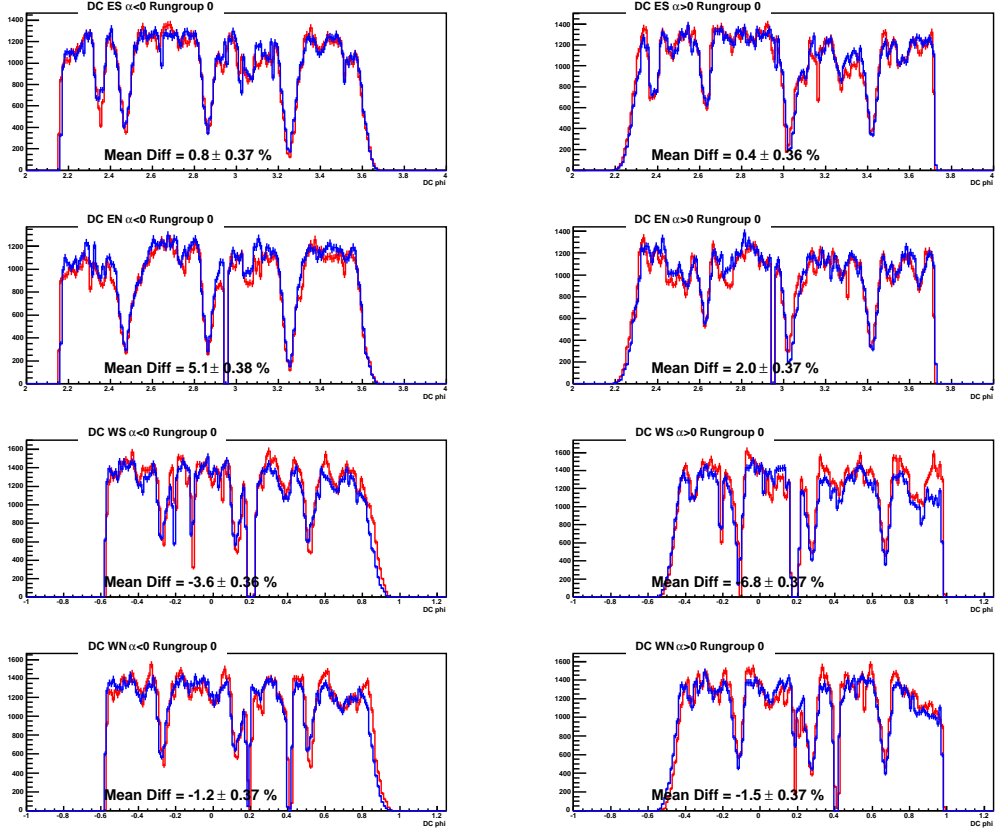


Figure 5.3: A comparison of the ϕ distributions between data (Red) and simulations (blue) for the first rungroup.

The accuracy of the simulations is tested by comparing simulated single electron distributions with those from real data. Five million single electrons(positrons) are generated

with an exponential momentum distribution ($e^{-3.71}$) from $0.5 < p[\text{GeV}/c] < 5$, based on a rough fit to the observed momentum spectra, and with flat rapidity and z vertex distributions. When comparing simulations to data, a tighter cut on the BBC zvertex of ± 20 cm is used to avoid conversions from the central arm magnets, as well as a low momentum cut on the electron of $> 0.5 \text{ GeV}/c$. The simulations are normalized to the data for a direct comparison by matching the electron p_T distribution in simulations to that observed in the data. Where large discrepancies between the data and simulations are found further geometric cuts were applied to both simulations and data. The uncertainty in the data to simulation matching is determined by calculating the mean difference between the ϕ distributions independently for each section of the DC, each bend angle (α), and each rungroup. An example is shown in Figure 5.3 from the first rungroup. The disagreement between data and simulations is found to range from 0.1 – 7%. The spread of the mean differences is found to be 3.2%, which is taken to be the systematic uncertainty in the single electron simulations. A conservative estimate, which assumes that the uncertainty is correlated for both electrons in a pair, of $2 \times 3.2\% = 6.4\%$ is assigned as a systematic uncertainty on the J/ψ acceptance based on the quality of the matching between simulations and data.

To determine the J/ψ acceptance, $J/\psi \rightarrow e^+e^-$ decays are simulated with uniform distributions in p_T , rapidity ($|y| < 0.5$) and collision vertex. While distributions uniform in p_T are not realistic, the corrections are made for small p_T bins where the real distribution can be approximated as linear. A test of this assumption, and the effect of bin sharing, is detailed later and taken into account when assigning systematic uncertainties. The fraction of J/ψ decays that are reconstructed corresponds to the combination of the geometric acceptance and the electron ID efficiency ($A \times \epsilon_{\text{eID}}^{J/\psi}$). The $J/\psi A \times \epsilon_{\text{eID}}^{J/\psi}$ is calculated separately for each rapidity and p_T bin, as well as each rungroup. The resulting $A \times \epsilon_{\text{eID}}^{J/\psi}$ curves are shown as a function of p_T in Figure 5.4, and given in Appendix G.2. The $A \times \epsilon_{\text{eID}}^{J/\psi}$ has an average value of 1.5% in 1 unit of rapidity when integrated over p_T , rapidity and rungroup. The dip in $A \times \epsilon_{\text{eID}}^{J/\psi}$ followed by a continual increase with p_T marks the transition from the e^+e^- pair at low p_T being produced back to back and being detected one in each of the PHENIX central arms, to the pair at high p_T being produced in a collinear manner and being detected both in the same PHENIX central arm. The low point at $p_T \approx 3 \text{ GeV}/c$ corresponds to the e^+e^- being produced at roughly 90° relative to each other in the lab frame, which due to the PHENIX geometry has the lowest probability for detection. The $A \times \epsilon_{\text{eID}}^{J/\psi}$ is larger at $-0.1 < y < 0.1$, as this range is fully covered by the PHENIX acceptance, while in the two other rapidity regions it is more likely that one of the electrons will miss the PHENIX central arms. The differences between $-0.5 < y < -0.1$ and $0.1 < y < 0.5$ are due to largely to the distribution of dead and malfunctioning channels across the detector.

The electron ID (eID) efficiency implemented in the simulations is cross checked with the eID efficiency determined from real data in [20]. The same simulation setup is used in this work, and therefore, the results of the comparison in [20] are used here as well. The eID efficiency is mainly due to track reconstruction cuts used to avoid the misidentification of hadrons as electrons, and is calculated using electrons from π^0 Dalitz decays and γ conversions. In [20], all dielectron pairs above the combinatorial background in the mass range $< 0.30 \text{ GeV}/c^2$ are assumed to be true dielectrons from Dalitz decays. The eID efficiency is calculated by taking the ratio of the number of dielectrons where both electron

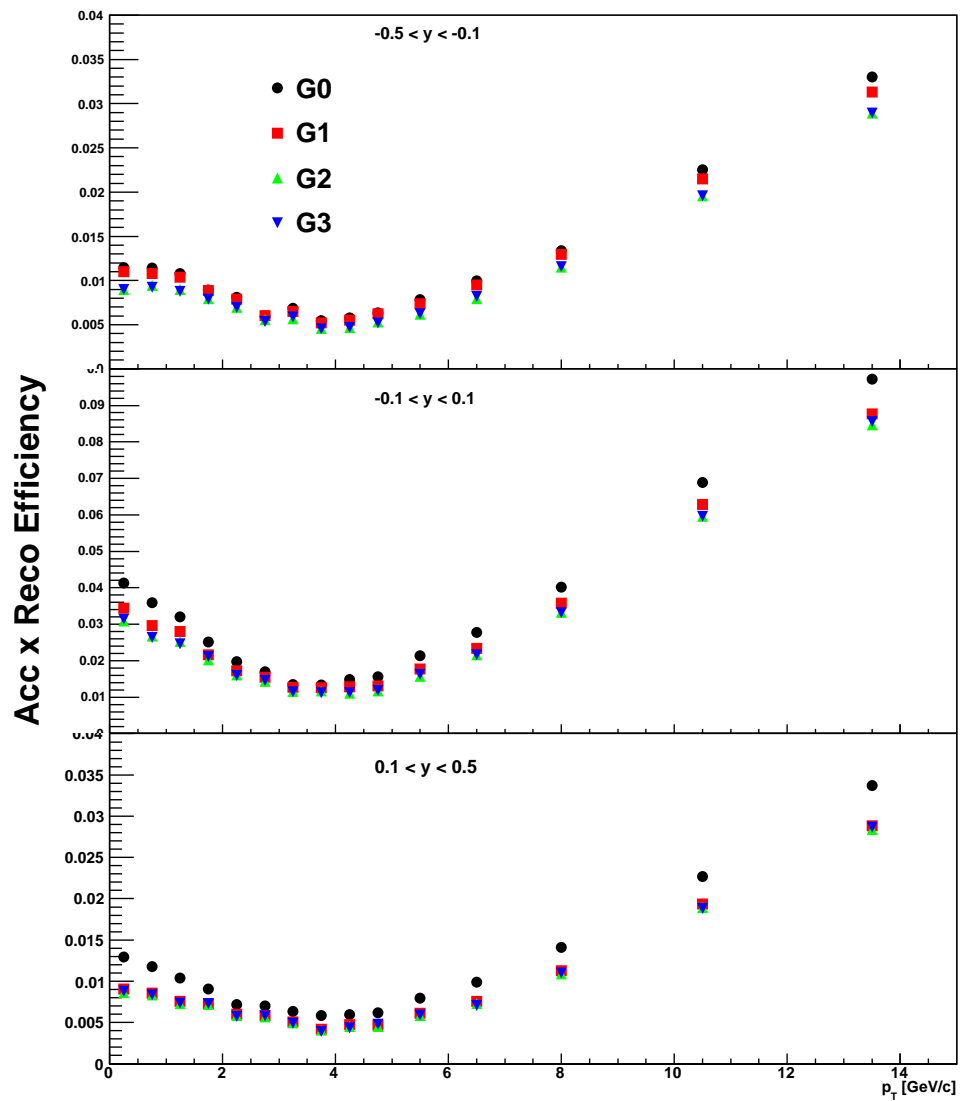


Figure 5.4: The J/ψ acceptance \times electron ID efficiency as a function of transverse momentum for each rungroup and each rapidity bin used in the analysis.

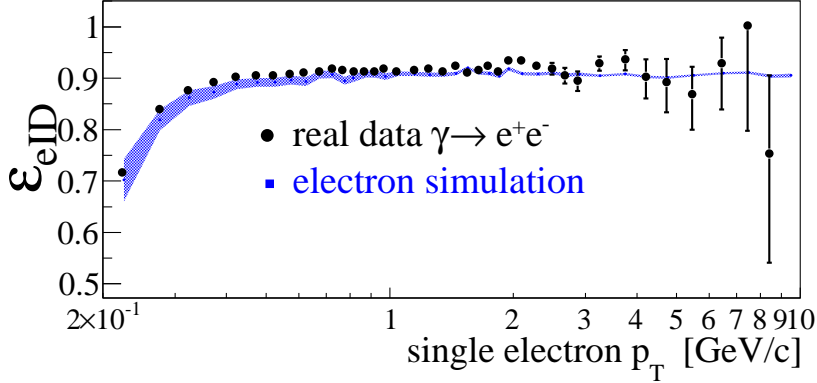


Figure 5.5: The eID efficiency in simulations compared with measured electrons from Dalitz decays [20].

and positron passed the electron identification criteria, to the number of dielectrons where only one of the pair passed the electron identification criteria. The resulting eID efficiency is shown in Figure 5.5 as a function of electron p_T , compared with the eID efficiency extracted from simulations of Dalitz decays. Overall, good agreement is found between the observed and simulated eID efficiencies, with an additional systematic uncertainty on the $A \times \epsilon_{\text{eID}}^{J/\psi}$ of 1.1% assigned due to the difference between the two results.

The measured momentum of electrons from J/ψ decays is smeared due to the detector resolution. This can cause a difference between the reconstructed p_T of the J/ψ and its true p_T . A Monte-Carlo model is used to test the impact of this effect on the $J/\psi A \times \epsilon_{\text{eID}}^{J/\psi}$. Kinematics for 5 million $J/\psi \rightarrow e^+e^-$ decays were generated using a p_T distribution of the form

$$p_T = 2.99 \times 10^4 * p_T (1 - 0.172 p_T^2)^{-3.5}, \quad (5.9)$$

which is based on a fit to the uncorrected $J/\psi p_T$ distribution. The momentum of the decay electrons was then randomly smeared using a parametrization of the detector momentum resolution given by

$$\frac{\delta p}{p} = 0.72 + p * 0.75, \quad (5.10)$$

and the $J/\psi p_T$ reconstructed. Figure 5.6 shows the reconstructed p_T distributions for a given generated p_T bin, using the same p_T bins used in the J/ψ yield extraction. We find that the spill-over between reconstructed p_T bins is small, even at large p_T .

The ratio of the reconstructed p_T to the generated p_T distribution is then taken for each of the p_T bins. This gives the percentage of J/ψ 's in a given measured p_T bin which were produced in that p_T range. This ratio is shown in Figure 5.7 for each rapidity and p_T bin. The mean ratio is 1.002, therefore a systematic uncertainty of 0.2% was taken to account for this effect.

A combined uncertainty of 6.5% is assigned to the $J/\psi A \times \epsilon_{\text{eID}}^{J/\psi}$ by adding the simulation/data matching, eID, and momentum smearing uncertainties in quadrature.

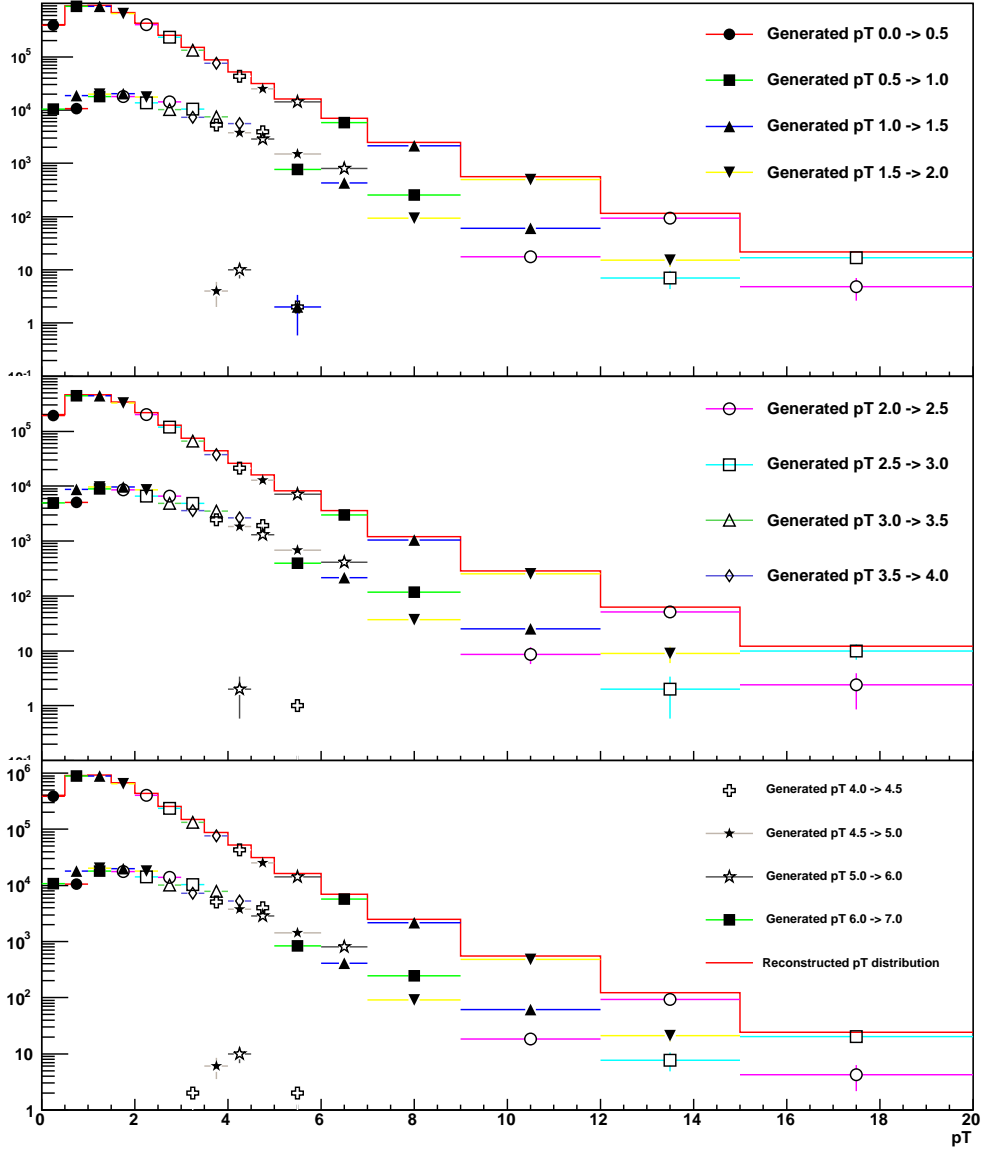


Figure 5.6: The reconstructed p_T distributions for a given generated p_T range, as well as the full reconstructed p_T distribution.

5.2.2 J/ψ Trigger Efficiency

The efficiency of the ERT trigger for firing on J/ψ decays is investigated using $J/\psi \rightarrow e^+e^-$ simulations and parametrizations of the single electron trigger efficiency. The ERT trigger used in this analysis requires a coincidence between energy deposited in a 2x2 array of towers in the EMCAL and a geometrically associated hit in the RICH.

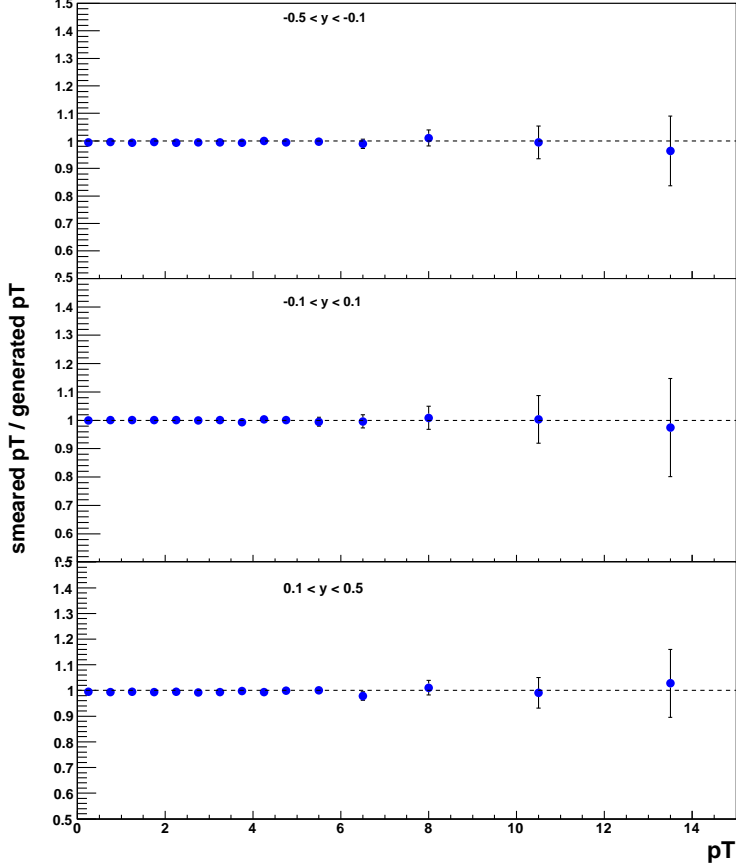


Figure 5.7: The ratio of the number of J/ψ 's reconstructed within a given p_T range to the number of J/ψ 's generated in that p_T range for each rapidity and p_T bin used in the analysis.

To parametrize the single electron trigger efficiency the p_T dependent triggering efficiency of each supermodule (SM) in the RICH and EMCal, where a SM in the EMCal and RICH is defined in Sections 4.2.2.3 and 4.2.2.4 respectively, was measured individually using a MB data sample of single electrons. The efficiency of each SM was calculated by taking the fraction of electrons that fired the trigger tile compared to all those passing through it. The resulting distributions in each of the EMCal SM's were then fitted with an error function, while the SM's in the RICH were fitted with a uniform function. This procedure was done separately for each rungroup. Figures 5.8 and 5.9 show the single electron trigger efficiencies for each SM in the EMCal and RICH respectively with the associated fits for the first rungroup. The fits for the other 3 rungroups can be found in Appendix F.1.

The J/ψ ERT efficiency ($\epsilon_{\text{ERT}}^{J/\psi}$) was then calculated using the $J/\psi \rightarrow e^+e^-$ simulations described in Section 5.2.1, and the parametrized SM efficiencies. Before calculating the trigger efficiency, both simulated electrons from the J/ψ decay were required to pass an acceptance check to avoid double counting the acceptance. For each decay electron, a

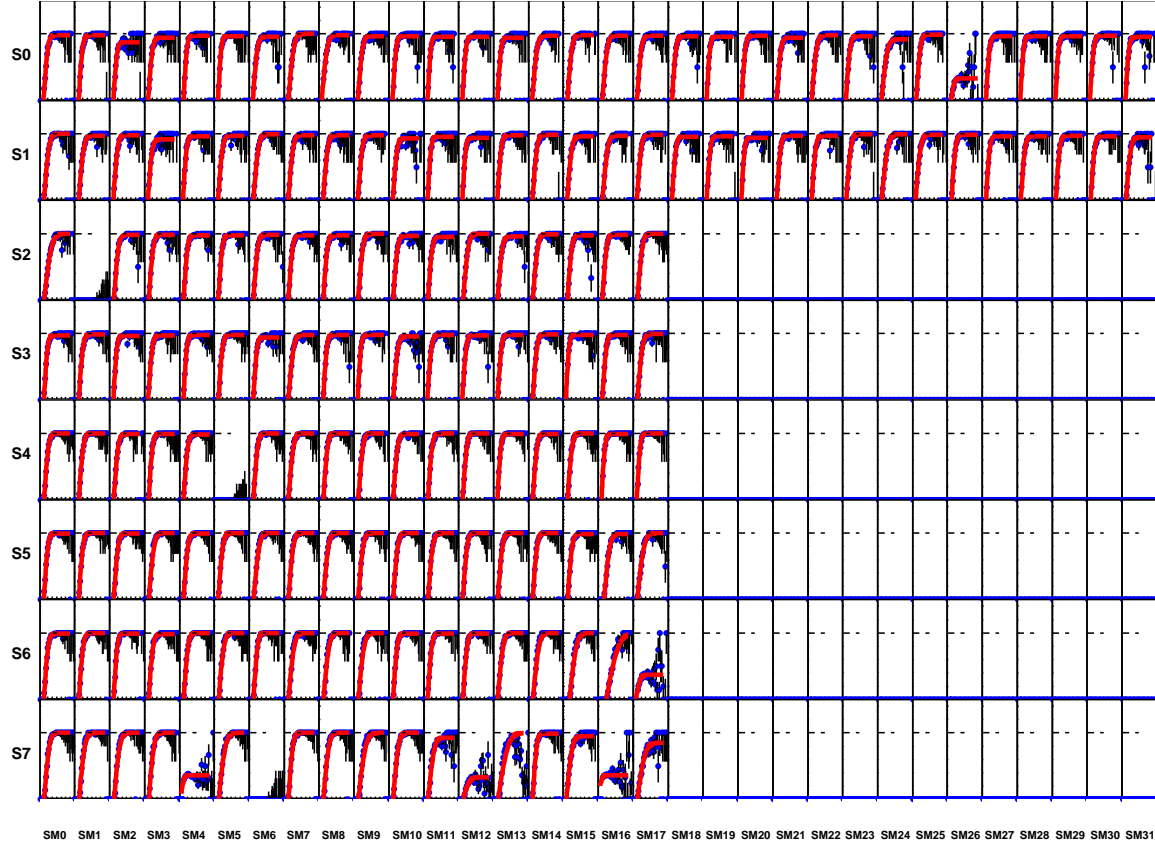


Figure 5.8: The single electron trigger efficiency for each SM in the EMCAL in the first rungroup. Each panel represents the single electron trigger efficiency as a function of electron momentum for a given sector (Y-axis of the figure) and SM (X-axis of the figure). The data is represented by the blue points and the red curve represents the error function fit to the measured data described in the text.

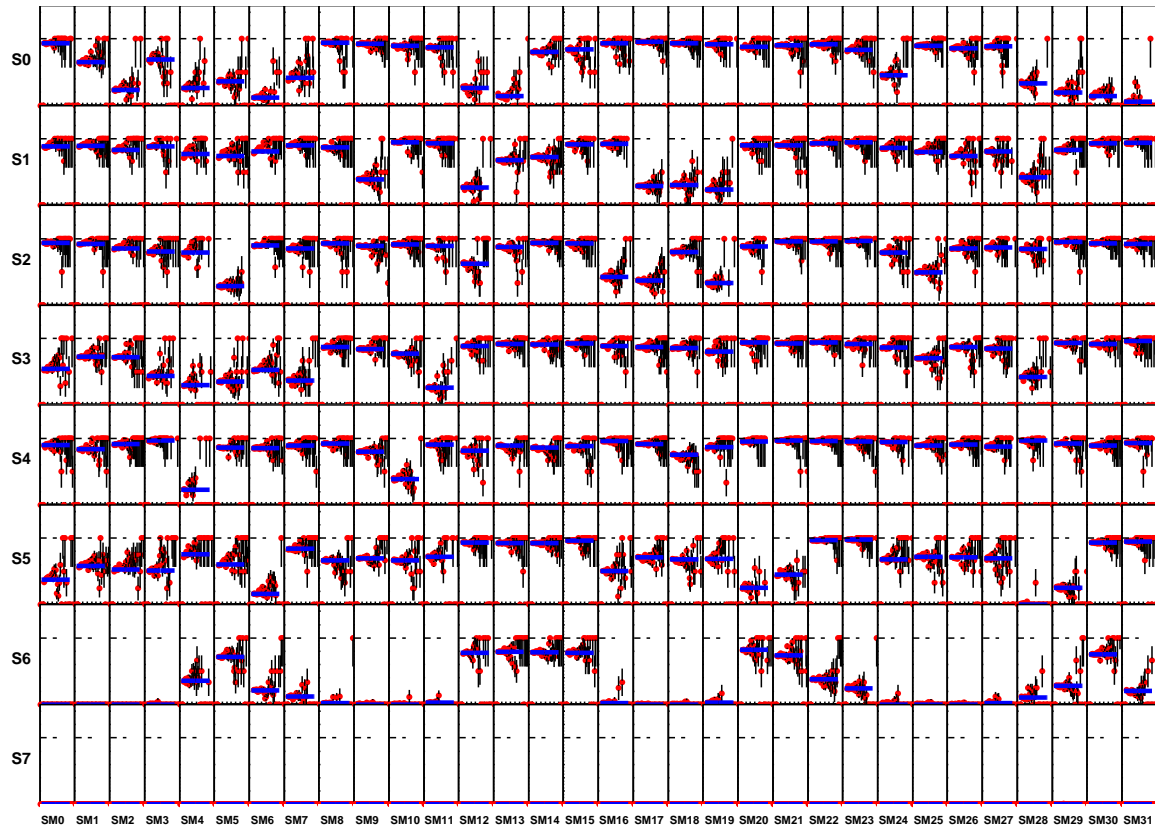


Figure 5.9: The single electron trigger efficiency for each SM in the RICH in the first rungroup. Each panel represents the single electron trigger efficiency as a function of electron momentum for a given sector (Y-axis of the figure) and SM (X-axis of the figure). The data is represented by the red points and the blue line represents the fit to the measured data described in the text.

random number was thrown and compared against the parametrized momentum dependent SM efficiencies to determine if it would have fired the RICH and EMCAL trigger for the SM the track passed through. The J/ψ ERT efficiency was then calculated by taking the ratio of all J/ψ 's for which at least one of the decay electrons fired both the EMCAL and RICH SM to all simulated J/ψ 's which passed the acceptance check. This procedure was done separately for each rungroup (and therefore each ERT trigger threshold). The p_T dependence of $\epsilon_{\text{ERT}}^{J/\psi}$ is shown in Figure 5.10 for each rungroup, and given in Appendix G.3. The dip seen at $p_T \approx 3 \text{ GeV}/c$ is due to the kinematics of the J/ψ decays. In that p_T range there is a high probability for the decay electrons to have unbalanced momenta, where one of the electrons will have a momentum below or near the trigger threshold, resulting in a lower probability for triggering on the J/ψ . The lower average efficiency for J/ψ 's with $p_T < 6 \text{ GeV}/c$ seen in the last two rungroups (G2 & G3) is due to the higher ERT trigger threshold (800 MeV) used during those runs.

The effect of the fit function used when fitting the EMCAL SM efficiencies was tested by replacing the error function with a double-Fermi function of the form

$$\frac{\epsilon_0^1}{\exp - (p_T - p_0^1)/k^1 + 1} + \frac{\epsilon_0^2}{\exp - (p_T - p_0^2)/k^2 + 1}, \quad (5.11)$$

which had been found to reproduce the low momentum behavior marginally better in other single electron analyses. This resulted in an average difference, weighted by the measured J/ψ yield, in $\epsilon_{\text{ERT}}^{J/\psi}$ of 0.31%.

The effect of the uncertainty in the fits to the measured SM efficiencies due to the statistical uncertainty in the data sample used was tested by varying the measured SM efficiencies independently and refitting. This procedure was repeated 20 times and the resulting $\epsilon_{\text{ERT}}^{J/\psi}$ calculated for each set of variations. This produced an average variation in $\epsilon_{\text{ERT}}^{J/\psi}$, weighted by the measured J/ψ yield, of 1.6%.

Both of these differences are taken as contributions to the systematic uncertainty in $\epsilon_{\text{ERT}}^{J/\psi}$. The total systematic uncertainty on $\epsilon_{\text{ERT}}^{J/\psi}$ is taken to be 1.6%, where both effects have been added in quadrature.

5.2.3 J/ψ Embedding Efficiency

The effect of detector occupancy on the reconstruction of a J/ψ is also taken into account. The centrality dependence of embedding studies in Cu+Cu [14], where simulated J/ψ 's are embedded in real events, predicts that in peripheral Cu+Cu collisions, where the number of binary collisions is similar to a central $d+\text{Au}$ collision, the efficiency of reconstructing J/ψ 's in the presence of a real event background is nearly 100%. An efficiency of 100%, with a conservative uncertainty of $\pm 1\%$ is assigned based on this study. This result agrees well with the studies done in [13], where a slightly larger systematic uncertainty was assigned because of the lower statistical precision of the simulations used.

5.3 Results

The calculation of the J/ψ invariant yield, as well as the J/ψ nuclear modification factor, $R_{d\text{Au}}$, is detailed here. These results, along with the results of $J/\psi \rightarrow \mu^+ \mu^-$ production

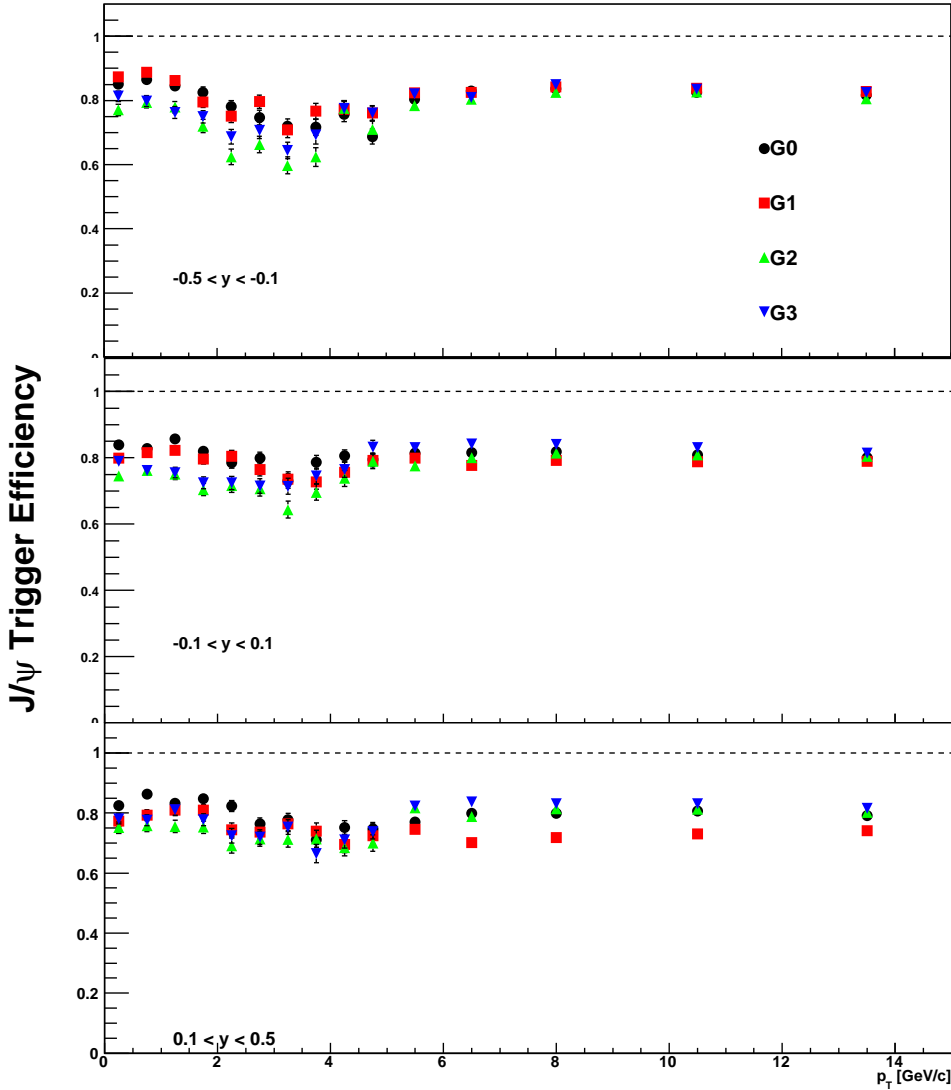


Figure 5.10: The J/ψ ERT efficiency for each rungroup in the 3 rapidity bins used in this analysis.

in the PHENIX muon arms, will be discussed in detail and compared with theoretical calculations in Chapter 7. First, the calculation of the J/ψ invariant yield will be described in Section 5.3.1. In Section 5.3.2 the calculation of the p_T broadening in $d+Au$ collisions is discussed. In Section 5.3.3, calculations of the nuclear modification at midrapidity as a function of centrality and p_T is described.

5.3.1 J/ψ Invariant Yield

The results of the $J/\psi \rightarrow e^+e^-$ analysis detailed above are presented here in the form of an invariant per-event yield. The J/ψ invariant yield as a function of rapidity in a given centrality bin can be calculated as

$$B_{ll} \frac{dN}{dy} = \frac{c N_{J/\psi}}{N_{\text{EVT}} \epsilon_{\text{tot}} \Delta y}, \quad (5.12)$$

and as a function of p_T in a given rapidity and centrality bin as

$$\frac{B_{ll}}{2\pi p_T} \frac{d^2N}{dy dp_T} = \frac{1}{2\pi p_T \Delta p_T \Delta y} \frac{c N_{J/\psi}}{N_{\text{EVT}} \epsilon_{\text{tot}}}, \quad (5.13)$$

where B_{ll} is the $J/\psi \rightarrow l^+l^-$ branching ratio, $N_{J/\psi}$ is the measured J/ψ yield, N_{EVT} is the number of sampled MB events, Δy is the width of the rapidity bin, Δp_T is the width of the transverse momentum bin, ϵ_{tot} is the total efficiency correction factor given by

$$\epsilon_{\text{tot}} = A \times \epsilon_{\text{eID}}^{J/\psi} \epsilon_{\text{ERT}}^{J/\psi} \epsilon_{\text{rad}}, \quad (5.14)$$

and c is the BBC bias correction factor described in Section 4.2.5 and given in Table 4.2. Here $N_{J/\psi} = N_{e^+e^-} (1 - \epsilon_{\text{cont}})$, where ϵ_{cont} is the correlated dielectron continuum contribution in the J/ψ mass range.

Table 5.2: A summary of the systematic uncertainties on the $J/\psi \rightarrow e^+e^-$ invariant yield and their associated types for each observable.

| Source | Value | y | p_T |
|--|----------|-----|-------|
| c (Invariant yield only) | 0.1-5.8% | C | C |
| $c/\langle N_{\text{coll}} \rangle$ ($R_{d\text{Au}}$ only) | 3-6% | C | C |
| Embedding | 1.0% | B | C |
| ϵ_{rad} | 0.2% | B | C |
| ϵ_{cont} | 0.2% | B | C |
| $A \times \epsilon_{\text{eID}}$. | 6.5% | B | B |
| $\epsilon_{\text{ERT}}^{J/\psi}$. | 1.6% | B | B |
| Stat. Uncertainty on the correlated e^+e^- yield | | A | A |

In PHENIX, systematic uncertainties are assigned to one of three categories. Type A uncertainties are uncertainties which are uncorrelated from point to point, and are represented as vertical error bars on all plots. Type B uncertainties are uncertainties which are correlated from point to point, and are represented by boxes around each data point. Type C uncertainties are uncertainties in the overall normalization, and are stated as percentages on the plot. A summary of the systematic uncertainties is shown in Table 5.2.

The J/ψ invariant yield as a function of rapidity for 0-100% centrality integrated $d+\text{Au}$ collisions, as well as the centrality dependent results, are given in Table 5.3. The J/ψ invariant yield as a function of p_T for 0-100% centrality integrated $d+\text{Au}$ collisions is shown

Table 5.3: The J/ψ invariant yield as a function of rapidity for 0-100% centrality integrated $d+\text{Au}$ collisions and as a function of centrality.

| Centrality | y | $B_{ll} \frac{dN}{dy} / N_{coll} [\times 10^{-7}]$ | Type A | Type B | Type C |
|------------|------|--|--------|--------|--------|
| 0-100% | -0.3 | 8.93 | 0.22 | 0.60 | 0.31 |
| 0-100% | 0.0 | 8.30 | 0.18 | 0.56 | 0.28 |
| 0-100% | 0.3 | 8.61 | 0.22 | 0.58 | 0.29 |
| 00-20% | -0.3 | 8.46 | 0.34 | 0.57 | 0.41 |
| 00-20% | 0.0 | 7.90 | 0.28 | 0.53 | 0.38 |
| 00-20% | 0.3 | 8.16 | 0.34 | 0.55 | 0.39 |
| 20-40% | -0.3 | 9.27 | 0.43 | 0.63 | 0.38 |
| 20-40% | 0.0 | 8.99 | 0.37 | 0.61 | 0.37 |
| 20-40% | 0.3 | 9.55 | 0.45 | 0.65 | 0.39 |
| 40-60% | -0.3 | 9.66 | 0.56 | 0.65 | 0.49 |
| 40-60% | 0.0 | 8.61 | 0.44 | 0.58 | 0.44 |
| 40-60% | 0.3 | 8.73 | 0.54 | 0.59 | 0.44 |
| 60-88% | -0.3 | 10.20 | 0.68 | 0.69 | 0.77 |
| 60-88% | 0.0 | 9.05 | 0.56 | 0.61 | 0.68 |
| 60-88% | 0.3 | 9.25 | 0.66 | 0.63 | 0.70 |

in Figure 5.11. The centrality dependent J/ψ invariant yield as a function of p_T is shown in Figure 5.12. In both Figures 5.11 and 5.12 the data points represent the invariant yield averaged over the p_T bin, and are plotted at the center of the bin. This provides the measured information without introducing further uncertainty due to a lack of knowledge of the detailed shape of the distribution within the p_T bin.

5.3.2 Calculation of the $J/\psi \langle p_T^2 \rangle$

The broadening of the p_T distribution in $d+\text{Au}$ collisions can be quantified by calculating the $\langle p_T^2 \rangle$. Unlike in previous analysis [13], where the $\langle p_T^2 \rangle$ was calculated only for $p_T \leq 5 \text{ GeV}/c$ due to statistical limitations at high p_T , here the $\langle p_T^2 \rangle$ is calculated over the full p_T range. The calculation of the $\langle p_T^2 \rangle$ of the J/ψ invariant yields presented in Section 5.3.1 is performed by first calculating the $\langle p_T^2 \rangle$ numerically up to the p_T limits of the measured distribution, $\langle p_T^2 \rangle|_{p_T \leq p_T^{max}}$, using

$$\langle p_T^2 \rangle|_{p_T \leq p_T^{max}} = \sum_{i=0}^N \frac{\langle p_T^2 \rangle_i \frac{dN_i}{dp_T} p_{Ti} \Delta p_{Ti}}{\frac{dN_i}{dp_T} p_{Ti} \Delta p_{Ti}} \quad (5.15)$$

where i labels the p_T bin, $\frac{dN_i}{dp_T}$ is the invariant yield as a function of p_T , p_{Ti} is the value of p_T at the center of the bin, $\langle p_T^2 \rangle_i$ is the mean p_T squared in the given p_T bin, and Δp_{Ti} is the width of the p_T bin. The $\langle p_T^2 \rangle_i$ is determined from a fit to the invariant yields, described below.

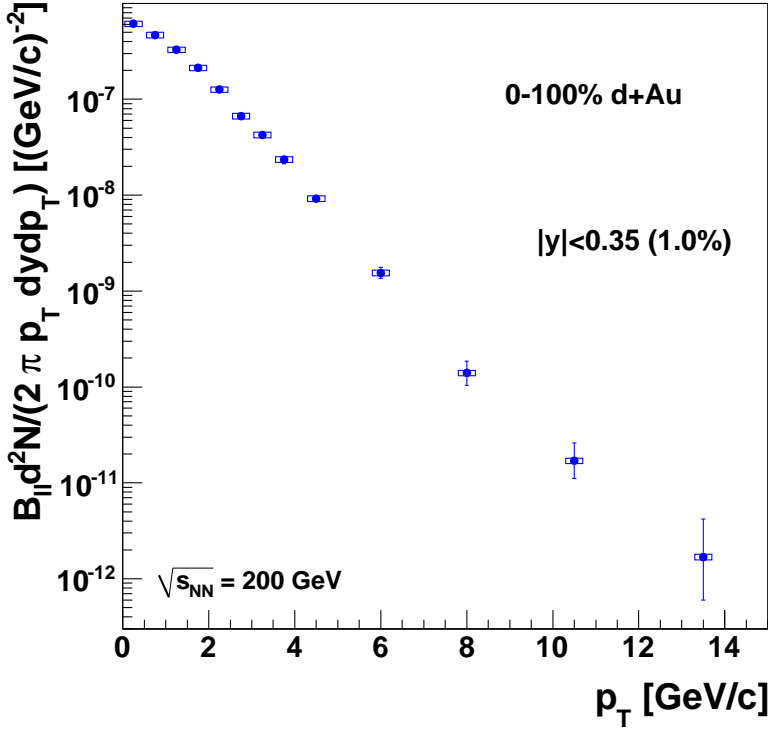


Figure 5.11: The J/ψ invariant yield as a function of transverse momentum for 0-100% centrality integrated $d+Au$ collisions at $|y| < 0.35$. The type C systematic uncertainty for each distribution is given as a percentage in the legend.

The uncertainty on $\langle p_T^2 \rangle$ due to the Type A systematic uncertainty on $\frac{dN_i}{dp_T}$ is calculated using

$$\sigma_{\langle p_T^2 \rangle}^2 = \frac{\sum_{i=0}^N (\sigma_{A_i} p_{T_i} \Delta p_{T_i})^2 (\langle p_T^2 \rangle_i - \langle p_T^2 \rangle)^2}{\sum_{i=0}^N \frac{dN_i}{dp_T} p_{T_i} \Delta p_{T_i}} \quad (5.16)$$

where σ_{A_i} is the Type A uncertainty on $\frac{dN_i}{dp_T}$. The derivation of this formula uses normal error propagation rules, and is given in Appendix C.

When propagating the Type B correlated systematic uncertainties on the J/ψ invariant yields to the calculated $\langle p_T^2 \rangle$ values, the type B uncertainties are assumed to be normally distributed. With this assumption, the uncertainty distribution of the first and the last data point of the p_T distribution are independently sampled. The Type B uncertainties are then assumed to be linearly correlated between these two values. The width of the resulting distribution of the $\langle p_T^2 \rangle$ values that arises from this procedure gives an estimate of the effect of the Type B uncertainties on the value of $\langle p_T^2 \rangle$.

The Type C systematic uncertainties on the J/ψ invariant yields do not affect the calculation of $\langle p_T^2 \rangle$. The Type C uncertainties are a global uncertainty, which cancels in the calculation.

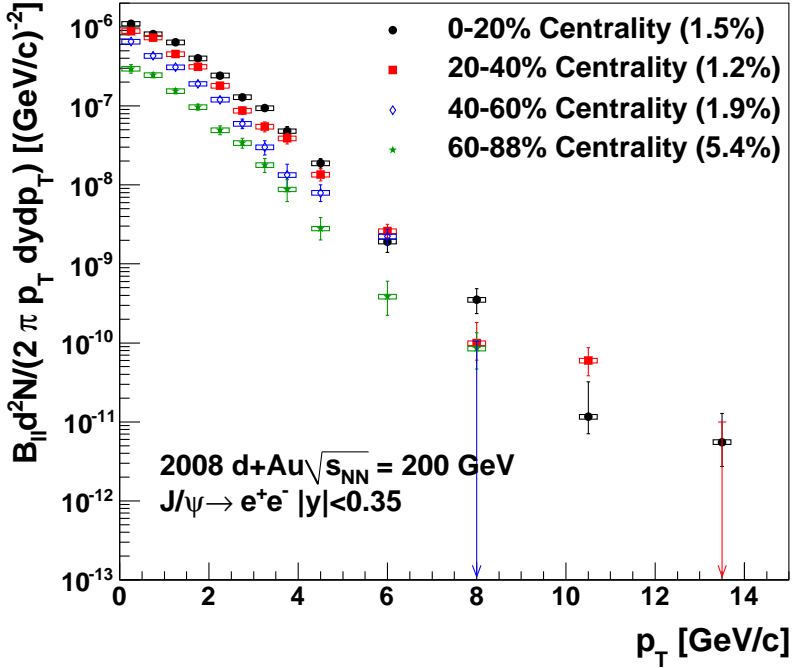


Figure 5.12: The J/ψ invariant yield as a function of transverse momentum for each centrality at $|y| < 0.35$. The type C systematic uncertainty for each distribution is given as a percentage in the legend.

Since the experimental upper p_T limits on the J/ψ invariant yield distributions vary with rapidity and centrality, a correction factor, k , was calculated in each case to extend these to infinite p_T . The J/ψ invariant yields as a function of p_T are first fitted with a modified Kaplan function of the form

$$f(p_T) = p_0 \left(1 - \left(\frac{p_T}{p_1} \right)^2 \right)^{p_2}, \quad (5.17)$$

where the data points are compared to the integral of the function over the p_T bin when calculating the χ^2 . The fit results, along with the ratio of the data to the fit are shown in Figure 5.13 for $p+p$ collisions and for 0-100% centrality integrated $d+Au$ collisions. The fit results for each centrality bin are shown in Figure 5.14.

Using these fits, the ratio

$$k = \frac{\langle p_T^2 \rangle [0, \infty]}{\langle p_T^2 \rangle [0, p_T^{\max}]} \quad (5.18)$$

is calculated from the fit and applied to the numerically calculated $\langle p_T^2 \rangle|_{p_T \leq p_T^{\max}}$. The correction factors are shown in Table 5.4, and are in all cases small ($k < 1.03$). The uncertainty on k is derived from the fit uncertainty by varying the data points within their statistical uncertainties, refitting, and thereby finding the variation in k . This uncertainty

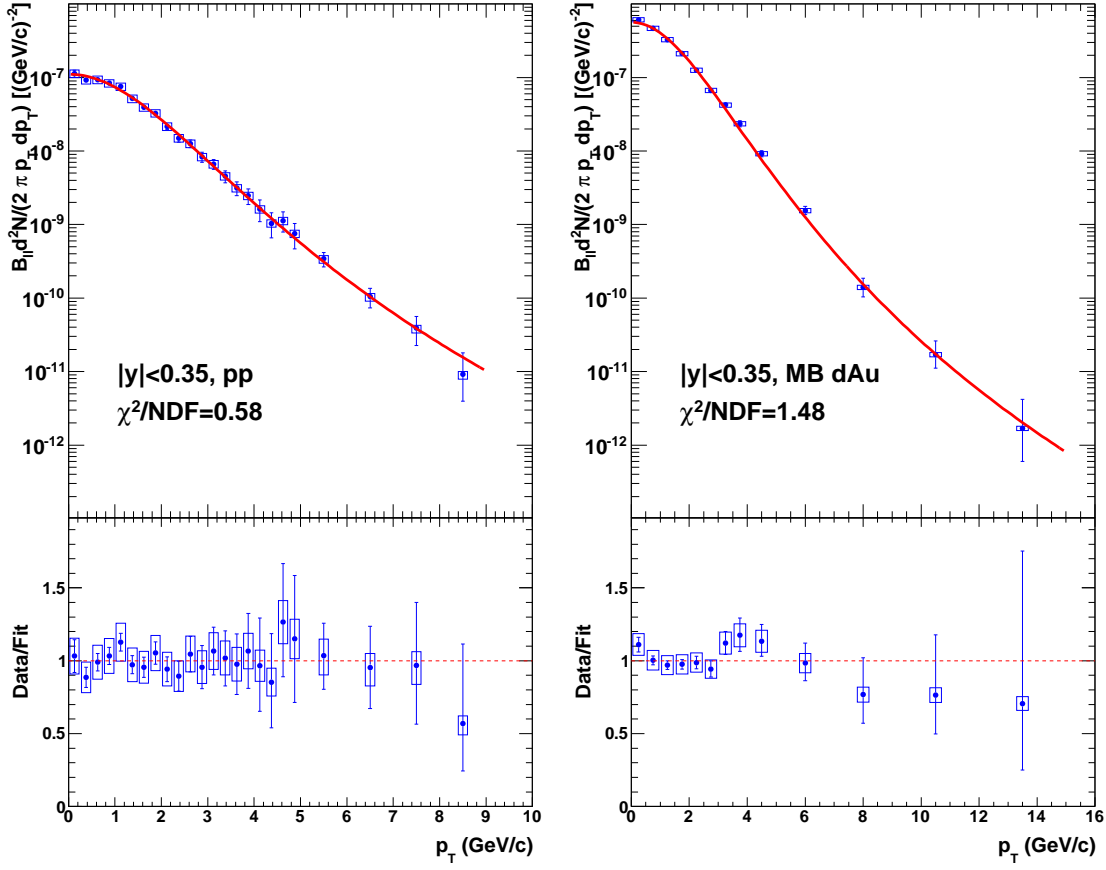


Figure 5.13: Results of modified Kaplan fits to midrapidity $p+p$ (Left) and midrapidity 0-100% $d+\text{Au}$ (Right).

Table 5.4: The $J/\psi \langle p_T^2 \rangle$ correction factors, k , for $p+p$ and $d+\text{Au}$ collisions.

| System | y range | Centrality | k |
|---------------|--------------|------------|-------------------|
| $p+p$ | $ y < 0.35$ | | 1.018 ± 0.007 |
| $d+\text{Au}$ | $ y < 0.35$ | 0-100% | 1.002 ± 0.001 |
| $d+\text{Au}$ | $ y < 0.35$ | 0-20% | 1.001 ± 0.001 |
| $d+\text{Au}$ | $ y < 0.35$ | 20-40% | 1.002 ± 0.002 |
| $d+\text{Au}$ | $ y < 0.35$ | 40-60% | 1.024 ± 0.017 |
| $d+\text{Au}$ | $ y < 0.35$ | 60-88% | 1.020 ± 0.024 |

is then summed in quadrature with the effect of the Type B systematic uncertainties to give an overall correlated systematic on $\langle p_T^2 \rangle$.

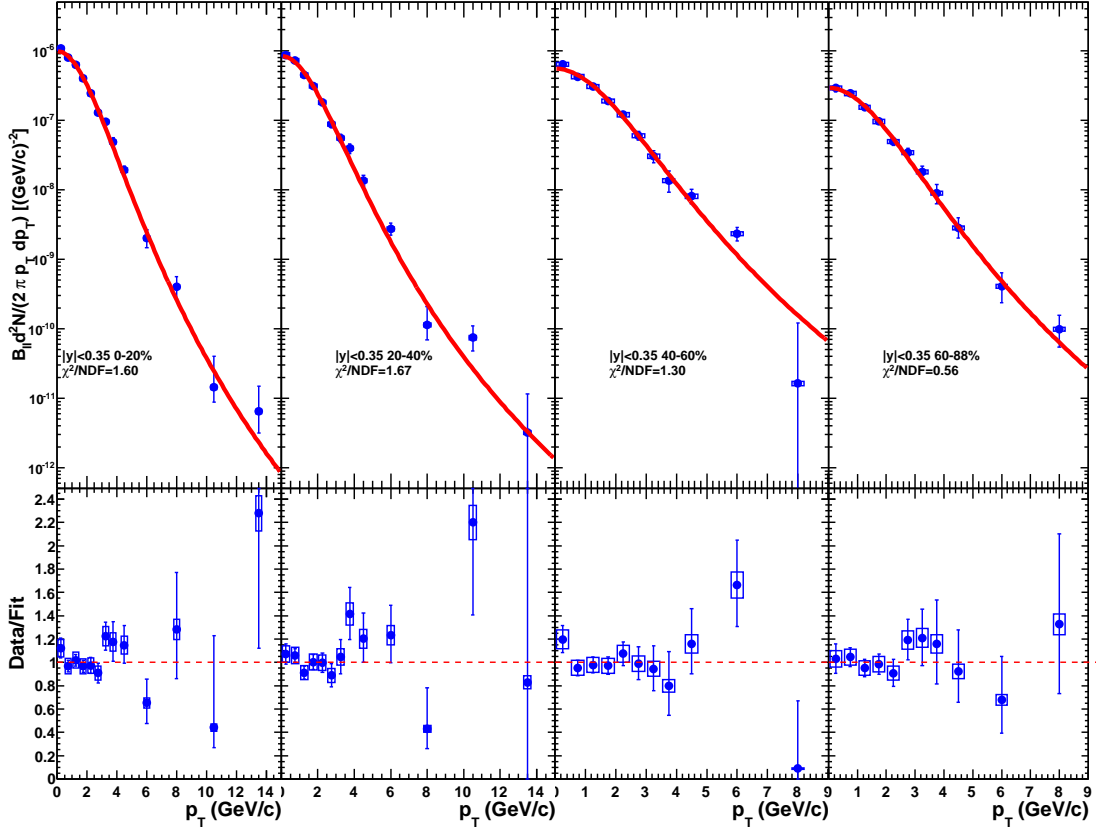


Figure 5.14: Results of modified Kaplan fits to midrapidity $d+Au$ collisions for each centrality.

The resulting $\langle p_T^2 \rangle$ values are given in Table 5.5.

Table 5.5: The $J/\psi \langle p_T^2 \rangle$ results for $p+p$ and $d+Au$ collisions where the first quoted uncertainty corresponds to the type A uncertainties and the second corresponds to the type B uncertainties.

| System | y range | Centrality | $\langle p_T^2 \rangle$ [GeV^2/c^2] |
|--------|--------------|------------|---|
| $p+p$ | $ y < 0.35$ | | $4.46 \pm 0.14 \pm 0.18$ |
| $d+Au$ | $ y < 0.35$ | 0-100% | $5.10_{-0.10}^{+0.12} \pm 0.11$ |
| $d+Au$ | $ y < 0.35$ | 0-20% | $5.24_{-0.16}^{+0.19} \pm 0.10$ |
| $d+Au$ | $ y < 0.35$ | 20-40% | $5.27_{-0.19}^{+0.22} \pm 0.12$ |
| $d+Au$ | $ y < 0.35$ | 40-60% | $5.08_{-0.26}^{+0.29} \pm 0.16$ |
| $d+Au$ | $ y < 0.35$ | 60-88% | $4.60_{-0.24}^{+0.30} \pm 0.15$ |

Table 5.6: The J/ψ nuclear modification factor, $R_{d\text{Au}}$, as a function of rapidity for each centrality bin and for 0-100% centrality integrated $d+\text{Au}$ collisions.

| Centrality | y | $R_{d\text{Au}}$ | Type A | Type B | Type C |
|------------|-------------|------------------|--------|--------|--------|
| 00-20% | -0.50→-0.10 | 0.725 | 0.043 | 0.094 | 0.062 |
| 00-20% | -0.10→0.10 | 0.727 | 0.036 | 0.094 | 0.062 |
| 00-20% | 0.10→0.50 | 0.743 | 0.043 | 0.096 | 0.063 |
| 20-40% | -0.50→-0.10 | 0.795 | 0.050 | 0.103 | 0.064 |
| 20-40% | -0.10→0.10 | 0.828 | 0.045 | 0.107 | 0.067 |
| 20-40% | 0.10→0.50 | 0.870 | 0.055 | 0.113 | 0.071 |
| 40-60% | -0.50→-0.10 | 0.828 | 0.060 | 0.107 | 0.072 |
| 40-60% | -0.10→0.10 | 0.793 | 0.049 | 0.102 | 0.069 |
| 40-60% | 0.10→0.50 | 0.795 | 0.059 | 0.103 | 0.069 |
| 60-88% | -0.50→-0.10 | 0.875 | 0.069 | 0.113 | 0.090 |
| 60-88% | -0.10→0.10 | 0.834 | 0.060 | 0.107 | 0.086 |
| 60-88% | 0.10→0.50 | 0.842 | 0.069 | 0.109 | 0.087 |
| 0-100% | -0.50→-0.10 | 0.765 | 0.038 | 0.099 | 0.060 |
| 0-100% | -0.10→0.10 | 0.764 | 0.032 | 0.098 | 0.060 |
| 0-100% | 0.10→0.50 | 0.784 | 0.038 | 0.100 | 0.061 |

5.3.3 J/ψ Nuclear Modification Factor

To quantify the $d+\text{Au}$ cold nuclear matter effects, the J/ψ nuclear modification factor $R_{d\text{Au}}$ is calculated as a function of rapidity as:

$$R_{d\text{Au}}(i) = \frac{c_i}{\langle N_{\text{coll}}(i) \rangle} \frac{dN_{J/\psi}^{d+\text{Au}}(i)/dy}{dN_{J/\psi}^{p+p}/dy}, \quad (5.19)$$

and as a function of transverse momentum, in a given rapidity and centrality bin as:

$$R_{d\text{Au}}(i) = \frac{c_i}{\langle N_{\text{coll}}(i) \rangle} \frac{d^2N_{J/\psi}^{d+\text{Au}}(i)/dydp_T}{d^2N_{J/\psi}^{p+p}/dydp_T}, \quad (5.20)$$

where $d^2N_{J/\psi}^{d+\text{Au}}(i)/dydp_T$ is the $d+\text{Au}$ invariant yield for the i^{th} centrality bin, $d^2N_{J/\psi}^{p+p}/dydp_T$ is the $p+p$ invariant yield for the same transverse momentum and rapidity bin, $\langle N_{\text{coll}}(i) \rangle$ is the average number of binary collisions for the given centrality bin, as listed in Table 4.2, and c_i is the BBC bias correction factor described in Section 4.2.5 and given in Table 4.2.

The $p+p$ baseline used to calculate the nuclear modification factor is extracted from 2006 data published in [20]. The integrated luminosity was $6.2 \pm 0.6 \text{ pb}^{-1}$. In the analysis, described in detail in [20], the effect of the J/ψ polarization on the $J/\psi A \times \epsilon_{\text{eID}}^{J/\psi}$ is included. This effect is not included in the $d+\text{Au}$ result presented here due to a lack of knowledge of the effects of a nuclear target on the J/ψ polarization. The J/ψ polarization is therefore assumed to be zero. To remain consistent, this effect is removed from the $p+p$ baseline as well, so that, assuming the polarization does not change drastically between $p+p$ and $d+\text{Au}$,

the effects will cancel in the nuclear ratio, $R_{d\text{Au}}$. The invariant cross sections published in [20] were converted to the $p+p$ invariant yields used in this work using an inelastic cross section of 42 mb.

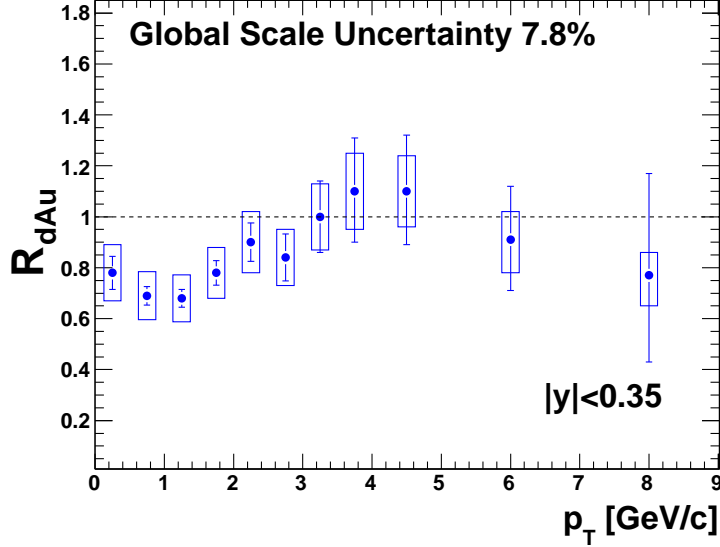


Figure 5.15: The J/ψ nuclear modification factor, $R_{d\text{Au}}$, as a function of transverse momentum for 0-100% centrality integrated $d+\text{Au}$ collisions at $|y| < 0.35$.

The J/ψ $R_{d\text{Au}}$ as a function of rapidity is given in Table 5.6 for 0-100% centrality integrated $d+\text{Au}$ collisions, and for each centrality bin. The J/ψ $R_{d\text{Au}}$ as a function of p_T is shown in Figure 5.15 for 0-100% centrality integrated $d+\text{Au}$ collisions, and in Figure 5.16 for each centrality bin.

The modification can also be quantified using R_{CP} , which measures the change in the modification from central to peripheral events. This is calculated using

$$R_{\text{CP}} = \frac{dN^{d+\text{Au}}(i)/dy / \langle N_{\text{coll}}(i) \rangle}{(dN^{d+\text{Au}}(60-88\%)/dy) / \langle N_{\text{coll}}(60-88\%) \rangle}, \quad (5.21)$$

where i labels the centrality bin. R_{CP} has significantly smaller systematic uncertainties than $R_{d\text{Au}}$, since many of the systematic uncertainties cancel when taking the ratio within the same data set. The J/ψ R_{CP} as a function of rapidity is given in Table 5.7.

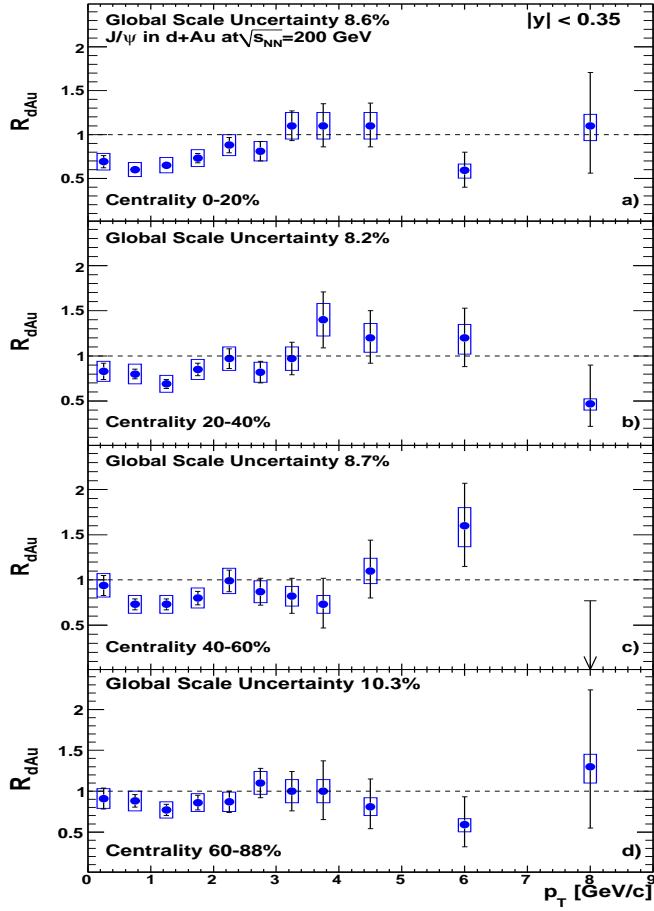


Figure 5.16: The J/ψ nuclear modification factor, $R_{d\text{Au}}$, as a function of transverse momentum for a) central, b) midcentral, c) midperipheral, and d) peripheral events at $|y| < 0.35$.

Table 5.7: The J/ψ modification factor, R_{CP} , as a function of rapidity for each centrality bin.

| Centrality | Rapidity | R_{CP} | Type A | Type B | Type C |
|-----------------|-------------|----------|--------|--------|--------|
| 00-20% / 60-88% | -0.5 → -0.1 | 0.836 | 0.055 | 0.0084 | 0.069 |
| 00-20% / 60-88% | -0.1 → 0.1 | 0.898 | 0.054 | 0.0090 | 0.074 |
| 00-20% / 60-88% | 0.1 → 0.5 | 0.879 | 0.062 | 0.0088 | 0.073 |
| 20-40% / 60-88% | -0.5 → -0.1 | 0.931 | 0.064 | 0.0093 | 0.061 |
| 20-40% / 60-88% | -0.1 → 0.1 | 1.000 | 0.062 | 0.0100 | 0.066 |
| 20-40% / 60-88% | 0.1 → 0.5 | 1.040 | 0.076 | 0.0100 | 0.068 |
| 40-60% / 60-88% | -0.5 → -0.1 | 0.975 | 0.072 | 0.0098 | 0.044 |
| 40-60% / 60-88% | -0.1 → 0.1 | 0.969 | 0.066 | 0.0097 | 0.044 |
| 40-60% / 60-88% | 0.1 → 0.5 | 0.961 | 0.077 | 0.0096 | 0.043 |

CHAPTER 6

ψ' ANALYSIS

This chapter presents the analysis of $\psi' \rightarrow e^+e^-$ production in $d+\text{Au}$ collisions using the PHENIX central arms. This uses the same data as the analysis of J/ψ production presented in Chapter 5, the selection of which is detailed in Section 4.3. While many of the analysis techniques are similar, the analysis of ψ' production is different in many ways from that of the J/ψ production. In this analysis we are working to measure the ratio of the ψ' yield to the J/ψ yield by fitting the mass distribution, whereas in the analysis of J/ψ production we were working to measure the full J/ψ yield independently. The arrangement of this chapter, then, will be significantly different than that of Chapter 5. A description of the simulations used in this analysis will be presented first, in Section 6.1. The efficiency calculations will be detailed in Section 6.2, followed by the determination of the raw ψ' to J/ψ yield ratio. The relative modification of the the ψ' to J/ψ ratio in $d+\text{Au}$ compared to $p+p$ collisions will be described in Section 6.3. Finally the ψ' $R_{d\text{Au}}$ will be calculated in Section 6.5.

6.1 Simulations

This section describes the various simulations used in both the determination of the $\psi'/(J/\psi)$ ratio, as well as those used in the acceptance and trigger efficiency corrections. As described in Section 5.2, simulations are used to estimate the detector acceptance and electron reconstruction efficiency. The same simulation setup that was described in Section 5.2 is used here. The details of each of the simulation sets are described below.

Table 6.1: Number of simulated electron pairs for J/ψ 's, ψ' 's, open charm, open bottom and DY. The number of pairs accepted into the central arms is dependent on the rungroup, but an approximate number is given in the third column.

| State | Generated [$\times 10^6$] | Accepted [$\times 10^3$] |
|----------|-----------------------------|-----------------------------|
| J/ψ | 5.5 | $\approx 57 \rightarrow 72$ |
| ψ' | 5.8 | $\approx 63 \rightarrow 81$ |
| charm | 23.8 | $\approx \rightarrow 971$ |
| bottom | 0.45 | $\approx \rightarrow 24$ |
| DY | 4.2 | $\approx \rightarrow 241$ |

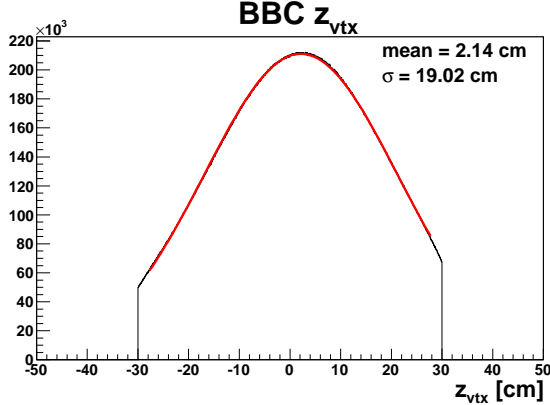


Figure 6.1: The ZVTX for all events in analyzed runs, along with a Gaussian fit to the distribution.

6.1.1 ψ' and J/ψ Simulations

Unlike the simulations of $J/\psi \rightarrow e^+e^-$ decays used in the analysis of the J/ψ production (detailed in Section 5.2), here PYTHIA is used to generate $J/\psi \rightarrow e^+e^-$ and $\psi' \rightarrow e^+e^-$ decays with realistic p_T and rapidity distributions. The PYTHIA configurations used for the J/ψ and ψ' simulations are detailed in Appendix D. The events generated using PYTHIA were between $|ZVTX| < 30$ cm, selected randomly from a Gaussian distribution with a mean of 2.14 cm and $\sigma = 19.02$ cm, determined from a fit to the measured ZVTX distribution for all events in the data sample described in Section 4.3. The fit is shown in Figure 6.1.

The $J/\psi \rightarrow e^+e^-$ and $\psi' \rightarrow e^+e^-$ decays were only selected if the rapidity of the J/ψ or ψ' was within $y < |0.5|$. The generated electrons from J/ψ and ψ' decays were then run through the GEANT-3 simulation of the PHENIX detector tuned to match the real detector response, as detailed in Section 5.2. The total number of generated e^+e^- pairs from J/ψ and ψ' decays, and the approximate number of accepted e^+e^- pairs are shown in Table 6.1. The effect of the ERT trigger efficiency was applied to each electron based on the parametrized single electron SM efficiencies in both the EMCAL and RICH, as described in Section 5.2.2.

6.1.2 Drell-Yan Simulations

The correlated electrons from DY decays were also simulated using PYTHIA. The PYTHIA configuration file is given in Appendix D.4. As in the simulations of $J/\psi \rightarrow e^+e^-$ and $\psi' \rightarrow e^+e^-$ decays, the events were given a random value within $|ZVTX| < 30$ cm, selected from a Gaussian distribution with a mean of 2.14 cm and $\sigma = 19.02$ cm. The electron pairs were only considered if the pair rapidity was within $y < |0.5|$. The electron pairs were then run through the GEANT-3 simulation of the PHENIX detector to model the full detector response. The total number of generated pairs and the approximate number of accepted pairs are shown in Table 6.1.

The effect of the ERT trigger efficiency was applied to each electron based on the parametrized single electron SM efficiencies in both the EMCAL and RICH, as described

in Section 5.2.2.

6.1.3 Pythia Heavy Flavor Simulations

The correlated electrons from open heavy flavor (D and B decays) were again simulated using PYTHIA. The PYTHIA configuration is given in Appendix D.3. For the heavy flavor simulations, PYTHIA is set to MSEL=1 to include all hard processes, as this gives a better estimate of the mass and p_T dependence of the correlated e^+e^- signal. The simulated events were given a vertex location within $|ZVTX| < 30$ cm, selected randomly from a Gaussian distribution with a mean of 2.14 cm and $\sigma = 19.02$ cm. The electron pairs were then run through the GEANT-3 simulation of the PHENIX detector to model the full detector response. The total number of generated pairs and the approximate number of accepted pairs are shown in Table 6.1.

The effect of the ERT trigger efficiency was applied to each electron based on the parametrized single electron SM efficiencies in both the EMCAL and RICH, as described in Section 5.2.2.

After the simulations were completed, a bug was found in the selection of the electrons from heavy flavor decays. A cut was made on the decay electrons of $|\eta| < 0.5$, rather than a cut on the pair of $|y| < 0.5$. This does not affect the reconstructed mass distributions inside PHENIX, as the PHENIX acceptance is fully sampled within the input distributions. It was deemed prohibitive to re-run these simulations on the time scale of this analysis. Since the mass distribution of accepted electron pairs from heavy flavor decays, which is unaffected by this bug, is what was used in fitting the data, this was deemed sufficient.

However, the bug does negate calculations of $A \times \epsilon_{eID}$, which is used for normalization purposes in the fitting procedure described in Section 6.3.2. Since the DY simulations do not have this bug, the $A \times \epsilon_{eID}$ of the DY is used for both the open charm and open bottom mass distribution in the range $2.5 < M_{ee} [\text{GeV}/c^2] < 6.0$ where necessary. The integrated $A \times \epsilon_{eID}$ for the open heavy flavor over the mass range used should be very similar to that of the DY.

6.1.4 MC@NLO Heavy Flavor Simulations

Simulations of electron pairs from charm and bottom using the MC@NLO generator were performed by J. Kamen in a PHENIX analysis of the $d+\text{Au}$ dielectron mass spectra [77]. The mass distributions from MC@NLO produce a very different mass dependence when compared to the PYTHIA distributions (MSEL=1) found in Section 6.1.3. A comparison of the charm and bottom mass distributions is shown in Figure 6.2. The PYTHIA simulations using MSEL=1 produce a charm spectrum which persists to higher mass when compared to that obtained using MC@NLO. Due to the extreme differences in the shape between MC@NLO and PYTHIA MSEL=1, the MC@NLO distributions are used as a systematic check when fitting the mass distributions, described below.

6.2 Efficiency Corrections

This section details the calculation of the acceptance and reconstruction efficiency (Section 6.2.1) as well as the trigger efficiency (Section 6.2.2). The calculation's of the efficiencies

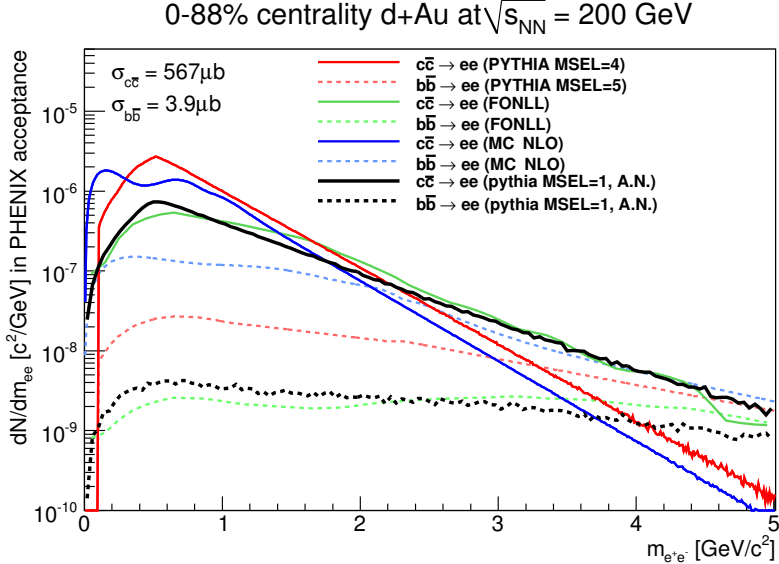


Figure 6.2: A comparison of dielectron mass spectra from open charm and open bottom generated using MC@NLO, PYTHIA, and FONLL. The PYTHIA simulations with MSEL=1 (described in Section 6.1.3) are arbitrarily normalized to the FONLL calculations for plotting and comparison purposes only.

for the individual mesons are required for normalization purposes when fitting the mass distributions, which is described in Section 6.3.2, and the ratio of the acceptances is necessary to correct the ratio of the ψ' to J/ψ yield, which is detailed in Section 6.3.

6.2.1 Acceptance Calculation

The $J/\psi \rightarrow e^+e^-$ and $\psi' \rightarrow e^+e^-$ acceptance times electron ID efficiency in the central arms ($A \times \epsilon_{eID}$) is calculated separately for each rungroup using the simulations from Section 6.1.1. The $A \times \epsilon_{eID}$ is calculated by taking the ratio of all reconstructed J/ψ 's (ψ' 's) in the mass range $1.0 < M_{ee} [\text{GeV}/c^2] < 4.0$ ($2.0 < M_{ee} [\text{GeV}/c^2] < 4.0$) to all generated J/ψ 's (ψ' 's). A summary of the calculated $A \times \epsilon_{eID}$ for both the J/ψ and ψ' , as well as the ratio of their efficiencies, is given in Table 6.2.

The uncertainty on the simulation to data matching, taken to be 6.4% in Section 5.2.1 should cancel when taking the ratio of the J/ψ to ψ' $A \times \epsilon_{eID}$. However, a systematic uncertainty of 2% on the $A \times \epsilon_{eID}$ ratio is taken here to be conservative.

An average DY $A \times \epsilon_{eID}$ value of 1.5% was found based on the same method detailed for the J/ψ and ψ' above. The same $A \times \epsilon_{eID}$ value of 1.5% is assumed for the open heavy flavor contributions as well. This $A \times \epsilon_{eID}$ value is used to calculate an initial value of a normalization parameter, which is allowed to vary in the fitting routine.

Table 6.2: The $A \times \epsilon_{\text{eID}}$ for the ψ' and J/ψ , as well as the J/ψ to ψ' ratio for each rungroup. The total shown in the bottom row is a weighted average based on the number of analyzed MB events in each rungroup given in Table 4.3

| Rungroup | $A \times \epsilon_{\text{eID}}^{J/\psi}$ | $A \times \epsilon_{\text{eID}}^{\psi'}$ | $A \times \epsilon_{\text{eID}}^{J/\psi} / A \times \epsilon_{\text{eID}}^{\psi'}$ |
|----------|---|--|--|
| 0 | 1.312 ± 0.005 | 1.376 ± 0.005 | 0.953 ± 0.005 |
| 1 | 1.134 ± 0.004 | 1.184 ± 0.004 | 0.958 ± 0.005 |
| 2 | 1.043 ± 0.004 | 1.083 ± 0.004 | 0.963 ± 0.005 |
| 3 | 1.047 ± 0.004 | 1.088 ± 0.004 | 0.962 ± 0.005 |
| Total | 1.111 ± 0.004 | 1.158 ± 0.004 | 0.960 ± 0.005 |

Table 6.3: The ϵ_{ERT} for the ψ' and J/ψ , as well as the J/ψ to ψ' ratio for each rungroup. The total shown in the bottom row is a weighted average based on the number of analyzed MB events in each rungroup given in Table 4.3

| Rungroup | $\epsilon_{\text{ERT}}^{J/\psi}$ | $\epsilon_{\text{ERT}}^{\psi'}$ | $\epsilon_{\text{ERT}}^{J/\psi} / \epsilon_{\text{ERT}}^{\psi'}$ |
|----------|----------------------------------|---------------------------------|--|
| 0 | 0.806 ± 0.001 | 0.832 ± 0.001 | 0.969 ± 0.002 |
| 1 | 0.794 ± 0.001 | 0.817 ± 0.001 | 0.972 ± 0.002 |
| 2 | 0.722 ± 0.001 | 0.773 ± 0.001 | 0.934 ± 0.002 |
| 3 | 0.748 ± 0.002 | 0.794 ± 0.001 | 0.948 ± 0.003 |
| Total | 0.754 ± 0.001 | 0.795 ± 0.001 | 0.948 ± 0.002 |

6.2.2 Trigger Efficiency Determination

The J/ψ and ψ' ERT trigger efficiency (ϵ_{ERT}) is calculated using parametrizations of the single electron trigger efficiencies for the RICH and EMCAL trigger super modules, where the SM efficiency is measured separately for each rungroup. The parametrization of the SM trigger efficiencies is taken from Section 5.2.2, where the momentum dependence of the ERT SM efficiencies are parametrized with a fit to the measured single electron SM efficiencies using an error function, and the momentum dependence of the RICH SM efficiencies are parametrized with a constant fit to the measured efficiencies. The decay electrons from the J/ψ (ψ') simulations described in Section 6.1.1 are then tested against the parametrizations of the SM efficiencies, and one of the two electrons is required to fire both the RICH and EMCAL trigger tile it passes through (or a nearby trigger tile, in the case of the RICH). As in the $A \times \epsilon_{\text{eID}}$ determination in Section 6.2.1, the calculated ϵ_{ERT} is averaged over p_T and rapidity. The results for each rungroup are given in Table 6.3.

The systematic uncertainty on ϵ_{ERT} , determined in Section 5.2.2, was calculated by varying the fits to the single electron SM efficiencies. The same variations in the fits to the single electron SM efficiencies are used here to calculate the uncertainty on the J/ψ to ψ' ϵ_{ERT} ratio. A variation of $\pm 2\%$ on the ϵ_{ERT} ratio was found due to the variation of the single electron SM efficiencies. Therefore a 2% systematic uncertainty is assigned to the ϵ_{ERT} ratio.

An average ϵ_{ERT} for both the DY and open heavy flavor of 0.77 was found using the

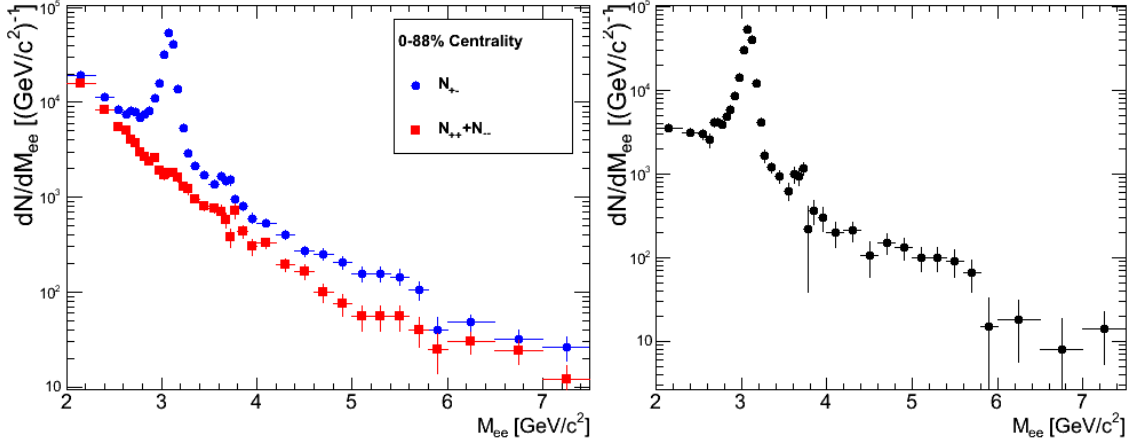


Figure 6.3: Plot of the 0-88% invariant mass distribution for unlike-sign and like-sign (Left) and like-sign subtracted (Right).

same method as detailed for the J/ψ and ψ' above. The bug on the open heavy flavor simulations mentioned in Section 6.1.3 does not affect the trigger efficiency determination.

6.3 Determining the Raw ψ' to J/ψ ratio

This section details the determination of the raw ψ' to J/ψ ratio ($N_{\psi'}/N_{J/\psi}$). The determination of the raw invariant mass distribution is described in Section 6.3.1 followed by the fitting of the invariant mass determination and extraction of $N_{\psi'}/N_{J/\psi}$ in Section 6.3.2.

6.3.1 Determining the Raw Invariant Mass Distribution

The invariant mass distribution is calculated for all electron pairs where at least one of the electrons fired the ERT trigger. This requirement is necessary to match the conditions under which the trigger efficiency is calculated (see Section 5.2.2). The combinatorial background is subtracted using the like-sign subtraction method. The combinatorial background is normalized using the standard method

$$A = \frac{2\sqrt{N_{++}N_{--}}}{(N_{++} + N_{--})} \quad (6.1)$$

where N_{++} is the number of positive like-sign pairs and N_{--} is the number of negative like-sign pairs. The normalization is calculated over the mass range $4 \rightarrow 13$ GeV/c^2 , and is found to be $A = 0.998$. Both the unlike-sign and like-sign mass distributions are shown for MB collisions in Figure 6.3, along with the like-sign subtracted mass spectra. The invariant mass spectra in different centrality bins are shown in Appendix F.2.

Table 6.4: The rungroup and p_T averaged $A \times \epsilon_{\text{eID}}$ and ϵ_{ERT} for each mass distribution.

| | $A \times \epsilon_{\text{eID}}$ | ϵ_{ERT} |
|-------------|----------------------------------|-------------------------|
| J/ψ | 0.0111 | 0.754 |
| ψ' | 0.01158 | 0.795 |
| DY | 0.015 | 0.77 |
| open charm | 0.015 | 0.77 |
| open bottom | 0.015 | 0.77 |

6.3.2 Fitting the Invariant Mass Distributions

Each of the invariant mass distributions described in Section 6.3.1 is fitted within $2.5 < M_{ee} [\text{GeV}/c^2] < 6.0$ with line shapes from the following contributions.

- J/ψ : Line shape determined from PYTHIA simulations coupled with a GEANT model of the PHENIX detector response (Section 6.1.1), and internal radiation calculated from Equation 5.8.
- ψ' : Line shape determined from PYTHIA simulations coupled with a GEANT model of the PHENIX detector response (Section 6.1.1). While the PDG shows no process for $\psi' \rightarrow \gamma e^+ e^-$, in some instances an internal radiation contribution is added to match the J/ψ line shape.
- **Open Charm:** $e^+ e^-$ pairs from D meson decays. Line shapes are taken either from PYTHIA (Section 6.1.3) or MC@NLO (Section 6.1.4).
- **Open Bottom:** $e^+ e^-$ pairs from B meson decays. Line shapes are taken either from PYTHIA (Section 6.1.3) or MC@NLO (Section 6.1.4).
- **Drell-Yan:** $e^+ e^-$ pairs from Drell-Yan decays. Line shapes are taken from PYTHIA (Section 6.1.2).

Before fitting, the raw data mass distributions shown in Section 6.3.1 are normalized by the number of MB events (141.6B) and the width of the centrality bin.

Before fitting, the mass resolution of the internal radiation contributions are smeared to match the mass resolution obtained from the reconstructed PYTHIA simulations ($\sigma = 40\text{MeV}$ for the J/ψ and $\sigma = 54\text{MeV}$ for the ψ'). Each of the contributions are then normalized to an integral of

$$Norm = \frac{1}{\sigma_{pp}^{inel}} \times \langle N_{coll} \rangle \times (A \times \epsilon_{\text{eID}}) \times (\epsilon_{\text{ERT}}) \quad (6.2)$$

where $\sigma_{pp}^{inel} = 42 \text{ mb}$. The $(A \times \epsilon_{\text{eID}}) \times (\epsilon_{\text{ERT}})$ are the average values over all rungroups given in Table 6.4. As discussed in Section 6.1.3, the $A \times \epsilon_{\text{eID}}$ for the bottom and charm contributions is taken to be the same as the Drell-Yan. The ϵ_{ERT} is determined separately for each continuum piece. This normalization makes the scale parameters in the fit to correspond to the $p+p$ cross sections integrated from $2.5 < M_{ee} [\text{GeV}/c^2] < 6.0$ in units of nb, allowing for some physical interpretation of the parameter values.

The ROOT Data Analysis Framework [52] is used, in conjunction with a user defined fitting function given in Appendix E.1, to fit the various components to the data using 8 parameters. They are:

- **par 0:** $\sigma_{c\bar{c}}$
- **par 1:** $\sigma_{b\bar{b}}/\sigma_{c\bar{c}}$
- **par 2:** σ_{DY}
- **par 3:** $\sigma_{J/\psi}$
- **par 4:** $\psi'/(J/\psi)$ yield ratio ($N_{\psi'}/N_{J/\psi}$)
- **par 5:** Additional Mass Resolution
- **par 6:** Internal radiation fraction for the J/ψ (and ψ' when included)
- **par 7:** Mass Scale

The defaults ROOT χ^2 minimization routine is used to determine the optimum values for the above parameters.

When fitting, a number of the parameters can be constrained based on physical values. An NLO calculation [106] gives $\sigma_{DY} = 1.11$ nb in $p+p$. Based on the PYTHIA line shape, the range $2.5 < M_{ee} [\text{GeV}/c^2] < 6.0$ samples 67% of the total yield, and therefore 67% of the total cross section. This gives a nominal value for σ_{DY} of 0.74 nb. An arbitrary uncertainty of $\pm 50\%$ is taken as the bounds of the parameter when fitting. Based on the PYTHIA line shapes, the range $2.5 < M_{ee} [\text{GeV}/c^2] < 6.0$ samples 3% and 34% of $\sigma_{c\bar{c}}$ and $\sigma_{b\bar{b}}$ respectively. Based on $\sigma_{c\bar{c}} = 567 \mu\text{b}$ and $\sigma_{b\bar{b}} = 3.9 \mu\text{b}$ [16] this gives $\sigma_{b\bar{b}}/\sigma_{c\bar{c}} = 0.08$. Again an arbitrary uncertainty band of $\pm 50\%$ is used to constrain the fit parameter. Results from the $d+\text{Au}$ dielectron analysis [77] show a very different $\sigma_{b\bar{b}}/\sigma_{c\bar{c}}$ ratio in the range $2.5 < M_{ee} [\text{GeV}/c^2] < 6.0$ of 0.747 when using the MC@NLO distributions. The effect of these assumptions on the $\psi'/(J/\psi)$ ratio are tested and included in the systematic uncertainty on the fitted ratio (discussed below).

In [20], the fraction of J/ψ internal radiation decays was found to be $9 \pm 5\%$, consistent with a QED calculation giving 10.4%, and a measurement of the fully reconstructed $J/\psi \rightarrow \gamma e^+ e^-$ by E760 which gives $14.7 \pm 2.2\%$. When constraining the internal radiation to fall within the range $9 \pm 5\%$ while fitting the $d+\text{Au}$ data, it was found that this provided a poor description of the low mass side of the J/ψ peak. Letting the parameter free gave a roughly consistent value across centrality of $\sim 34\%$, more than twice the measured value. A comparison between the two cases is shown in Figure 6.4. Here we allow the internal radiation fraction to be free, as this provides a much better description of the data. This assumption is tested and included in the systematic uncertainty on the ratio.

According to [48], there is no observed $\psi' \rightarrow \gamma e^+ e^-$ decay. Therefore we do not include an internal radiation component on the ψ' . However, the fact that the fitted internal radiation contribution to the J/ψ peak is a factor of two greater than other measurements and QED predictions could be indicating that the external radiation line shape from PYTHIA does not agree well with the observed line shape in $d+\text{Au}$. If this is indeed the case, then

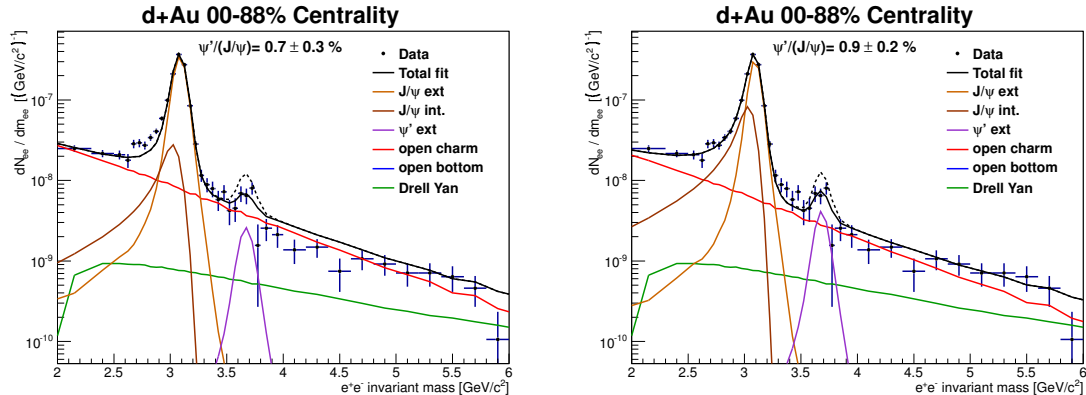


Figure 6.4: A comparison of fits to the 0-88% d +Au mass spectrum with the J/ψ internal radiation fraction constrained to $9\pm 5\%$ (Left) and fitted to the data (Right), giving a value of 36%. The fits give an overall χ^2/NDF of 3.98(Left) and 1.26(Right).

the ψ' line shape is likely also modified. The effect of this is tested by fixing the J/ψ internal radiation fraction to 31% and including a corresponding internal radiation component to the ψ' . In this way we are requiring the same line shapes between the J/ψ and the ψ' . Fits using this assumption are included in the systematic uncertainty determination described below.

In the two peripheral bins, the subtraction of the like-sign background gives negative counts in a few mass bins above 4 GeV, as seen in Figures F.11 and F.11. It was unclear if the fit takes these negative values into account when fitting, so the fit was repeated while explicitly rejecting points with bin contents less than 0 in the fitting routine. A comparison of the results is shown in Figure 6.5. The change in the results when explicitly rejecting bins with negative counts shows that they are in fact being included in the fit.

The fits that give the central value for $N_{\psi'}/N_{J/\psi}$ are performed with the following assumptions:

- Line shapes for the J/ψ , ψ' , Drell-Yan, open charm, and open bottom are generated using PYTHIA (MSEL=1 for charm and bottom).
- The $p+p$ Drell-Yan cross section is constrained to $0.37 < \sigma_{DY} < 1.11$ nb integrated over $2.5 < M_{ee} [\text{GeV}/c^2] < 6.0$.
- The ratio of bottom to charm in the range $2.5 < M_{ee} [\text{GeV}/c^2] < 6.0$ is constrained to be $0.04 < \sigma_{b\bar{b}}/\sigma_{c\bar{c}} < 0.12$.
- The internal radiation fraction on the J/ψ is left as a free parameter.
- There is *no* internal radiation added to the ψ' line shape.

The fit results for each of the centrality ranges under these assumptions are shown in Figures 6.6-6.10. The fit values and uncertainties on $N_{\psi'}/N_{J/\psi}$ are given in Table 6.5.

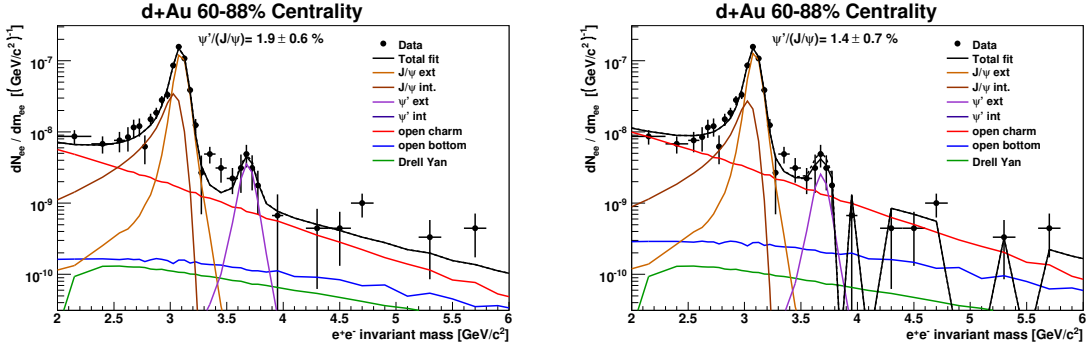


Figure 6.5: (Left) Result of fit to the 60-88% $d+Au$ mass distribution. (Right) The same fit, with all bins with negative counts explicitly rejected from the fitting algorithm. When the negative bins are rejected in the right plot, it creates a plotting artifact where the fit (black line) goes to 0 at the boundaries of each negative bin.

Table 6.5: Results for $N_{\psi'}/N_{J/\psi}$ from different fitting schemes.

| Case | 0-20% | 20-40% | 40-60% | 60-88% | 0-88% |
|------------|---------------|---------------|---------------|---------------|---------------|
| Best | 0.3 ± 0.4 | 0.9 ± 0.4 | 1.6 ± 0.5 | 1.9 ± 0.6 | 0.9 ± 0.2 |
| Case 1 | 0.5 ± 0.4 | 1.0 ± 0.4 | 1.7 ± 0.5 | 2.0 ± 0.6 | 1.1 ± 0.2 |
| Case 2 | 0.3 ± 0.3 | 0.8 ± 0.4 | 1.5 ± 0.5 | 1.9 ± 0.7 | 0.9 ± 0.2 |
| Case 3 | 0.3 ± 0.4 | 1.2 ± 0.5 | 2.0 ± 0.6 | 2.5 ± 1.9 | 1.2 ± 0.3 |
| Case 4 | 0.6 ± 0.4 | 1.3 ± 0.4 | 2.0 ± 0.4 | 2.5 ± 2.2 | 1.4 ± 0.3 |
| Case 5 | 0.5 ± 0.4 | 1.0 ± 0.4 | 1.6 ± 0.5 | 2.0 ± 0.6 | 1.1 ± 0.2 |
| Case 6 | 0.4 ± 0.4 | 0.9 ± 0.5 | 2.0 ± 0.6 | 2.4 ± 2.0 | 1.1 ± 0.3 |
| Case 7 | 0.0 ± 2.2 | 0.6 ± 0.5 | 1.5 ± 0.6 | 1.8 ± 0.7 | 0.7 ± 0.3 |
| Case 8 | 0.3 ± 0.4 | 0.8 ± 0.4 | 1.5 ± 0.5 | 1.9 ± 0.6 | 0.9 ± 0.2 |
| Case 9 | 0.4 ± 0.4 | 1.1 ± 0.5 | 1.9 ± 0.6 | 2.4 ± 2.4 | 1.2 ± 0.3 |
| Case 10 | 0.4 ± 0.4 | 1.1 ± 0.5 | 1.9 ± 0.6 | 2.4 ± 2.3 | 1.1 ± 0.3 |
| Case 11 | 0.4 ± 0.4 | 1.1 ± 0.5 | 1.9 ± 0.6 | 2.4 ± 2.4 | 1.2 ± 0.3 |
| Systematic | ± 0.3 | ± 0.4 | ± 0.4 | ± 0.5 | ± 0.3 |

To estimate the systematic uncertainty on $N_{\psi'}/N_{J/\psi}$, a total of 11 alternative fitting schemes were employed, testing the previously stated assumptions. The fitting schemes are detailed below, with **Best** being the central value.

- **Best:** HF line shapes from PYTHIA, $\sigma_{b\bar{b}}/\sigma_{c\bar{c}}$ constrained to be within 0.04→0.12, σ_{DY} constrained to be within 0.37→1.11 nb, the internal radiation fraction on the J/ψ free, and no internal radiation on the ψ' .
- **Case 1:** HF line shapes from MC@NLO, $\sigma_{b\bar{b}}/\sigma_{c\bar{c}}$ constrained to be within 0.5→1.0, σ_{DY} constrained to be within 0.37→1.11 nb, the internal radiation fraction on the J/ψ free, and no internal radiation on the ψ' .
- **Case 2:** HF line shapes from PYTHIA, all parameters free, no internal radiation on the ψ' .
- **Case 3:** HF line shapes from PYTHIA, $\sigma_{b\bar{b}}/\sigma_{c\bar{c}}$ constrained to be within 0.04→0.12, σ_{DY} constrained to be within 0.37→1.11 nb, and the internal radiation fraction on both the J/ψ and ψ' fixed to 0.34.
- **Case 4:** HF line shapes from MC@NLO, $\sigma_{b\bar{b}}/\sigma_{c\bar{c}}$ fixed to 0.75, σ_{DY} constrained to be within 0.37→1.11 nb, and the internal radiation fraction on both the J/ψ and ψ' fixed to 0.34.
- **Case 5:** HF line shapes from MC@NLO, $\sigma_{b\bar{b}}/\sigma_{c\bar{c}}$ fixed to 0.75, $\sigma_{DY} = 1.11$ nb, the internal radiation fraction on the J/ψ free, no internal radiation on the ψ' .
- **Case 6:** HF line shapes from PYTHIA, all parameters free, internal radiation on the ψ' forced to match that of the J/ψ .
- **Case 7:** HF line shapes from PYTHIA, $\sigma_{DY} = 1.1$ nb, internal radiation on the J/ψ constrained to $9\pm5\%$ based on [20], no internal radiation on the ψ' .
- **Case 8:** HF line shapes from PYTHIA, $\sigma_{DY} = 1.1$ nb, internal radiation on the J/ψ free, no internal radiation on the ψ' .
- **Case 9:** HF line shapes from PYTHIA, $\sigma_{DY} = 0.74$ nb, internal radiation of both the J/ψ and ψ' fixed to 0.34.
- **Case 10:** HF line shapes from PYTHIA, $\sigma_{DY} = 0.37$ nb, internal radiation of both the J/ψ and ψ' fixed to 0.34.
- **Case 11:** HF line shapes from PYTHIA, $\sigma_{DY} = 1.1$ nb, internal radiation of both the J/ψ and ψ' fixed to 0.34.

The systematic uncertainty in the ratio at each centrality was taken as the maximum difference between the central value and the 11 alternative fits, and is shown in the last row of Table 6.5. The fits for **Case 1**, using the MC@NLO charm and bottom line shapes, are shown in Figures 6.6-6.10 for comparison with the **Best** case. The fits for the remaining cases are shown in Appendix E.2.

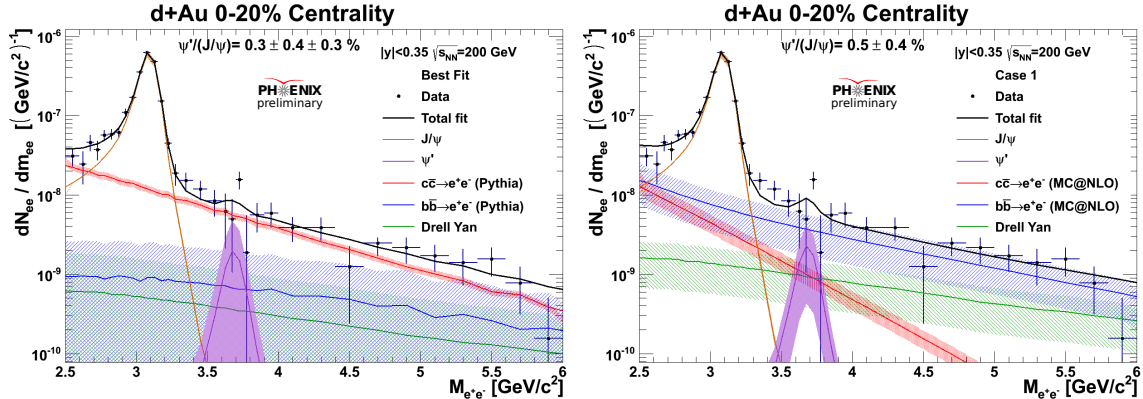


Figure 6.6: Fits to the 0-20% $d+\text{Au}$ invariant mass distribution for the **Best** case (Left) and **Case 1**(Right).

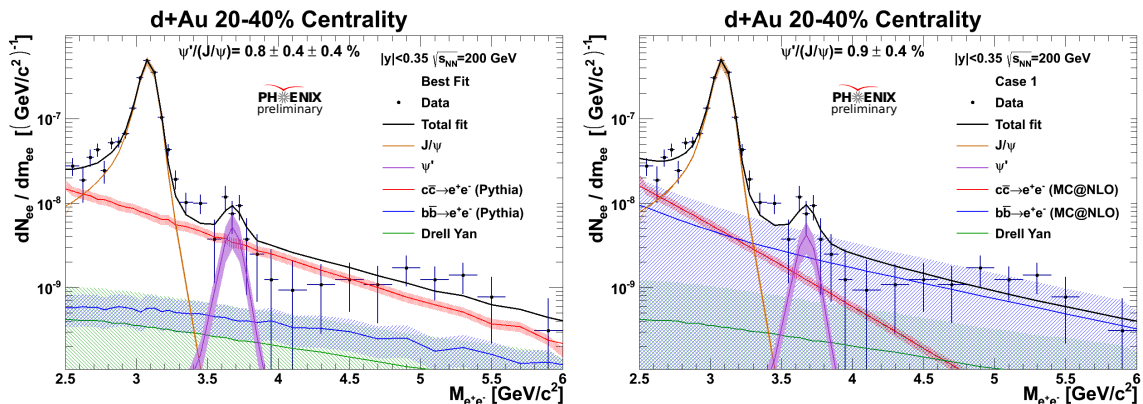


Figure 6.7: Fits to the 20-40% $d+\text{Au}$ invariant mass distribution for the **Best** case (Left) and **Case 1**(Right).

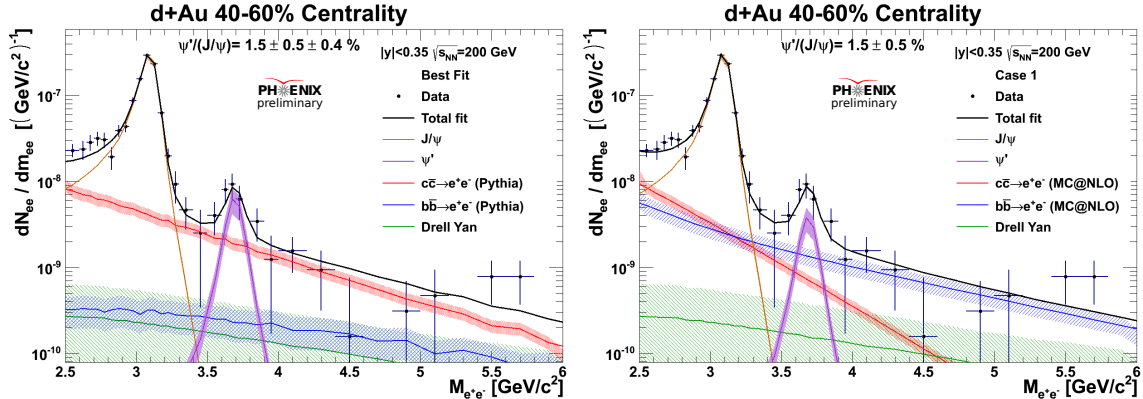


Figure 6.8: Fits to the 40-60% $d+Au$ invariant mass distribution for the **Best** case (Left) and **Case 1**(Right).

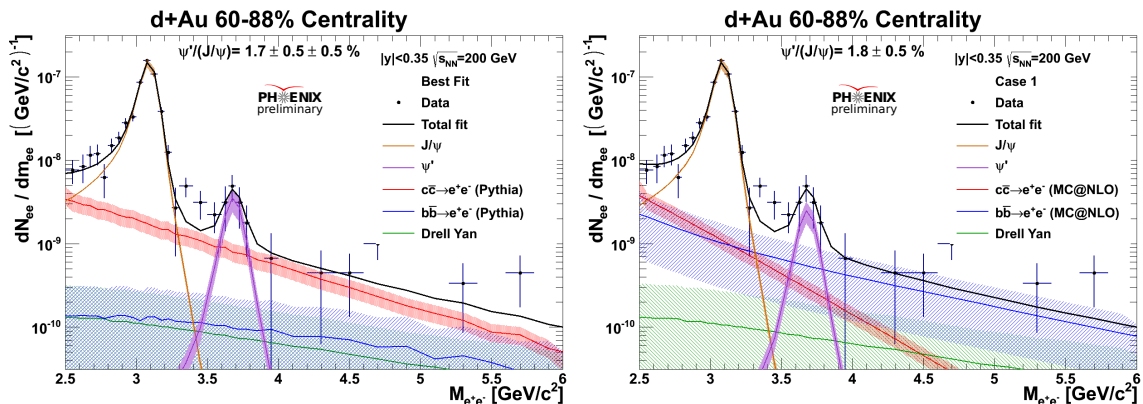


Figure 6.9: Fits to the 60-88% $d+Au$ invariant mass distribution for the **Best** case (Left) and **Case 1**(Right).

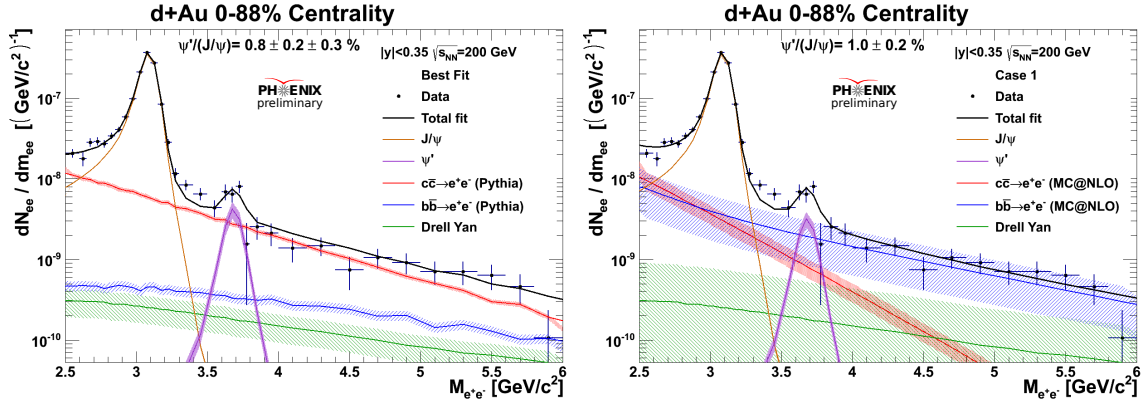


Figure 6.10: Fits to the 0-88% $d+Au$ invariant mass distribution for the **Best** case (Left) and **Case 1** (Right).

6.3.3 Testing against the $p+p$ $\psi'/(J/\psi)$ ratio

To test how significant the deviations of the fitted $N_{\psi'}/N_{J/\psi}$ ratios are from the $p+p$ values, the fits were redone using the **Best** fitting scheme with the $N_{\psi'}/N_{J/\psi}$ ratio fixed to the $p+p$ value. In [20], the $\psi'/(J/\psi)$ ratio was found to be $2.1 \pm 0.5\%$. This is the physics value, corrected for detector efficiencies. When testing against the $d+Au$ data, which is not efficiency corrected, this value needs to be multiplied by the efficiency ratios. This gives a raw $N_{\psi'}/N_{J/\psi}$ ratio of 2.31%. The resulting fits are shown in Figure 6.11 for each of the 4 centrality bins.

The χ^2 values for both the best fit, and the fit with $N_{\psi'}/N_{J/\psi}$ fixed to the $p+p$ value and all other parameters re-optimized, are shown in Table 6.6 over both the ψ' mass range, and the full fit range. The $\Delta\chi^2$ value that comes from changing the single parameter and re-optimizing everything else, along with the p -value associated with that change in χ^2 is also shown in Table 6.6 for both ranges. In this case the p -value represents the probability that the change in $N_{\psi'}/N_{J/\psi}$ from the best fit to the $p+p$ value can be obtained by statistical fluctuations in the data only. This shows that for the 0-20%, 20-40%, and 0-88% cases it is extremely unlikely that the change in $N_{\psi'}/N_{J/\psi}$ is due to statistical fluctuations alone.

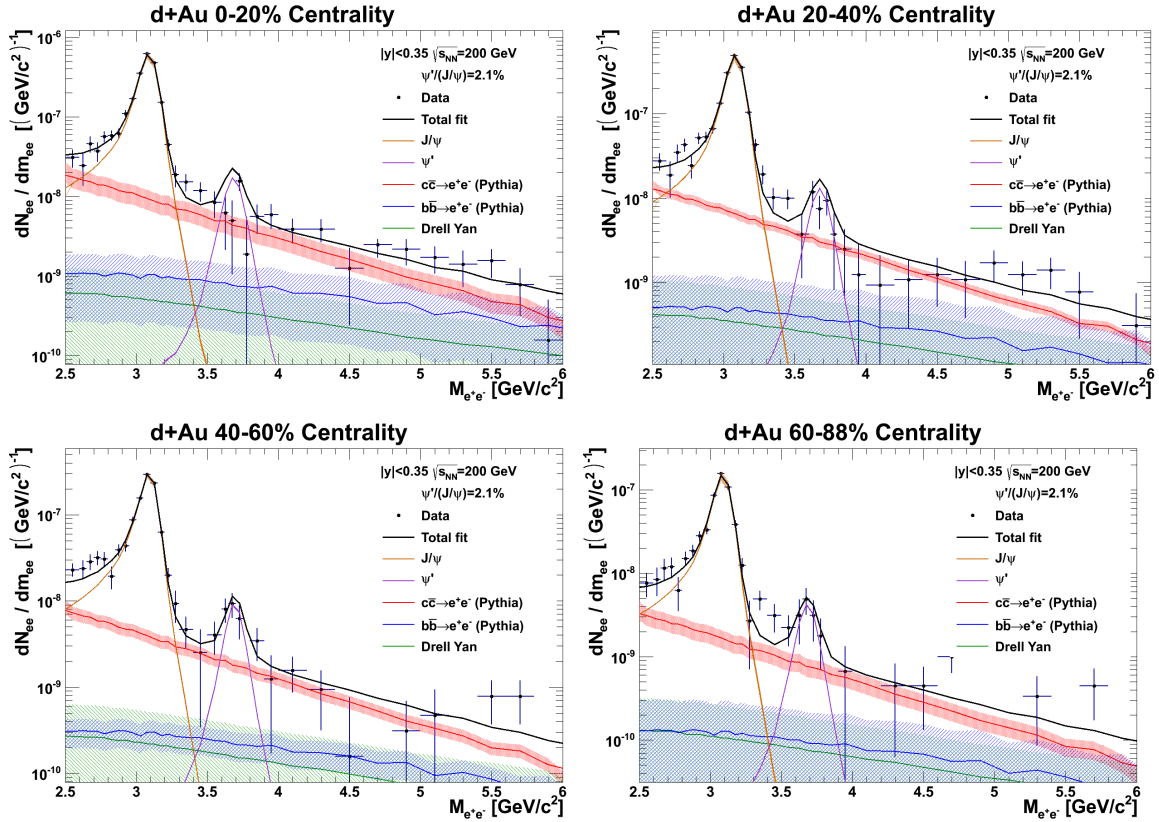


Figure 6.11: Fits to the d +Au invariant mass spectrum in 4 centrality bins using the **Best** fitting scheme and fixing the $\psi'/(J/\psi)$ ratio to the $p+p$ value.

Table 6.6: Comparing the χ^2 values from fits where $N_{\psi'}/N_{J/\psi}$ is left free (χ^2_{free}) to those where it is fixed to the $p+p$ value. In the case where $N_{\psi'}/N_{J/\psi}$ is fixed to the $p+p$ value, all other parameters are refitted.

| Centrality | $3.4 < M_{ee} [\text{GeV}/c^2] < 3.9$ | | | | | $2.5 < M_{ee} [\text{GeV}/c^2] < 6.0$ | | | | |
|------------|---------------------------------------|-----------------|------------------|----------------|---------|---------------------------------------|-----------------|------------------|----------------|---------|
| | N | χ^2_{free} | χ^2_{fixed} | $\Delta\chi^2$ | p-value | N | χ^2_{free} | χ^2_{fixed} | $\Delta\chi^2$ | p-value |
| 00-20% | 6 | 7.64 | 33.49 | 25.85 | 3.69e-7 | 33 | 21.52 | 49.27 | 27.75 | 1.38e-7 |
| 20-40% | 6 | 5.33 | 15.70 | 10.36 | 0.0012 | 33 | 34.05 | 45.10 | 11.04 | 0.0008 |
| 40-60% | 6 | 5.74 | 7.54 | 1.79 | 0.1809 | 32 | 32.71 | 34.67 | 1.96 | 0.1615 |
| 60-88% | 6 | 4.40 | 4.84 | 0.44 | 0.5071 | 32 | 43.20 | 43.57 | 0.37 | 0.5430 |
| 00-88% | 6 | 9.80 | 42.22 | 32.43 | 1.24e-8 | 33 | 37.49 | 72.05 | 34.56 | 4.14e-9 |

Table 6.7: The ψ' to J/ψ ratio.

| Centrality | $N_{\psi'}/N_{J/\psi}$ | $\frac{A \times \epsilon_{eID}^{J/\psi} \epsilon_{ERT}^{J/\psi}}{A \times \epsilon_{eID}^{\psi'} \epsilon_{ERT}^{\psi'}}$ | $\psi'/(J/\psi)$ |
|------------|-----------------------------|---|---------------------------------------|
| 00-20% | $0.003 \pm 0.004 \pm 0.003$ | 0.910 ± 0.005 | $0.003 \pm 0.004 \pm 0.003 \pm 0.005$ |
| 20-40% | $0.009 \pm 0.004 \pm 0.004$ | 0.910 ± 0.005 | $0.008 \pm 0.004 \pm 0.004 \pm 0.005$ |
| 40-60% | $0.016 \pm 0.005 \pm 0.004$ | 0.910 ± 0.005 | $0.014 \pm 0.005 \pm 0.004 \pm 0.005$ |
| 60-88% | $0.019 \pm 0.006 \pm 0.005$ | 0.910 ± 0.005 | $0.017 \pm 0.006 \pm 0.005 \pm 0.005$ |
| 00-88% | $0.009 \pm 0.002 \pm 0.003$ | 0.910 ± 0.005 | $0.008 \pm 0.002 \pm 0.006$ |

 Table 6.8: The relative modification between the ψ' and the J/ψ .

| Centrality | $(\psi'/(J/\psi))^{pp}$ | $(\psi'/(J/\psi))^{dAu}$ | $\frac{[\psi'/(J/\psi)]^{dAu}}{[\psi'/(J/\psi)]^{pp}}$ |
|------------|-------------------------|---------------------------------------|--|
| 00-20% | 0.021 ± 0.005 | $0.003 \pm 0.004 \pm 0.003 \pm 0.005$ | $0.13 \pm 0.17 \pm 0.13 \pm 0.03$ |
| 20-40% | 0.021 ± 0.005 | $0.008 \pm 0.004 \pm 0.004 \pm 0.005$ | $0.39 \pm 0.17 \pm 0.17 \pm 0.09$ |
| 40-60% | 0.021 ± 0.005 | $0.014 \pm 0.005 \pm 0.004 \pm 0.005$ | $0.69 \pm 0.22 \pm 0.17 \pm 0.17$ |
| 60-88% | 0.021 ± 0.005 | $0.017 \pm 0.006 \pm 0.005 \pm 0.005$ | $0.82 \pm 0.26 \pm 0.22 \pm 0.20$ |
| 00-88% | 0.021 ± 0.005 | $0.008 \pm 0.002 \pm 0.006$ | $0.39 \pm 0.09 \pm 0.16$ |

6.4 Relative modification

The ψ' to J/ψ ratio in $d+Au$ is calculated using

$$\psi'/(J/\psi) = \frac{N_{\psi'}}{N_{J/\psi}} \frac{A \times \epsilon_{eID}^{J/\psi} \epsilon_{ERT}^{J/\psi}}{A \times \epsilon_{eID}^{\psi'} \epsilon_{ERT}^{\psi'}}, \quad (6.3)$$

where $N_{\psi'}/N_{J/\psi}$ is taken directly from the fits to the invariant mass distributions, as discussed in Section 6.3.2. The corrected ψ' to J/ψ ratios for each centrality are given in Table 6.7.

The relative modification is calculated by dividing the $d+Au$ $\psi'/(J/\psi)$ ratio by that for $p+p$. The $\psi'/(J/\psi)$ ratio in $p+p$ is taken from [20]. The ratio for both $d+Au$ and $p+p$, as well as the relative modification, are given in Table 6.8.

The Type C systematic uncertainties quoted in Tables 6.7 and 6.8 include the 2% systematic uncertainty on the $A \times \epsilon_{eID}$ ratio and the 2% systematic uncertainty on the ϵ_{ERT} ratio.

6.5 $\psi' R_{dAu}$

The $\psi' R_{dAu}$ is calculated using the relative modification and the $J/\psi R_{dAu}$ (calculated in Section 5.3.3) by

$$R_{dAu}^{\psi'} = \frac{[\psi'/(J/\psi)]^{dAu}}{[\psi'/(J/\psi)]^{pp}} R_{dAu}^{J/\psi}, \quad (6.4)$$

where the relative modification is taken from Table 6.8.

Table 6.9: The ψ' $R_{d\text{Au}}$.

| Centrality | $R_{d\text{Au}}^{J/\psi}$ | $R_{d\text{Au}}^{\psi'}$ |
|------------|---------------------------------------|-----------------------------------|
| 00-20% | $0.731 \pm 0.023 \pm 0.036 \pm 0.107$ | $0.10 \pm 0.13 \pm 0.10 \pm 0.03$ |
| 20-40% | $0.829 \pm 0.028 \pm 0.035 \pm 0.122$ | $0.32 \pm 0.14 \pm 0.14 \pm 0.09$ |
| 40-60% | $0.805 \pm 0.032 \pm 0.042 \pm 0.118$ | $0.56 \pm 0.18 \pm 0.14 \pm 0.16$ |
| 60-88% | $0.849 \pm 0.038 \pm 0.064 \pm 0.124$ | $0.70 \pm 0.22 \pm 0.19 \pm 0.20$ |
| 00-100% | $0.77 \pm 0.02 \pm 0.16$ | $0.30 \pm 0.07 \pm 0.13$ |

The J/ψ $R_{d\text{Au}}$ values reported in Section 5.3.3 are divided into three rapidity bins, and so can not be used directly here. The J/ψ $R_{d\text{Au}}$ values used here are averaged over rapidity using the raw J/ψ yield as weights. The systematic uncertainties on the J/ψ $R_{d\text{Au}}$ are also rearranged to be appropriate for plotting vs centrality, rather than rapidity. The J/ψ $R_{d\text{Au}}$ values used here are given in Table 6.9.

The resulting ψ' $R_{d\text{Au}}$ values are given in Table 6.9, and plotted as a function of N_{coll} in Figure 6.12.

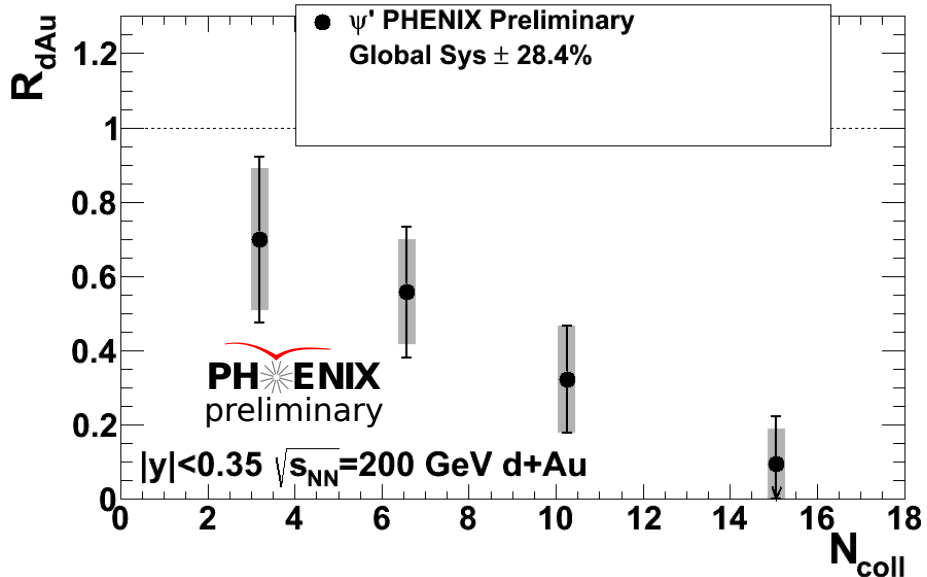


Figure 6.12: The ψ' $R_{d\text{Au}}$ at $|y| < 0.35$ as a function of N_{coll} .

CHAPTER 7

DISCUSSION OF RESULTS AND COMPARISON WITH THEORY

The results of the measurement of J/ψ production in $d+\text{Au}$ collisions at midrapidity are interesting by themselves. However, a much greater understanding is gained by measuring J/ψ production over a wide range in rapidity, as different rapidities probe different kinematic regimes, and therefore different processes. PHENIX has measured $J/\psi \rightarrow \mu^+ \mu^-$ production at backward and forward rapidity in $d+\text{Au}$ collisions from the same 2008 data set [19, 10]. Those results are discussed in conjunction with the midrapidity results presented in Chapter 5. This chapter also presents a discussion of the measured modification of ψ' production in $d+\text{Au}$ collisions at midrapidity, as detailed in Chapter 6, and its implications on measurements of J/ψ production in both $d+\text{Au}$ and $A + A$ collisions.

First, a discussion of the $J/\psi \langle p_T^2 \rangle$ results are presented in Section 7.1. A discussion of the implications of the measured $J/\psi R_{d\text{Au}}$ at all rapidities follows in Section 7.2, along with a comparison to model calculations of the rapidity dependence of the $J/\psi R_{d\text{Au}}$ in Section 7.2.1 and the p_T dependence of the $J/\psi R_{d\text{Au}}$ in Section 7.2.2. Implications of the measured modification of ψ' production at midrapidity are presented in Section 7.3. Finally, the geometric dependence of the $J/\psi R_{d\text{Au}}$ is discussed in Section 7.5.

7.1 $J/\psi \langle p_T^2 \rangle$

The $J/\psi \langle p_T^2 \rangle$ values at backward and forward rapidities in $d+\text{Au}$ collisions are reported in [10]. The $\langle p_T^2 \rangle$ is found to be greater at midrapidity than either backward or forward rapidities, where the $\langle p_T^2 \rangle$ is similar. This indicates that J/ψ production falls off more rapidly with increasing p_T at backward and forward rapidity than at midrapidity, a result which is also reflected in the $J/\psi \langle p_T^2 \rangle$ measured in $p+p$ collisions at the same energy [20].

The experimental value of $\Delta \langle p_T^2 \rangle = \langle p_T^2 \rangle_{AA} - \langle p_T^2 \rangle_{pp}$ quantifies the change in the shape of the p_T distribution between $A + A$ and $p+p$ collisions. The $\Delta \langle p_T^2 \rangle$ for $d+\text{Au}$ collisions as a function of N_{coll} is shown in Figure 7.1 for each of the rapidity regions measured by PHENIX. There is an increase in the $\langle p_T^2 \rangle$ relative to $p+p$ collisions, reflecting a broadening in the p_T distribution with respect to $p+p$, which increases with N_{coll} . The increase in $\Delta \langle p_T^2 \rangle$ is similar at forward and backward rapidities and appears to be larger at midrapidity, though this is tempered somewhat by the relatively large uncertainties present in the data.

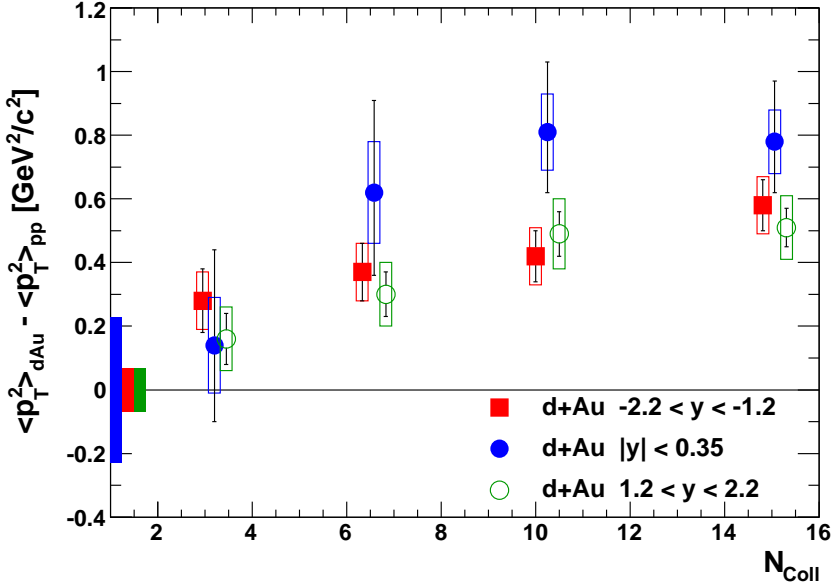


Figure 7.1: The difference between $\langle p_T^2 \rangle$ in $d+\text{Au}$ and $p+p$ as a function of N_{coll} at each rapidity. The uncertainties in the $\langle p_T^2 \rangle_{pp}$ are shown as boxes at $\Delta\langle p_T^2 \rangle = 0$ [10].

The J/ψ $\langle p_T^2 \rangle$ has also been measured in Cu+Cu [14] and Au+Au [11] collisions at $\sqrt{s_{NN}} = 200$ GeV. In those instances the low statistics at high- p_T prevented a full extraction from $0 \rightarrow \infty$, as is done in the $d+\text{Au}$ and $p+p$ case. Because of this the $\langle p_T^2 \rangle$ was instead calculated only over the range $0 \leq p_T [\text{GeV}/c] \leq 5$. For comparison purposes, the $\langle p_T^2 \rangle$ values in $p+p$ and $d+\text{Au}$ are also calculated over the truncated range. The $\Delta\langle p_T^2 \rangle$ values for each of the collision species are plotted as a function of N_{part} in Figure 7.2. Due to the large uncertainties on the $A + A$ data no clear trend is observed.

7.2 The J/ψ Nuclear Modification Factor

As discussed in Section 5.3.3, the J/ψ nuclear modification factor, $R_{d\text{Au}}$, is a measure of the modification of J/ψ production in $d+\text{Au}$ compared to $p+p$ collisions. If there are no nuclear effects, and a $d+\text{Au}$ collision is simply a series of independent nucleon-nucleon collisions, then $R_{d\text{Au}} = 1$.

The 0-100% centrality integrated $R_{d\text{Au}}$ as a function of rapidity is shown in Figure 7.3. This includes the forward(positive) and backward(negative) rapidity $R_{d\text{Au}}$ measured via $J/\psi \rightarrow \mu^+\mu^-$ production as well as the midrapidity data presented in Section 5.3.3. At backward rapidity minimal suppression is observed within the systematic uncertainties. Moving toward forward rapidity yields a large increase in suppression with $R_{d\text{Au}} \approx 0.7$ at $y > 1.2$.

The centrality dependent modification, shown in Figure 7.4, shows a similar behavior of low suppression at backward rapidity with the suppression increasing with increasing

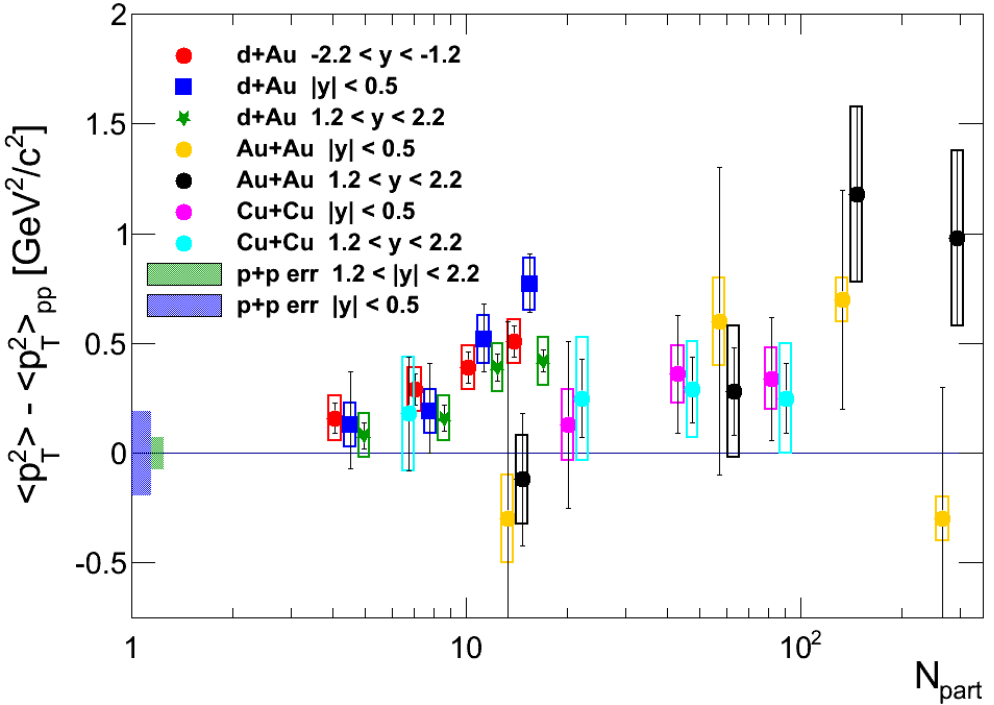


Figure 7.2: The $\Delta \langle p_T^2 \rangle$ calculated for $0 \leq p_T [\text{GeV}/c] \leq 5$ as a function of N_{part} for $p+p$ [10], $d+\text{Au}$ [10], $\text{Cu}+\text{Cu}$ [14], and $\text{Au}+\text{Au}$ [11] collisions at $\sqrt{s_{NN}} = 200$ GeV. For clarity the $d+\text{Au}$ points at backward and forward rapidity have been shifted by $\pm 10\%$ in N_{part}

rapidity for central (0-20%) and mid-central (20-40%) collisions. Moving towards peripheral collisions produces a decrease in the suppression seen at mid and forward rapidities. For the most peripheral (60-88%) collisions the $R_{d\text{Au}}$ is essentially constant with rapidity with an average value of $R_{d\text{Au}} \approx 0.9$ which is consistent with no modification ($R_{d\text{Au}} = 1$) within the systematic uncertainties. The centrality dependence of the modification factor R_{CP} is also shown in Figure 7.4. This shows that at backward rapidity the modification does not vary strongly between central and peripheral collisions, while at forward rapidity there is a very clear increase in the suppression of J/ψ production when moving from peripheral to central $d+\text{Au}$ collisions

The J/ψ $R_{d\text{Au}}$ as a function of transverse momentum is shown for 0-100% centrality integrated $d+\text{Au}$ collisions in Figure 7.5. In this case the $R_{d\text{Au}}$ has been integrated over the rapidity range of each of the PHENIX spectrometers to maximize the statistics and increase the p_T reach of the data. One striking feature of the $R_{d\text{Au}}$ vs p_T shown in Figure 7.5 is the difference in the shape of the p_T distribution at backward rapidity when compared with mid and forward rapidities. At mid and forward rapidity, a suppression is measured at

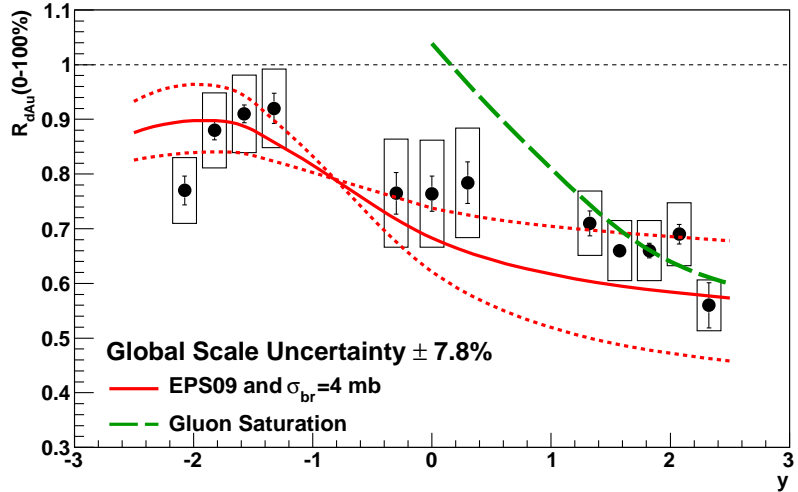


Figure 7.3: The J/ψ nuclear modification factor, $R_{d\text{Au}}$, as a function of rapidity for 0-100% centrality integrated $d+\text{Au}$ collisions. Curves are model calculations detailed in Section 7.2.1. [19]

low- p_T with a gradual increase in $R_{d\text{Au}}$ with increasing p_T , increasing to $R_{d\text{Au}} = 1.0$ at $p_T \approx 4 \text{ GeV}/c$. At backward rapidity, however, the $R_{d\text{Au}}$ exhibits a similar suppression at low- p_T , but a much more rapid increase in $R_{d\text{Au}}$, with $R_{d\text{Au}} = 1.0$ at $p_T \approx 1.5 \text{ GeV}/c$. This difference is shown more clearly in Figure 7.6 which contains the same 0-100% centrality integrated $R_{d\text{Au}}$ at each rapidity, with each distribution overlayed on the same axis. What is also striking in Figure 7.6 is that the shape and overall normalization of the mid and forward rapidity $R_{d\text{Au}}$ is nearly consistent across the entire p_T range.

The centrality dependence of $R_{d\text{Au}}$ vs p_T is shown in Figure 7.7 for backward rapidity and in Figure 7.8 for mid and forward rapidities. At low- p_T the $R_{d\text{Au}}$ at each rapidity shows a behavior similar to that shown in the rapidity dependent $R_{d\text{Au}}$. This is not surprising, as the $\langle p_T \rangle \approx 2.0 \text{ GeV}/c$ in $d+\text{Au}$ means that the majority of the J/ψ production occurs below $p_T \approx 2 \text{ GeV}/c$. For the most peripheral case, the $R_{d\text{Au}}$ is roughly constant at all rapidity, indicating that nuclear effects are weak for peripheral collisions. It is also clear that for the most central collisions, the $R_{d\text{Au}}$ at backward rapidity is greater than 1.0 at high p_T , while the $R_{d\text{Au}}$ at mid and forward rapidity does not appear to increase to $R_{d\text{Au}} > 1.0$ even at the highest p_T .

As discussed in Section 3.3, various physical effects have been suggested which modify the J/ψ production in a nuclear medium, such as shadowing, nuclear breakup, initial state energy loss, and the Cronin effect. Various models which include some combination of these effects are compared to the measured modification of J/ψ production in $d+\text{Au}$ collisions in the next two sections.

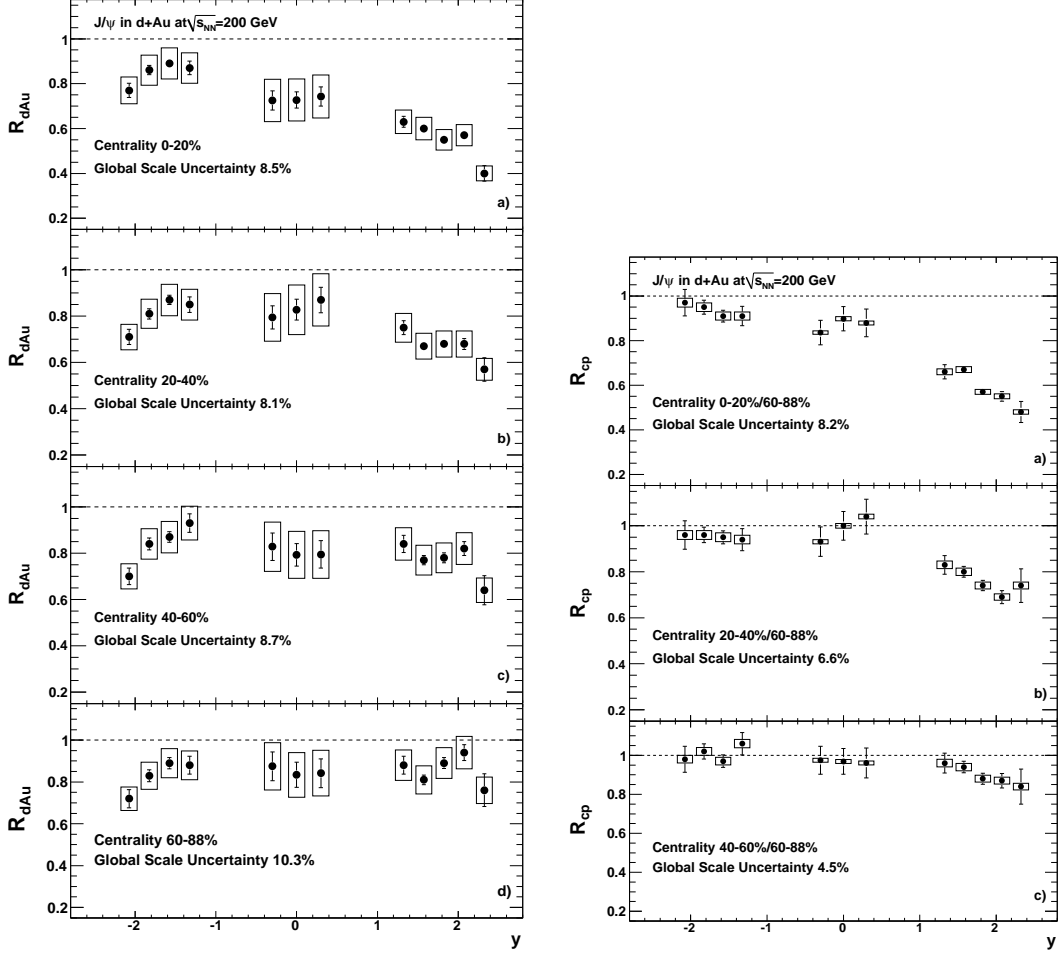


Figure 7.4: The J/ψ nuclear modification factors, $R_{d\text{Au}}$ (Left) and R_{CP} (Right), as a function of rapidity for each centrality.

7.2.1 Models of the Rapidity Dependent Modification

The first set of model calculations are compared to the 0-100% centrality integrated $R_{d\text{Au}}$ as a function of rapidity as the red curves in Figure 7.3. This model includes shadowing, using the EPS09 nPDF set, combined with a breakup cross section (σ_{abs}) of 4 mb following the prescription of [107]. The solid red curve represents the central EPS09 nPDF set, while the dashed red curves represent sets which give the maximum variation in the shape of the EPS09 modification. Here the σ_{abs} is not fitted to the data, but rather chosen by eye to match the $R_{d\text{Au}}$ at backward rapidity. The results show good agreement with the measured $R_{d\text{Au}}$ at backward rapidity, while a slight over-prediction of the suppression is seen at mid and forward rapidity. As EPS09 only provides the shadowing modification integrated over impact parameter, an impact parameter dependence must be introduced to compare with the measured centrality dependent data. Calculations are shown in Figure 7.9 which assume

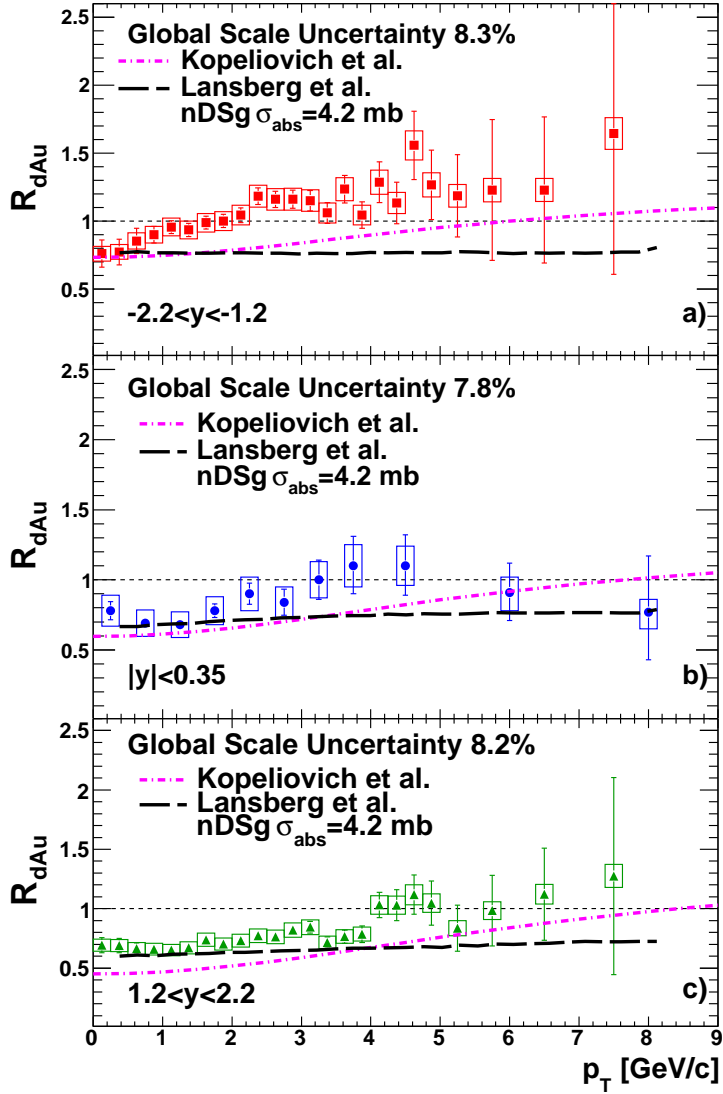


Figure 7.5: The J/ψ nuclear modification factor, $R_{d\text{Au}}$, as a function of transverse momentum for a) backward rapidity, b) midrapidity, and c) forward rapidity 0–100% centrality integrated $d+\text{Au}$ collisions. Curves are model calculations detailed in Section 7.2.2. [10]

a modification which is linearly dependent on the nuclear thickness when calculating the shadowing modification as a function of the measured PHENIX centrality. Calculations are shown in Figure 7.9 for most central and most peripheral $R_{d\text{Au}}$ as a function of rapidity. Also shown in Figure 7.9 is the comparison to the measured central R_{CP} as a function of rapidity. The calculations agree well with the most central $R_{d\text{Au}}$, while for peripheral $R_{d\text{Au}}$ the suppression is over-predicted at mid and forward rapidity. This problem is clearer when comparing with the central R_{CP} , which is the ratio of the central $R_{d\text{Au}}$ to the peripheral

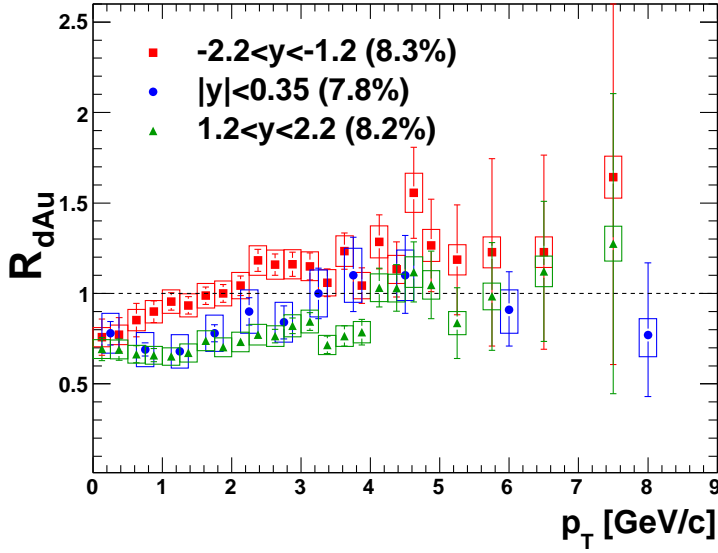


Figure 7.6: The 0-100% centrality integrated $R_{d\text{Au}}$ as a function of p_T at all rapidities. The Type C systematic uncertainty for each distribution is given as a percentage in the legend. [10]

$R_{d\text{Au}}$, and has smaller systematic uncertainties. This striking divergence at forward rapidity when comparing to R_{CP} is indicative of an incorrect form of the geometric modification. The choice of a modification which is linearly dependent on the nuclear thickness therefore does not work. The choice of $\sigma_{abs} = 4 \text{ mb}$ used in the calculation, which was not fitted to the data but rather chosen to match the 0-100% $R_{d\text{Au}}$ at backward rapidity, can not explain this difference. It is shown in [94] that any choice of σ_{abs} when coupled with a shadowing modification which is linearly dependent on the nuclear thickness will not accurately predict the behavior at forward rapidity. This will be discussed further in Section 7.5.

The second set of model calculations includes gluon saturation effects at small- x [78, 81], and is shown as the green dashed curves in Figures 7.3 and 7.9. At forward rapidities, they argue that the J/ψ formation time is much greater than the $c\bar{c}$ formation time, which is much greater than the nuclear interaction time. This leads to coherent scattering of the $c\bar{c}$ off all nucleons in its path as it traverses the nucleus. Coherent scattering leads to a suppression of the total J/ψ production in $d+\text{Au}$ collisions. The calculated $R_{d\text{Au}}$ is in good agreement with the measured $R_{d\text{Au}}$ at forward rapidity, both in 0-100% centrality integrated $d+\text{Au}$ collisions shown in Figure 7.3, and as a function of centrality shown in Figure 7.9. At midrapidity the $c\bar{c}$ production time becomes larger than the nuclear radius, and therefore the $c\bar{c}$ no longer scatters coherently off all nucleons. Instead, double gluon exchange causes an enhancement in the J/ψ production in $d+\text{Au}$ relative to $p+p$ collisions. This enhancement is not observed in the measured $R_{d\text{Au}}$. At backward rapidities the J/ψ formation time becomes larger than the nuclear radius, and therefore the coherence is lost, and the calculations are no longer valid.

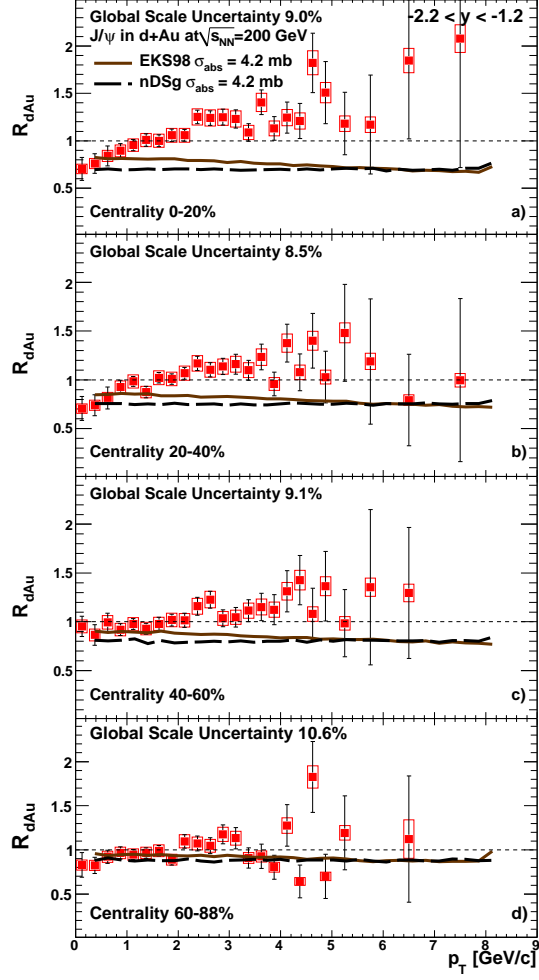


Figure 7.7: The J/ψ nuclear modification factor, R_{dAu} , as a function of transverse momentum for a) central, b) midcentral, c) midperipheral, and d) peripheral events at $-2.2 < y < -1.2$. Curves are calculations by Ferreiro et al. [67] discussed in Section 7.2.2. [10]

7.2.2 Models of the Transverse Momentum Dependent Modification

There are a number of models which calculate the modification of J/ψ production due to CNM effects as a function of transverse momentum. Below we compare calculations from 4 of those models with the measured p_T dependence of the J/ψ R_{dAu} .

The first set of model calculations of the J/ψ R_{dAu} as a function of p_T is by Kopeliovich et al. [84, 82]. This model calculates the effects on a frozen $c\bar{c}$ dipole propagating through a nucleus. The $c\bar{c}$ is not considered to evolve into a fully formed J/ψ , based on arguments of the larger formation time of the J/ψ compared to the time spent in the nucleus. The J/ψ production is calculated based on 2 \rightarrow 1 kinematics, where the parton momentum fraction,

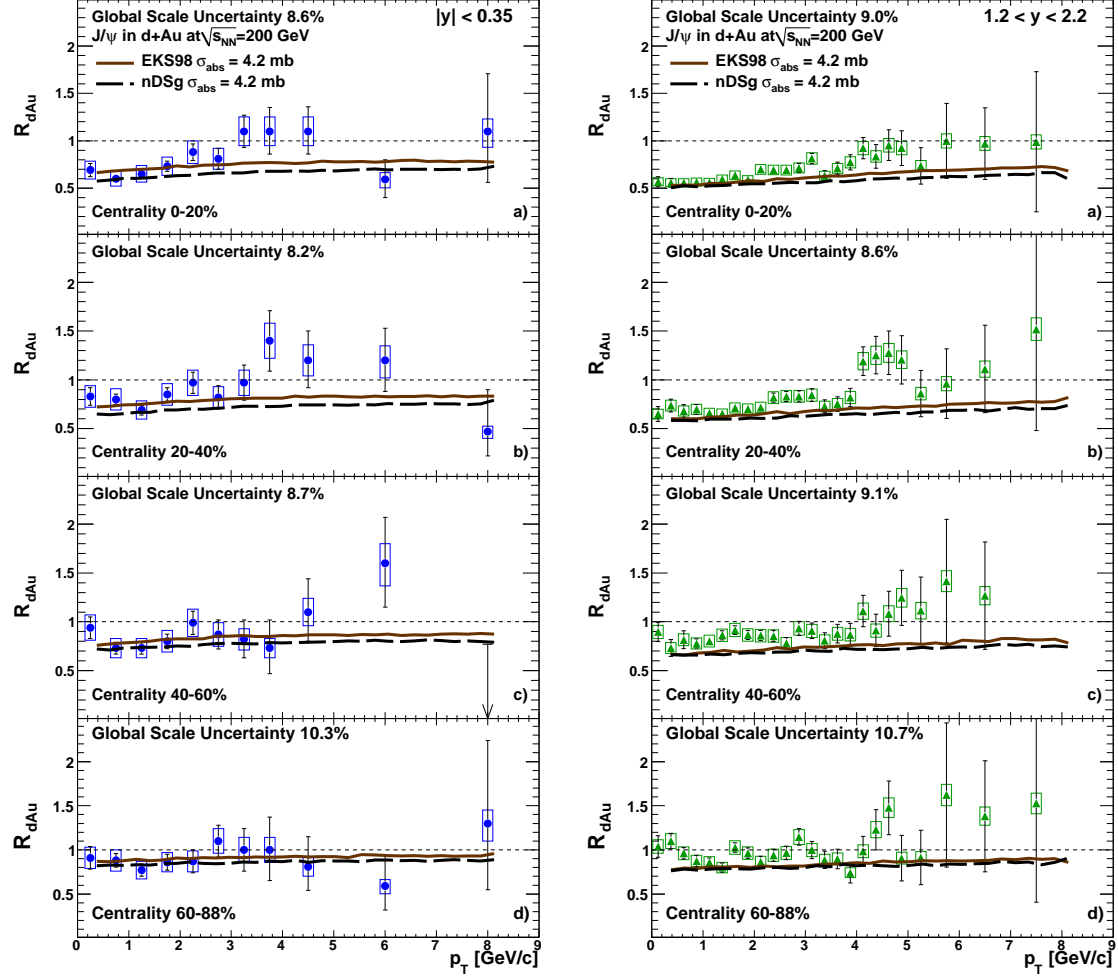


Figure 7.8: The J/ψ nuclear modification factor, R_{dAu} , as a function of transverse momentum for a) central, b) midcentral, c) midperipheral, and d) peripheral events at (Left) $|y| < 0.35$ and (Right) $1.2 < y < 2.4$. Curves are calculations by Ferreiro et al. [67] discussed in Section 7.2.2. [10]

x , is calculated using

$$x = \frac{\sqrt{\langle M_{cc}^2 \rangle + \langle p_T^2 \rangle}}{\sqrt{s}} e^{-y}. \quad (7.1)$$

In [84] $\langle M_{cc}^2 \rangle = 2M_{J/\psi}^2$ is fixed based on the color singlet model. The calculation includes shadowing as well as nuclear breakup and the Cronin effect. The nuclear shadowing is taken from the nDSg nPDF set [58], a NLO parametrization of DIS data. The nuclear breakup is calculated using a parametrization of the dipole cross section fitted to measurements of the proton structure function at HERA [71]. This yields a breakup cross section that is dependent on kinematics of the J/ψ . A p_T broadening (Cronin effect) is added through a

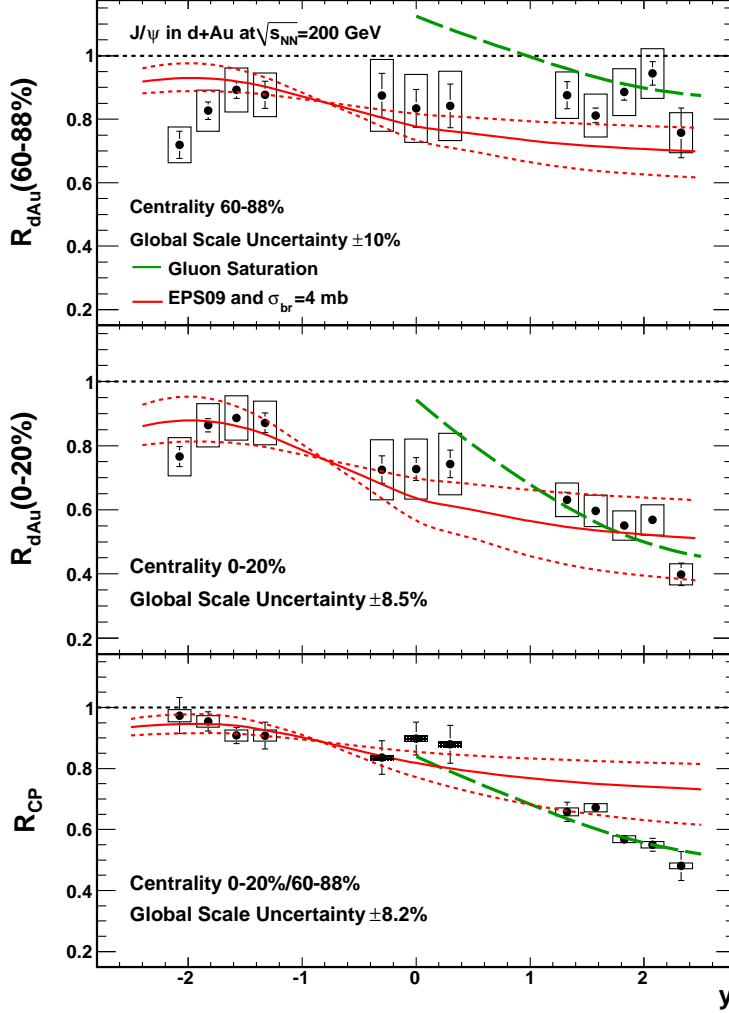


Figure 7.9: The J/ψ nuclear modification factor $R_{d\text{Au}}$ central (a), $R_{d\text{Au}}$ peripheral (b) and R_{CP} central (c). Curves are model calculations detailed in Section 7.2.1. [19]

p_T dependence of the R_{pA} which is given by [84]

$$R_{pA}(p_T, b) = \frac{\langle p_T^2 \rangle_{pp} R_{pA}}{\langle p_T^2 \rangle_{pp} + \Delta_{pA}(b)} \left(1 + \frac{p_T^2}{6\langle p_T^2 \rangle_{pp}}\right)^6 \left(1 + \frac{p_T^2}{6[\langle p_T^2 \rangle_{pp} + \Delta_{pA}(b)]}\right)^{-6}, \quad (7.2)$$

where R_{pA} is the nuclear modification for a $p+A$ collision, b is the impact parameter, $\langle p_T^2 \rangle_{pp} = 3.96 \text{ GeV}^2$ is the $\langle p_T^2 \rangle$ in $p+p$ collisions, and $\Delta_{pA}(b)$ describes the modification of $\langle p_T^2 \rangle$ in $p+A$ collisions [83]. The results from this calculation are shown for the 0-100% $R_{d\text{Au}}$ at all rapidities in Figure 7.5 as the dot-dashed curves. This is a parameter free calculation with respect to the RHIC data, with no overall normalization applied to the calculation,

or fits to the RHIC data used. The p_T shape is in good agreement with the data at mid and forward rapidity, but the theory shows a greater overall level of suppression than is seen in the data. At backward rapidity there is a disagreement with the shape of the p_T distribution, while the theory predicts a similar p_T shape at all rapidities, the data show a much faster rise in $R_{d\text{Au}}$ with increasing p_T at backward rapidity.

A second set of model calculations, performed by Ferreiro et al. [68, 67], are also shown in Figure 7.5. This model uses a Monte-Carlo approach within a Glauber model of $d+\text{Au}$ collisions. The J/ψ production is calculated using the color singlet model, which has $2 \rightarrow 2$ kinematics ($g+g \rightarrow J/\psi + g$) where the majority of the $J/\psi p_T$ is balanced by the emission of a hard gluon in the final state. This is distinct from the $2 \rightarrow 1$ processes, where the $J/\psi p_T$ comes entirely from the transverse momentum carried by the colliding gluons. Nuclear shadowing is included through several different nPDF sets, to investigate the dependence of the result on the different nPDF parametrizations. The calculations shown in Figure 7.5 utilize the nDSg nPDF set. Similar calculations using the EKS98 and EPS08 [64] nPDF sets can be found in [67]. Nuclear breakup of the J/ψ is taken into account through the use of an effective, p_T -independent, absorption cross section of 4.2 mb. Results using $\sigma_{abs} = 0$, 2.6, and 6 mb can also be found in [67]. Only the calculations with $\sigma_{abs} = 4.2$ mb are highlighted here as, of the σ_{abs} values used, they best reproduce the rapidity dependence of the 60-88% $R_{d\text{Au}}$ [67] where shadowing corrections are expected to be small. The results of this calculation, shown in Figure 7.5 for 0-100% $R_{d\text{Au}}$ at all rapidities, are in reasonable agreement with the overall level of modification seen at low p_T in the data at mid and forward rapidities, while the calculation predicts a flatter distribution with increasing p_T than is seen in the data. The shape of the distribution at backward rapidity is markedly different than that of the data. While the data rapidly increase to $R_{d\text{Au}} \approx 1$ at low p_T , the calculated $R_{d\text{Au}}$ is essentially constant with increasing p_T .

The calculations by Ferreiro et al. utilizing the nDSg nPDF set were chosen for Figure 7.5 because the use of the same nPDF set in the two calculations should produce the same modification due to shadowing. However, the J/ψ production kinematics are calculated differently, which will lead to some difference in the shadowing contribution. A pronounced difference in the p_T shape of the $R_{d\text{Au}}$ is observed between the two sets of calculations. The calculations from Kopeliovich et al. include the Cronin effect, which provides a decrease in J/ψ production at low p_T and an increase at higher p_T , creating an $R_{d\text{Au}}$ that exhibits less suppression at high p_T than at low p_T . The calculations from Ferreiro et al. do not include the Cronin effect, and therefore the p_T shape of $R_{d\text{Au}}$ should be dominated by the effect of shadowing, and therefore the choice of nPDF set. A further difference between the two calculations is the handling of the nuclear breakup, which in the case of the calculations by Kopeliovich should depend on the rapidity and p_T of the J/ψ , while the σ_{abs} in the calculations by Ferreiro is constant with p_T and rapidity.

Ferreiro et al. have also taken into account the geometric dependence of the shadowing [67], where it is assumed that the shadowing strength is proportional to the local density. This assumption allows for calculation of the $R_{d\text{Au}}$ vs p_T in different centrality bins. The results of the calculation in the four PHENIX centrality bins are shown in Figure 7.7 for backward rapidity, and in Figure 7.8 for mid and forward rapidities. Here calculations using the EKS98 nPDF set (solid line) are included, along with those using the nDSg nPDF set (dashed line), as this provides a direct comparison between the effects due to different

nPDF sets. At mid and forward rapidity the calculations are similar to each other and show reasonable agreement with the $R_{d\text{Au}}$ distributions within the current statistical and systematic uncertainties, although the calculation appears to predict a slightly larger average suppression for peripheral collisions at forward rapidity than is seen in the data. This could be due to the value of σ_{abs} used at forward rapidity, as the value of 4.2 mb was chosen by eye rather than fitted to the data, and σ_{abs} may not be independent of y .

At backward rapidity the calculations are in disagreement with the data for all but the most peripheral collisions. While the calculations using the nDSg nPDF set are roughly constant with p_T for each centrality, the calculations using the EKS98 nPDF set show an enhancement in the suppression of $R_{d\text{Au}}$ with increasing p_T for central and midcentral collisions, whereas the data shows the opposite trend. At backward rapidity and low p_T (Bjorken $x \approx 0.1$ for the parton in the Au nucleus) production occurs in the anti-shadowing region, while at high p_T ($x \approx 0.3$) production begins to move towards the EMC region. Few constraints on the nPDF's exist in this region, and there is large disagreement in the modification of the gluon density between nPDF's. The nDSg nPDF set shows no suppression in the EMC region, and only a small anti-shadowing effect. The EKS98 nPDF, on the other hand, exhibits a suppression in the EMC region similar to that observed in the quark distributions, and a larger anti-shadowing effect (see [63] for a comparison of nPDF sets). The larger anti-shadowing combined with the inclusion of an EMC effect in the EKS98 nPDF set cause a decrease in the calculated $R_{d\text{Au}}$ as p_T (and correspondingly, x) increases. The lack of a strong anti-shadowing effect combined with the absence of an EMC effect in the nDSg nPDF causes the calculated $R_{d\text{Au}}$ to remain roughly constant with increasing p_T .

A third set of model calculations by Sharma and Vitev [102] is compared with the midrapidity 0-100% centrality integrated $R_{d\text{Au}}$ in Figure 7.10. This model describes J/ψ production using NRQCD. The effect of nuclear shadowing is calculated using EKS98 in the EMC region ($x > 0.25$), while for lower values, power suppressed coherent final-state scattering leads to a modification of the parton x [105]. Initial state energy loss, and a calculation of the Cronin effect are also included. The solid curve in Figure 7.10 shows the full calculation including the Cronin effect. The dashed curve in Figure 7.10 is the same calculation without the Cronin effect. This comparison gives a direct indication of the contribution from the Cronin effect in this model, which is evidently over predicted when compared to the data.

The final model calculates the modification of J/ψ production within the gluon saturation, or CGC, regime. The calculations, performed by Kharzeev et al. [79], are compared with the data in Figure 7.11. In the CGC picture, at high energies the coherence length becomes large, where the coherence length is given by $l_c = \tau_P/c$ where τ_P is the production time. When the coherence length becomes large relative to the nuclear radius, the J/ψ cross section is dominated by multiple gluon exchanges with many nucleons. This regime is characterized by the saturation scale Q_s (discussed in Section 2.1.2), above which calculations within the CGC should be valid. For J/ψ production at RHIC, this occurs at forward rapidity and $p_T \lesssim 5 \text{ GeV}/c$, and is only marginally satisfied at midrapidity [79]. The authors of [79] stress that the calculations at midrapidity should be used as a qualitative estimate only. The comparison of the calculations with the data in Figure 7.11 show remarkably good agreement over the range of the calculations.

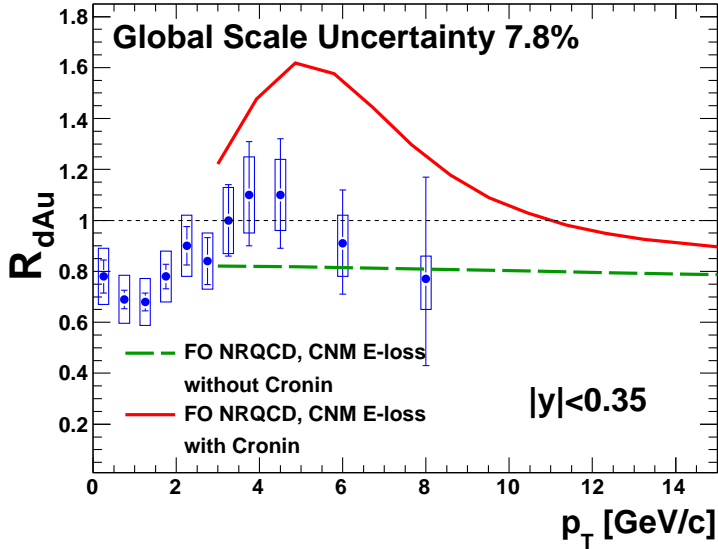


Figure 7.10: The J/ψ $R_{d\text{Au}}$, as a function of p_T momentum for midrapidity 0-100% centrality integrated $d+\text{Au}$ collisions. The curves are theoretical calculations from [102] described in the text. [10]

7.3 ψ' Production in $d+\text{Au}$ collisions

The large suppression of ψ' production in $d+\text{Au}$ collisions came as a great surprise, especially when compared to the measured J/ψ suppression, as shown in Figure 7.12. Low energy results from E866/NuSea [86] and NA50 [35] show similar suppression for the J/ψ and ψ' in some kinematic regions, while in others the ψ' is found to be more suppressed than the J/ψ . In [38], the authors try to explain this result using a model of the time evolution of the $c\bar{c}$ pair. If the $c\bar{c} \rightarrow J/\psi(\psi')$ evolution time is shorter than the time it takes to traverse the target nucleus, than a larger suppression of the ψ' compared to the J/ψ should be observed since the ψ' is a physically larger meson than the J/ψ . If the nuclear breakup increases simply as the size of the $c\bar{c}$ pair, then this explanation makes intuitive sense.

In order to test this theory against the RHIC data, we calculate the average proper time spent in the nucleus by the quarkonia (or $c\bar{c}$ precursor) for the RHIC, E866, and NA50 data. The average time is calculated by multiplying the average velocity of the quarkonia by the mean length of the target nucleus ($\langle L \rangle$). In the case of RHIC, the $\langle L \rangle$ values for each centrality bin are calculated from the PHENIX Glauber model of $d+\text{Au}$ collisions, and are given in Table 7.1.

To calculate the average J/ψ velocity relative to the nucleus, β , the J/ψ velocity is first calculated in the lab frame. The relative velocity of the J/ψ to the target nucleus in the

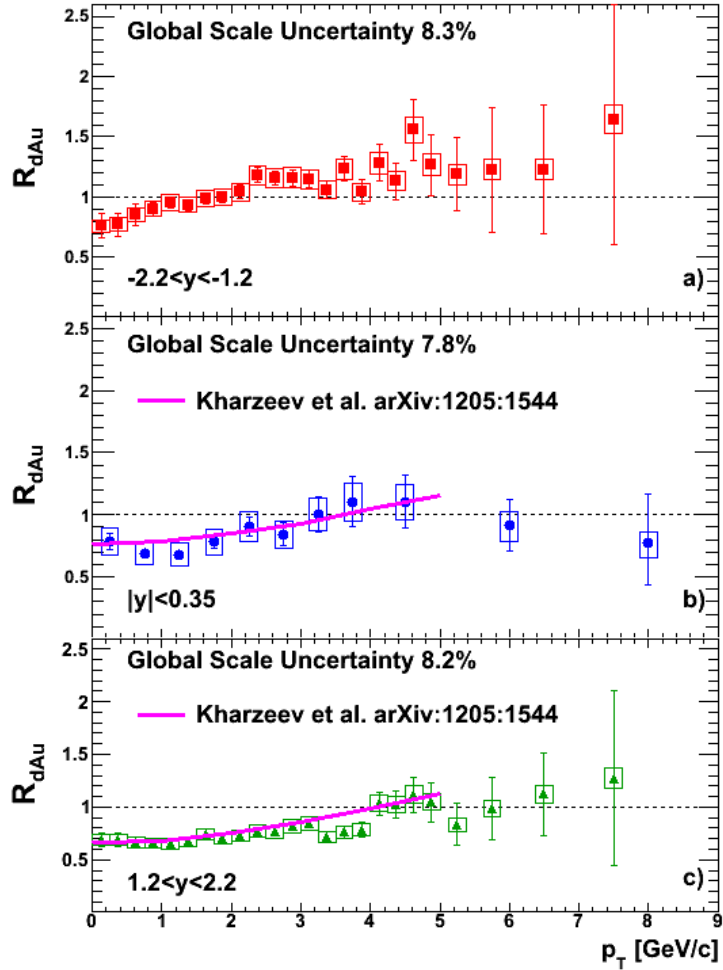


Figure 7.11: The J/ψ $R_{d\text{Au}}$ as a function of transverse momentum for a) backward rapidity, b) midrapidity, and c) forward rapidity 0-100% centrality integrated $d+\text{Au}$ collisions. Curves are model calculations from [79] detailed in Section 7.2.2.

lab frame, β_z , is calculated simply as

$$\beta_z = \frac{p_z}{E} = \frac{\sqrt{p_T^2 + M_{J/\psi}^2} \sinh y_{rel}}{\sqrt{(p_T^2 + M_{J/\psi}^2)(1 + \sinh^2 y_{rel})}}, \quad (7.3)$$

where y_{rel} is the rapidity difference between the J/ψ and the target nucleus. In this case the J/ψ p_T is assumed to be 0. For fixed target experiments (NA50, E866) y_{rel} is half of the beam rapidity, while for collider experiments (RHIC) the full beam rapidity is used. The values of the beam rapidity, y_{beam} , at each of the experiments is given in Table 7.1. The J/ψ velocity in the lab frame is then converted to the velocity in the rest frame of the nucleus by $\beta = \beta_z/\gamma$, where γ is the Lorentz factor. The resulting values for β are given

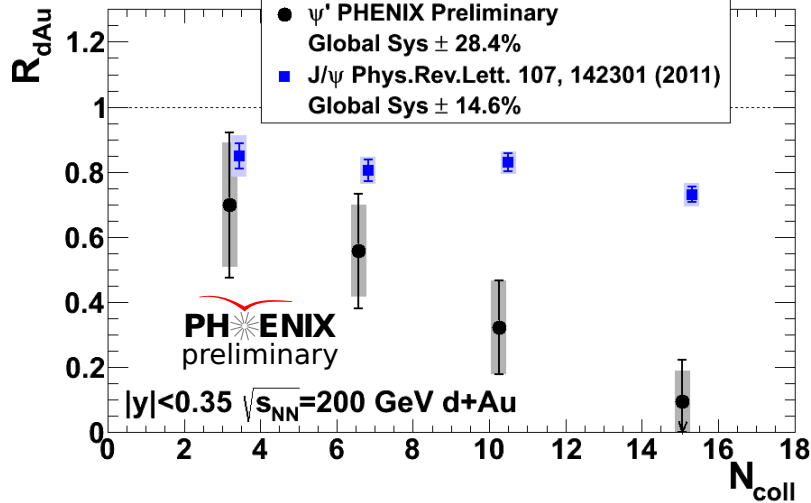


Figure 7.12: The ψ' and J/ψ $R_{d\text{Au}}$ at $|y| < 0.35$ as a function of N_{coll} .

in Table 7.1. Multiplying β by $\langle L \rangle$ then gives the proper time spent in the nucleus by the quarkonia (or $c\bar{c}$ precursor) state, τ . The values for τ are also given Table 7.1.

The relative modification of the ψ' to J/ψ in $p+A$ collisions vs the average time spent in the nucleus is shown in Figure 7.13. Also shown in Figure 7.13 is the calculation from Arleo et al [38] which describes the NA50 and E866 data well. The low energy data shows a trend of similar suppression of the J/ψ and ψ' for short times spent in the nucleus, and a larger suppression of the ψ' relative to the J/ψ for long times spent in the nucleus. This trend is broken with the introduction of the RHIC data. This result shows that the modification of the ψ' compared to the J/ψ at RHIC can not be explained by the time spent in the nucleus alone.

The explanation for the larger suppression of the ψ' compared to the J/ψ remains an open question. However there are a number of possibilities that can be considered. The binding energy of the ψ' is only 50 MeV, compared to 640 MeV for the J/ψ . This means that relatively little energy needs to be added to the ψ' system before it breaks into D meson pairs. This could be achieved through relatively soft collisions as the ψ' precursor state traverses the nucleus, an effect which would likely not occur for the J/ψ . Alternatively this could indicate a difference in the production mechanism for the J/ψ and ψ' . If the J/ψ is only created in the color singlet state it would be very hard to breakup. If the ψ' , on the other hand, is predominantly created in the color octet state, than it has a higher chance of interacting due to its color charge. More information about the J/ψ and ψ' production mechanisms in $p+p$ is needed to clarify this situation.

7.4 Correcting the J/ψ $R_{d\text{Au}}$ for Feed-down Effects

The measured J/ψ $R_{d\text{Au}}$ is for inclusive J/ψ production. This includes not only direct J/ψ production, but also feed-down from higher charmonia resonances as well as J/ψ 's

Table 7.1: Compilation of the values used to calculate the proper time spent in the nucleus by the J/ψ (or $c\bar{c}$ precursor).

| Experiment | E_{beam} | y_{beam} | $\langle L \rangle$ [fm] | β [1/c] | τ [fm/c] |
|-------------|------------|------------|--------------------------|----------------|---------------|
| E866 p-W | 800 GeV | 7.44 | 3.95 | 0.0061 - 0.068 | 0.024 - 0.27 |
| NA50 p-Be | 400 GeV | 6.75 | 0.87 | 0.068 | 0.06 |
| NA50 p-Al | 400 GeV | 6.75 | 1.88 | 0.068 | 0.13 |
| NA50 p-Cu | 400 GeV | 6.75 | 2.67 | 0.068 | 0.18 |
| NA50 p-Ag | 400 GeV | 6.75 | 3.45 | 0.068 | 0.24 |
| NA50 p-W | 400 GeV | 6.75 | 3.95 | 0.068 | 0.27 |
| NA50 p-Pb | 400 GeV | 6.75 | 4.30 | 0.068 | 0.29 |
| RHIC 00-20% | 100 GeV | 5.36 | 5.17 | 0.0094 | 0.048 |
| RHIC 20-40% | 100 GeV | 5.36 | 4.62 | 0.0094 | 0.043 |
| RHIC 40-60% | 100 GeV | 5.36 | 3.94 | 0.0094 | 0.037 |
| RHIC 60-88% | 100 GeV | 5.36 | 2.85 | 0.0094 | 0.027 |

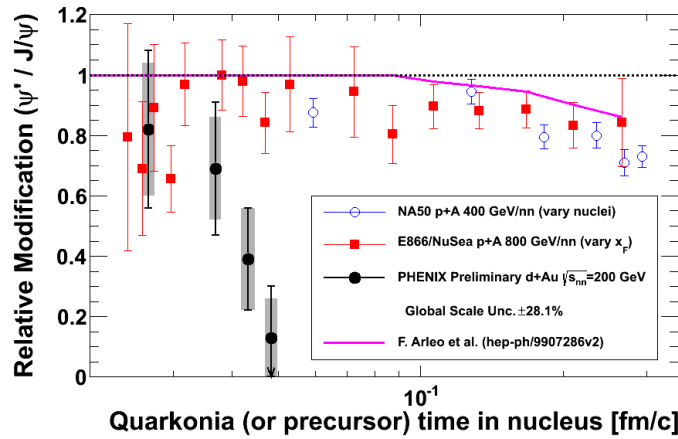


Figure 7.13: The relative modification of the ψ' to J/ψ in d +Au ad $|y| < 0.35$ as a function of time spent in the nucleus.

produced from B meson decays. At the p_T and energies reached at RHIC, the $B \rightarrow J/\psi + X$ contribution should be only a small contribution to the inclusive J/ψ measurement. From $p+p$ data, however, feed-down from both ψ' and χ_c decays contribute $\sim 40\%$ of the observed J/ψ production. In principal, measurements of the modification of χ_c and ψ' production in $d+\text{Au}$ collisions can be used to extract the modification of the *direct* J/ψ production.

PHENIX has also made a preliminary measurement of χ_c production in $d+\text{Au}$ [57]. The measured $R_{d\text{Au}}$ in centrality integrated $d+\text{Au}$ collisions for the χ_c is $R_{d\text{Au}}(\chi_c) = 0.77 \pm 0.44 \pm 0.18$. The statistics do not allow for a measurement of the centrality dependence in the case of the χ_c . However, combining this with the centrality integrated ψ' $R_{d\text{Au}}$ we can construct a direct J/ψ $R_{d\text{Au}}$ using the formula

$$R_{d\text{Au}}^{J/\psi} = R_{d\text{Au}}^{\text{incl}} \times \frac{\left(1 - F_{\psi'}^{J/\psi} R_{d\text{Au}}^{\psi'} - F_{\chi_c}^{J/\psi} R_{d\text{Au}}^{\chi_c}\right)}{\left(1 - F_{\psi'}^{J/\psi} - F_{\chi_c}^{J/\psi}\right)}, \quad (7.4)$$

where here $R_{d\text{Au}}^{J/\psi}$ is the modification of direct J/ψ production and $R_{d\text{Au}}^{\text{incl}}$ is the modification of inclusive J/ψ production, as given in Section 5.3.3. The world's average values for the $\psi' \rightarrow J/\psi$ feed-down fraction, $F_{\psi'}^{J/\psi}$, and the $\chi_c \rightarrow J/\psi$ feed-down fraction, $F_{\chi_c}^{J/\psi}$, of $(8.1 \pm 0.3)\%$ and $(25 \pm 5)\%$ respectively [66] are used. This gives a value for the modification of direct J/ψ production integrated over all centrality of

$$R_{d\text{Au}}^{J/\psi} = 0.90 \pm 0.12 \pm 0.16. \quad (7.5)$$

In the calculation of both the χ_c and ψ' $R_{d\text{Au}}$, the inclusive J/ψ modification ($R_{d\text{Au}}^{\text{incl}}$) is used. This means there are correlations in the uncertainties, which are taken into account when calculating the uncertainties in Equation 7.5. The results in Equation 7.5 indicate that $\sim 50\%$ of the observed suppression of inclusive J/ψ production is accounted for by feed-down, albeit with large uncertainties on the extraction. In fact, the direct J/ψ $R_{d\text{Au}}$ is consistent with 1, allowing the possibility that direct J/ψ production is unmodified.

A compilation of the measured modification of direct production in $d+\text{Au}$ collisions for the ψ' , χ_c , and J/ψ as a function of the binding energy of the state is shown in Figure 7.14. This shows an interesting trend of decreasing suppression with increasing binding energy. There is a clear separation in the modification of the ψ' and the J/ψ . The weak link in the chain is currently the measurement of χ_c production, both in $p+p$ and $d+\text{Au}$. This is a very challenging measurement which reconstructs the χ_c through its $\chi_c \rightarrow J/\psi + \gamma$ decay, where the photon has an energy of only ~ 400 MeV.

While there is no measured centrality dependence of the χ_c $R_{d\text{Au}}$, we can correct the J/ψ $R_{d\text{Au}}$ for the ψ' feed-down. The J/ψ $R_{d\text{Au}}$ corrected for the modification of the ψ' feed-down includes the modification of both direct J/ψ and $\chi_c \rightarrow J/\psi$ production ($R_{d\text{Au}}(J/\psi + \chi_c \rightarrow J/\psi)$). It is shown as a function of N_{coll} in Figure 7.15. A significant decrease in the modification for central events compared to peripheral events is seen. This is due to the much stronger ψ' suppression seen in central events. The change in the N_{coll} dependence can be quantified by fitting a straight line to both the inclusive J/ψ $R_{d\text{Au}}$ and $R_{d\text{Au}}(J/\psi + \chi_c \rightarrow J/\psi)$. This gives

$$\text{Slope of } R_{d\text{Au}}^{\text{incl}} = -0.010 \pm 0.003 \pm 0.006 \quad (7.6)$$

$$\text{Slope of } R_{d\text{Au}}(J/\psi + \chi_c \rightarrow J/\psi) = -0.006 \pm 0.004 \pm 0.006. \quad (7.7)$$

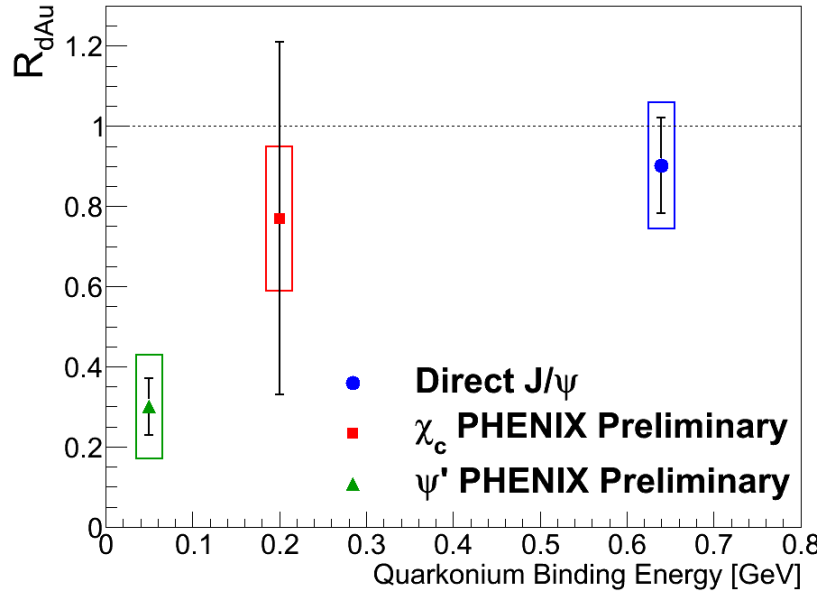


Figure 7.14: The modification in d +Au collisions of direct production for different charmonia states as a function of the binding energy. These are integrated over all centrality.

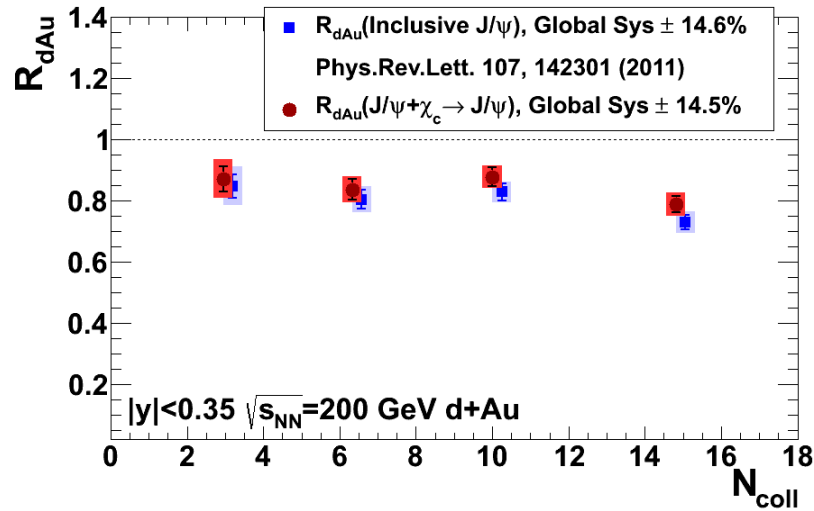


Figure 7.15: A comparison between the inclusive J/ψ $R_{d\text{Au}}$, and the J/ψ $R_{d\text{Au}}$ corrected for ψ' feed-down, $R_{d\text{Au}}(J/\psi + \chi_c \rightarrow J/\psi)$ as a function of N_{coll} .

This is a decrease in the slope of 40%, and further the slope of $R_{dAu}(J/\psi + \chi_c \rightarrow J/\psi)$ is consistent with 0 within the uncertainties.

What is truly needed to fully understand the system is a precise measurement of the modification of χ_c production in $d+Au$. While it is unlikely that the current detector upgrades to PHENIX will provide an increase in the precision of the measurement, the increased luminosity currently provided by RHIC coupled with a long $d+Au$ run may provide enough statistics for an improved measurement.

7.5 Geometric Dependence of the J/ψ R_{dAu}

The observation, discussed in Section 7.2.1, that EPS09 with a linear dependence on nuclear thickness combined with a breakup cross section was unable to reproduce the forward rapidity R_{dAu} , likely points to a failure of the centrality dependence of the nPDF modification. To investigate the centrality dependence of the data, a simple geometric model is used [19]. In this model the PHENIX centrality bins are categorized by the transverse radial positions of each nucleon-nucleon collision relative to the center of the Au nucleus (r_T). The r_T distributions corresponding to the four PHENIX centrality bins used in the $d+Au$ measurement are shown in Figure 7.16.

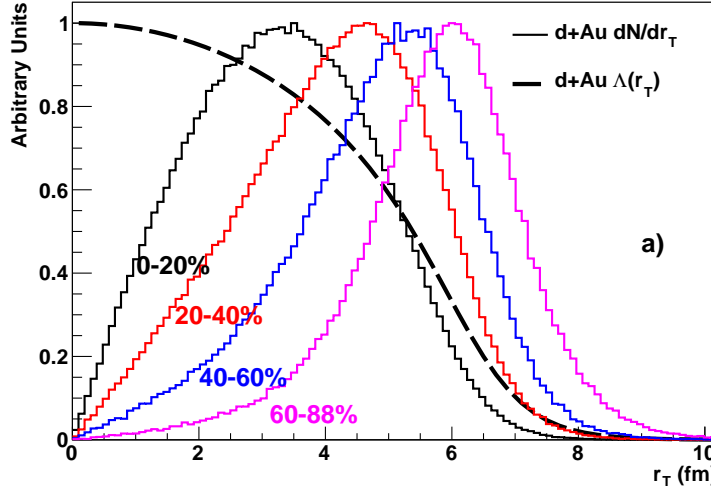


Figure 7.16: The r_T distributions for each of the four PHENIX centrality bins along with the $\Lambda(r_T)$ distribution. The distributions are all re-normalized to a maximum of 1 for a clearer comparison. [19]

The nuclear modification is then assumed to be proportional to the density weighted longitudinal thickness, $\Lambda(r_T)$, given by

$$\Lambda(r_T) = \frac{1}{\rho_0} \int dz \rho(z, r_T), \quad (7.8)$$

where ρ_0 is the density at the center of the nucleus, and ρ is assumed to follow, on average, a Woods-Saxon distribution. To investigate the centrality dependence of the data, three functional dependencies of the nuclear modification on $\Lambda(r_T)$ were posited. They are:

$$\text{Linear : } M(r_T) = 1.0 - a\Lambda(r_T) \quad (7.9)$$

$$\text{Quadratic : } M(r_T) = 1.0 - a\Lambda(r_T)^2 \quad (7.10)$$

$$\text{Exponential : } M(r_T) = e^{-a\Lambda(r_T)} \quad (7.11)$$

where a is a parameter which dictates the average strength of the modification. As mentioned in Section 7.2.1, the EPS09 modification shown in Figure 7.9 utilizes the linear dependence, while the nuclear breakup is inherently exponential.

Using the r_T distributions of the PHENIX centrality bins and the functional forms of the modifications in Equations 7.9-7.11 the R_{dAu} can be calculated for any value of the parameter a . These calculations give a unique relationship between the 0-100% centrality integrated R_{dAu} and the most central R_{CP} . When plotting in the R_{CP} - R_{dAu} plane, varying the parameter a for a given functional form of the modification produces a curve, since the functional form of the modification predicts a unique ratio of R_{CP} to R_{dAu} for each a . Therefore, any model using the given geometric dependence for the modification must fall somewhere along that curve. The curves for the three functional forms in Equations 7.9-7.11 which arise from varying the parameter a are shown in Figure 7.17 along with the PHENIX data points. When plotting the R_{CP} vs R_{dAu} the Type B & C systematic uncertainties are added in quadrature and depicted as ellipses around the data points. As there is little correlation between the uncertainties on R_{CP} and R_{dAu} this should give a reasonable visualization of the region covered by the systematic uncertainties.

Figure 7.17 shows immediately that a modification which is linearly or exponentially dependent on the density weighted longitudinal thickness will be unable to describe the forward rapidity data. Moreover, even a modification which is quadratically dependent on $\Lambda(r_T)$ does not adequately describe the forward rapidity data. At mid and backward rapidity, however, each of the three functional forms does adequately well at reproducing the data. This is, perhaps, not surprising, as the linear EPS09 combined with exponential nuclear breakup describes the centrality dependence of the mid and backward rapidity R_{dAu} reasonably well. It is further shown in [94] that combining an exponential nuclear breakup with EPS09 assuming a quadratic $\Lambda(r_T)$ dependence only makes the agreement at forward rapidity worse.

This finding provides motivation to use a simple geometric model, like the one presented here, to find a functional form for the modification which best reproduces the measured R_{dAu} . This is discussed in the following chapter in the context of parametrizing the R_{dAu} for use in predicting the CNM effects in Au+Au collisions.

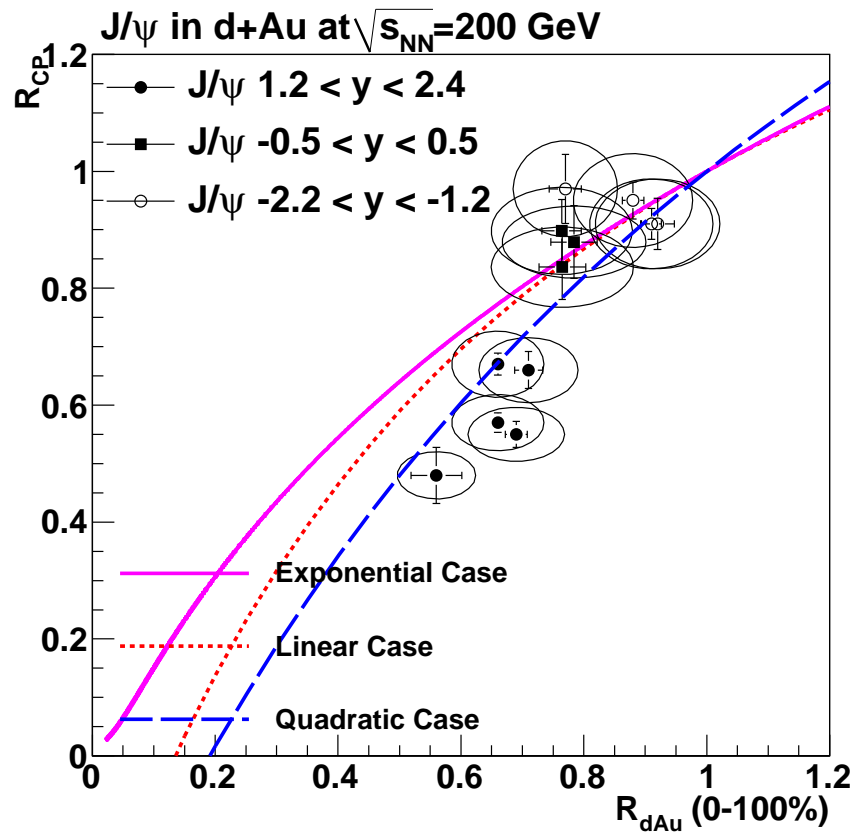


Figure 7.17: The J/ψ nuclear modification factors R_{CP} vs R_{dAu} for experimental data compared with three geometric dependencies of the nuclear modification (curves). [19]

CHAPTER 8

INVESTIGATING THE GEOMETRIC DEPENDENCE OF THE J/ψ R_{dAu}

As discussed in Section 7.5, it was found that a geometric dependence which was linearly or exponentially dependent on the nuclear thickness could not describe the J/ψ R_{dAu} and R_{CP} at forward rapidity. This chapter describes an investigation of this using a model which assumes that the nuclear modification can be described by two effects, nuclear shadowing and nuclear breakup.

There are three main goals of this study. The first is to investigate whether the effects of nuclear shadowing and nuclear breakup can be separated. As the strength of the nuclear breakup is exponentially dependent on the nuclear thickness, if the nuclear shadowing has a significantly different geometric dependence, this may be possible. The second goal is to test the sensitivity of the data to the form of the geometric dependence of nuclear shadowing. The final goal is to use a parametrization of the measured J/ψ R_{dAu} to calculate the CNM effects on J/ψ production in Au+Au collisions. This final goal will be discussed in Chapter 9, while the first two will be addressed in this chapter.

8.1 Modeling the Nuclear Modification

Models in which the nuclear modification is described by nuclear shadowing combined with nuclear breakup have been used at both the SPS [87] and RHIC [13] to aid in interpreting the modification of J/ψ production in $p+A$ collisions. The nuclear breakup is usually parametrized with a single absorption cross section, σ_{abs} , representing an *effective* cross section which may include other physics with a similar geometric dependence. Here the modification due to nuclear breakup is calculated as

$$M_{\text{br}} = e^{(-\sigma_{abs} \Lambda(r_T, z_1))}. \quad (8.1)$$

In Equation 8.1, $\Lambda(r_T)$ is the nuclear thickness through the gold nucleus at the transverse radial position of the struck nucleon in the Au nucleus, r_T , given by

$$\Lambda(r_T) = \int dz \rho_A(z, r_T), \quad (8.2)$$

where z is the direction in which the deuteron travels, and $\rho_A(z, r_T)$ is the density of the nucleus. $\Lambda(r_T)$ has units of fm^{-2} . Here it is assumed that the breakup of the J/ψ is

dominated by collisions with nucleons which pass through the J/ψ production point after the J/ψ precursor is produced, and therefore depends on the nuclear thickness integral starting at the J/ψ production point, z_1 .

At RHIC energies J/ψ production is dominated by gluon-gluon interactions. Therefore, the nuclear shadowing of J/ψ production in d +Au collisions must represent the modification of the gluon distribution in Au nuclei. It is assumed that there is no nuclear modification for the d . For this study it is assumed that the gluon modification, integrated over all r_T , can be described by the EPS09 gluon modification. The gluon modification averaged over r_T at a given Bjorken x in the Au nucleus (x_2), and energy transfer (Q^2), $R_g(x_2, Q^2)$, is taken from the central EPS09 set. The uncertainty on the EPS09 gluon modification is not considered in this study. The values of x_2 and Q^2 are calculated based on $2 \rightarrow 1$ kinematics using

$$x_2 = \frac{\sqrt{M_{J/\psi}^2 + p_T^2}}{\sqrt{s_{NN}}} e^{-y}, \quad (8.3)$$

and

$$Q^2 = M_{J/\psi}^2 + p_T^2, \quad (8.4)$$

where $M_{J/\psi}$, p_T and y are the mass, transverse momentum, and rapidity of the J/ψ respectively. Production via a $2 \rightarrow 1$ process is forbidden for J/ψ production due to conservation of angular momentum. However, a comparison of the EPS09 modification as a function of p_T and y obtained using $2 \rightarrow 1$ kinematics with a more rigorous NLO calculation [108] is shown in Figures 8.1 and 8.2 respectively. Good agreement can be seen between the results using the two calculations, and therefore it is concluded that the use of $2 \rightarrow 1$ kinematics compared to the more rigorous NLO calculations has a minimal effect on the final results.

To investigate the r_T dependence of the nuclear shadowing required by the J/ψ data, two functional forms for the modification due to nuclear shadowing (M_{shad}) are introduced (discussed separately in Sections 8.3 and 8.4), each with one or two free parameters. These free parameters, along with the magnitude of σ_{abs} , are then extracted from fits to the measured $J/\psi R_{d\text{Au}}$.

8.2 d +Au Glauber Model

The calculations of the $J/\psi R_{d\text{Au}}$ for comparison with the measured data are performed within the framework of a Glauber Monte-Carlo model [91] of nuclear collisions. The Glauber model treats each nuclear collision as a series of nucleon-nucleon (NN) collisions, where the initial spatial positions of the nucleons are randomly generated based on the nuclear density. Here the nuclear density, ρ_A , is taken to follow, on average, a Woods-Saxon distribution of the form

$$\rho_A(z, r_T) = \frac{\rho_0}{1 + e^{(\sqrt{z^2 + r_T^2} - r_{\text{WS}})/d_{\text{WS}}}}, \quad (8.5)$$

where ρ_0 is the normalization of the nuclear density, calculated such that

$$\int d^3r \rho_A(z, r_T) = A. \quad (8.6)$$

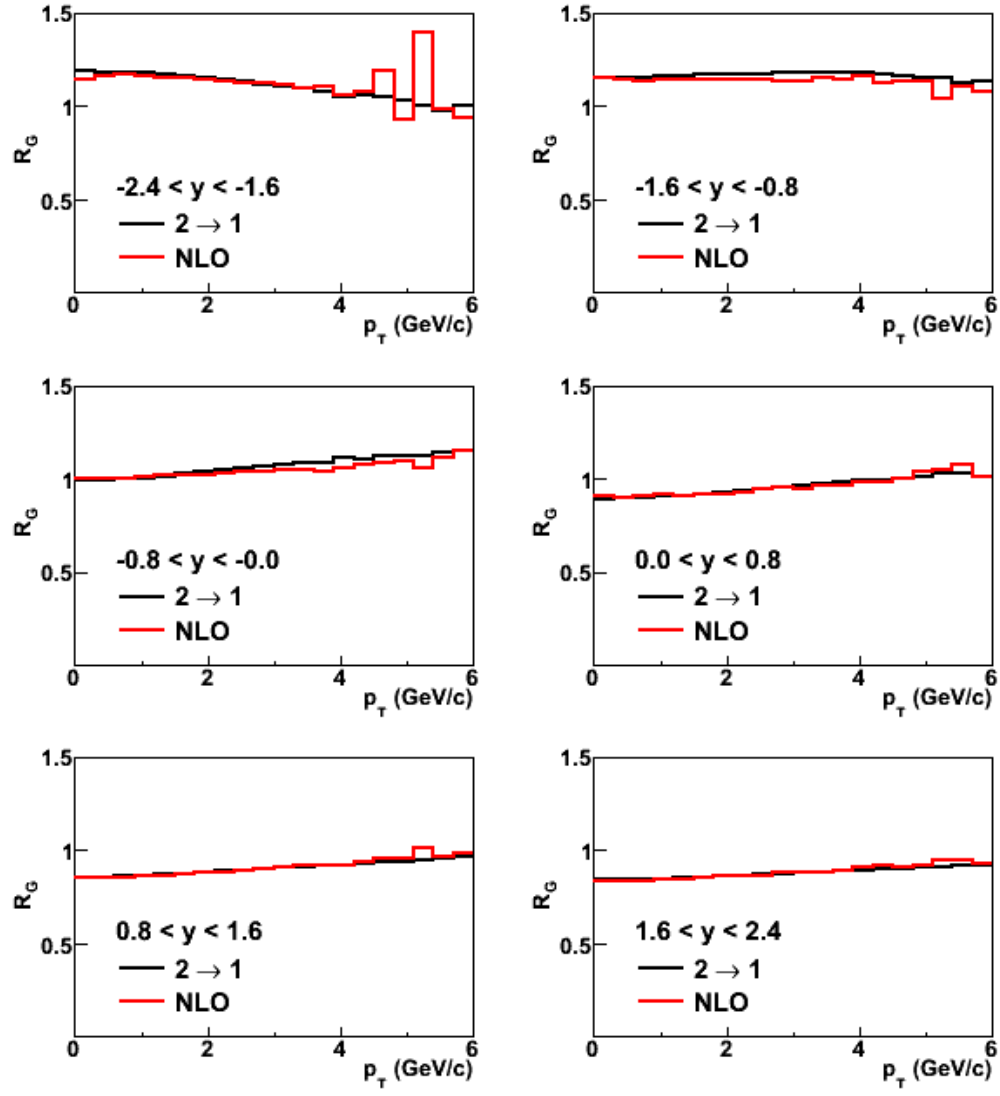


Figure 8.1: Distribution of the gluon modification vs p_T obtained from EPS09 by using the x_2 and Q^2 values obtained from a NLO calculation (NLO) and from Equations 8.3 and 8.4 ($2 \rightarrow 1$ kinematics). Each panel corresponds to a different cut on the rapidity of the J/ψ , as indicated.

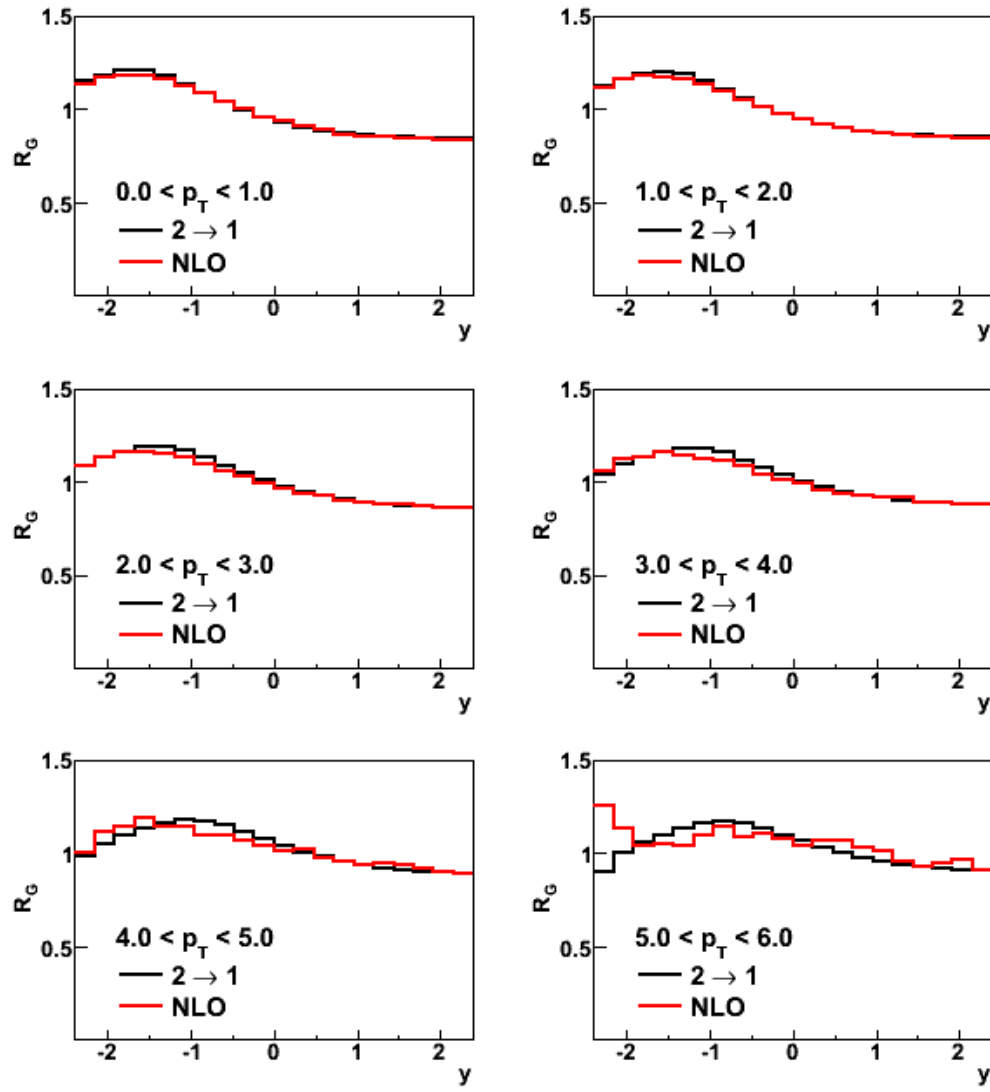


Figure 8.2: Distribution of the gluon modification vs rapidity obtained from EPS09 by using the x_2 and Q^2 values obtained from a NLO calculation (NLO) and from Equations 8.3 and 8.4 (2 → 1 kinematics). Each panel corresponds to a different cut on the p_T of the J/ψ , as indicated.

The parameters of the Woods-Saxon distribution are taken to be $r_{WS} = 6.38$ fm and $d_{WS} = 0.54$ fm for a Au nucleus. The distribution of the radial separation of the proton and neutron in the deuteron is taken from the Hulthen wave function [76]

$$\phi_d(r_{np}) = \sqrt{\frac{\alpha\beta(\alpha + \beta)}{2\pi(\alpha - \beta)^2}} \left(e^{-\alpha r_{np}} - e^{-\beta r_{np}} \right) / r_{np}, \quad (8.7)$$

where r_{np} is the separation between the neutron and proton, $\alpha = 0.228$ fm $^{-1}$, and $\beta = 1.18$ fm $^{-1}$. The deuteron is given a random spatial orientation. Nucleon-nucleon collisions occur based on an inelastic NN cross section (σ_{pp}), taken to be 42 mb at $\sqrt{s} = 200$ GeV. Individual d +Au collisions are generated with a randomly selected d impact parameter and a list of all parameters for each NN collision is saved.

For d +Au collisions, the soft particle yield in the PHENIX south BBC is simulated, for each NN collision, by choosing a random value from a negative binomial distribution (NBD), which takes the form

$$P(n) = \frac{\Gamma(n + \kappa)}{\Gamma(n + 1)\Gamma(\kappa)} e^{\left(n \ln \frac{\mu}{\kappa} - (n + \kappa) \ln(1 + \frac{\mu}{\kappa})\right)}, \quad (8.8)$$

with parameters $\mu = 3.038$ and $\kappa = 0.464$. The parameters μ and κ were chosen from fits to real data of charge collected in the south BBC, confined to multiplicities where the trigger inefficiency is negligible. The trigger efficiency of the south BBC is calculated using the ratio of the measured multiplicity distribution and the multiplicity distribution predicted by the fitted negative binomial distribution. It is taken to have the form

$$\epsilon_{eff}^{d+\text{Au}}(N_{\text{hits}}) = 1.0 - e^{-(N_{\text{hits}}/p_0)^{p_1}}, \quad (8.9)$$

where N_{hits} is the total soft particle yield in the south BBC calculated using Equation 8.8, $p_0 = 0.897$ and $p_1 = 0.612$. The sum of the simulated yield in the south BBC, modified by the trigger efficiency, over all NN collisions is used to assign an event to one of the PHENIX centrality bins, as is done in real data. This allows for a direct comparison with the PHENIX centrality results.

The parametrizations of the BBC trigger efficiency and soft particle yield in the BBC, as well as the parameters of the nuclear density distribution, were chosen to provide a match to the Glauber model used by PHENIX to calculate the N_{coll} values in each of the d +Au centrality bins. This provides the most direct comparison of the results calculated here with the measured PHENIX results.

For a given rapidity, p_T , centrality, and set of model parameters, the $R_{d\text{Au}}$ is calculated for events which pass a trigger efficiency test by summing over the total modification ($M_{br}M_{\text{shad}}$) for each NN collision and dividing by the total number of NN collisions. In this way the calculations are completely analogous to the way in which the measured values are determined.

Table 8.1: Average centrality values calculated from the Glauber model.

| Centrality | $\langle N_{\text{coll}} \rangle$ | $\langle \Lambda(r_T) \rangle [\text{fm}^{-2}]$ | $\langle r \rangle [\text{fm}]$ | $\langle r_T \rangle [\text{fm}]$ |
|------------|-----------------------------------|---|---------------------------------|-----------------------------------|
| 00-20% | 15.0 | 1.74 | 4.62 | 3.25 |
| 20-40% | 10.3 | 1.54 | 5.03 | 3.93 |
| 40-60% | 6.6 | 1.30 | 5.47 | 4.60 |
| 60-88% | 3.2 | 0.93 | 6.16 | 5.56 |

8.3 Nuclear Shadowing Parametrization 1

The r_T dependence of the nuclear shadowing was first assumed to be dependent on the nuclear thickness, raised to an arbitrary power,

$$M_{\text{shad}} = 1 - \left(\frac{1 - R_g(x_2, Q^2)}{a(n)} \right) \Lambda^n(r_T), \quad (8.10)$$

where n is an integer. The normalization factor $a(n)$ is adjusted so that the modification integrated over all collisions is equal to the EPS09 value of $R_g(x_2, Q^2)$. The modification is set to zero if it becomes negative. This parametrization is motivated by the results discussed in Section 7.5. Here n was allowed to be unphysically large, $n \leq 50$, to test the sensitivity of the data to the centrality dependence of the nuclear shadowing.

The values of σ_{abs} and n were initially fitted to the centrality dependence of the measured $J/\psi R_{d\text{Au}}$ independently at each rapidity. While treating each rapidity independently is not realistic, as it ignores correlations among the systematic uncertainties within the three PHENIX arms, it allows an exploration of how the centrality dependence varies with rapidity.

The fitting was performed using a modified χ^2 method that takes into account both the statistical and systematic uncertainties in the data, following [15]. The systematic uncertainties are incorporated into the modified χ^2 by changing the value of the data point by small steps within $\pm 3\sigma$ for each systematic uncertainty, and applying the appropriate penalty to the modified χ^2 . The modified χ^2 is defined as

$$\bar{\chi}^2 = \left(\sum_{i=1}^k \frac{[R_{d\text{Au}i} + \epsilon_{B_i} \sigma_{B_i} + \epsilon_C \sigma_{C_i} - R_{d\text{Au}i}(n, \sigma_{abs})]^2}{\bar{\sigma}_{A_i}} \right) + \epsilon_B^2 + \epsilon_s^2 + \epsilon_C^2, \quad (8.11)$$

$$\bar{\sigma}_{A_i} = \sigma_{A_i} \left(\frac{R_{d\text{Au}i} + \epsilon_{B_i} \sigma_{B_i} + \epsilon_C \sigma_{C_i}}{R_{d\text{Au}i}} \right), \quad (8.12)$$

$$\epsilon_{B_i} = \epsilon_B + \epsilon_s \left(1 - 2 \frac{\langle \Lambda(r_T) \rangle_i - \langle \Lambda(r_T) \rangle_1}{\langle \Lambda(r_T) \rangle_k - \langle \Lambda(r_T) \rangle_1} \right), \quad (8.13)$$

where i is the index of the centrality bin, k is the number of centrality bins, $R_{d\text{Au}i}$ is the data point, $R_{d\text{Au}i}(n, \sigma_{abs})$ is the model calculation for the trial values of the breakup cross section and shadowing power, $\sigma_{A_i(B_i, C_i)}$ are the type A (B,C) uncertainties on the data point, and $\epsilon_{B(C)}$ is the fraction of one standard deviation by which the data point

moves. Note that equation 8.13 contains a term that allows for some anti-correlation of the type B uncertainties. Here the type B uncertainties are allowed to be linearly correlated about the center of the distribution, i.e. $+\epsilon_s$ in the first point and $-\epsilon_s$ in the last, with a corresponding penalty for this correlation included. The value of ϵ_s was varied in the range $\pm 3\epsilon_B$. Although this is a reasonable prescription, the amount of correlation in the type B's is unknown, and could vary. However the type B uncertainty is small (2%) and therefore any correlation has a negligible effect on the end result when compared to the type A and C uncertainties.

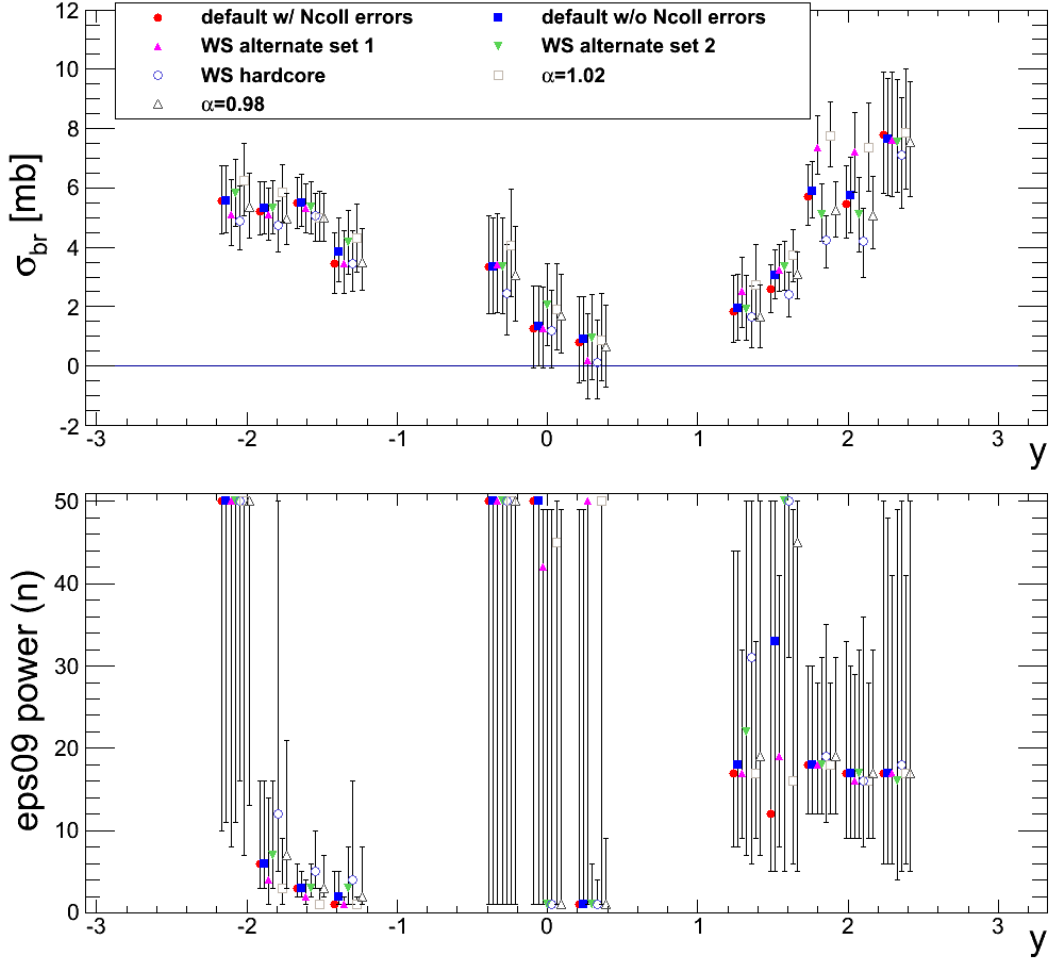


Figure 8.3: Resulting optimum σ_{abs} and n values for different Glauber parameter sets.

When plotting the PHENIX R_{dAu} versus centrality, the dominant contribution to the type B correlated systematic uncertainty comes from the uncertainty in the determination of $\langle N_{coll}(i) \rangle$. When fitting the optimum values of σ_{abs} and n , this error is removed from the χ^2 calculation, as the same Glauber model parameter set, with the same modeling of the PHENIX trigger efficiency and centrality selection, is used in both the $\langle N_{coll}(i) \rangle$ determination and the model calculation. The validity of this assumption was tested by

modifying the Glauber input parameters, which changes both the model calculations and the values of $\langle N_{\text{coll}}(i) \rangle$. The optimum values of σ_{abs} and n are then re-fitted to the data, which was recalculated using the $\langle N_{\text{coll}}(i) \rangle$ values for that given Glauber input parameter set. A total of 7 variations in the Glauber input parameters are tested, corresponding to the 7 variations used by PHENIX to calculate the uncertainty in $\langle N_{\text{coll}}(i) \rangle$. The σ_{abs} and n values for each variation at each of the 12 rapidities are shown in Fig. 8.3. The 7 variations shown in Figure 8.3 are as follows:

- Default Glauber parameter set with the errors on $\langle N_{\text{coll}}(i) \rangle$ included in the determination of σ_{abs} and n .
- Default Glauber parameter set with the errors on $\langle N_{\text{coll}}(i) \rangle$ excluded in the determination of σ_{abs} and n .
- Using WS parameters for the Au nucleus of $r_{WS} = 6.65$ fm and $d_{WS} = 0.55$ fm.
- Using WS parameters for the Au nucleus of $r_{WS} = 6.25$ fm and $d_{WS} = 0.53$ fm.
- Using a WS distribution with a hard core potential which prevents nucleons from occupying the same space, thus modifying the radial distribution of the nucleons.
- Assuming that the BBC south arm charge is proportional to the number of binary collisions to the power α where $\alpha = 0.98$ (Default is $\alpha = 1$).
- Assuming that the BBC south arm charge is proportional to the number of binary collisions to the power α where $\alpha = 1.02$.

The error due to uncertainty in the nucleon-nucleon inelastic cross section is assumed to cancel when calculating R_{dAu} , as it is present in both $d+Au$ and $p+p$ J/ψ production, and is therefore ignored in this study. Figure 8.3 shows good agreement of the σ_{abs} and n values for the different parameter sets. While there are large fluctuations in σ_{abs} at $y = 1.825$ and $y = 2.075$, the values for the alternate parameter sets are in agreement with the default case within the statistical uncertainties. As the σ_{abs} and n values are well controlled at all other rapidities, the uncertainty on $\langle N_{\text{coll}}(i) \rangle$ is taken to cancel between the data and calculations. Further, excluding the $\langle N_{\text{coll}}(i) \rangle$ errors has almost no effect on the results compared with including them, as expected.

The two dimensional $\bar{\chi}^2$ contours in σ_{abs} and n for $\Delta\bar{\chi}^2 = 1.0$ and $\Delta\bar{\chi}^2 = 2.3$ for each rapidity are shown in Figure 8.4 for $y \leq 0$ and in Figure 8.5 for $y > 0$. The three points nearest midrapidity are insensitive to n because the shadowing in that region is weak. At forward/backward rapidity the optimum is $n \geq 7$, except at two rapidities, where it is 2 and 4. This indicates that the data require a highly nonlinear onset of shadowing or antishadowing. Additionally there is relatively little correlation between n and σ_{abs} for n greater than a few, indicating that our initial premise of separating the nuclear shadowing and nuclear breakup contributions is valid.

The optimum values for σ_{abs} , along with their uncertainties, are shown versus rapidity in Figure 8.6. The uncertainty in σ_{abs} is calculated from the maximum extent of the $\Delta\bar{\chi}^2 = 1.0$ contour shown in Figures 8.4 and 8.5. The value of σ_{abs} is smallest at midrapidity, increasing in either direction.

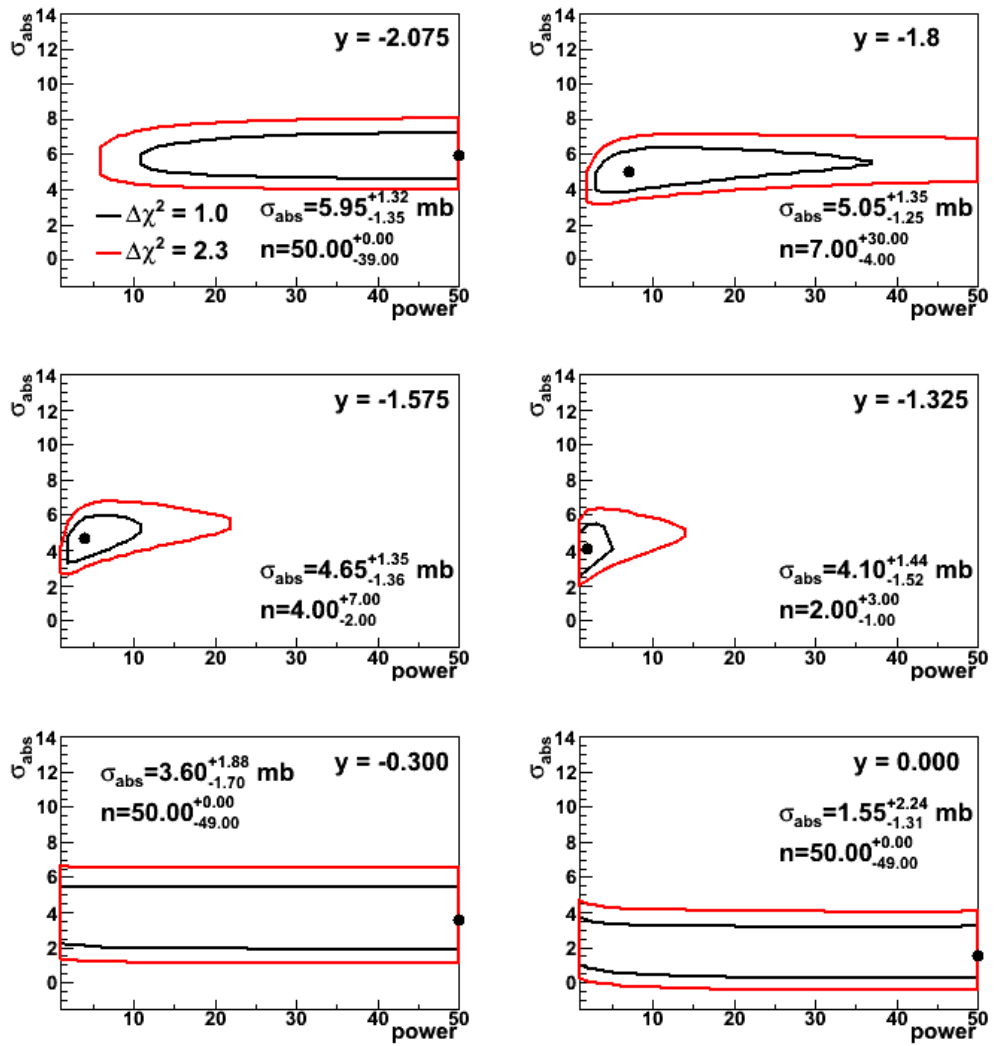


Figure 8.4: The $\bar{\chi}^2$ contours for $y \leq 0$ where σ_{abs} and n are optimized separately at each rapidity. [90]

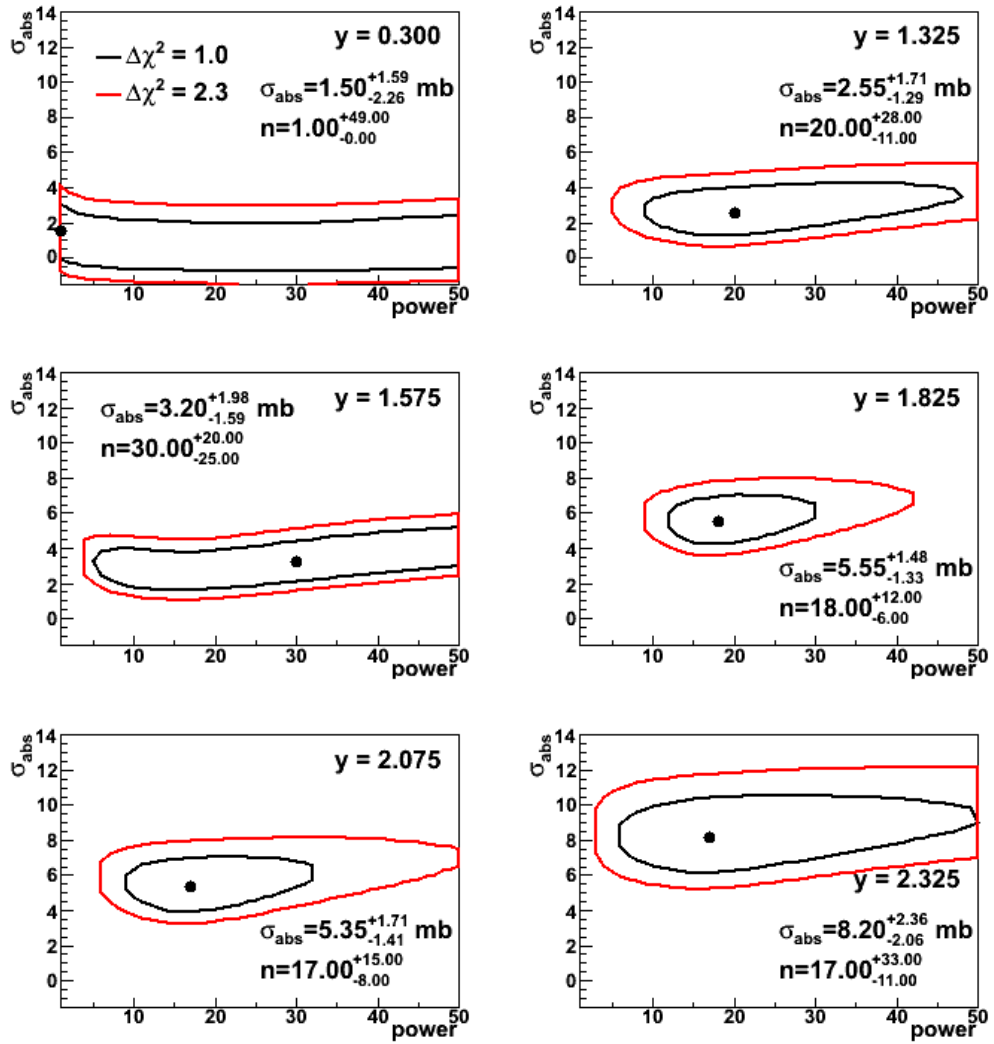


Figure 8.5: The $\bar{\chi}^2$ contours for $y > 0$ where σ_{abs} and n are optimized separately at each rapidity. [90]

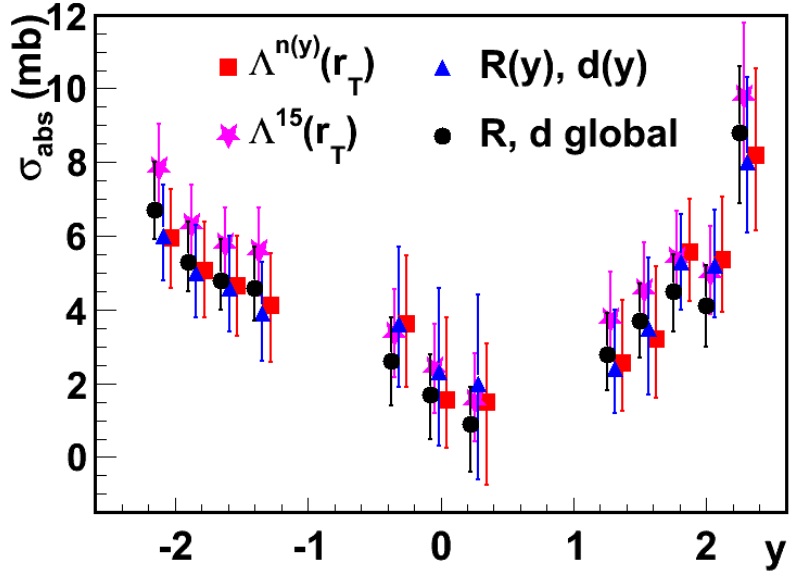


Figure 8.6: The optimum values and uncertainties on σ_{abs} as a function of rapidity obtained from the fits described in Section 8.3 and Section 8.4. For clarification purposes the individual fits at each rapidity are slightly offset. [90]

As shown in the $\bar{\chi}^2$ contours in Figures 8.4 and 8.5, the data are all consistent with a constant $n \geq 5$ across all rapidity. Therefore, the fit was repeated assuming a constant value of n with rapidity. In this case, those systematic uncertainties which were correlated with rapidity were accounted for correctly. The optimum power was found to be $n = 15^{+5}_{-4}$ with an overall $\bar{\chi}^2/dof = 1.94$. The values of σ_{abs} and their uncertainties extracted in this case are shown in Figure 8.6, where they are compared with those extracted with the independent fits at each rapidity. Good agreement within the uncertainties is seen between the two cases, although the optimum values of σ_{abs} tend to be larger for the fit using a constant n at backward rapidity. The r_T dependence of the gluon modification for $n = 15$ at each rapidity is shown in Figure 8.7, showing a modification which is negligible for large r_T , but which turns on sharply for $r_T \lesssim 3$ fm.

8.4 Nuclear Shadowing Parametrization 2

The negligible shadowing at large r_T , coupled with a sharp turn-on for $r_T \lesssim 3$ fm, that was found using the $\Lambda^n(r_T)$ case in Section 8.3 suggests that the use of a step function dependence on r_T , including a radius R and diffuseness d ,

$$M_{\text{shad}} = 1 - \left(\frac{1 - R_g(x_2, Q^2)}{a(R, d)} \right) / \left(1 + e^{(r_T - R)/d} \right), \quad (8.14)$$

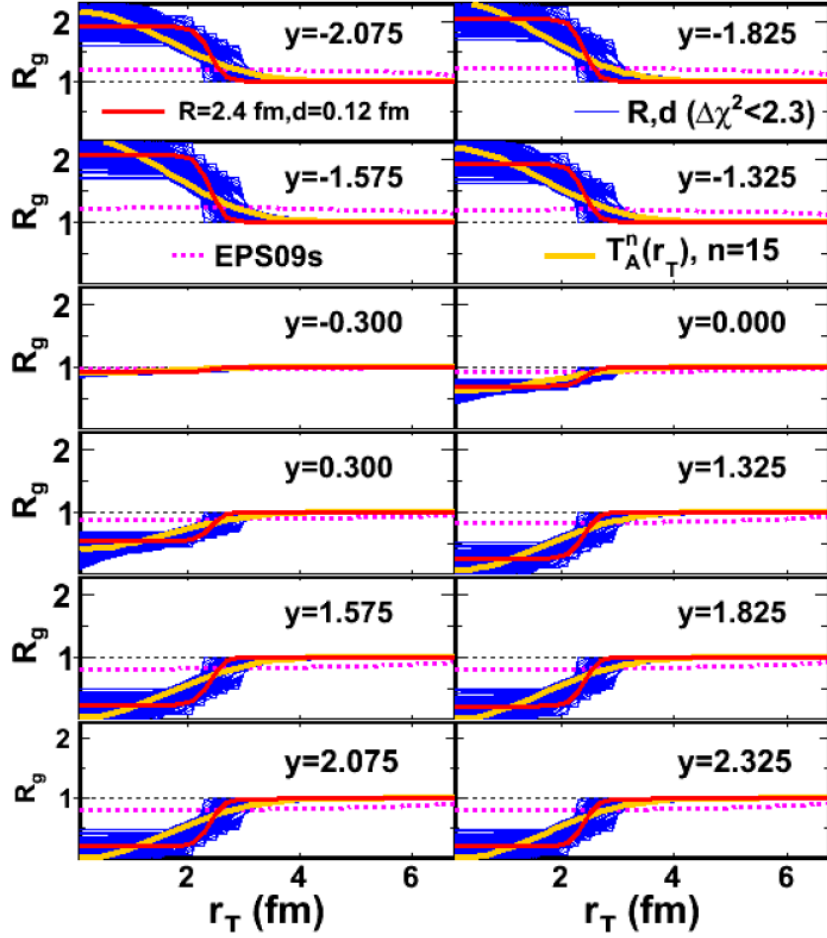


Figure 8.7: The gluon modification as a function of r_T for the best fit R and d parameters (solid red line), along with the modifications from all combinations of R and d within $\Delta\chi^2 = 2.3$ (thin blue lines). The modification from the best fit global analysis of $\Lambda^n(r_T)$ ($n = 15$) is shown by the solid orange line. The impact parameter dependence of the recently released EPS09s is given by the dashed magenta line [74]. [90]

may be more appropriate. As in Equation 8.10, $a(R, d)$ is a normalization which is adjusted so that the modification integrated over all collisions equals the EPS09 value for the given x_2 and Q^2 .

Fits to the data were first performed independently at each rapidity to compare with the results extracted in Section 8.3. The optimum σ_{abs} values and their uncertainties are shown in Figure 8.6, and are in good agreement with those extracted under the $\Lambda^n(r_T)$ dependence. The fits favored values of $R \lesssim 3.5$ fm, consistent with roughly half the Au radius. The fits were relatively insensitive to the value of d , although small values were favored.

Finally, as in the $\Lambda^n(r_T)$ case, we fitted the data using global values of R and d . As before, when fitting global values of R and d the correlations in the systematic uncertainties are taken into account correctly. The fits are compared to the data as a function of r_T in Figure 8.8, where the dashed curves indicate the extracted uncertainties on σ_{abs} only. It should be noted that, as the global scale uncertainty is included in the fitting, the best $\bar{\chi}^2$ value may be obtained by a slight vertical shift in the data, and hence the calculations may be slightly offset from the data points. An overall $\bar{\chi}^2/dof = 1.96$ was observed. Good agreement between the fits and the data is seen at all rapidities within the systematic uncertainties. The optimum values of σ_{abs} are shown in Figure 8.6 as the black circles.

The 2D $\bar{\chi}^2$ contours in R vs d , where R and d are fitted globally, are shown in Figure 8.9. The optimum values are found to be $R = 2.40^{+0.53}_{-0.83}$ and $d = 0.12^{+0.52}_{-0.10}$, where the uncertainties are derived from the maximum extent of the $\Delta\bar{\chi}^2 = 1.0$ contour.

8.5 Discussion

The gluon modification as a function of r_T using Equation 8.14 and globally fitted values of R and d is shown as the solid red line in Figure 8.7. The uncertainty in the r_T distribution due to the uncertainty in R and d can be visualized by plotting the curves for all parameter combinations that lie within the $\Delta\bar{\chi}^2 = 2.3$ contour [96]. These curves are shown as the thin blue lines in Figure 8.7. At all rapidities the modification is only significant for $r_T \lesssim 3$ fm, indicating that the data places strong constraints on the centrality dependence of the nuclear shadowing. Comparing with the r_T dependence for $\Lambda^{15}(r_T)$ in Figure 8.7 shows that while the details of the modification are different, the overall trend of significant modification only for $r_T \lesssim 3$ fm remains. This indicates that, while the data require strong shadowing only for small r_T , the detailed shape of the turn-on is not well constrained. This is likely due to the large overlap in the r_T distributions probed by the PHENIX centrality bins, as shown in Figure 7.16.

The recently released EPS09s [74] provides an impact parameter dependence of the gluon modification found in EPS09. This is plotted in Figure 8.7 as the dashed magenta line, for comparison to the present results. EPS09s is found to have a much weaker dependence on r_T than that extracted here, with significant modification out to $r_T \approx 6$ fm. The impact parameter dependence of EPS09s was determined by fitting the target mass dependence of the EPS09 parametrization, assuming that the shadowing is a power series in $\Lambda(r_T)$. They found that powers up to $[\Lambda(r_T)]^4$ were necessary to describe the EPS09 results. This is a very different procedure than the one performed here, and on a broader body of data

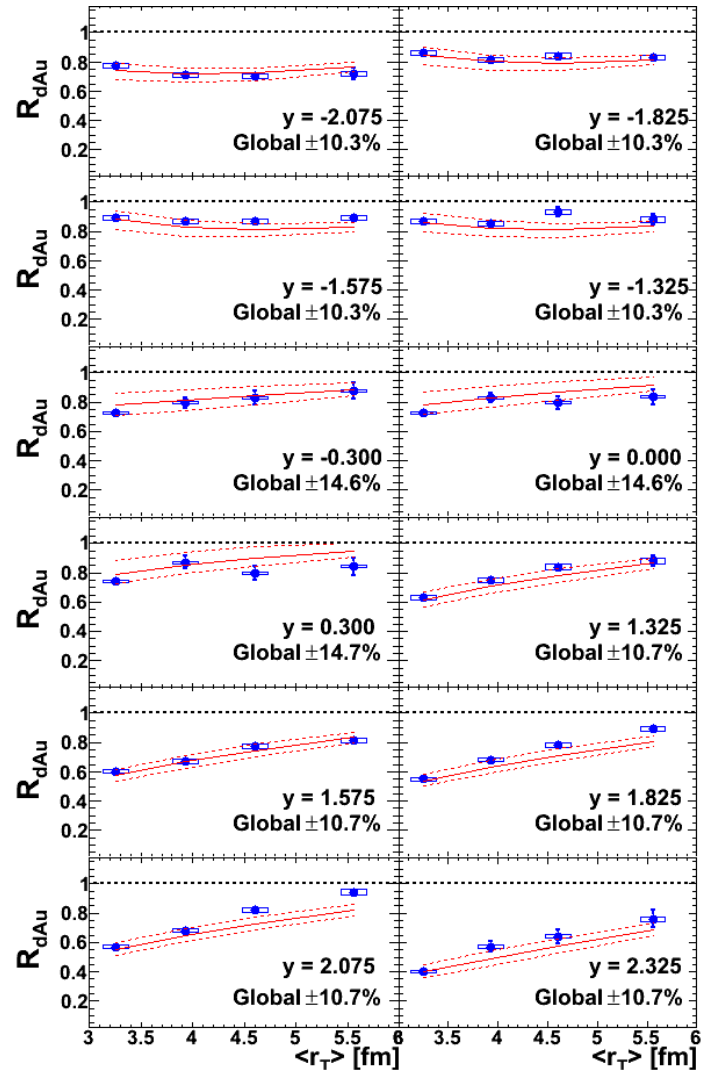


Figure 8.8: Comparison to the data of the fits using a global R and d in Equation 8.14. The dashed curves represent the uncertainty in σ_{abs} only.

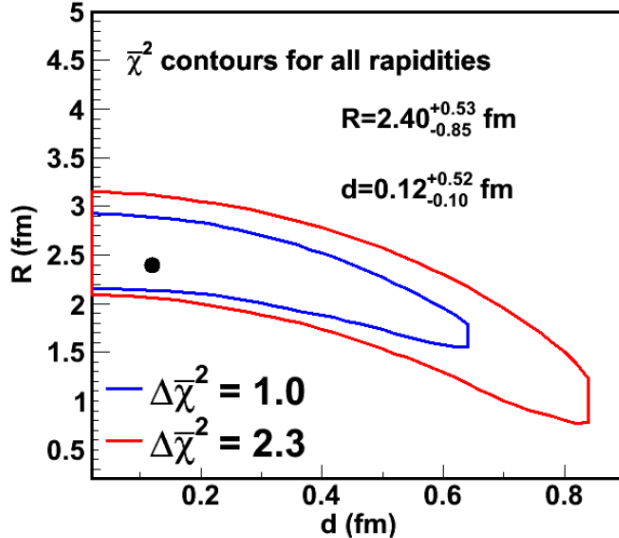


Figure 8.9: The $\bar{\chi}^2$ contours obtained from the global fits of R and d using Equation 8.14. [90]

primarily from lower energy collisions. Evidently, probing the internal structure of the nucleus, as is done here, is inherently different from studying the mass dependence of the average modification, or there are different physics effects in play at RHIC energies than at lower energies. A study of the target mass dependence of the J/ψ suppression at RHIC may be able to shed some light on this discrepancy.

The optimum values of σ_{abs} and their uncertainties extracted from all four of the fitting scenarios are compared in Figure 8.6. There is remarkable agreement between the different sets, indicating that the nuclear breakup can indeed be separated from the nuclear shadowing. The strongly nonlinear r_T dependence of the nuclear shadowing evidently provides a distinctly different modification than the exponential dependence of σ_{abs} on $\Lambda(r_T)$.

There is little theoretical guidance on the nuclear breakup effect, and so the values of σ_{abs} are frequently fitted to the data, as is done here. However, in [82], the authors use a saturated parametrization of the dipole cross section [71] to quantify the change in the J/ψ σ_{abs} with rapidity. Instead of extracting the values of σ_{abs} by directly fitting the data to be described, that theory uses a parametrization of lower energy data, along with a model of the $c\bar{c}$ dipole, to calculate the σ_{abs} at $\sqrt{s_{NN}} = 200$ GeV directly. The J/ψ σ_{abs} is calculated using

$$\sigma_{J/\psi}(r_T, x_2) = \sigma_0 \left(1 - e^{-r_T^2/r_0^2(x_2)}\right) \quad (8.15)$$

$$r_0(x_2) = 0.4 \text{ fm} \times (x_2/x_0)^{0.144} \quad (8.16)$$

$$x_2 = e^{-y} \sqrt{2\langle M_{J/\psi}^2 \rangle + \langle p_T^2 \rangle} / \sqrt{s} \quad (8.17)$$

where $\sigma_0 = 23.03$ mb, $x_0 = 3.04 \times 10^{-4}$, and $\langle p_T^2 \rangle = 4 \text{ GeV}^2$. The latter is in agreement with

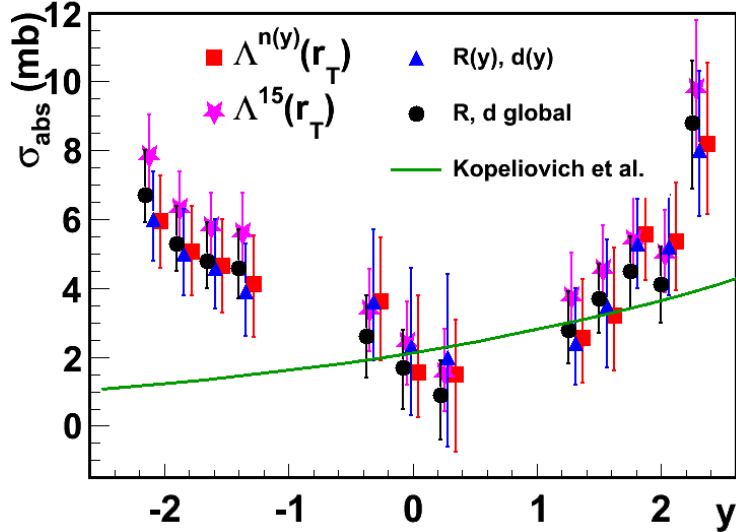


Figure 8.10: The optimum σ_{abs} values with 1 standard deviation uncertainties extracted using the thickness dependent modification compared with σ_{abs} values calculated using a saturated parametrization of the dipole cross section [82].

the measured PHENIX data [10]. The results of this calculation are compared in Figure 8.10 to the fitted σ_{abs} values found here. Good agreement is found between the fitted σ_{abs} values and the calculation at mid and forward rapidity, although the calculation does not show as rapid an increase in σ_{abs} at forward rapidity. At backward rapidity there is a large discrepancy. Where the calculations predict a decrease in σ_{abs} compared to midrapidity, an increase which mirrors that at forward rapidity is observed in the values extracted here. However, it should be noted that at backward rapidity the saturated parametrization may break down due to the longer formation time of the J/ψ in this kinematic region [82], and therefore the disagreement at backward rapidity may be because the model is outside its range of validity there.

The midrapidity σ_{abs} values extracted here are in good agreement with a systematic study of lower energy results. In [87] the authors fitted data on J/ψ production in $p + A$ collisions at lower energies using various NPDF sets plus a breakup cross section. The energy dependence of the σ_{abs} values extracted using the EKS98 NPDF, which has similar shadowing modification to EPS09, is shown in Figure 3.11, along with an exponential fit to the available data. There is a very strong energy dependence in Figure 3.11 which predicts $\sigma_{abs} \approx 2$ mb at midrapidity for RHIC energies, consistent with the values extracted here.

8.5.1 Comparison with the p_T dependence of R_{dAu}

Using this model, the p_T dependence of R_{dAu} can also be calculated and compared to the p_T dependence of the $J/\psi R_{dAu}$ presented in Section 7.2. This is essentially a prediction, as there is no information from the measured p_T dependence of $d+Au$ used in the calculation.

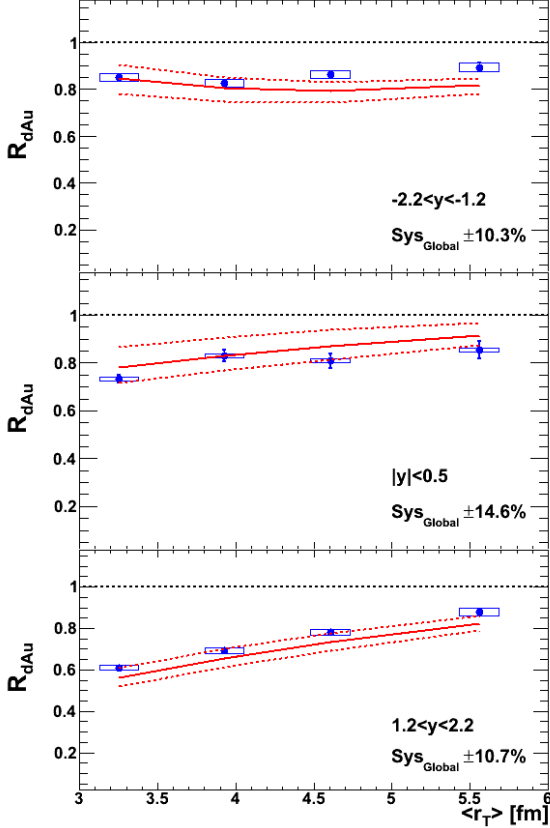


Figure 8.11: The $R_{d\text{Au}}$ values integrated over the rapidity acceptance of the three PHENIX spectrometers. The solid curves are obtained by combining the fits from the 12 rapidity bins as described in the text. The dashed curves show the uncertainty band arising from the fit uncertainties for the σ_{abs} values.

Since the parameters σ_{abs} and n (or R, a) are extracted from fits to p_T integrated data. The only p_T information taken from data is the $J/\psi p+p$ p_T distribution, which itself contains none of the CNM effects of interest.

Before the p_T dependence of the modification from this model can be compared to the data, the model calculations must be integrated over the rapidity coverage of each of the PHENIX spectrometers, as was done in the data. Note that when calculating the p_T dependence of $R_{d\text{Au}}$ at forward rapidity, the rapidity coverage was truncated at $y = 2.2$, and does not include the $2.2 < y < 2.4$ information included in the rapidity dependent $R_{d\text{Au}}$. The calculations in the finer rapidity bins are combined by weighting the calculations at each rapidity bin by the measured J/ψ invariant yield times acceptance in $p+p$ collisions, measured in the same fine rapidity bins. This is tested by comparing the rapidity integrated calculations to the measured $J/\psi R_{d\text{Au}}$ as a function of $R_{d\text{Au}}$, also integrated over the rapidity coverage of each arm. This is shown in Figure 8.11 using the globally fitted values of R and d and the σ_{abs} values presented in Section 8.3. As expected, the agreement between

the calculations and data is comparable with the fits at the 12 rapidities.

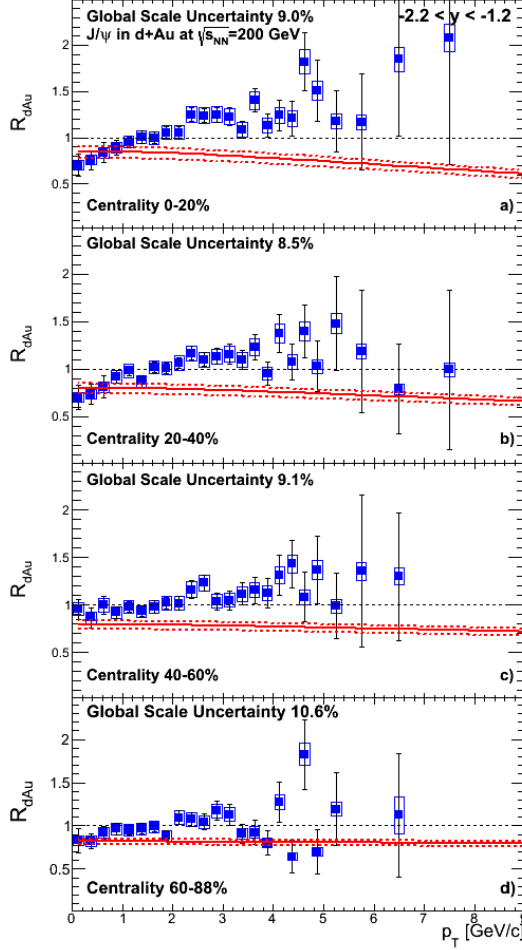


Figure 8.12: The $R_{d\text{Au}}$ versus p_T for backward rapidity, calculated from the best fits to the centrality dependence of the d+Au data in finer rapidity bins, as explained in the text.

The p_T dependent calculations are compared with the measured results for each centrality bin in Figure 8.12 at backward rapidity and in Figure 8.13 at mid and forward rapidities. At mid and forward rapidity the calculations describe the measured $R_{d\text{Au}}$ adequately well in each centrality bin. At backward rapidity, however, the calculations show a markedly different p_T dependence than is seen in the data. Where the measured $R_{d\text{Au}}$ increases with increasing p_T , the calculations decrease with increasing p_T .

It should be stressed that in the calculations here the p_T dependence comes entirely from the x and Q^2 dependence of EPS09. The σ_{abs} is assumed to be constant with p_T , and no other p_T dependent effect is introduced. This indicates that, as seen in the case of other theoretical calculations shown in Section 7.2.2, the x and Q^2 dependence of EPS09 alone can not explain the observed p_T dependence of the modification at backward rapidity.

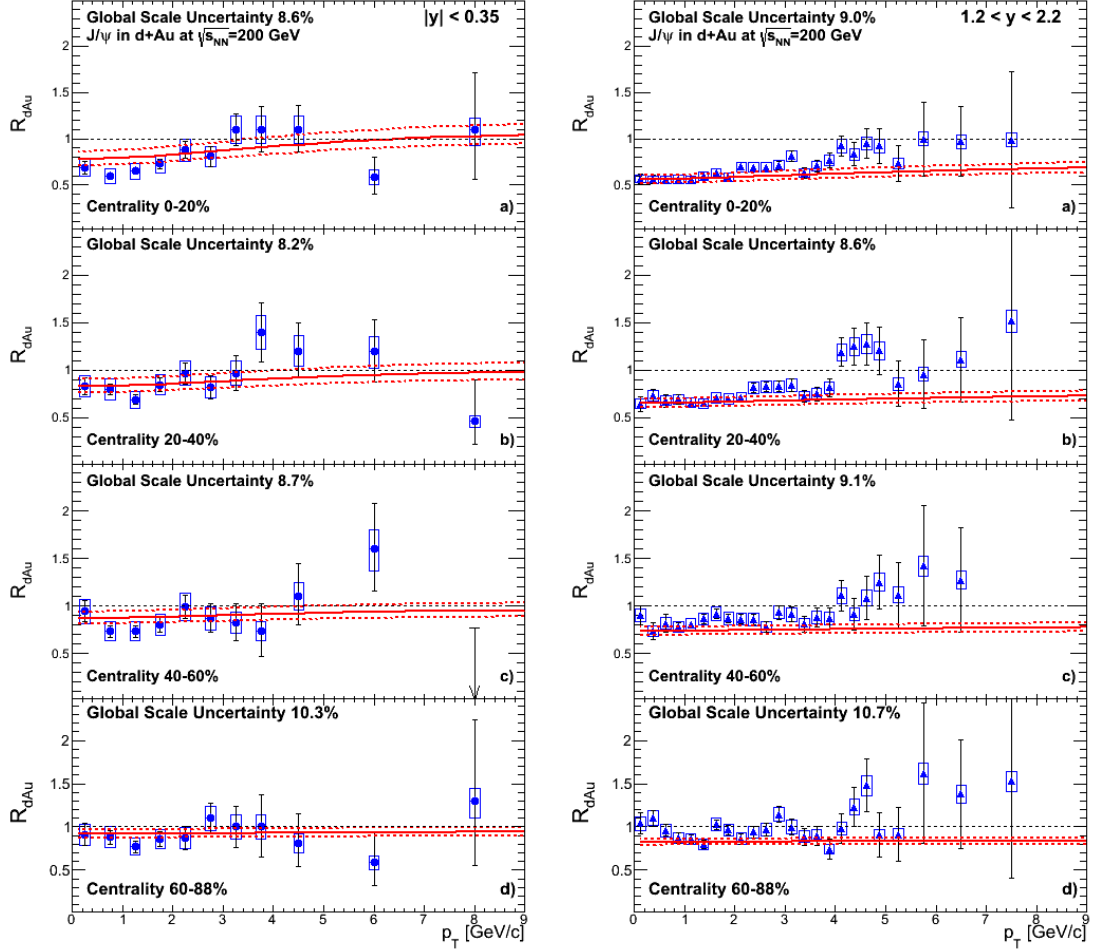


Figure 8.13: The $R_{d\text{Au}}$ versus p_T for midrapidity (Left), and forward rapidity (Right), calculated from the best fits to the centrality dependence of the d+Au data in finer rapidity bins, as explained in the text.

While there are other CNM effects not included in this model that could introduce further p_T dependent modification, such as the Cronin effect, it is not clear what would produce a large effect at backward rapidity, but only a small effect at mid and forward rapidities. It is also possible that σ_{abs} is p_T (and y) dependent. If σ_{abs} is dependent on the physical size of the meson, one would in fact expect it to be dependent on both p_T and rapidity. For instance, a high- p_T J/ψ (or $c\bar{c}$ precursor) should spend less time in the nucleus and therefore give a smaller cross section.

CHAPTER 9

CALCULATING THE CNM BASELINE IN AU+AU COLLISIONS

This chapter presents the results of calculating the J/ψ modification in Au+Au collisions at $\sqrt{s_{NN}} = 200$ GeV due to CNM effects based on the parametrization presented in Chapter 8. The CNM baseline is then used, in combination with the measured $J/\psi R_{AA}$ at the same energy, to calculate the effects of the produced medium on J/ψ production.

9.1 Modeling of $R_{AA}(CNM)$

After successfully describing the centrality dependence of the $J/\psi R_{dAu}$, and under the assumption that the CNM effects in each of the nuclei can be factorized, the CNM effects can now be calculated for Au+Au collisions. As in the $d+Au$ case, calculations of the nuclear modification due to cold nuclear matter effects in Au+Au, $R_{AA}(CNM)$, are performed within the Glauber framework.

The nucleon density distribution in each of the Au nuclei is described by a Woods-Saxon distribution, given by Equation 8.5, with $r_{WS} = 6.38$ fm and $d_{WS} = 0.54$ fm. In Au+Au collisions the PHENIX centrality is determined using the combination of charge collected in the north and south BBC. In this case the soft particle yield is simulated, for each participant nucleon (rather than each NN collision as in the $d+Au$ case), by choosing a random value from a NBD distribution, given by Equation 8.8, with parameters $\mu = 3.99$ and $\kappa = 1.4$, which were determined by PHENIX from fits of Equation 8.8 to BBC yields in Au+Au collisions, confined to higher multiplicities where the trigger efficiency is 100%. The total yield in the BBC's is summed over all participant nucleons in each event and used to assign the event to a centrality category, as in real data. The trigger efficiency was modeled using

$$\epsilon_{eff}^{Au+Au}(N_{hits}) = 1.0 - e^{-\left(\frac{N_{hits}-p_0}{p_1}\right)^{p_2}}, \quad (9.1)$$

with parameters $p_0 = 2.81$, $p_1 = 8.9$, and $p_2 = 0.82$. As in the $d+Au$ case, the BBC trigger efficiency is calculated from the ratio of the measured multiplicity distribution and the multiplicity distribution predicted by the fitted negative binomial distribution. The parameters used here are again chosen to match those used in the PHENIX calculation of $\langle N_{part} \rangle$ in each measured centrality bin.

To calculate $R_{AA}(CNM)$ we utilize the modification due to nuclear shadowing given by Equation 8.14, along with the globally fitted values of R and d , described in Section 8.4, and the corresponding σ_{abs} values. When calculating $R_{AA}(CNM)$, only the uncertainties on the values of σ_{abs} are considered. This amounts to choosing the optimum R and d values as the best model, and then using the corresponding σ_{abs} values and their uncertainties. The Au+Au data covers a range $1.2 < |y| < 2.2$, and therefore the fitted σ_{abs} value in the range $2.2 < y < 2.4$ is not included in the calculation of $R_{AA}(CNM)$.

Since the Au+Au system is symmetric, $R_{AA}(CNM)$ is identical at, for example $y = 1$ and $y = -1$. When calculating $R_{AA}(CNM)$, then, the modification at $y = 1.325$ is a product of the parametrization of the d +Au data at $y = 1.325$ and $y = -1.325$. At $y = 0$, the $R_{AA}(CNM)$ is simply a product of the d +Au parametrization with itself. The procedure for calculating the modification for each NN collision is

- Determine the location of the struck nucleon in nucleus 1 ($r_T(1), z_1(1)$) and nucleus 2 ($r_T(2), z_1(2)$).
- Calculate $\Lambda(r_T(1))$ and $\Lambda(r_T(2))$ from Equation 8.2.
- Calculate $\Lambda(z_1(1), r_T(1))$ and $\Lambda(z_1(2), r_T(2))$.
- For each rapidity ($y = 0.0, 0.3, 1.325, 1.575, 1.825$ and 2.075), and each p_T (0-15 GeV in 0.25 GeV wide steps)
 - Calculate Q^2 based on the center of the p_T bin from Equation 8.4
 - Use the fitted σ_{abs} values at $-y$, and the globally fitted values of R and d , for nucleon 1.
 - * Calculate $M_{br}(1)$ from Equation 8.1.
 - * Calculate $x(1)$ based on the center of the rapidity bin from Equation 8.3.
 - * Calculate $M_{shad}(1)$ from Equation 8.14
 - Use the fitted σ_{abs} values at $+y$, and the globally fitted values of R and d , for nucleon 2.
 - * Calculate $M_{br}(2)$ from Equation 8.1.
 - * Calculate $x(2)$ based on the center of the rapidity bin from Equation 8.3.
 - * Calculate $M_{shad}(2)$ from Equation 8.14.
 - The contribution to the modification from this NN collision at this y and p_T is $M_{br}(1)M_{shad}(1)M_{br}(2)M_{shad}(2)$.
 - This contribution to the modification is weighted by the measured $p+p$ yield at this y and this p_T .

The modification in each centrality bin is summed over all collisions and divided by the total N_{coll} .

The calculated $R_{AA}(CNM)$ from this method is shown in Figure 9.1. The uncertainties shown in Figure 9.1 are determined from the uncertainties on σ_{abs} (shown in Figure 8.6). The uncertainties in σ_{abs} at each rapidity are assumed to be uncorrelated, as the fits are performed separately at each rapidity. When calculating $R_{AA}(CNM)$, the σ_{abs} uncertainty

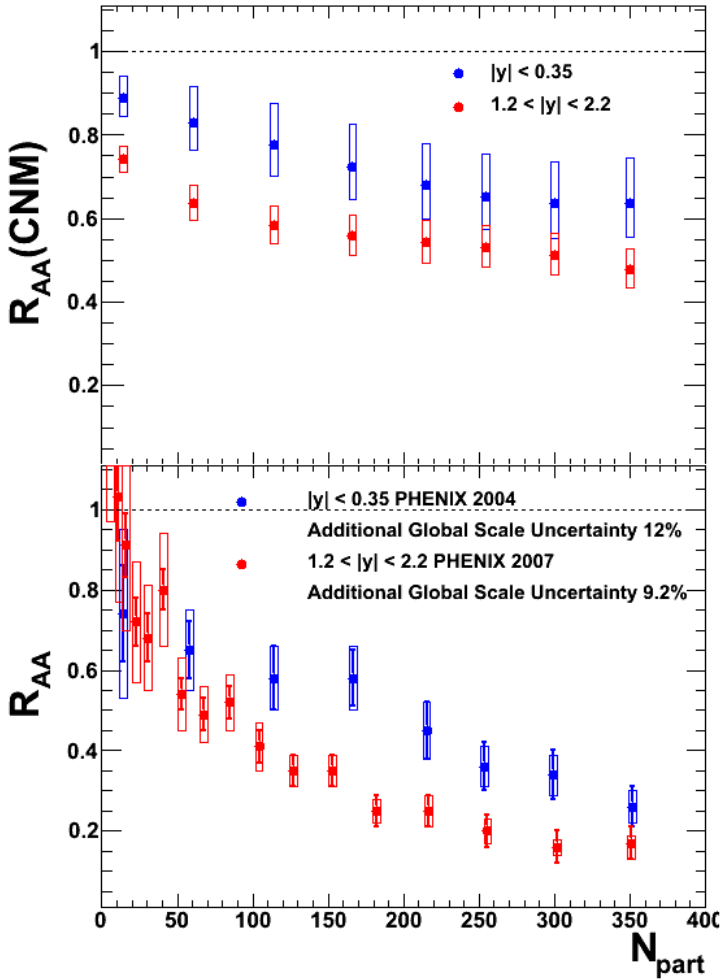


Figure 9.1: (Top) The calculated $R_{\text{AA}}(\text{CNM})$ for mid and forward rapidity, as described in the text. (Bottom) The measured $J/\psi R_{\text{AA}}$ at mid [11] and forward [21] rapidities in Au+Au collisions at $\sqrt{s_{NN}} = 200$ GeV.

distributions are sampled for each NN collision independently for both y and $-y$. At $y = 0$ the uncertainty on σ_{abs} is completely correlated with itself, and the sampled uncertainty is simply doubled. The widths of the resulting $R_{\text{AA}}(\text{CNM})$ distributions are taken as the uncertainty in $R_{\text{AA}}(\text{CNM})$. The $J/\psi R_{\text{AA}}$ measured by PHENIX in Au+Au collisions at $\sqrt{s_{NN}} = 200$ GeV [11, 21] is shown alongside the calculated $R_{\text{AA}}(\text{CNM})$ in Figure 9.1. It is clear that CNM effects play an important role on J/ψ production in Au+Au collisions.

The CNM effects in Au+Au collisions are found to be larger at $1.2 < |y| < 2.2$ than at $|y| < 0.35$. To investigate the origin of this difference, the contributions to $R_{\text{AA}}(\text{CNM})$ due to nuclear shadowing and nuclear breakup are shown separately in Figure 9.2. Evidently the large shadowing present at forward rapidity in $d+\text{Au}$ cancels with the anti-shadowing

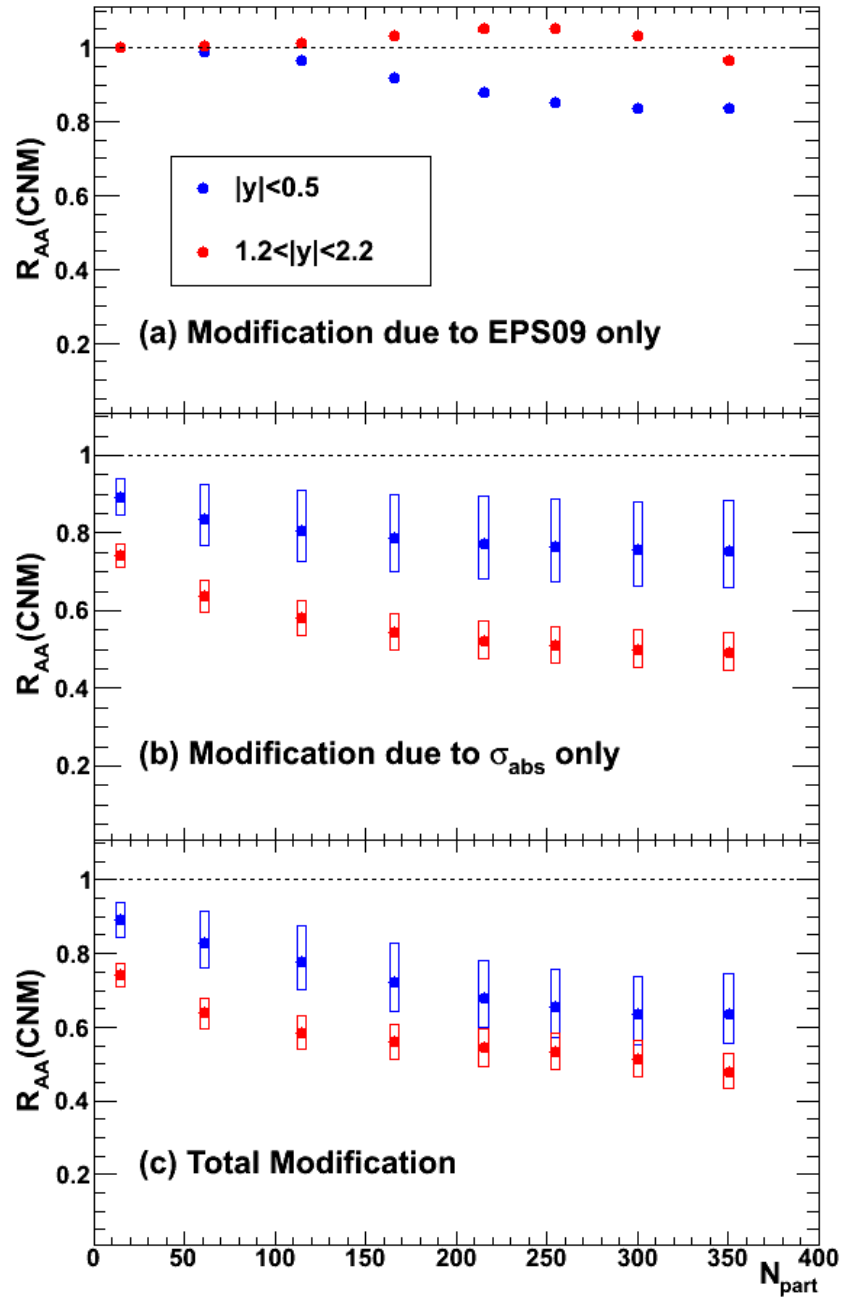


Figure 9.2: The calculated J/ψ $R_{AA}(\text{CNM})$ considering nuclear shadowing only (a), nuclear breakup only (b), and the combination of the two effects (c).

present at backward rapidity, yielding only a small overall effect in the $R_{AA}(CNM)$. At midrapidity, however, the relatively small shadowing is folded with itself, giving an $R_{AA}(CNM) \approx 0.85$ for central collisions. It is clear from Figure 9.2, that the largest contribution to $R_{AA}(CNM)$ comes from nuclear breakup. The large values of σ_{abs} at both forward and backward rapidity yield a large effect on the forward rapidity $R_{AA}(CNM)$, giving $R_{AA}(CNM) \approx 0.5$. The smaller values of σ_{abs} extracted at midrapidity lead to a significantly smaller contribution to the midrapidity $R_{AA}(CNM)$ of ≈ 0.75 for the most central collisions. The larger uncertainties on the σ_{abs} values fitted to the midrapidity data, as well as the fact that the uncertainty is doubled at $y = 0$, also yield a significantly larger uncertainty on the midrapidity $R_{AA}(CNM)$ compared to the forward rapidity.

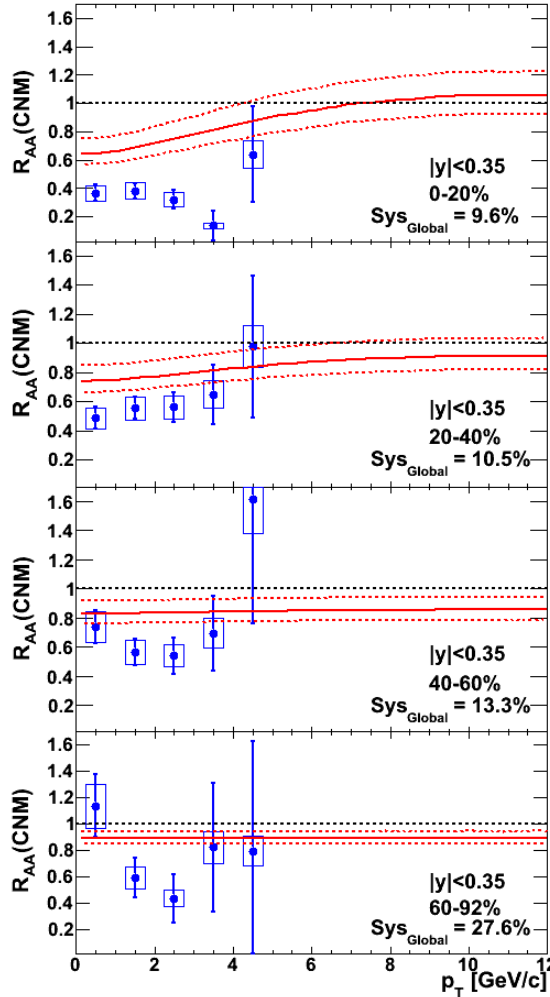


Figure 9.3: Comparison of the p_T dependence of $R_{AA}(CNM)$ calculated using Equation 8.14 with the measured R_{AA} [11] at midrapidity.

As in the $d+Au$ case, the p_T dependence of $R_{AA}(CNM)$ is also calculated. This is shown for $|y| < 0.35$ in Figure 9.3. The inability of the calculations to describe the measured R_{dAu}

at backward rapidity makes a similar calculation at $1.2 < |y| < 2.2$ unreliable, and therefore it is not shown here.

9.2 Hot Nuclear Matter Effects

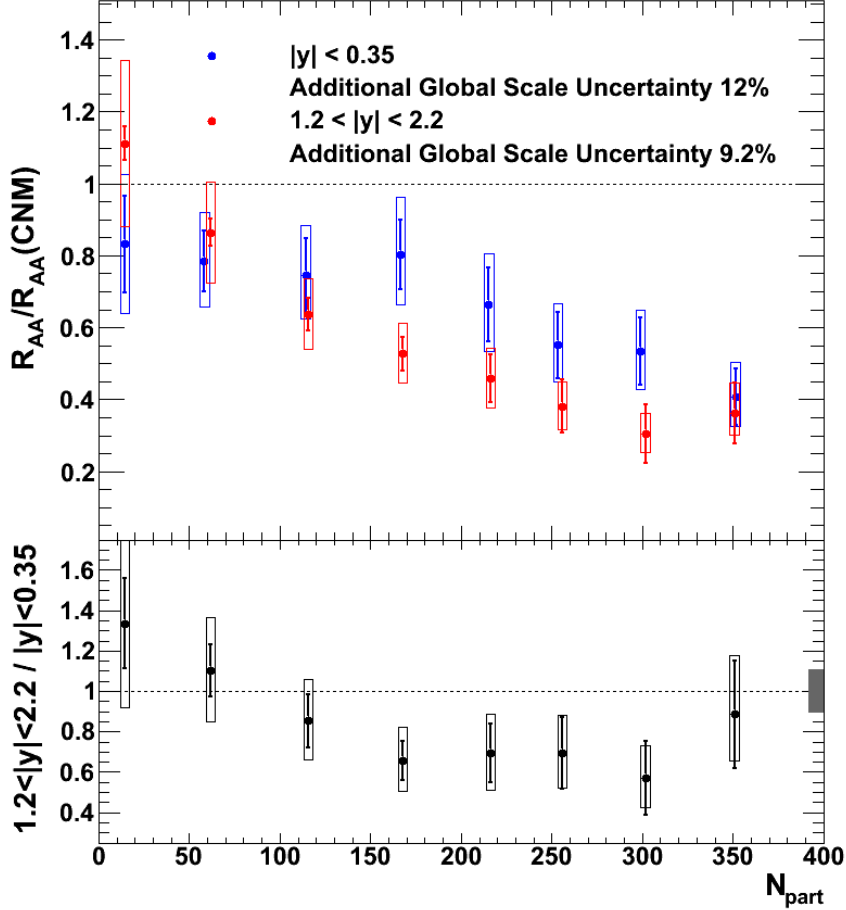


Figure 9.4: (Top) The experimental R_{AA} vs centrality divided by the calculated $R_{\text{AA}}(\text{CNM})$. To the extent that CNM effects can be factorized from hot matter effects, the modifications shown in this plot should show the effects of hot nuclear matter on J/ψ production. (Bottom) The ratio of $R_{\text{AA}}/R_{\text{AA}}(\text{CNM})$ at forward to mid rapidity, where the Type C systematic uncertainty on the ratio is represented by a box at $y = 1$.

The measured R_{AA} can be divided by the calculated $R_{\text{AA}}(\text{CNM})$. The measured R_{AA} divided by the calculated $R_{\text{AA}}(\text{CNM})$, $R_{\text{AA}}/R_{\text{AA}}(\text{CNM})$, is shown in Figure 9.4. The uncertainty boxes shown in Figure 9.4 represent the combined uncertainties of the measured R_{AA} and calculated $R_{\text{AA}}(\text{CNM})$. The uncertainty on N_{part} in the measured R_{AA} has been removed, following the same argument as for the removal of the N_{coll} uncertainties when fitting the $R_{d\text{Au}}$.

Under the assumption that the CNM effects can be factorized from the effects of the produced medium, Figure 9.4 shows the effects of hot nuclear matter (HNM) at RHIC.

Suppression of J/ψ production in Au+Au collisions beyond that expected from CNM effects is observed, indicating that J/ψ production is indeed suppressed due to the produced medium. For central collisions the value of $R_{AA}/R_{AA}(CNM)$ at $|y| < 0.35$ is ≈ 0.42 , and at $1.2 < |y| < 2.2$ is ≈ 0.35 with strongly overlapping uncertainties. This represents a factor of ≈ 2 reduction in the suppression at forward rapidity, and a reduction of $\approx 40\%$ in the suppression at midrapidity, compared to the uncorrected R_{AA} . However, even considering the larger CNM effects at forward rapidity, the HNM effects still tend to be larger at forward rapidity than midrapidity, as seen in the ratio of the $1.2 < |y| < 2.2$ results to the $|y| < 0.35$ results shown in Figure 9.4. This remains a puzzle, as arguments based on the energy density predict a larger suppression at midrapidity than at forward rapidity.

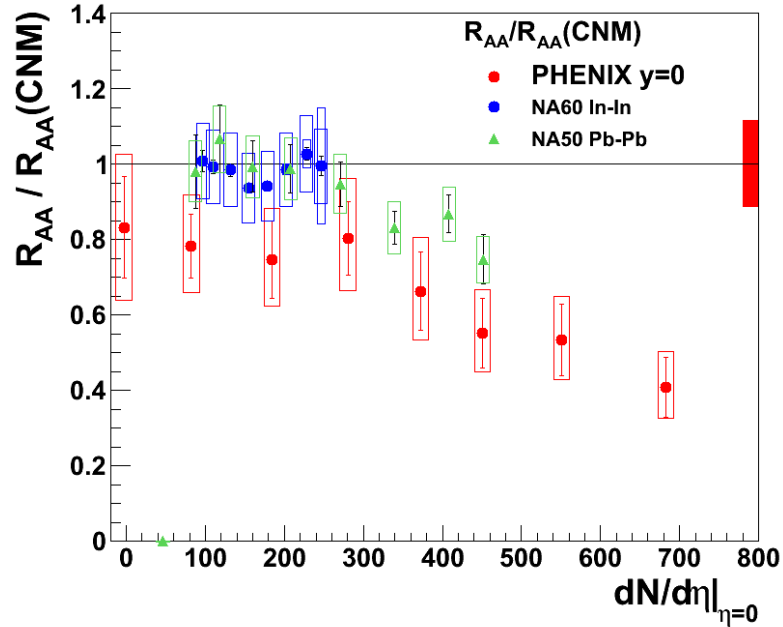


Figure 9.5: A comparison of the calculate $R_{AA}/R_{AA}(CNM)$ for $y = 0$ at RHIC and the SPS [51] as a function of the particle production. The global scale uncertainty on the $y = 0$ RHIC calculation is represented by the red box at $R_{AA}/R_{AA}(CNM) = 1$.

The HNM effects have also been extracted from SPS In+In and Pb+Pb collisions at $\sqrt{s_{NN}} = 17$ GeV and $y = 0$, as discussed briefly in Section 3.4. These are compared with the HNM effects at RHIC at $y = 0$ in Figure 9.5 as a function of $\frac{dN}{d\eta}|_{y=0}$, which gives a measure of the energy produced in the collision. The HNM effects at RHIC are consistent within uncertainties with those at the SPS over the region of overlap, although the RHIC results are systematically lower. Suppression of J/ψ production is seen for $\frac{dN}{d\eta}|_{y=0} > 300$ at the SPS, a picture which is consistent with the RHIC results. J/ψ suppression is found to be a factor of ~ 2 greater at the higher energy densities of RHIC. Therefore, correcting the measured

J/ψ suppression in $A + A$ collisions at both the SPS and RHIC results in a relatively simple picture, solving the puzzle presented by the measured R_{AA} alone. Suppression of J/ψ production due a produced medium is observed for $\frac{dN}{d\eta}|_{y=0} > 300$, and the suppression increases with increasing energy density. This is the behavior expected from the production of a QGP above some critical energy density.

The p_T dependence of $R_{AA}/R_{AA}(CNM)$ at $|y| < 0.35$ is not calculated, as the uncertainties in the measured R_{AA} are large, and the shape of the p_T distribution ill defined. However, from the $R_{AA}(CNM)$ overlayed with the measured R_{AA} at $|y| < 0.35$ in Figure 9.3, the measured R_{AA} shows greater suppression than $R_{AA}(CNM)$ at low p_T for central and mid-central collisions. The R_{AA} and $R_{AA}(CNM)$ show similar levels of suppression for $p_T > 4 \text{ GeV}/c$. This could indicate that there is little modification due to hot nuclear matter effects at high- p_T , however the current uncertainties on the measured R_{AA} make any strong conclusions difficult.

CHAPTER 10

SUMMARY AND OUTLOOK

This dissertation described the analysis of $J/\psi \rightarrow e^+e^-$ and $\psi' \rightarrow e^+e^-$ production in $d+\text{Au}$ collisions at $\sqrt{s_{NN}} = 200$ GeV, including the calculation of the nuclear modification factor, $R_{d\text{Au}}$. It was found that both J/ψ and ψ' production is suppressed in $d+\text{Au}$ relative to $p+p$ collisions, with ψ' production being suppressed in central collisions by a factor of ~ 5 , where the J/ψ is suppressed by only $\sim 25\%$. It was also found that J/ψ production is suppressed more at low- p_T than high- p_T , with the $J/\psi R_{d\text{Au}}$ being consistent with 1 for $p_T > 4$ GeV/ c .

The $J/\psi R_{d\text{Au}}$ at midrapidity was compared to that measured at backward and forward rapidities in the same data sample. It was found that J/ψ suppression is greatest at forward rapidity and weakest at backward rapidity, and greater in central collisions than in peripheral collisions. It was also found that while the mid and forward rapidity p_T dependence of $R_{d\text{Au}}$ have a similar shape, the backward rapidity exhibits a more rapid increase in $R_{d\text{Au}}$ with increasing p_T , and is consistent with $R_{d\text{Au}} > 1$ for $p_T > 2$ GeV/ c . This difference in the p_T shape of the $R_{d\text{Au}}$ is unexplained by current theoretical models.

A parametrization of the measured $J/\psi R_{d\text{Au}}$ was presented, in which the magnitude of σ_{abs} and the r_T dependence of nuclear shadowing were fitted to the data. This was prompted by evidence that a linear or quadratic dependence on the nuclear thickness could not describe the forward rapidity $J/\psi R_{d\text{Au}}$. We found that the data requires a modification due to nuclear shadowing which is large for $r_T \lesssim 3$ fm, and negligible beyond that. This may be the first direct evidence of the ‘hot spots’ suggested to exist in a saturated medium of high gluon density. It was found that the nuclear breakup was well separated from nuclear shadowing due to the difference in the r_T dependence of the two effects. The fitted values of σ_{abs} were found have a minimum at midrapidity, where $\sigma_{abs} \approx 2$ mb, and then increase to > 6 mb when moving to either backward or forward rapidity.

The parametrization of the $J/\psi R_{d\text{Au}}$ was then used to calculate the CNM effects on J/ψ production in $\text{Au}+\text{Au}$ collisions at the same energy. The suppression of J/ψ production in $\text{Au}+\text{Au}$ collisions due to CNM effects was found to be greater at forward rapidity than at midrapidity. Under the assumption that the CNM effects can be factorized from those due to the formation of a QGP, the CNM effects were removed from the measured modification of J/ψ production in $\text{Au}+\text{Au}$ collisions. It was found that a J/ψ suppression of $\sim 40\%$ remains beyond that expected from CNM effects.

While we now have a reasonably complete picture of inclusive J/ψ production at $\sqrt{s_{NN}} = 200$ GeV, there is still much to be learned. The larger suppression of ψ' production in $d+\text{Au}$ collisions came as a surprise, given the results of measurements made at lower energies, and it appears to explain much of the observed centrality dependence of the inclusive J/ψ production. Precise measurements of χ_c production in $p+p$ and $d+\text{Au}$ collisions at the same energy are necessary to fully understand the CNM effects on the charmonia mesons.

Data on $p+\text{Pb}$ collisions at $\sqrt{s_{NN}} = 2.76$ TeV are scheduled to be taken at the LHC in early 2013. This will open up a whole new and interesting energy regime in which to study CNM effects, and is an important step towards understanding the \sqrt{s} dependence of QGP effects. It will be interesting to see if the new observations about CNM effects found at $\sqrt{s_{NN}} = 200$ GeV are also seen at the higher energies of the LHC.

APPENDIX A

CALIBRATION OF THE EMCAL TRACK MATCHING VARIABLES

A.1 emcsdphi_e

The mean and width (σ) of the emcdphi distribution is a function of both p_T and z , where z is the direction along the beam axis measured from the center of the interaction region. The variable emcsdphi_e is created to remove this dependence, providing a variable independent of p_T and z on which to cut.

The calibration of emcsdphi_e is performed independently for each EMCAL sector, and both $\alpha < 0$ and $\alpha > 0$, where α is the bend angle of the track. For each momentum bin, 0.4-0.5, 0.5-0.6, 0.6-0.7, 0.7-0.8, 0.8-0.9, 0.9-1.0, 1.0-1.25, 1.25-1.5, 1.5-2.0, 2.0-3.5, 3.5-10 [GeV/c²], and each z bin, -80→-60, -60→-40, -40→-20, -20→0, 0→20, 20→40, 40→60, 60→80 [cm], the emcsdphi distribution is fit with a gaussian in the range -0.01 to 0.01 cm to determine the mean and σ . The z dependence of the mean and σ values are then fitted using a function of the form

$$f(z) = p_0^z + p_1^z * z + p_2^z * z^2. \quad (\text{A.1})$$

An example fit for EMCAL sector 1 and $\alpha > 0$ is shown in Figures A.1 and A.2 for z dependence fits of the mean and σ of the emcdphi distributions respectively. The p_T dependence of the fit parameters, p_0^z , p_1^z , and p_2^z are then fitted with a function of the form

$$f(p_T) = p_0^{p_T} + \frac{p_1^{p_T}}{p_T} + \frac{p_2^{p_T}}{p_T^2}. \quad (\text{A.2})$$

An example fit to the p_T dependence of the parameters p_0^z , p_1^z , and p_2^z is shown in Figure A.3 for sector 1 $\alpha < 0$.

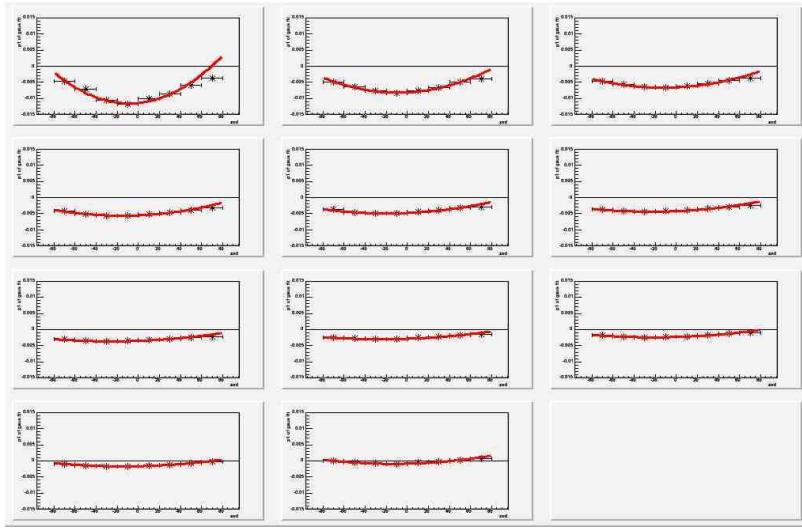


Figure A.1: Fits of the mean values of emcdphi as a function of zed for EMCal sector 1 $\alpha > 0$.

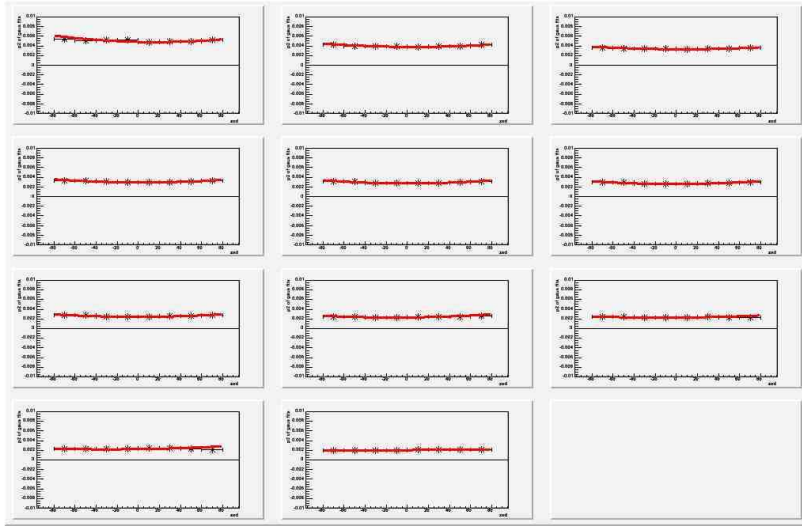


Figure A.2: Fits of the σ values of emcdphi as a function of zed for EMCal sector 1 $\alpha < 0$.

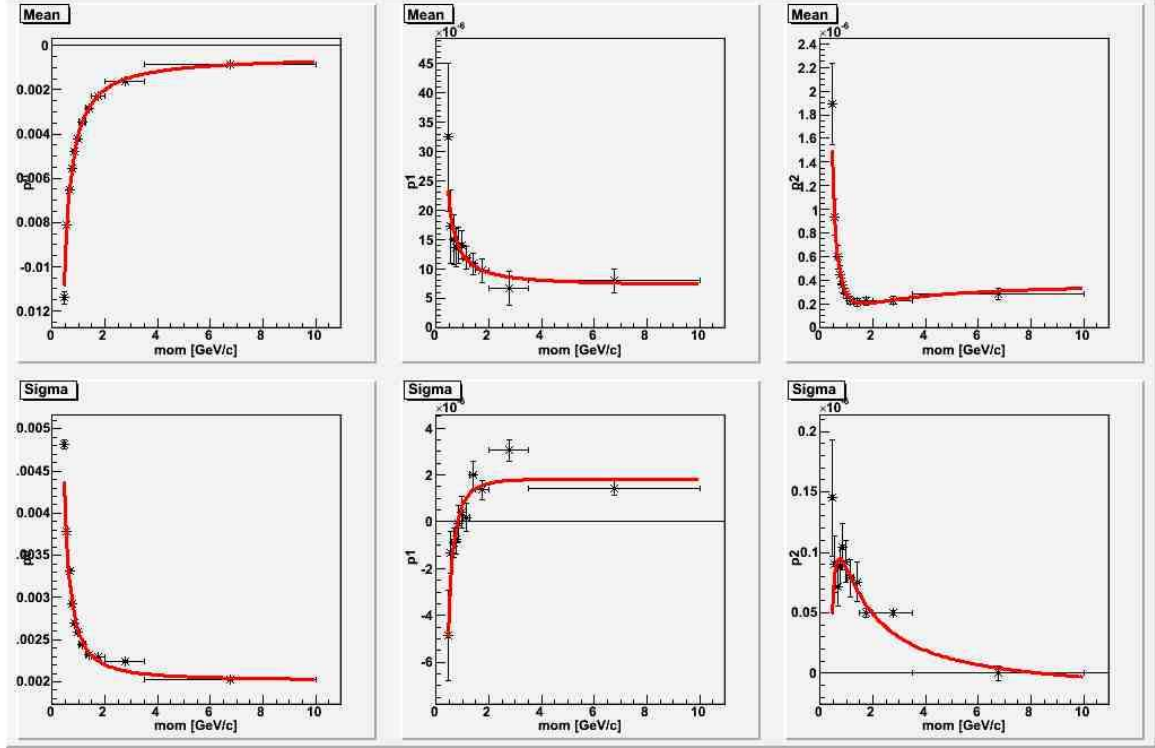


Figure A.3: Fits to the p_T dependence of the mean and σ parameters of emcdphi for EMCal sector 1 $\alpha < 0$.

The variable emcsdphi_e was then calculated using

$$emcsdphi_e = \frac{emcdphi - offset}{sigma} \quad (A.3)$$

$$offset = m0 + m1 * zed + m2 * zed^2 \quad (A.4)$$

$$sigma = s0 + s1 * zed + s2 * zed^2 \quad (A.5)$$

$$m0 = \left(p0_{m0} + \frac{p1_{m0}}{p_T} + \frac{p2_{m0}}{p_T^2} \right) \quad (A.6)$$

$$m1 = \left(p0_{m1} + \frac{p1_{m1}}{p_T} + \frac{p2_{m1}}{p_T^2} \right) \quad (A.7)$$

$$m2 = \left(p0_{m2} + \frac{p1_{m2}}{p_T} + \frac{p2_{m2}}{p_T^2} \right) \quad (A.8)$$

$$s0 = \left(p0_{s0} + \frac{p1_{s0}}{p_T} + \frac{p2_{s0}}{p_T^2} \right) \quad (A.9)$$

$$s1 = \left(p0_{s1} + \frac{p1_{s1}}{p_T} + \frac{p2_{s1}}{p_T^2} \right) \quad (A.10)$$

$$s2 = \left(p0_{s2} + \frac{p1_{s2}}{p_T} + \frac{p2_{s2}}{p_T^2} \right), \quad (A.11)$$

$$(A.12)$$

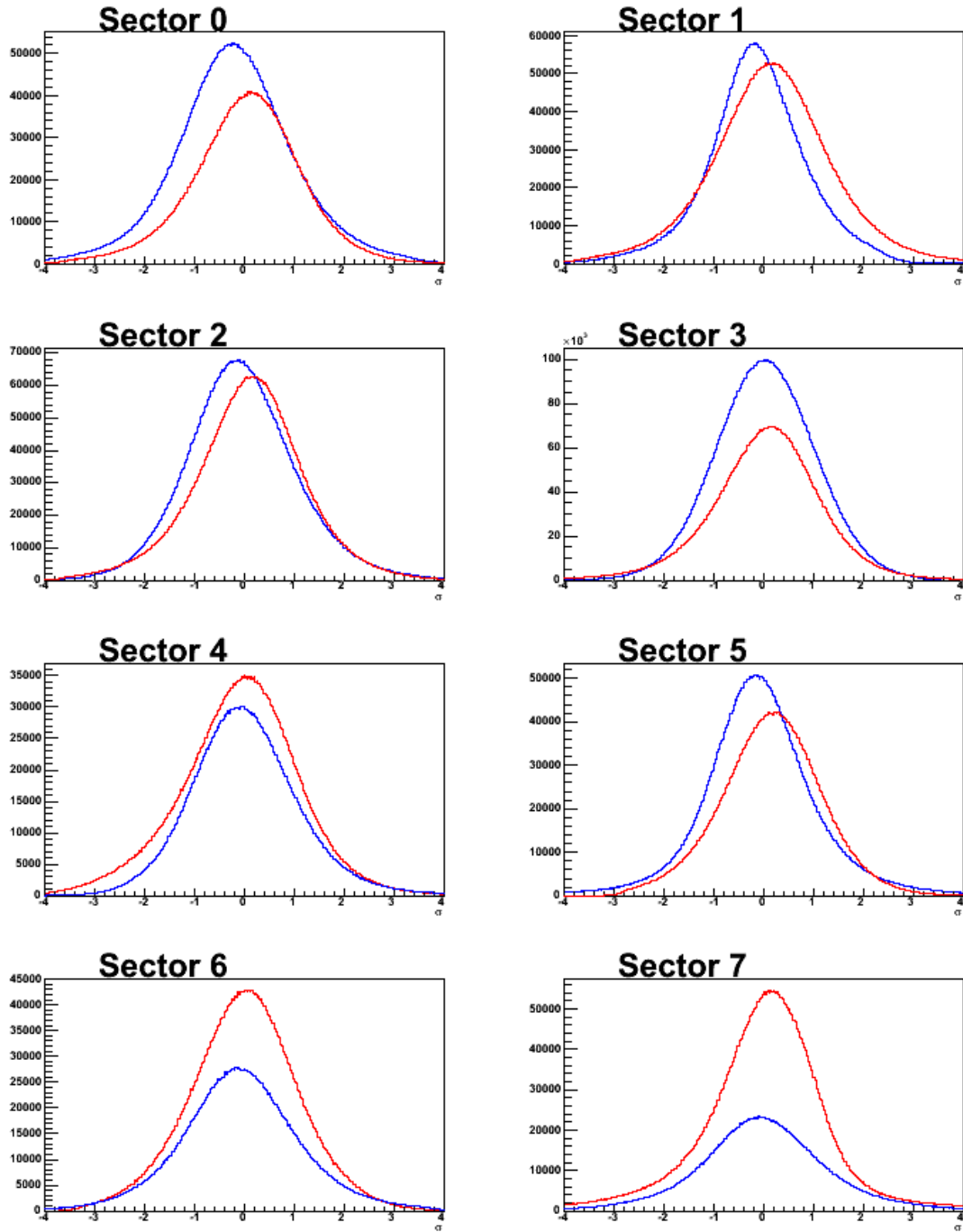


Figure A.4: Recalibrated emcsdphi_e for each sector of the EMCal (blue is $\alpha < 0$ & red is $\alpha > 0$)

The corrected emcsdphi_e distributions for each EMCal sector and alpha are shown in Figure A.4. The mean and sigma values of these distributions are shown in Figure A.5.

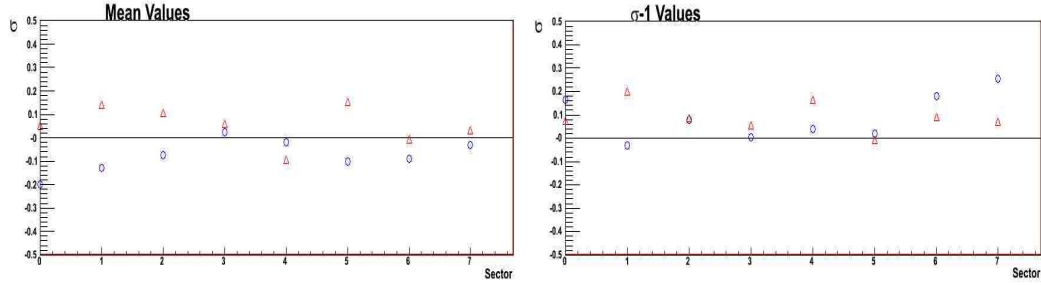


Figure A.5: Mean (Left) and σ (Right) values for the emcsdphi_e distributions (blue is $\alpha < 0$ & red is $\alpha > 0$)

All mean and sigma values are within $\pm 0.2\sigma$ of the expected values. The recalibration parameters are shown in table A.1.

Table A.1: emcsdphi_e recalibration parameters.

| EMCal sector | alpha | i | $p0_{mi}$ | $p1_{mi}$ | $p2_{mi}$ | $p0_{si}$ | $p1_{si}$ | $p2_{si}$ |
|--------------|-------|---|--------------|--------------|---------------|--------------|--------------|--------------|
| 0 | 0 | 0 | 0.00243869 | 0.00185262 | 0.00151157 | 0.00197905 | -0.000267599 | 0.000734629 |
| 0 | 0 | 1 | -4.70723e-06 | 1.15539e-05 | -4.90151e-06 | -1e-06 | -3.47198e-06 | 1.6902e-06 |
| 0 | 0 | 2 | -3.99855e-07 | 6.68123e-07 | -5.58297e-07 | -1.36847e-07 | 2.57251e-07 | -1.20863e-07 |
| 1 | 0 | 0 | 0.00389138 | 0.00238136 | 0.000884076 | 0.00248711 | -0.00162418 | 0.00165942 |
| 1 | 0 | 1 | 5.42116e-06 | 2.1413e-22 | -2.65492e-06 | 4.94535e-07 | 7.86977e-06 | -4.51963e-06 |
| 1 | 0 | 2 | -4.26098e-07 | 5.30167e-07 | -3.97782e-07 | -1.30683e-07 | 6.46543e-07 | -3.46993e-07 |
| 2 | 0 | 0 | 0.00304207 | 0.000487558 | 0.000674825 | 0.00191771 | 0.000172265 | 0.00038842 |
| 2 | 0 | 1 | 7.61149e-06 | -7.99583e-07 | -1.15061e-06 | 4.65972e-06 | -8.57232e-06 | 4.16344e-06 |
| 2 | 0 | 2 | -3.51203e-07 | 6.45813e-07 | -5.00534e-07 | 3.19477e-08 | -1.02502e-07 | 1.10297e-07 |
| 3 | 0 | 0 | 0.0044926 | 6.79762e-06 | 0.00144012 | 0.00199337 | -9.66457e-05 | 0.000697163 |
| 3 | 0 | 1 | 1e-05 | -1e-05 | -4.12753e-07 | -5.9432e-07 | -1.96989e-06 | 1.94958e-06 |
| 3 | 0 | 2 | -2.89857e-07 | 3.92126e-07 | -5.65962e-07 | 7.21221e-08 | -1.15221e-07 | 1.24569e-07 |
| 4 | 0 | 0 | -0.000969841 | 0.000928231 | 0.000531714 | 0.00198292 | 0.000682058 | 0.0002229 |
| 4 | 0 | 1 | -6.6445e-06 | 1.26925e-05 | -6.83556e-06 | -3.98885e-06 | 5.55016e-06 | -2.82356e-06 |
| 4 | 0 | 2 | -4.57391e-07 | 6.16287e-07 | -4.70314e-07 | -6.51076e-08 | 1.4401e-07 | -1.67121e-08 |
| 5 | 0 | 0 | -0.00101689 | 0.000896069 | 0.000689711 | 0.00184432 | 0.000980818 | 0.00025449 |
| 5 | 0 | 1 | -2.27676e-06 | 6.61205e-06 | -3.38451e-06 | -4.1284e-06 | 2.13317e-05 | -1.85783e-05 |
| 5 | 0 | 2 | -2.97154e-07 | 2.59072e-07 | -3.0658e-07 | 3.26103e-08 | -4.43084e-08 | 3.64848e-08 |
| 6 | 0 | 0 | -0.000333184 | 0.0011494 | 0.000510425 | 0.00165899 | 0.00133911 | 3.82235e-05 |
| 6 | 0 | 1 | -1e-05 | 4.09609e-06 | -1.30571e-06 | -4.44575e-06 | 1.10249e-05 | -5.72873e-06 |
| 6 | 0 | 2 | -3.46644e-07 | 3.51409e-07 | -3.68299e-07 | -5.08938e-09 | 2.34066e-08 | 6.52225e-09 |
| 7 | 0 | 0 | 0.00114673 | 0.00261395 | -0.000259869 | 0.00173285 | 0.00116042 | -5.69491e-05 |
| 7 | 0 | 1 | -2.42206e-05 | 1.91379e-05 | -8.72192e-06 | -4.11618e-06 | 1.49395e-05 | -8.18172e-06 |
| 7 | 0 | 2 | -3.24564e-07 | -8.73348e-08 | -1.29171e-07 | 2.32329e-08 | 2.44536e-08 | 1.45872e-08 |
| 0 | 1 | 0 | -0.00180685 | -0.00216211 | -0.00091103 | 0.0016053 | 0.000409688 | 0.000392517 |
| 0 | 1 | 1 | 6.15242e-06 | -6.25629e-06 | 4.31184e-06 | -1.92812e-06 | -3.42834e-07 | 4.02449e-07 |
| 0 | 1 | 2 | 4.50664e-07 | -7.29024e-07 | 4.9347e-07 | 2.67697e-09 | -2.40306e-08 | 4.35284e-08 |
| 1 | 1 | 0 | -0.000470148 | -0.00258296 | -0.0009030571 | 0.00200739 | 0.000193563 | 0.000389131 |
| 1 | 1 | 1 | 6.97098e-06 | 4.02189e-06 | 1.50825e-06 | 1.76752e-06 | 5.32481e-07 | -1.58149e-06 |
| 1 | 1 | 2 | 3.86212e-07 | -5.9962e-07 | 4.92038e-07 | -1.89739e-08 | 1.65963e-07 | -6.06302e-08 |
| 2 | 1 | 0 | -0.000404294 | -0.000615433 | -0.0007358 | 0.00180641 | 0.00040534 | 0.000367741 |
| 2 | 1 | 1 | 9.13149e-06 | -9.6385e-07 | 1.98442e-06 | 4.09729e-06 | -6.09925e-06 | 3.0645e-06 |
| 2 | 1 | 2 | 4.0988e-07 | -4.82325e-07 | 4.19168e-07 | 2.5517e-08 | -3.12338e-08 | 3.91007e-08 |
| 3 | 1 | 0 | 0.00122466 | -0.000812229 | -0.000439563 | 0.00191172 | 0.000512055 | 0.000231888 |
| 3 | 1 | 1 | 9.17712e-06 | -1.05266e-06 | 1.74687e-06 | -4.49098e-07 | -9.28874e-07 | 3.9023e-06 |
| 3 | 1 | 2 | 3.76035e-07 | -4.26786e-07 | 3.48544e-07 | 1.08199e-08 | -5.48716e-08 | 6.77213e-08 |
| 4 | 1 | 0 | -0.00452438 | -0.000562027 | -0.000412166 | 0.00187609 | 0.000574789 | 0.000233838 |
| 4 | 1 | 1 | -3.73374e-06 | 6.35607e-06 | 1.09283e-06 | -1.26783e-06 | 2.8876e-06 | -1.74175e-06 |
| 4 | 1 | 2 | 4.71711e-07 | -7.87382e-07 | 5.44185e-07 | -2.44576e-08 | 7.6648e-08 | -5.6756e-09 |
| 5 | 1 | 0 | -0.00423516 | -0.000600647 | -0.000991817 | 0.00216569 | 3.25737e-05 | 0.000728327 |
| 5 | 1 | 1 | -2.15233e-08 | -8.81023e-06 | 4.83866e-06 | -2.6735e-06 | 6.74403e-06 | -3.8191e-06 |
| 5 | 1 | 2 | 2.67648e-07 | -4.08425e-07 | 3.89535e-07 | 2.01067e-09 | -2.09848e-08 | 4.52438e-08 |
| 6 | 1 | 0 | -0.00299845 | -0.00238829 | 4.49313e-05 | 0.00210927 | 0.000247483 | 0.000440019 |
| 6 | 1 | 1 | -1.43595e-07 | -2.79891e-05 | 1.36583e-05 | -4.22696e-07 | 3.07326e-06 | -3.28924e-07 |
| 6 | 1 | 2 | 2.53868e-07 | -3.29154e-07 | 3.34108e-07 | -2.50765e-08 | 4.78795e-08 | 3.77381e-08 |
| 7 | 1 | 0 | -0.00109838 | -0.00196721 | -0.000703974 | 0.00181732 | 0.000975893 | 0.000230971 |
| 7 | 1 | 1 | -2.01871e-05 | -5.0406e-06 | 8.03819e-06 | -1.23573e-05 | 3.59526e-05 | -2.15186e-05 |
| 7 | 1 | 2 | 1.92824e-07 | -1.1693e-07 | 3.83927e-07 | 5.08843e-08 | -1.30614e-08 | 4.7663e-08 |

A.2 emcsdz_e

The mean and σ of the emcdz distribution is a function of both p_T and θ , where θ is the angle of the track relative to a straight line trajectory, measured at the back of the DC. The variable emcsdz_e is created to remove this dependence, providing a variable independent of p_T and θ on which to cut.

The calibration of emcsdz_e is performed independently for each EMCal sector, and both $\alpha < 0$ and $\alpha > 0$, where α is the bend angle of the track. For each momentum bin, 0.4-0.5, 0.5-0.6, 0.6-0.7, 0.7-0.8, 0.8-0.9, 0.9-1.0, 1.0-1.25, 1.25-1.5, 1.5-2.0, 2.0-3.5, 3.5-10 [GeV/c²], and each θ bin, -0.35→-0.3, -0.3→-0.25, -0.25→-0.2, -0.2→-0.15, -0.15→-0.1, -0.1→-0.05, -0.05→0, 0→0.05, 0.05→0.1, 0.1→0.15, 0.15→0.2, 0.2→0.25→0.3, 0.3→0.35 [degrees], the emcsdz distribution is fit with a gaussian in the range -0.01 to 0.01 cm to determine the mean and σ . The z dependence of the mean values are then fitted using a function of the form

$$f(\theta) = m0 + m1 * \tan(\theta - \pi/2), \quad (\text{A.13})$$

while the σ values are fitted with a function of the form

$$f(\theta) = s0 * \cos(\theta - \pi/2) + s1. \quad (\text{A.14})$$

An example fit for EMCal sector 0 and $\alpha < 0$ is shown in Figures A.6 and A.7 for θ dependence fits of the mean and σ of the emcdphi distributions respectively. The p_T dependence of the fit parameters are then fitted with a function of the form

$$f(p_T) = p0 + \frac{p1}{pT} + \frac{p2}{pT^2}, \quad (\text{A.15})$$

An example fit to the p_T dependence of the parameters is shown in Figure A.8 sector 1 $\alpha < 0$.

The variable emcsdz_e was then calculated using

$$\text{emcsdz_e} = \frac{\text{emcdz} - \text{offset}}{\text{sigma}} \quad (\text{A.16})$$

$$\text{offset} = m0 + m1 * \tan\left(\theta - \frac{\pi}{2}\right) \quad (\text{A.17})$$

$$\text{sigma} = s0 * \cos\left(\theta - \frac{\pi}{2}\right) + s1 \quad (\text{A.18})$$

$$m0 = p0_{m0} + \frac{p1_{m0}}{pT} + \frac{p2_{m0}}{pT^2} \quad (\text{A.19})$$

$$m1 = p0_{m1} + \frac{p1_{m1}}{pT} + \frac{p2_{m1}}{pT^2} \quad (\text{A.20})$$

$$s0 = p0_{s0} + \frac{p1_{s0}}{pT} + \frac{p2_{s0}}{pT^2} \quad (\text{A.21})$$

$$s1 = p0_{s1} + \frac{p1_{s1}}{pT} + \frac{p2_{s1}}{pT^2}. \quad (\text{A.22})$$

$$(A.23)$$

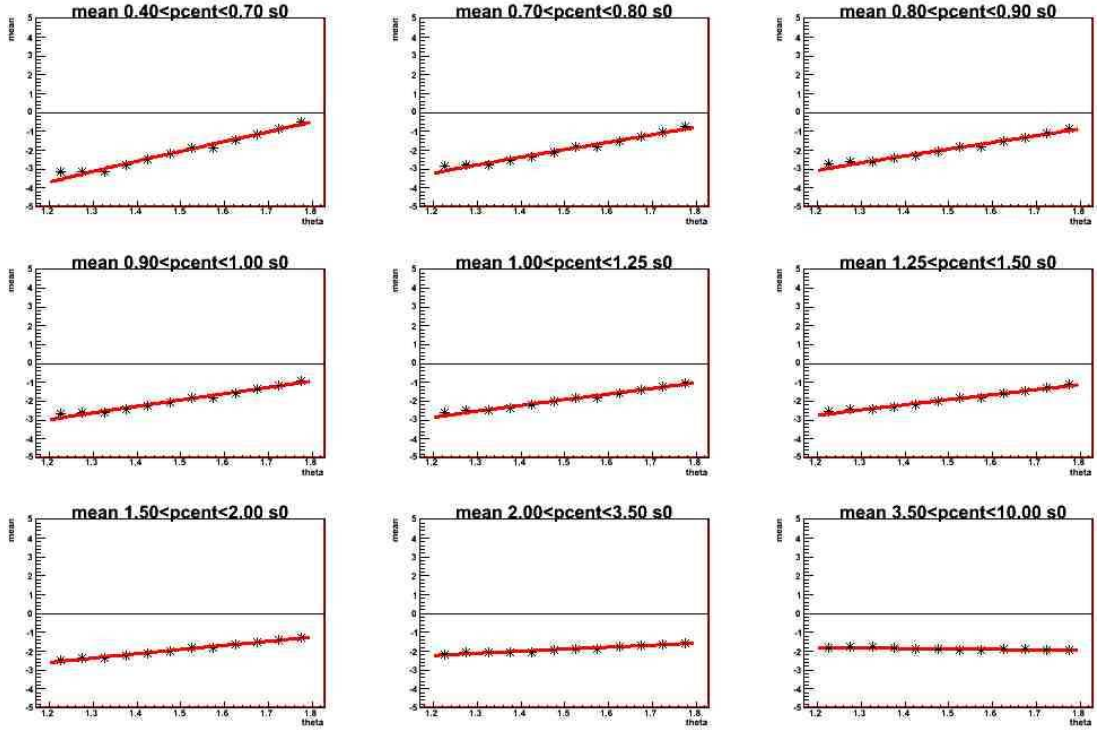


Figure A.6: Fit of the mean values as a function of theta for EMCAL sector 0 and $\alpha < 0$. Fit function is $m_0 + m_1 * \tan(\theta - \pi/2)$

The corrected `emcsdz_e` distributions for each EMCAL sector and alpha are shown in Figure A.9. The mean and sigma values of these distributions are shown in Figure A.10. All mean and sigma values are within $\pm 0.2\sigma$ of the expected values. The recalibration parameters are shown in Table A.2.

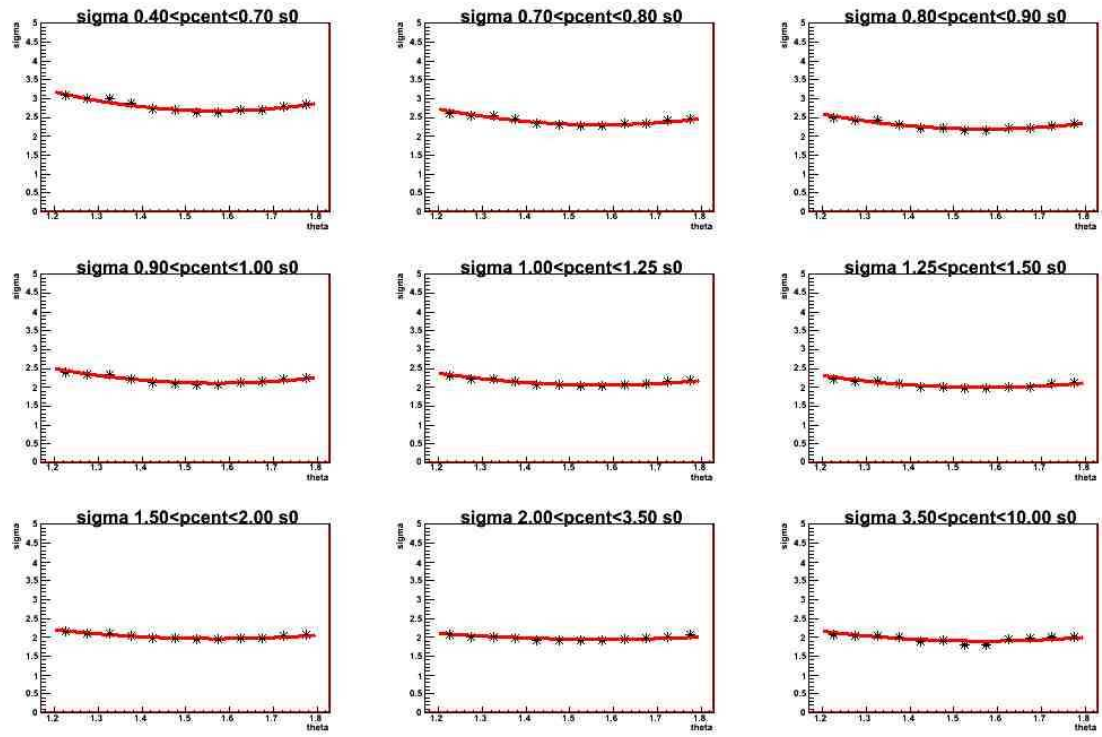


Figure A.7: Fit of sigma values as a function of theta for EMCAL sector 0 and $\alpha < 0$. Fit function is $s0 * \cos(\theta - \pi/2) + s1$

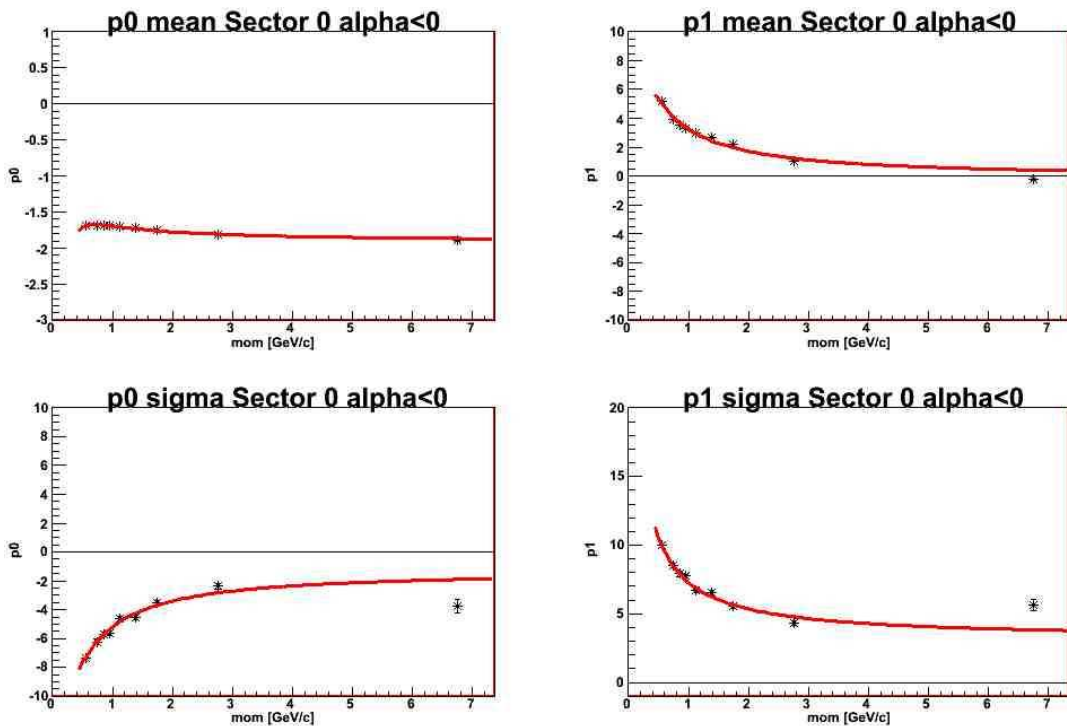


Figure A.8: Fit of parameters as a function of momentum for EMCal sector 0 and $\alpha < 0$. Fit function is $p_0 + \frac{p_1}{p_T} + \frac{p_2}{p_T^2}$

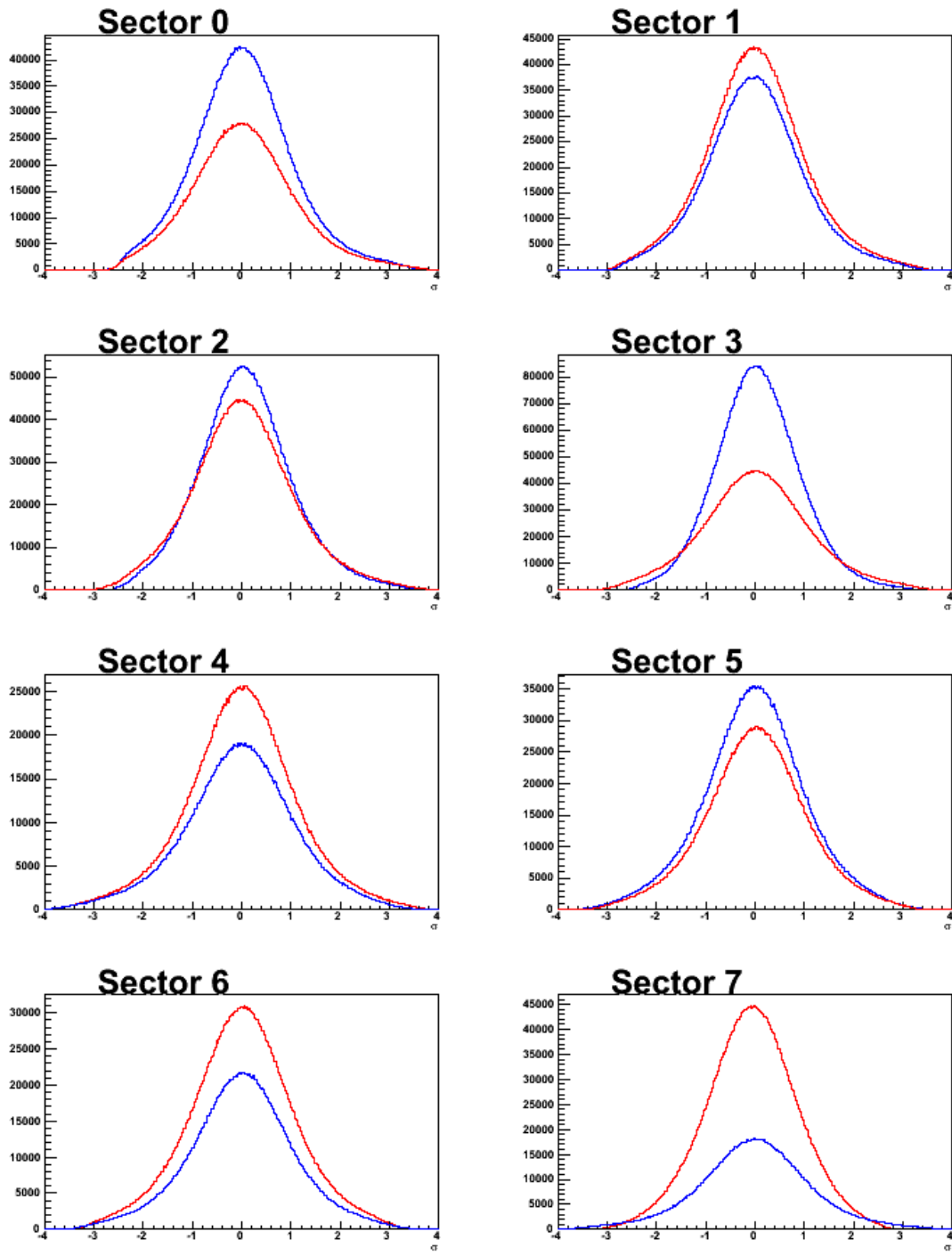


Figure A.9: Recalibrated emcsdz_e for each EMCal sector (blue is $\alpha < 0$ & red is $\alpha > 0$)

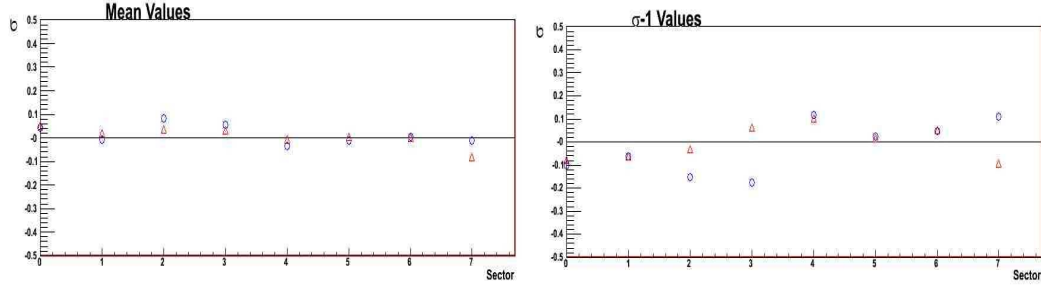


Figure A.10: Mean (Left) and σ (Right) values for the emcsdz_e distributions (blue is alpha<0 & red is alpha>0)

Table A.2: emcsdz_e recalibration parameters.

| EMCal sector | alpha | i | $p0_{mi}$ | $p1_{mi}$ | $p2_{mi}$ | $p0_{si}$ | $p1_{si}$ | $p2_{si}$ |
|--------------|-------|---|-----------|------------|-------------|-----------|-----------|-----------|
| 0 | 0 | 0 | -1.91497 | 0.337299 | -0.118182 | -1.21847 | -4.72412 | 0.752439 |
| 0 | 0 | 1 | -0.181519 | 4.11501 | -0.681976 | 3.16714 | 4.58333 | -0.453818 |
| 1 | 0 | 0 | -1.16871 | 0.0345881 | -0.0304813 | -1.82054 | -1.97959 | -0.575213 |
| 1 | 0 | 1 | 1.15295 | 3.54427 | -0.486156 | 3.72845 | 1.91048 | 0.850299 |
| 2 | 0 | 0 | -1.30247 | 0.00360722 | -0.0516948 | -2.06634 | 3.55442 | -3.58447 |
| 2 | 0 | 1 | -4.90774 | 2.88164 | -0.628754 | 3.83934 | -3.65803 | 3.87433 |
| 3 | 0 | 0 | -0.982921 | -0.172644 | 0.0359242 | 0.404968 | -4.25196 | 0.11265 |
| 3 | 0 | 1 | -5.35863 | 1.71198 | 0.379502 | 1.56644 | 3.49325 | 0.630283 |
| 4 | 0 | 0 | 0.0768184 | 0.139763 | 0.000106994 | -5.61379 | 7.08978 | -3.2048 |
| 4 | 0 | 1 | -3.42918 | 3.59005 | -0.543532 | 7.17638 | -6.97334 | 3.38927 |
| 5 | 0 | 0 | 0.125785 | 0.031888 | 0.0203935 | -3.7725 | 4.1915 | -2.25623 |
| 5 | 0 | 1 | -3.39607 | 4.24416 | -1.03662 | 5.37973 | -4.16492 | 2.55595 |
| 6 | 0 | 0 | 0.0093248 | 0.051043 | -0.00948161 | -3.66855 | 1.62131 | -1.49295 |
| 6 | 0 | 1 | -4.29358 | 3.63203 | -0.789127 | 5.20371 | -1.45579 | 1.68713 |
| 7 | 0 | 0 | 0.273647 | 0.0402519 | -0.0153466 | -2.35375 | -5.74509 | 2.80376 |
| 7 | 0 | 1 | -5.63382 | 3.73865 | -0.637664 | 3.93335 | 5.84151 | -2.61042 |
| 0 | 1 | 0 | -1.83726 | -0.107617 | 0.00112587 | -1.76864 | -5.70912 | 1.4501 |
| 0 | 1 | 1 | -0.33307 | 6.2578 | -1.15654 | 3.54788 | 5.72366 | -1.19615 |
| 1 | 1 | 0 | -1.1873 | 0.0359735 | -0.0280682 | -1.74412 | -2.25805 | -0.443892 |
| 1 | 1 | 1 | 1.29861 | 4.22754 | -0.477228 | 3.54744 | 2.27702 | 0.700139 |
| 2 | 1 | 0 | -1.28276 | 0.0392154 | -0.00202888 | -2.3881 | 2.14789 | -1.13555 |
| 2 | 1 | 1 | -4.86615 | 3.79551 | -0.742394 | 4.03531 | -2.18428 | 1.3802 |
| 3 | 1 | 0 | -1.06196 | 0.215291 | -0.0301111 | -2.33276 | -4.13514 | 1.9054 |
| 3 | 1 | 1 | -5.9846 | 4.13179 | -0.850335 | 3.97846 | 4.04722 | -1.66438 |
| 4 | 1 | 0 | 0.0981911 | -0.0325235 | 0.00512609 | -5.79127 | 5.86174 | -1.9991 |
| 4 | 1 | 1 | -3.53411 | 3.07387 | -0.83345 | 7.34897 | -5.87829 | 2.23838 |
| 5 | 1 | 0 | 0.091199 | 0.0739778 | -0.0217199 | -0.560973 | -1.7638 | 0.395894 |
| 5 | 1 | 1 | -3.4765 | 3.57121 | -1.09255 | 2.27911 | 1.7793 | -0.124258 |
| 6 | 1 | 0 | 0.0232665 | 0.0472649 | 0.0191766 | 0.980132 | -5.10954 | 0.519597 |
| 6 | 1 | 1 | -5.27456 | 3.84177 | -1.06718 | 0.684118 | 5.12883 | -0.278464 |
| 7 | 1 | 0 | 0.340143 | 0.128559 | 0.0160072 | 2.52559 | -11.6433 | 3.502 |
| 7 | 1 | 1 | -5.3713 | 1.44466 | 0.681589 | -0.789666 | 11.294 | -2.94976 |

APPENDIX B

CALIBRATION OF THE DEP VARIABLE

Since E/p is a function of p_T , the variable Dep is created which represents the standard deviation from the mean of the E/p distribution. This provides a p_T independent variable to cut on in the data analysis. It was found that using E/p from single electrons for Dep calibrations caused problems in the 2008 run due to background contamination from the HBD support structure. Therefore Dalitz electron pairs were used for the calibration. The advantage of using Dalitz pairs is the clean signal with very little background. However, using Dalitz pairs does not allow for calibration of positive and negative charges separately due to statistics, and due to kinematics statistics are lost at low momentum at the edge sectors. Dalitz pairs were selected with all the normal electron cuts, and $m_{e^+e^-} < 0.03$ GeV, $\phi_v > 0.25$, and requiring opposite charges. A massplot is shown in Figure B.1.

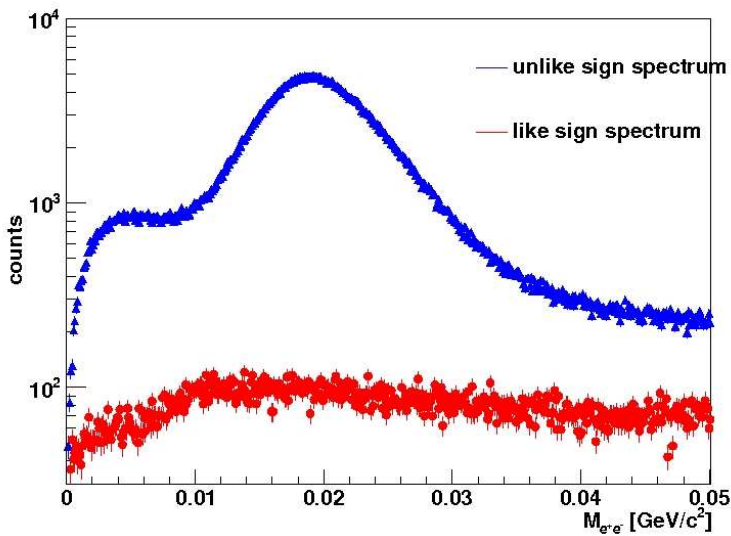


Figure B.1: Dalitz electron mass spectrum.

The E/p distributions are then extracted for each sector for various momentum bins. The E/p distributions are then fit with a gaussian. The E/p distributions for EMCAL Sector

3 are shown as an example in Figure B.2.

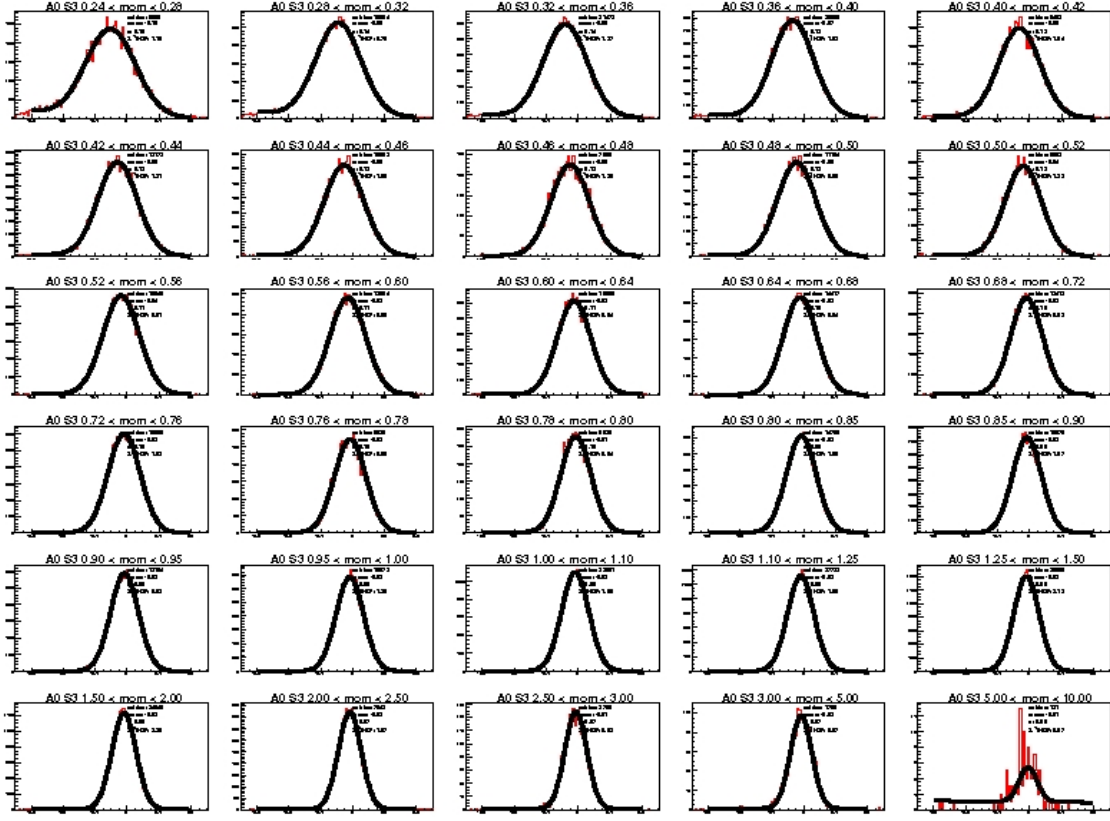


Figure B.2: E/p distributions from Dalitz electron pairs for EMCal Sector 3.

The means of the E/p distributions for each sector are then fit as a function of momentum using Equation B.2. The results are shown in Figure B.3. The width of the guassian fit's to the E/p distributions were fit as a function of momentum with Equation B.3. The results are shown in Figure B.4. The resulting parameters for these fits are shown in Table B.1. The Dep parameter is then calculated using these fit results using Equation B.1.

$$Dep = \frac{E/p - offset}{sigma} \quad (B.1)$$

$$offset = p_{m0} - e^{p_{m1} - p_{m2}p_T} + \frac{0.5p_{m3}p_{m4}}{\pi((p_T - p_{m5})^2 + 0.25p_{m4}^2)} \quad (B.2)$$

$$sigma = \sqrt{p_{s0}^2 + \frac{s_{p1}^2}{p_T} + s_{p2}^2 p_T^2 + s_{p3}}. \quad (B.3)$$

The mean and width of the calibrated Dep distributions as a function of momentum for each sector are shown in Figures B.5&B.6. The results are all within 10% of the expected values in all cases where statistics are good enough for an accurate fit.

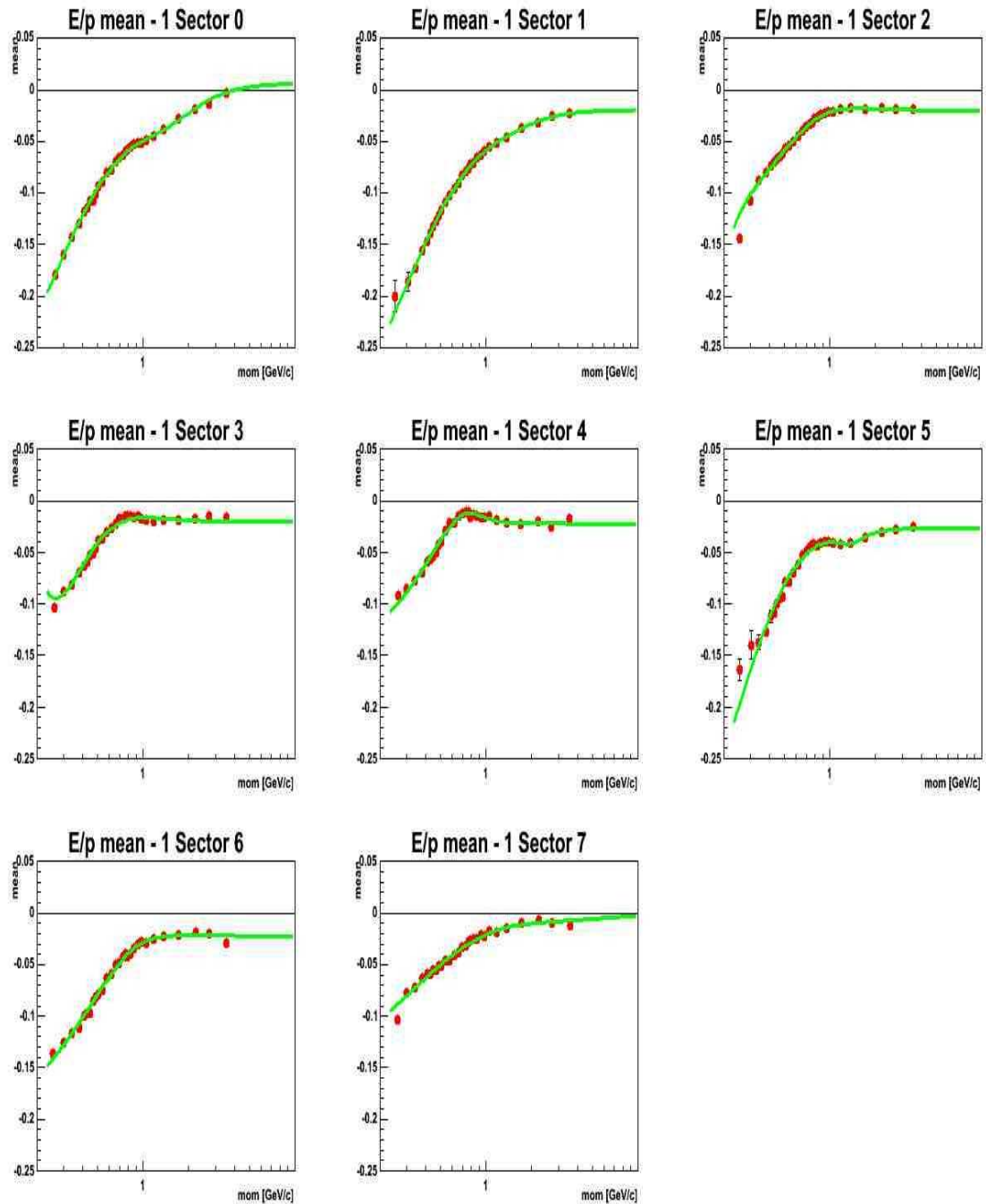


Figure B.3: Fits to the mean of the E/p distributions as a function of momentum for each EMCal sector.

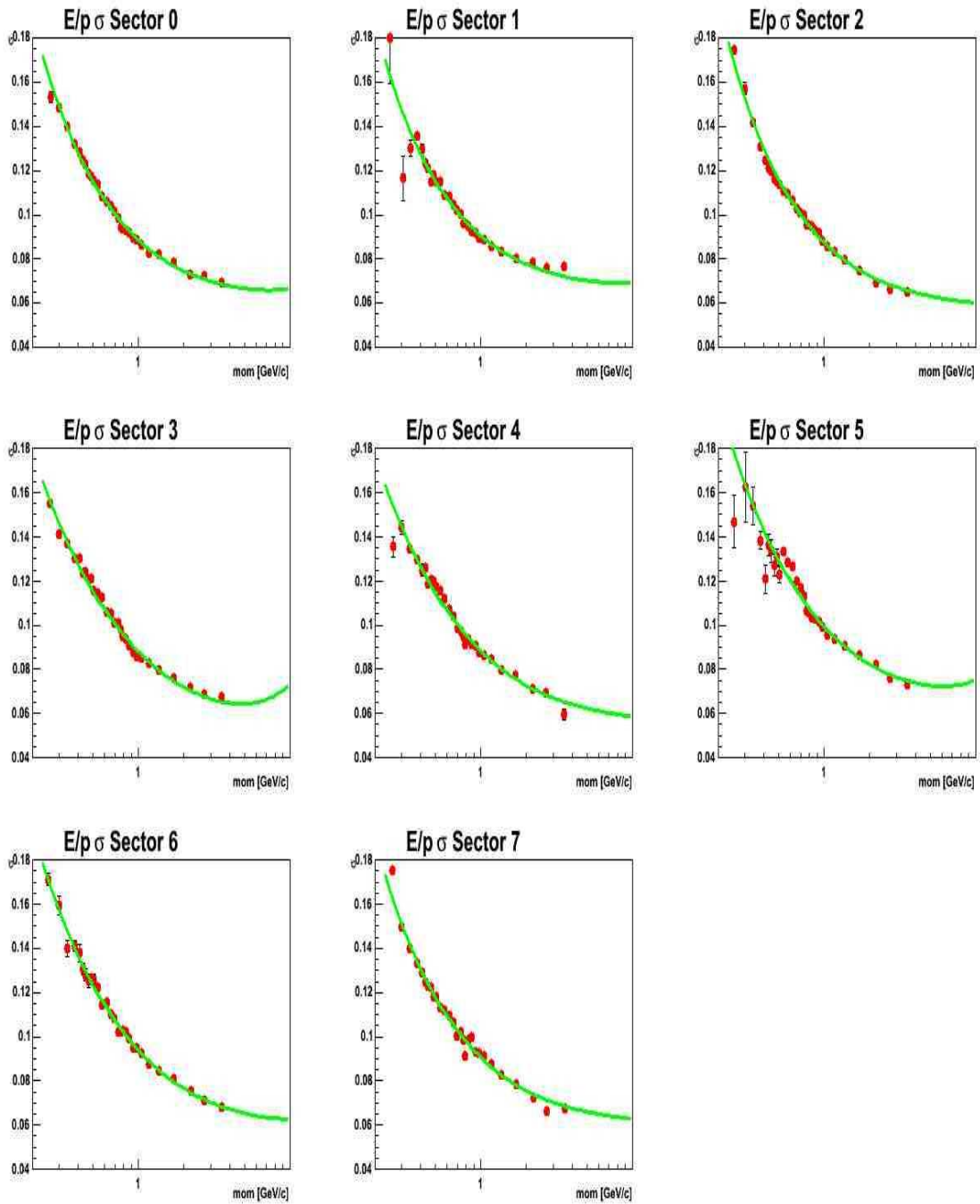


Figure B.4: Fits to the mean of the E/p distributions as a function of momentum for each EMCal sector.

Table B.1: Dep recalibration parameters for each sector. For Dep, the parameters are the same for both $\alpha < 0$ and $\alpha > 0$.

| EMCal sector | p_{m0} | p_{m1} | p_{m2} | p_{m3} | p_{m4} | p_{m5} |
|--------------|-------------|--------------|-------------|------------|------------|-----------|
| 0 | 0.00706319 | -0.89784 | 3.75738 | 0.192288 | -2.62347 | 0.990388 |
| 1 | -0.0191104 | -0.899892 | 3.23633 | 0.0841567 | -2.29205 | 0.981847 |
| 2 | -0.0199981 | -0.437789 | 4.24143 | 0.084681 | 0.399624 | 0.179665 |
| 3 | -0.020639 | -6.80826e-10 | 5.94406 | 4.83096 | 0.00786371 | 0.0516481 |
| 4 | -0.0230473 | -1.70213 | 2.18693 | 0.0611539 | 0.776338 | 0.638872 |
| 5 | -0.0263821 | -0.567812 | 4.73194 | 0.0196802 | -0.859525 | 1.34638 |
| 6 | -0.0236751 | -1.4455 | 1.76718 | 0.0950096 | 1.38866 | 0.668388 |
| 7 | 1.00344e-08 | -1.83624 | 2.8866 | 0.455156 | -9.99971 | -4.99689 |
| EMCal sector | s_{m0} | s_{m1} | s_{m2} | s_{m3} | | |
| 0 | 0.460342 | 0.165009 | 0.006 | -0.400505 | | |
| 1 | 0.881729 | 0.215437 | 0.00599998 | -0.817231 | | |
| 2 | 0.686876 | 0.206258 | 0.000422638 | -0.629796 | | |
| 3 | 0.0923977 | 0.0892433 | 0.006 | -0.0406768 | | |
| 4 | 0.106762 | 0.0907033 | 7.17284e-09 | -0.0518866 | | |
| 5 | 0.146396 | 0.109914 | 0.00516708 | -0.0838642 | | |
| 6 | 0.124782 | 0.103171 | 0.00217475 | -0.068126 | | |
| 7 | 0.238356 | 0.125449 | 1.40357e-09 | -0.178841 | | |

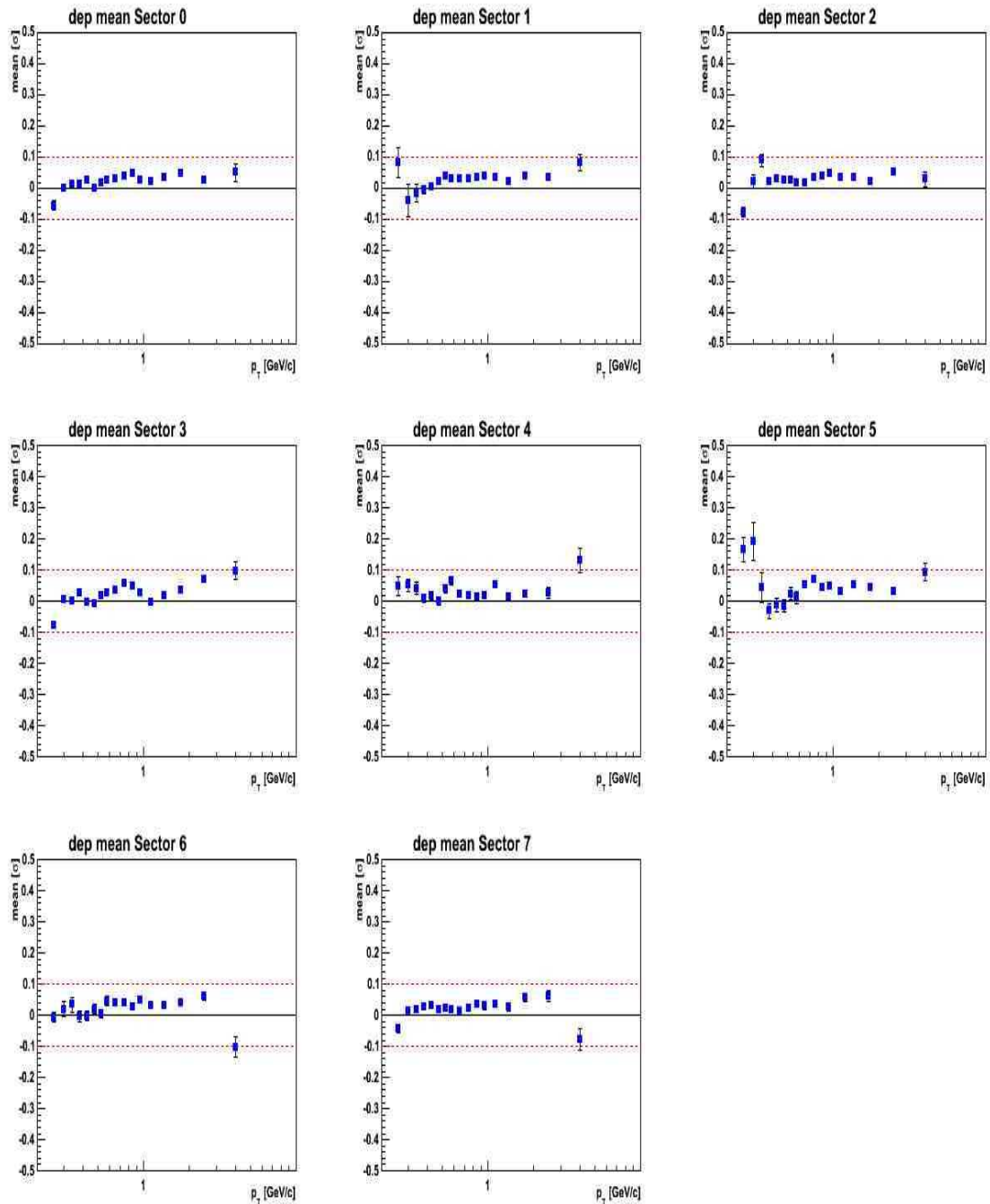


Figure B.5: Mean of the calibrated Dep distributions as a function of momentum for each EMCal sector.

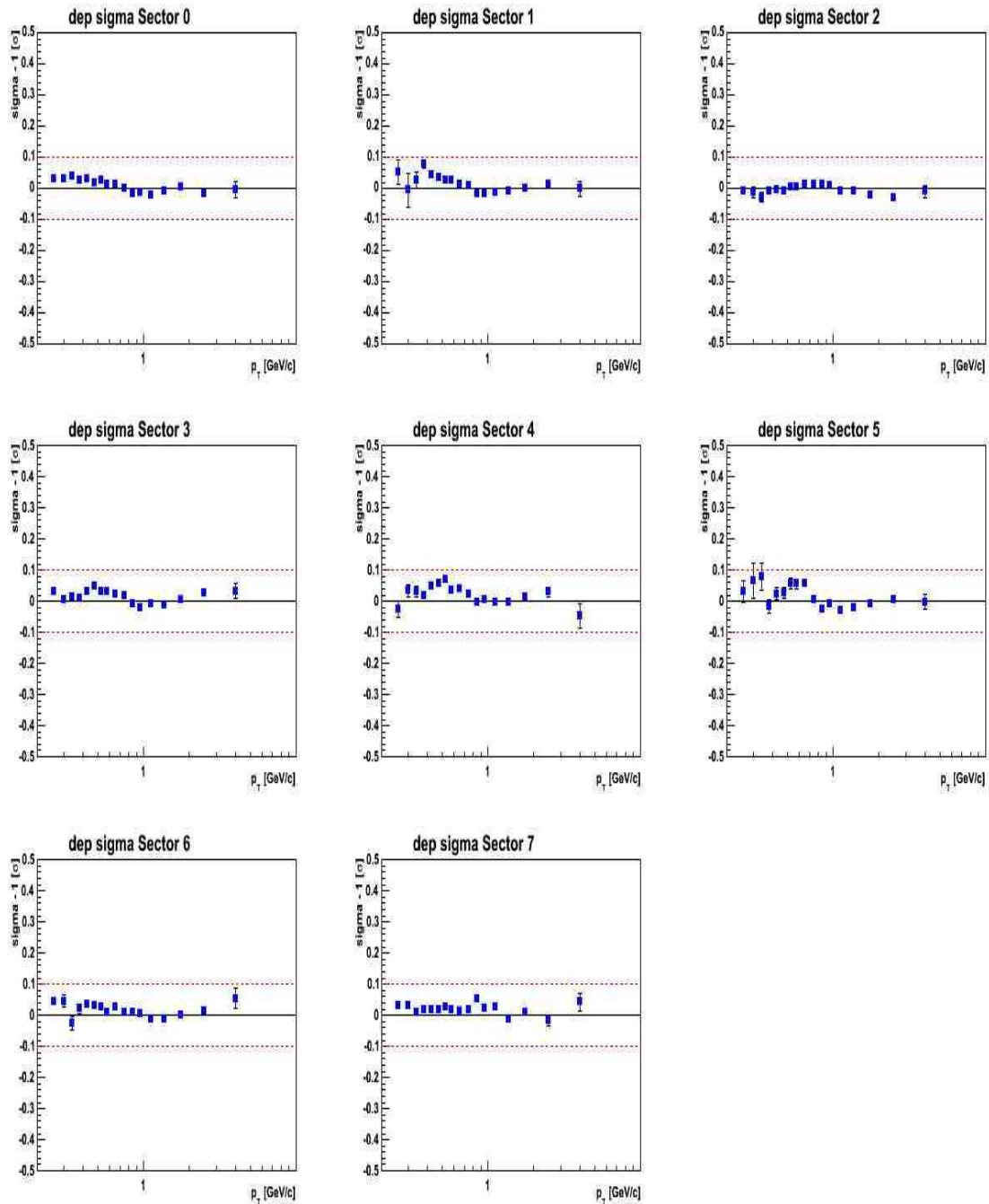


Figure B.6: Width of the calibrated Dep distributions as a function of momentum for each EMCal sector.

APPENDIX C

DERIVATION OF THE STATISTICAL UNCERTAINTY ON $\langle p_T^2 \rangle$

This chapter details the derivation of the formula used to calculate the statistical uncertainty on the $\langle p_T^2 \rangle$ calculated in Section 5.3.2. The $\langle p_T^2 \rangle|_{p_T \leq p_T^{max}}$ is calculated as (reproducing Equation 5.15)

$$\langle p_T^2 \rangle = \sum_{i=0}^N \frac{\langle p_T^2 \rangle_i \frac{dN_i}{dp_T} p_{Ti} \Delta p_{Ti}}{\frac{dN_i}{dp_T} p_{Ti} \Delta p_{Ti}}. \quad (\text{C.1})$$

Defining the new variables

$$y = \langle p_T^2 \rangle \quad (\text{C.2})$$

$$x_i = \frac{dN_i}{dp_T} p_{Ti} \Delta p_{Ti} \quad (\text{C.3})$$

$$w_i = \langle p_T^2 \rangle_i, \quad (\text{C.4})$$

allows us to rewrite Equation 5.15 as

$$y = \frac{\sum_{i=0}^N (w_i x_i)}{\sum_{i=0}^N (x_i)}. \quad (\text{C.5})$$

From (Bevington page 59 Eq. 4-8) the uncertainty in any function y due to the uncertainty on a variable x , can be written as

$$\sigma_y^2 = \sigma_x^2 \left(\frac{\partial y}{\partial x} \right)^2. \quad (\text{C.6})$$

Using Equation C.6 to write the uncertainty on y (σ_y) gives

$$\sigma_y^2 = \sum_{i=0}^N \left[\sigma_{x_i}^2 \left(\frac{\partial y}{\partial x_i} \right)^2 \right], \quad (\text{C.7})$$

where σ_{x_i} is the uncertainty on x_i . Calculating $\frac{\partial y}{\partial x_i}$ gives

$$\frac{\partial y}{\partial x_i} = \frac{1}{\left[\sum_{j=0}^N x_j \right]^2} \left[\sum_{j=0}^N x_j \frac{\partial}{\partial x_i} \sum_{i=0}^N (w_i x_i) - \sum_{j=0}^N (w_j x_j) \frac{\partial}{\partial x_i} \sum_{i=0}^N x_i \right] \quad (\text{C.8})$$

$$\frac{\partial y}{\partial x_i} = \frac{1}{\left[\sum_{j=0}^N x_j \right]^2} \left[\sum_{j=0}^N x_j (w_i) - \sum_{j=0}^N (w_j x_j) \right] \quad (\text{C.9})$$

$$\frac{\partial y}{\partial x_i} = \left[w_i / \sum_{j=0}^N x_j - \left(\sum_{j=0}^N (w_j x_j) \right) / \left(\sum_{j=0}^N x_j \right)^2 \right] \quad (\text{C.10})$$

$$\frac{\partial y}{\partial x_i} = \left[w_i / \sum_{j=0}^N x_j - y / \left(\sum_{j=0}^N x_j \right) \right] \quad (\text{C.11})$$

$$\frac{\partial y}{\partial x_i} = (w_i - y) / \left(\sum_{j=0}^N x_j \right). \quad (\text{C.12})$$

Substituting this back into Equation C.7 gives

$$\sigma_y^2 = \sum_{i=0}^N \left[\sigma_{x_i}^2 \left((w_i - y) / \left(\sum_{j=0}^N x_j \right) \right)^2 \right] \quad (\text{C.13})$$

$$\sigma_y^2 = \sum_{i=0}^N \left[\sigma_{x_i}^2 (w_i - y)^2 \right] / \left(\sum_{j=0}^N x_j \right)^2. \quad (\text{C.14})$$

Finally substituting Equations C.2-C.4 into Equation C.14 gives

$$\sigma_{\langle p_T^2 \rangle}^2 = \frac{\sum_{i=0}^N (\sigma_{A_i} p_{T_i} \Delta p_{T_i})^2 (\langle p_T^2 \rangle_i - \langle p_T^2 \rangle)^2}{\sum_{i=0}^N \frac{dN_i}{dp_T} p_{T_i} \Delta p_{T_i}} \quad (\text{C.15})$$

where σ_{A_i} is the Type A uncertainty on $\frac{dN_i}{dp_T}$.

APPENDIX D

PYTHIA CONFIGURATIONS

This appendix presents the PYTHIA configuration files used to generate the simulations for the $\psi' \rightarrow e^+e^-$ analysis detailed in Chapter 6. The J/ψ PYTHIA configuration is given in Section D.1. The ψ' PYTHIA configuration is given in Section D.2. The configuration used to generate the PYTHIA open heavy flavor line shapes is given in Section D.3. Finally, the DY configuration is given in Section D.4.

D.1 J/ψ Pythia Configuration

```
roots 200
proj p
targ p
frame cms

msel 0 // turn on all prod. mechanisms manually

msub 86 1 // g+g->j/psi
msub 106 1 // g+g -> J/psi+gamma turned ON
msub 107 1 // g+gamma -> J/psi+g turned ON
msub 108 1 // gamma+gamma->J/psi+gamma turned ON

mdme 858 1 1 // j/psi -> ee turned off
mdme 859 1 0 // j/psi -> mumu turned ff
mdme 860 1 0 // j/psi -> random turned off

// mstp 51 4 // structure function for GRV94 L
mstp 51 7 // structure function for CTEQ5L
```

D.2 ψ' Pythia Configuration

```
roots 200
proj p
targ p
```

```

frame cms

msel 0 // turn on all prod. mechanisms manually

msub 86 1 // g+g->j/psi
msub 106 1 // g+g -> J/psi+gamma turned ON
msub 107 1 // g+gamma -> J/psi+g turned ON
msub 108 1 // gamma+gamma->J/psi+gamma turned ON

kfpr 86 1 100443 // request PsiPrime (2s) instead of psi for process 86
kfpr 106 1 100443 // request PsiPrime (2s) instead of psi for process 106
kfpr 107 1 100443 // request PsiPrime (2s) instead of psi for process 107
kfpr 108 1 100443 // request PsiPrime (2s) instead of psi for process 108

mdme 1567 1 1 // psi' -> ee turned ON
mdme 1568 1 0 // psi' -> mumu turned OFF
mdme 1569 1 0 // psi' -> random turned OFF

mdme 858 1 0 // j/psi -> ee turned off
mdme 859 1 0 // j/psi -> mumu turned ff
mdme 860 1 0 // j/psi -> random turned off

mstp 51 7 // structure function for CTEQ5L

```

D.3 Heavy Flavor Pythia Configuration

```

roots   200
proj    p
targ    p
frame   cms
msel    1
#mstp 7 5    // bottom
#msub 81 1 //
#msub 82 1
#msub 83 1
#msub 84 1
#msub 85 1
#msub 1  1
#msub 2  1
#msub 142 1
#msub   28 1    // flavour excitation
mstp    52 2    // use LHAPDF
mstp    54 2
mstp    56 2

```

```

mstp      51 10041 // CTEQ6LL
mstp      91 1    // gaussian intrinsic kt
parp      91 1.5 // intrinsic kt value
parp      93 10.0
pmas      4 1 1.25 // charm mass
pmas      5 1 4.1 // bottom mass
mstp      33 1    // use k factor
parp      31 3.4 // k factor
mstp      32 4    // Q^2
ckin      3 0.5 // min parton pt
mstp 71 0 // master switch for final state radiation (1=ON, 0=OFF)
#mrpy     1 1019290 // random seed
#mstj     1 2    // independent fragmentation
mdme     684 1 0
..... Config file has all processes from 684 to 1027 set to 0
mdme     1027 1 0

```

D.4 DY Pythia Configuration

```

nevents 1000 // doesn't actually do anything
roots   200
proj    p
targ    p
frame   cms
msel    0
mstp    43 3 //treatment of Z0/gamma*
           // interference in matrix elements.
           // 1=gamma* 2=Z0 3=gamma*/Z0
mstp    33 1 //details, don't worry about it
mstp    32 1 //details, don't worry about it
#mstp 7 5 // bottom
#msub 81 1 //
#msub 82 1
#msub 83 1
#msub 84 1
#msub 85 1
msub 1 1
#msub 2 1
#msub 142 1
#msub 28 1 // flavour excitation
mstp    52 2 // use LHAPDF
mstp    54 2
mstp    56 2
mstp    51 10041 // CTEQ6LL

```

```
mstp    91 1    // gaussian intrinsic kt
parp    91 1.5   // intrinsic kt value
pmas    4 1 1.5  // charm mass
pmas    5 1 4.8  // bottom mass
mstp    33 1    // use k factor
parp    31 1.38  // k factor
mstp    32 4    // Q^2
ckin    3 1.0   // min parton pt
mstp 71 0 // master switch for final state radiation (1=ON, 0=OFF)
#mrpy    1 1019290 // random seed
#mstj    1 2    // independent fragmentation
mdme    170 1 1
mdme    684 1 0
..... Config file has all processes from 684 to 1027 set to 0
mdme    1027 1 0
```

APPENDIX E

FITTING IN THE $\psi' \rightarrow E^+E^-$ ANALYSIS

This appendix presents further details of the fitting routine used in the $\psi' \rightarrow e^+e^-$ analysis detailed in Chapter 6. The coding for the fit function used is given in Section E.1. Fit results for the alternate fitting cases not shown in Chapter 6 are given in Section E.2.

E.1 Fit Function

```
////////// This is the fitting function ///////////
double continuum_1d(double* x, double* par)
{
    /*
    parameter explanations
    par[0] = DD yield
    par[1] = BB / DD fraction
    par[2] = DY yield (fixed by NLO calculations?)
    par[3] = J/psi yield
    par[4] = psi' / J/psi fraction
    par[5] = resolution
    par[6] = C_hard (C_hard = 0.324 in AN722)
    par[7] = mass scale
    par[8] = mass scale int

    x[0] = mass;
    */

    double DD_frac = par[0];
    double BB_frac = par[1]*DD_frac;
    double DY_frac = par[2];
    double jpsi_frac = par[3];
    double psip_frac = par[4]*jpsi_frac;

    double ext_res = par[5];

    double intfrac = par[6];
    double mass_scale = par[7];
    double mass_scale_int = par[8]; // governs the shift of the internal rad seperately

    double mass = x[0];

    int massbin = hmass_sim_DD_var->GetXaxis()->FindBin(mass);

    double DD_sim   = hmass_sim_DD_var->GetBinContent(massbin);
    double BB_sim   = hmass_sim_BB_var->GetBinContent(massbin);
    double DY_sim   = hmass_sim_DY_var->GetBinContent(massbin);

    // Need to make sure that continuum histograms
    // bins match those of the histogram that is being fit!
    double massLow = hmass_sim_DD_var->GetXaxis()->GetBinCenter(massbin) - 0.5*hmass_sim_DD_var->GetXaxis()->GetBinWidth(massbin);
    double massHigh = hmass_sim_DD_var->GetXaxis()->GetBinCenter(massbin) + 0.5*hmass_sim_DD_var->GetXaxis()->GetBinWidth(massbin);

    double err = 0;
    //smearing
    double jpsi_ext_res = calculate_smearing(hmass_sim_jpsi, massLow, massHigh, mass_scale, ext_res, err);
```

```

double jpsi_int_res = calculate_smearing(hmass_sim_jpsi_int, massLow, massHigh, mass_scale*mass_scale_int, ext_res, err);
double psip_ext_res = calculate_smearing(hmass_sim_psip, massLow, massHigh, mass_scale, ext_res, err);
double psip_int_res = calculate_smearing(hmass_sim_psip_int, massLow, massHigh, mass_scale*mass_scale_int, ext_res, err);

//Add everything up!

double continuum_piece = ( DD_frac*DD_sim +
    BB_frac*BB_sim +
    DY_frac*DY_sim );

double jpsi_piece = jpsi_frac * ( (1-intfrac)*jpsi_ext_res + intfrac*jpsi_int_res );
double psip_piece = psip_frac * ( (1-intfrac)*psip_ext_res + intfrac*psip_int_res );
//double psip_piece = psip_frac * psip_ext_res;

return continuum_piece + jpsi_piece + psip_piece;
}

///////////////////////////////
// This function performs the smearing used in the fitter
/////////////////////////////
double calculate_smearing(TH1D* h, double massl, double massh, double mass_scale, double smear, double& err, bool print)
{
    err = 0;
    double res = 0;
    for (int i=0; i<=h->GetNbinsX(); i++)
    {
        float mass_ = h->GetXaxis()->GetBinCenter(i);
        double dm_ = h->GetXaxis()->GetBinWidth(i);

        double smearing = 1.0;

        //the TF1->Integral function screws up for small smearing width's
        //since the J/psi width is around 50 MeV a smearing less than 0.002
        //doesn't do anything anyway so just add the bins up instead
        //the fine bins are width = 0.01, so a three sigma smearing is .005/3
        if (smear > 0.005/3.0)

        {
            //check that we aren't doing unnecessary calculations
            if ( (mass_* mass_scale + 5.0 * smear) < massl ) continue;
            if ( (mass_* mass_scale - 5.0 * smear) > massh ) break;

            //set the fit parameters
            fgaus->SetParameter(0, mass_* mass_scale);
            fgaus->SetParameter(1, smear);

            smearing = fgaus->Integral(massl, massh);
        }
        else
        {
            if (mass_ < massl) continue;
            if (mass_ > massh) break;
        }

        res += h->GetBinContent(i) * dm_ * smearing;
        err += h->GetBinError(i) * dm_ * smearing;

        if (print)
        {
            cout << " " << h->GetTitle() << " " << massl << " " << massh << " | "
                << mass_ << " " << h->GetBinContent(i) * dm_ << " " | "
                << mass_scale << " " << smear << " | ";
        }

        if (smear > 0.002)
            cout << fgaus->GetParameter(0) << " "
                << fgaus->GetParameter(1) << " "
                << fgaus->Integral(0.0,12.0) << " | ";

        cout << smearing << " " << res << " | "
            << endl;
    }

    res = res / (massh - massl);
    err = err / (massh - massl);

    return res;
}

```

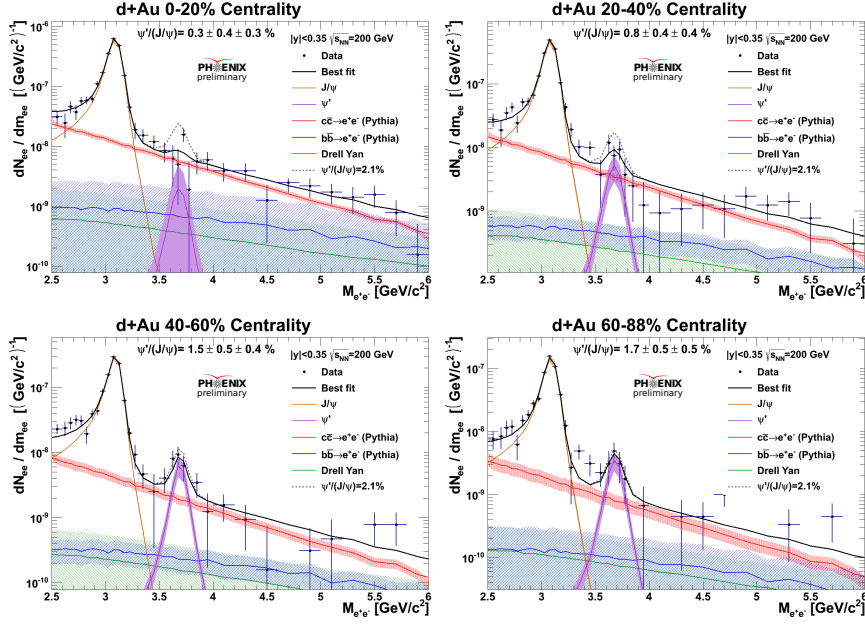


Figure E.1: Fits to the $d+Au$ invariant mass spectrum in 4 centrality bins using the **Best** fitting scheme with an overlay where the $\psi'/(J/\psi)$ ratio is set to the $p+p$ value.

E.2 Alternate Fit Results

This section contains the plots for the alternate fitting cases detailed in Section 6.3.2. The fit results using the **Best** case fitting scheme overlaid with the $p+p$ $\psi'/(J/\psi)$ ratio is shown for each centrality bin in Figure E.1. The results using the **Case 1** fitting scheme for each centrality bin is shown in Figure E.2. The results using the **Case 2** fitting scheme for each centrality bin is shown in Figure E.3. The results using the **Case 3** fitting scheme for each centrality bin is shown in Figure E.4. The results using the **Case 4** fitting scheme for each centrality bin is shown in Figure E.5. The results using the **Case 5** fitting scheme for each centrality bin is shown in Figure E.6. The results using the **Case 6** fitting scheme for each centrality bin is shown in Figure E.7. The results using the **Case 7** fitting scheme for each centrality bin is shown in Figure E.8. The results using the **Case 8** fitting scheme for each centrality bin is shown in Figure E.9. The results using the **Case 9** fitting scheme for each centrality bin is shown in Figure E.10. The results using the **Case 10** fitting scheme for each centrality bin is shown in Figure E.11.

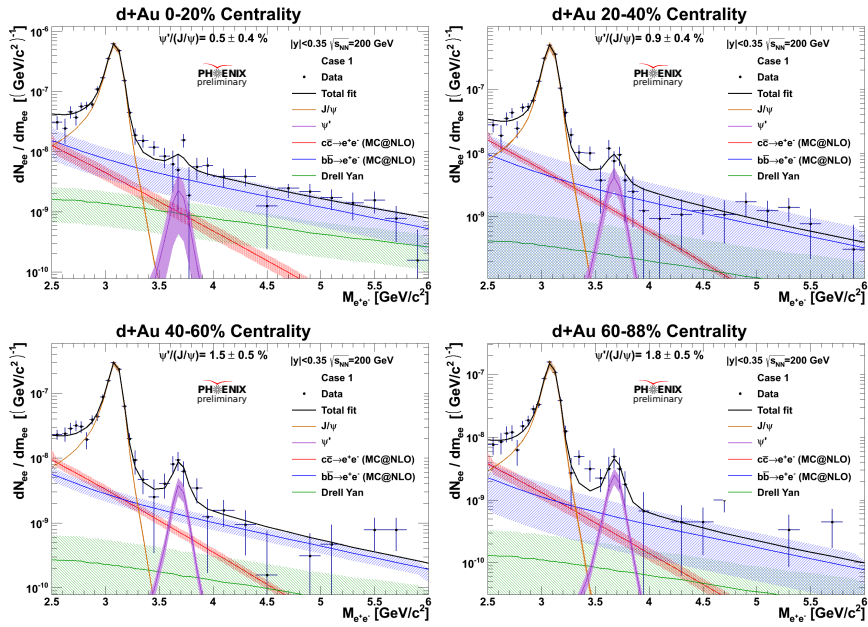


Figure E.2: Fits to the $d+\text{Au}$ invariant mass spectrum in 4 centrality bins using the **Case 1** fitting scheme.

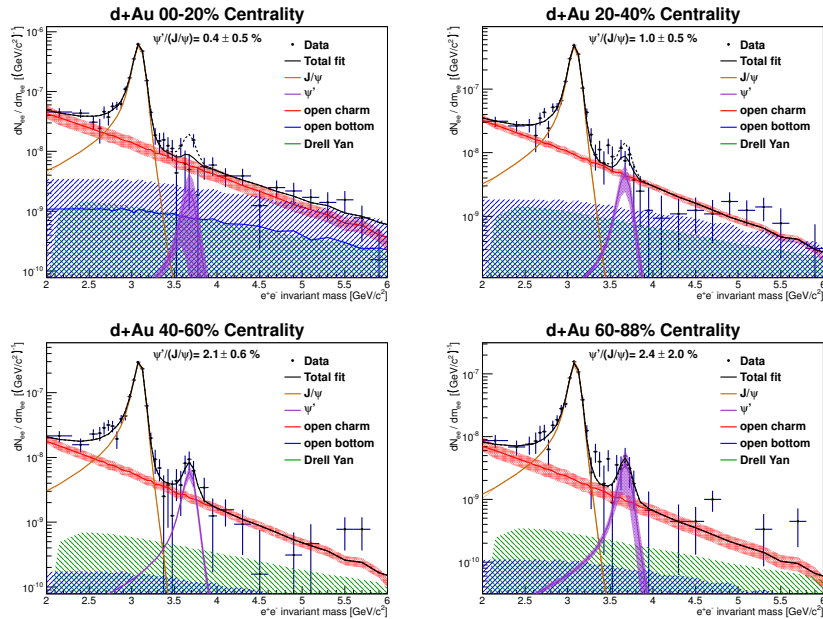


Figure E.3: Fits to the $d+\text{Au}$ invariant mass spectrum in 4 centrality bins using the **Case 2** fitting scheme.

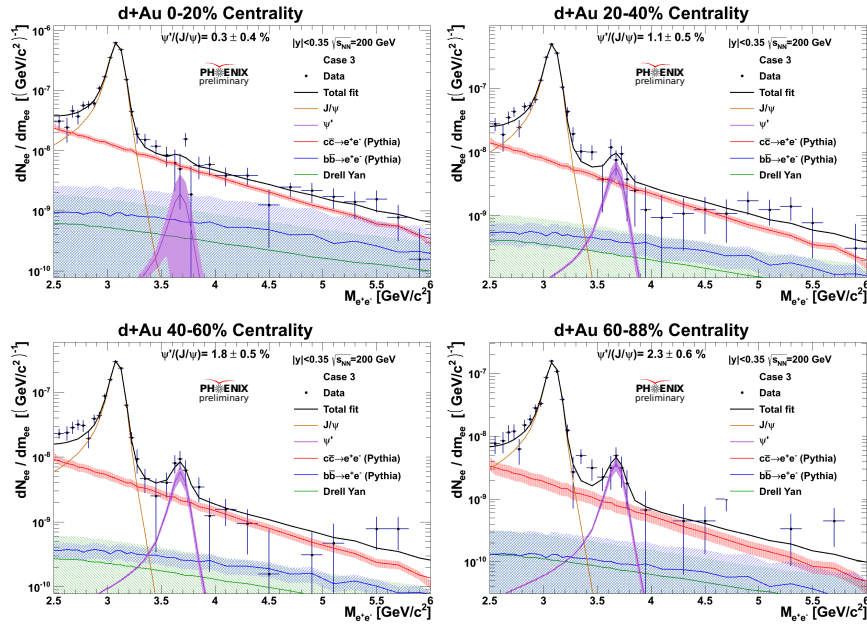


Figure E.4: Fits to the $d+Au$ invariant mass spectrum in 4 centrality bins using the **Case 3** fitting scheme.

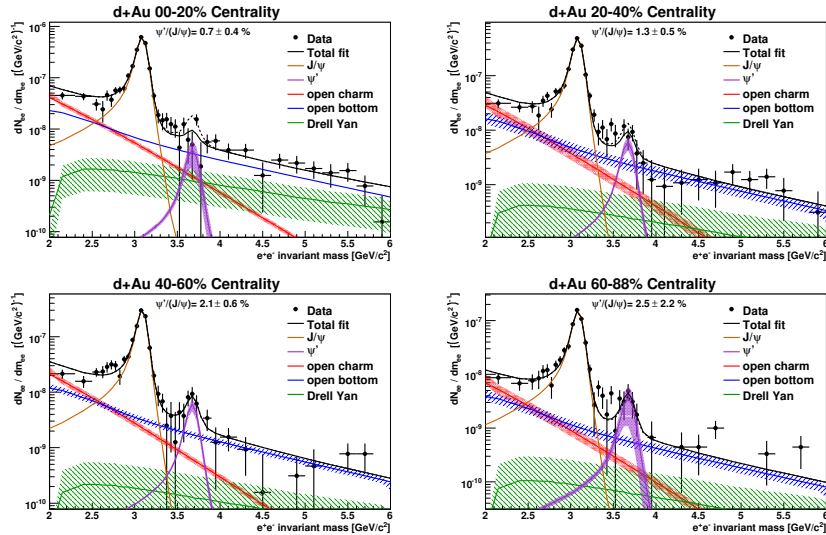


Figure E.5: Fits to the $d+Au$ invariant mass spectrum in 4 centrality bins using the **Case 4** fitting scheme.

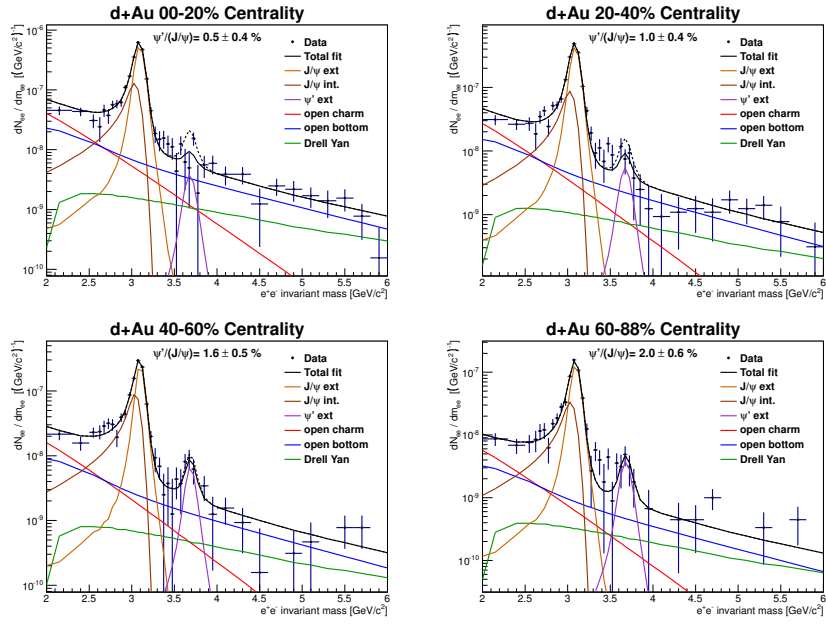


Figure E.6: Fits to the $d+\text{Au}$ invariant mass spectrum in 4 centrality bins using the **Case 5** fitting scheme.

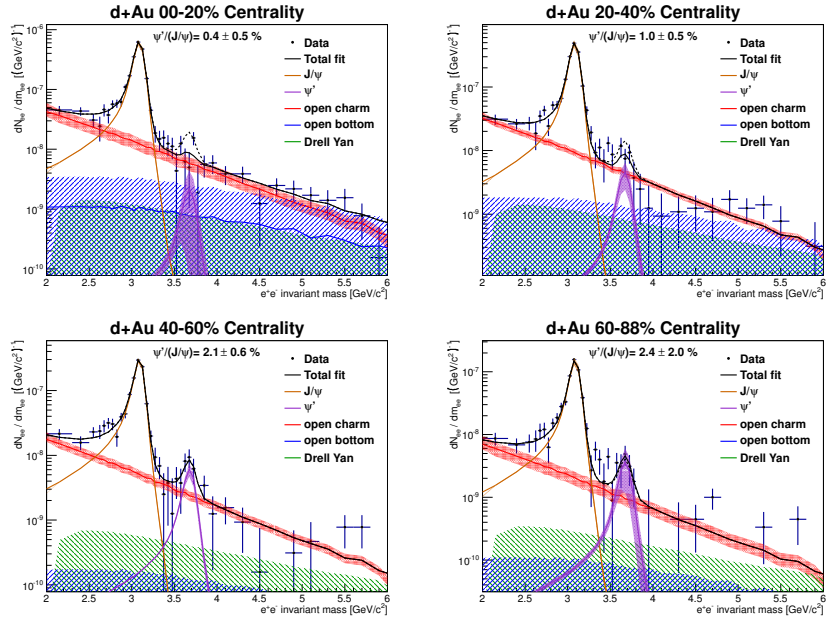


Figure E.7: Fits to the $d+\text{Au}$ invariant mass spectrum in 4 centrality bins using the **Case 6** fitting scheme.

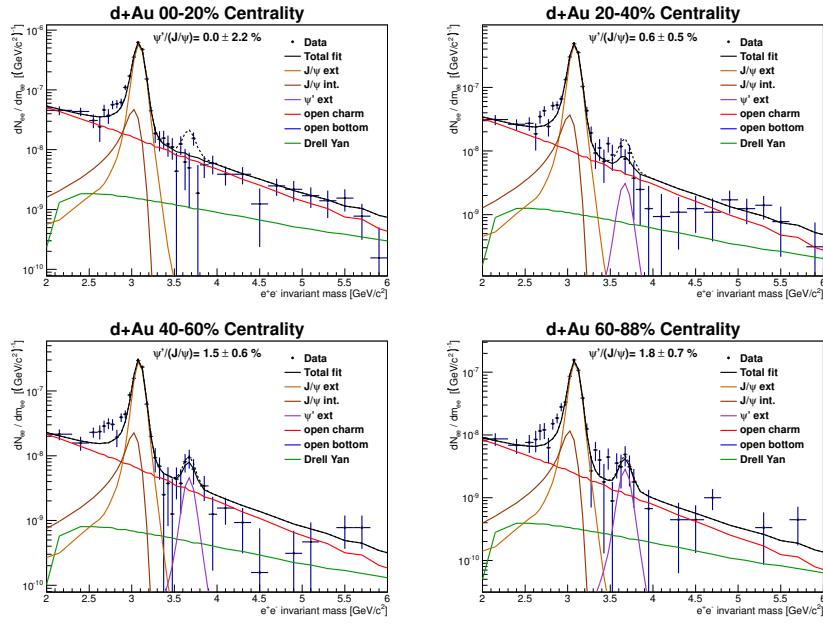


Figure E.8: Fits to the $d+Au$ invariant mass spectrum in 4 centrality bins using the **Case 7** fitting scheme.

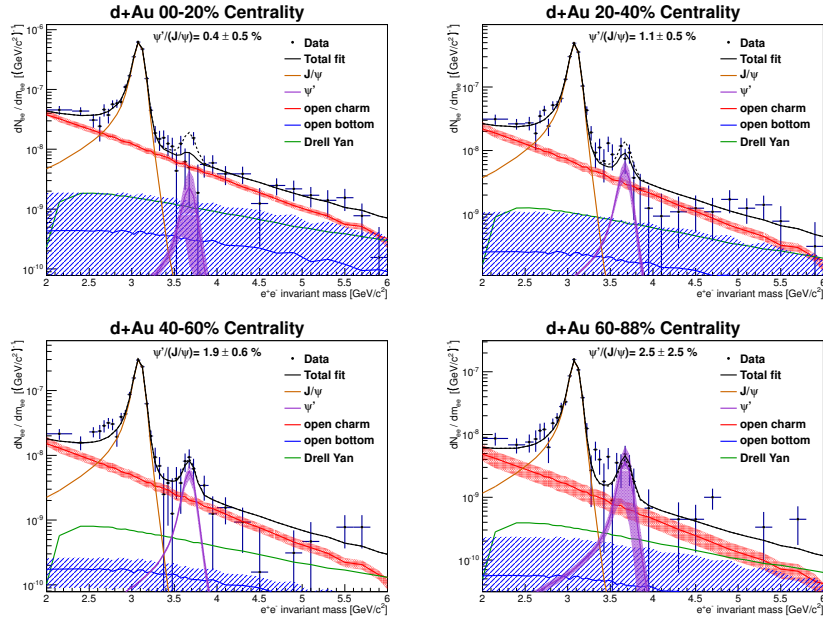


Figure E.9: Fits to the $d+Au$ invariant mass spectrum in 4 centrality bins using the **Case 8** fitting scheme.

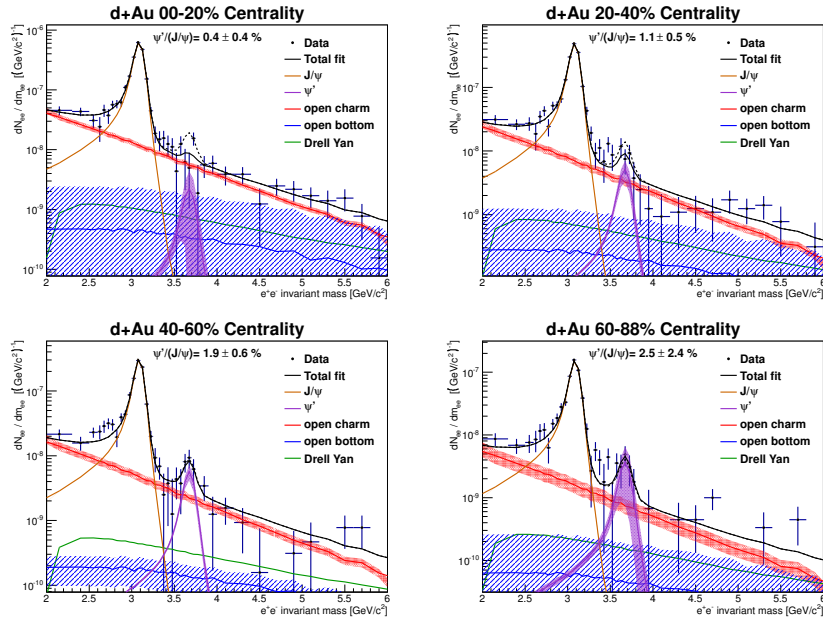


Figure E.10: Fits to the $d+Au$ invariant mass spectrum in 4 centrality bins using the **Case 9** fitting scheme.

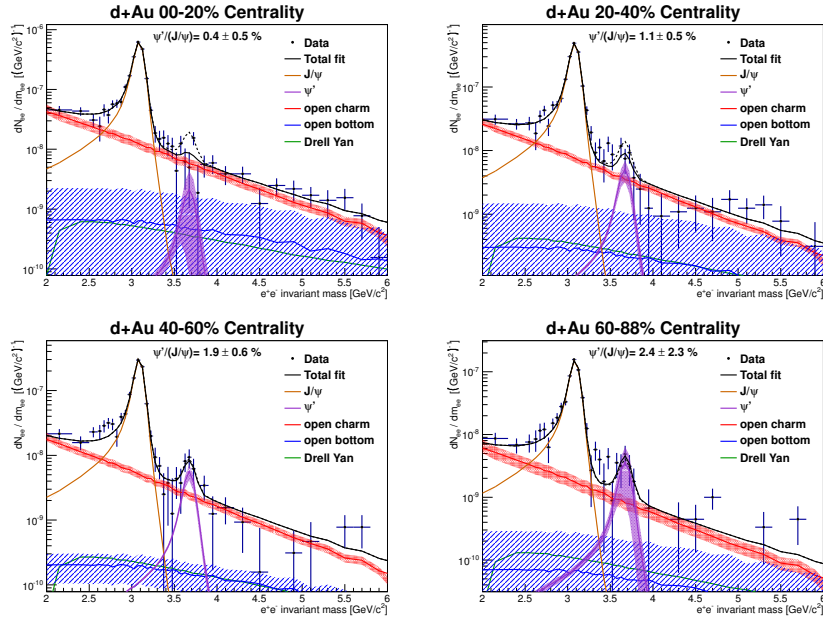


Figure E.11: Fits to the $d+Au$ invariant mass spectrum in 4 centrality bins using the **Case 10** fitting scheme.

APPENDIX F

ADDITIONAL FIGURES

F.1 Single electron trigger efficiency

The fits to the measured single electron trigger efficiency for SM in the EMCal are shown in Figures F.1, F.3, F.5, and F.7 for rungroups 0, 1, 2, and 3 respectively. The fits to the measured single electron trigger efficiency for SM in the RICH are shown in Figures F.2, F.4, F.6, and F.8 for rungroups 0, 1, 2, and 3 respectively

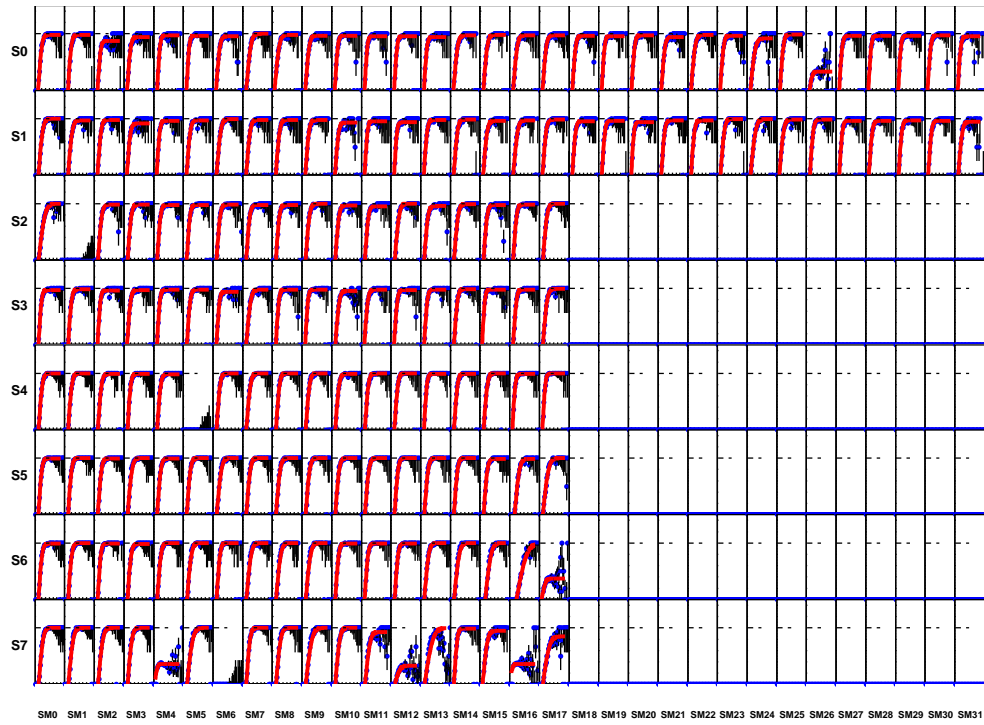


Figure F.1: (color online) EMCal SM efficiencies for rungroup 0 where the blue points are the data and the red lines the fit.

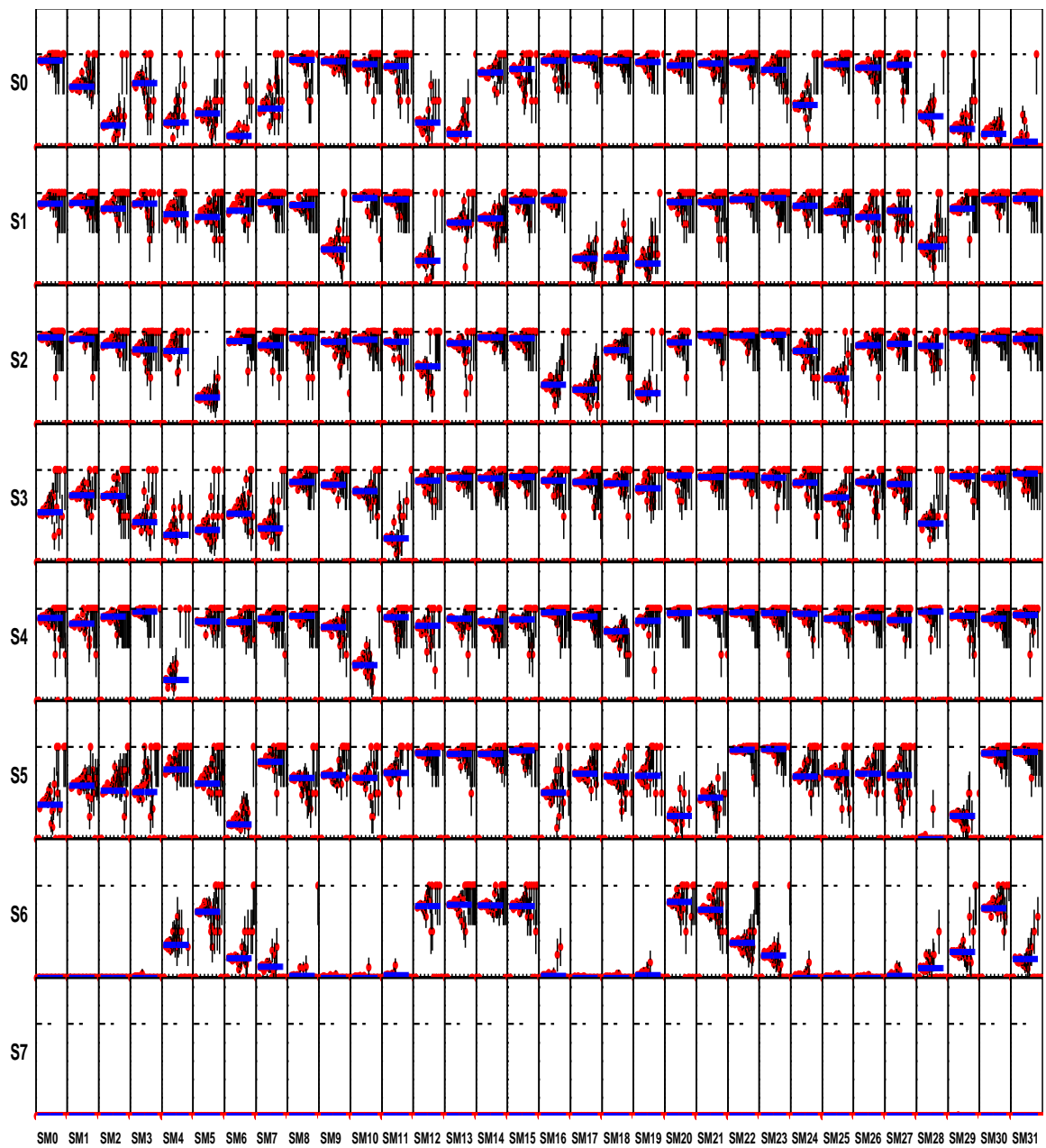


Figure F.2: (color online) RICH SM efficiencies for rungroup 0 where the bred points are the data and the blue lines the fit.

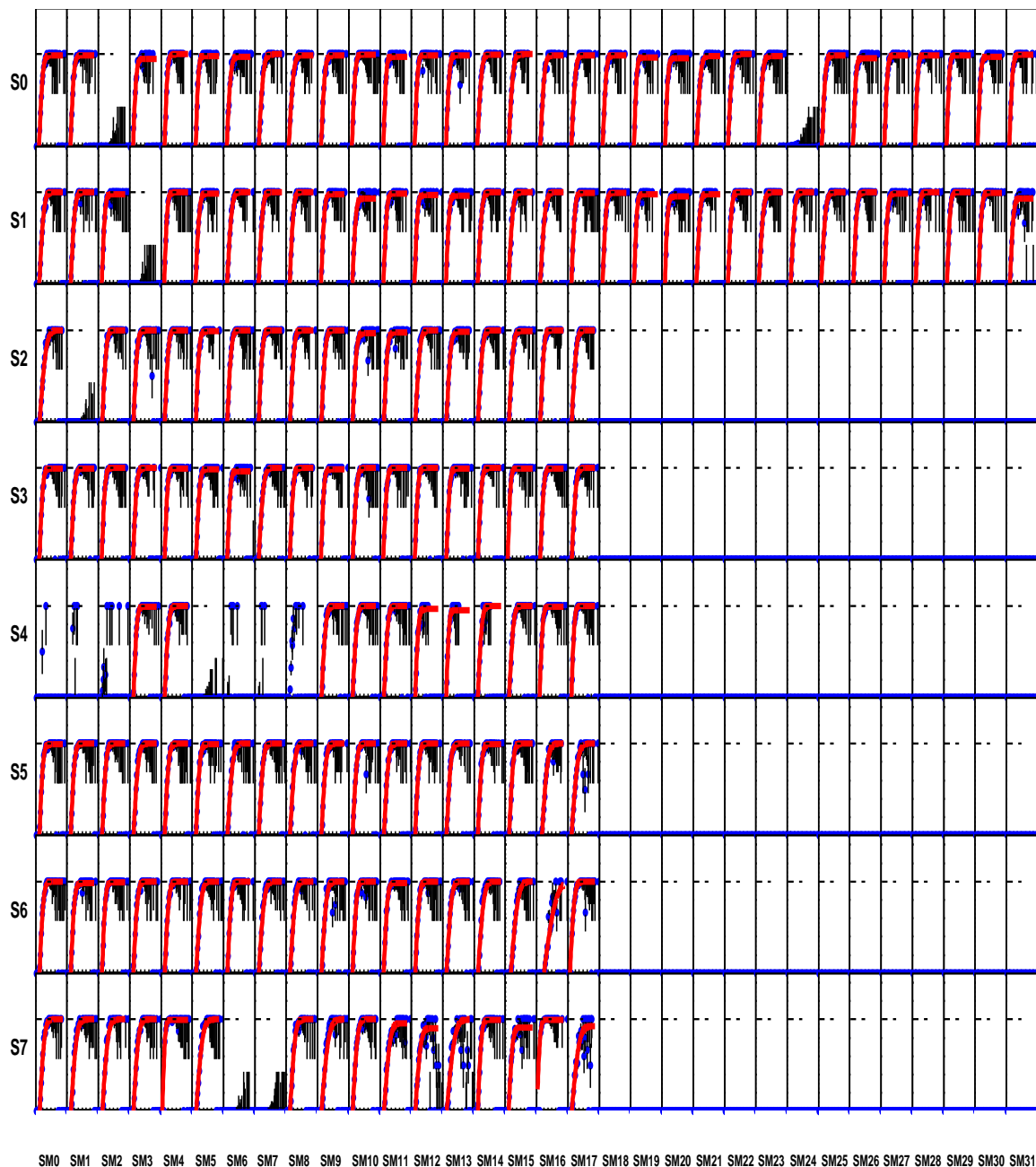


Figure F.3: (color online) EMCAL SM efficiencies for rungroup 1 where the blue points are the data and the red lines the fit.

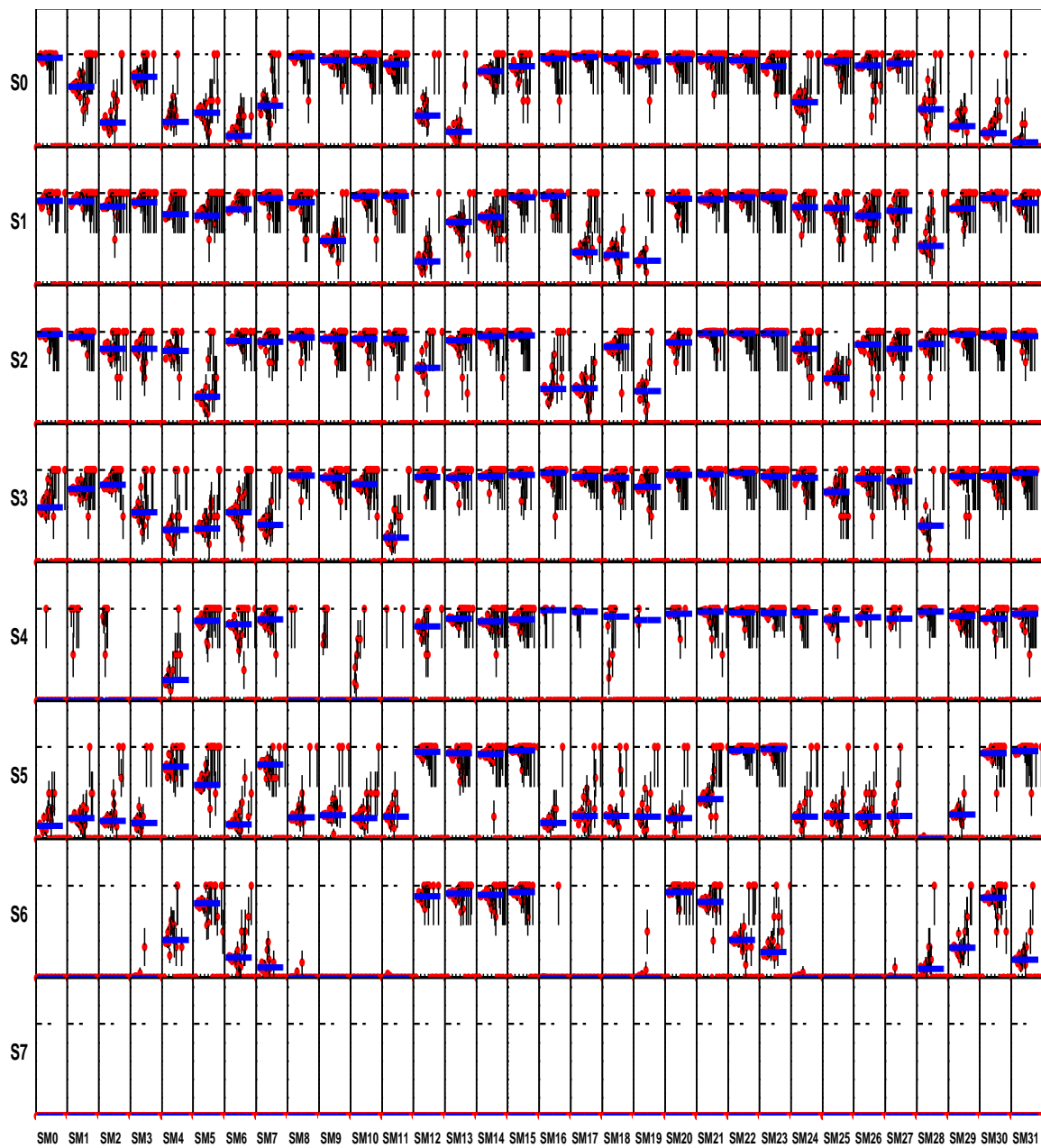


Figure F.4: (color online) RICH SM efficiencies for rungroup 1 where the bred points are the data and the blue lines the fit.

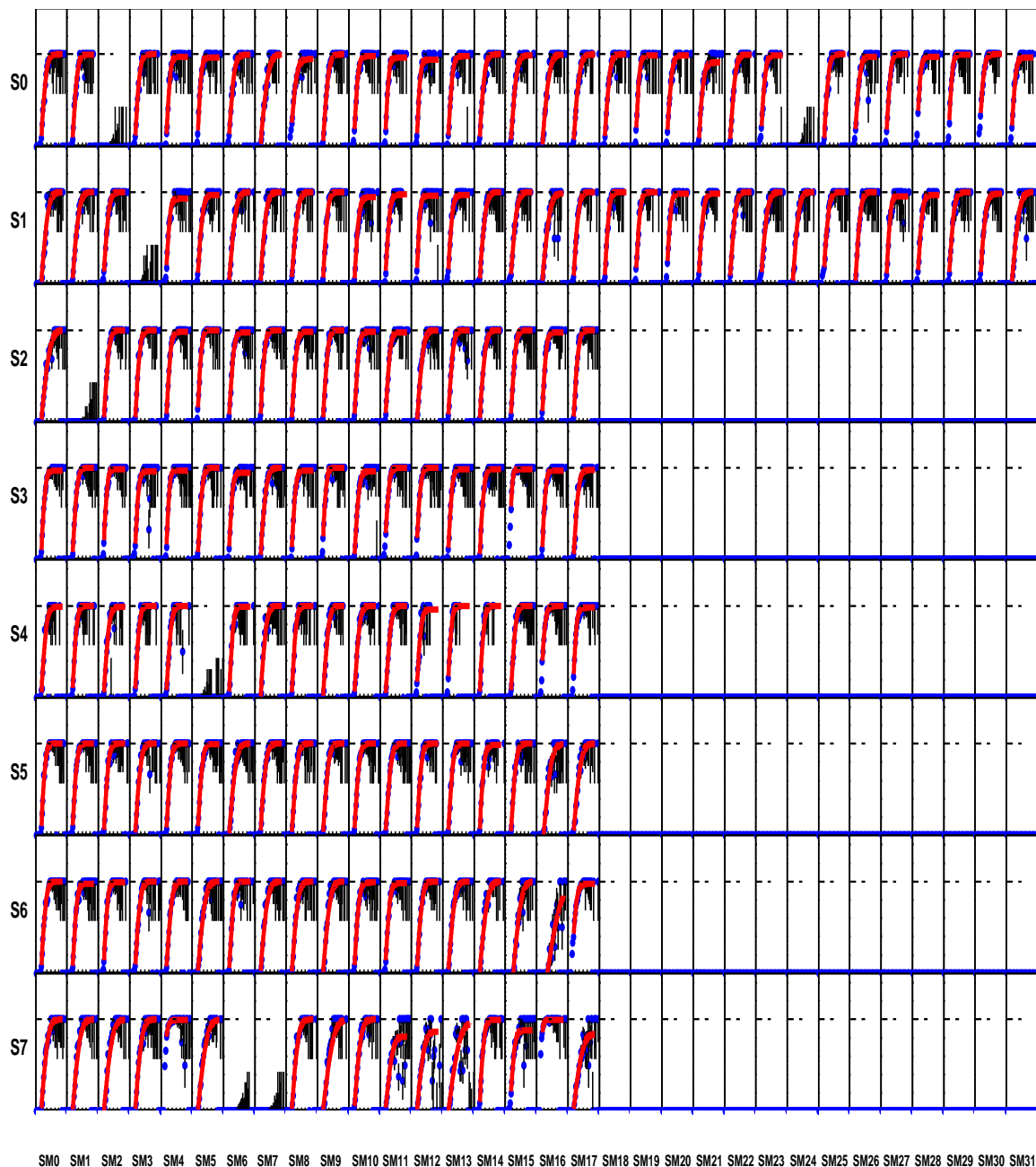


Figure F.5: (color online) EMCAL SM efficiencies for rungroup 2 where the blue points are the data and the red lines the fit.

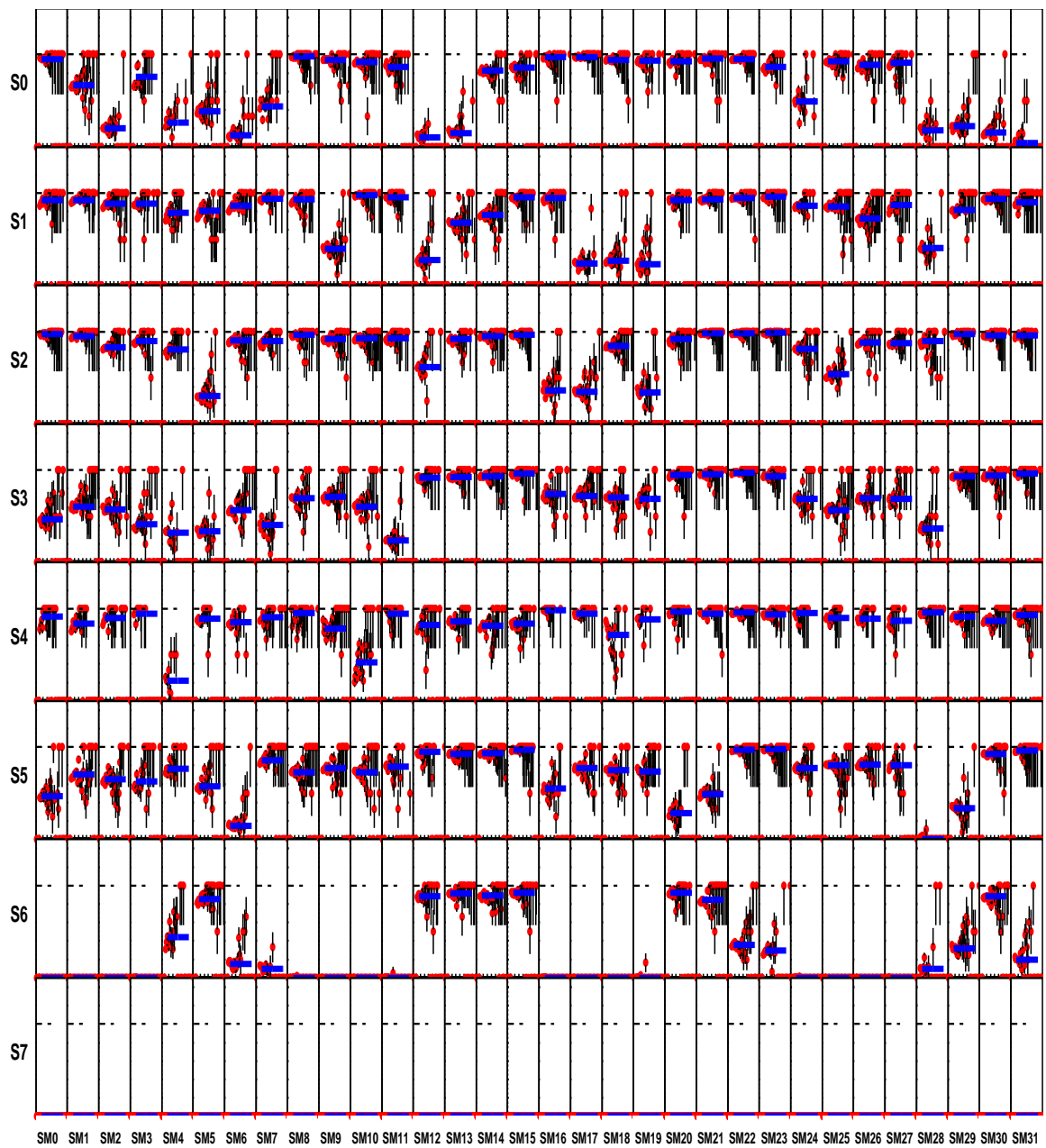


Figure F.6: (color online) RICH SM efficiencies for rungroup 2 where the bred points are the data and the blue lines the fit.

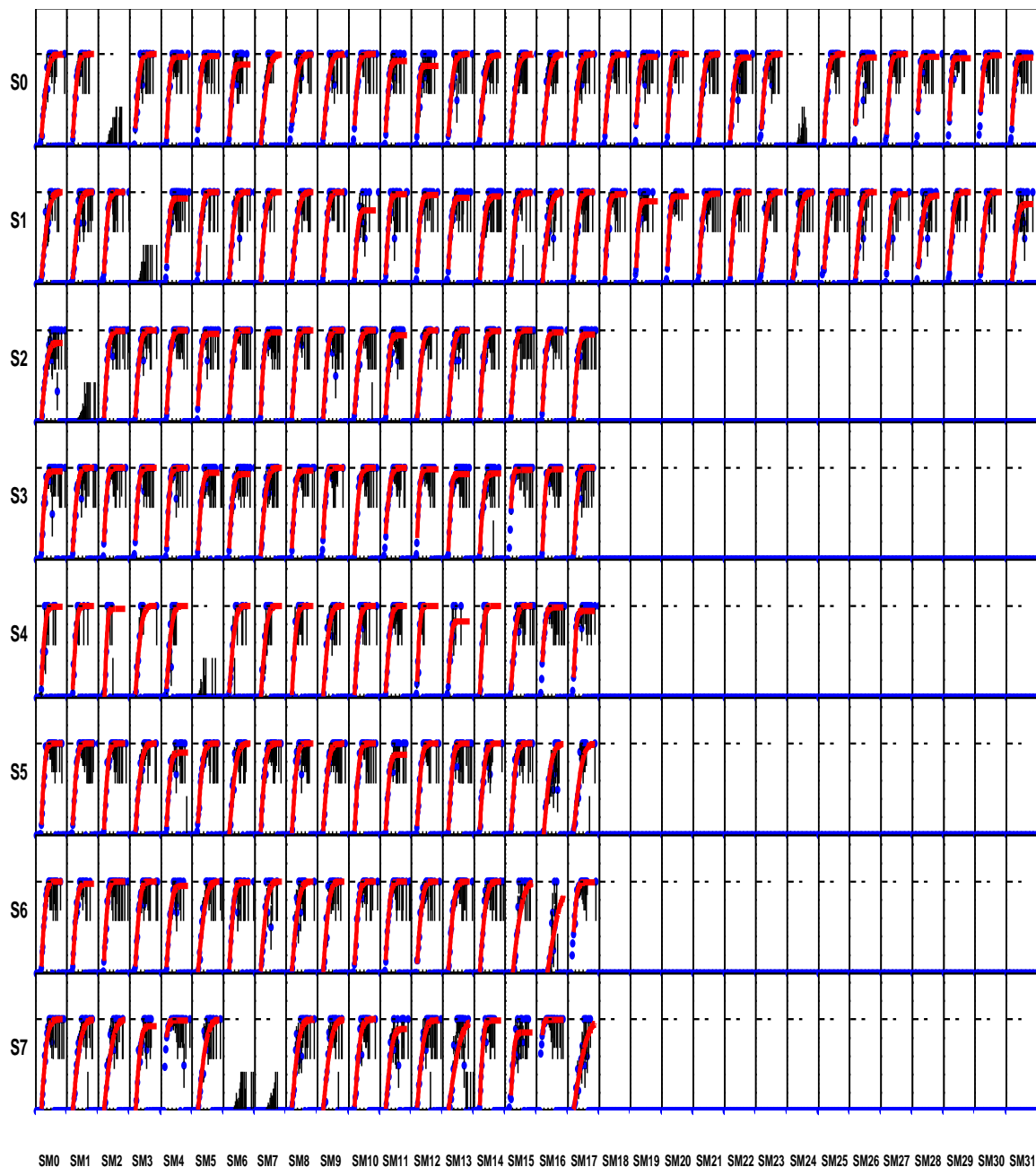


Figure F.7: (color online) EMCAL SM efficiencies for rungroup 3 where the blue points are the data and the red lines the fit.

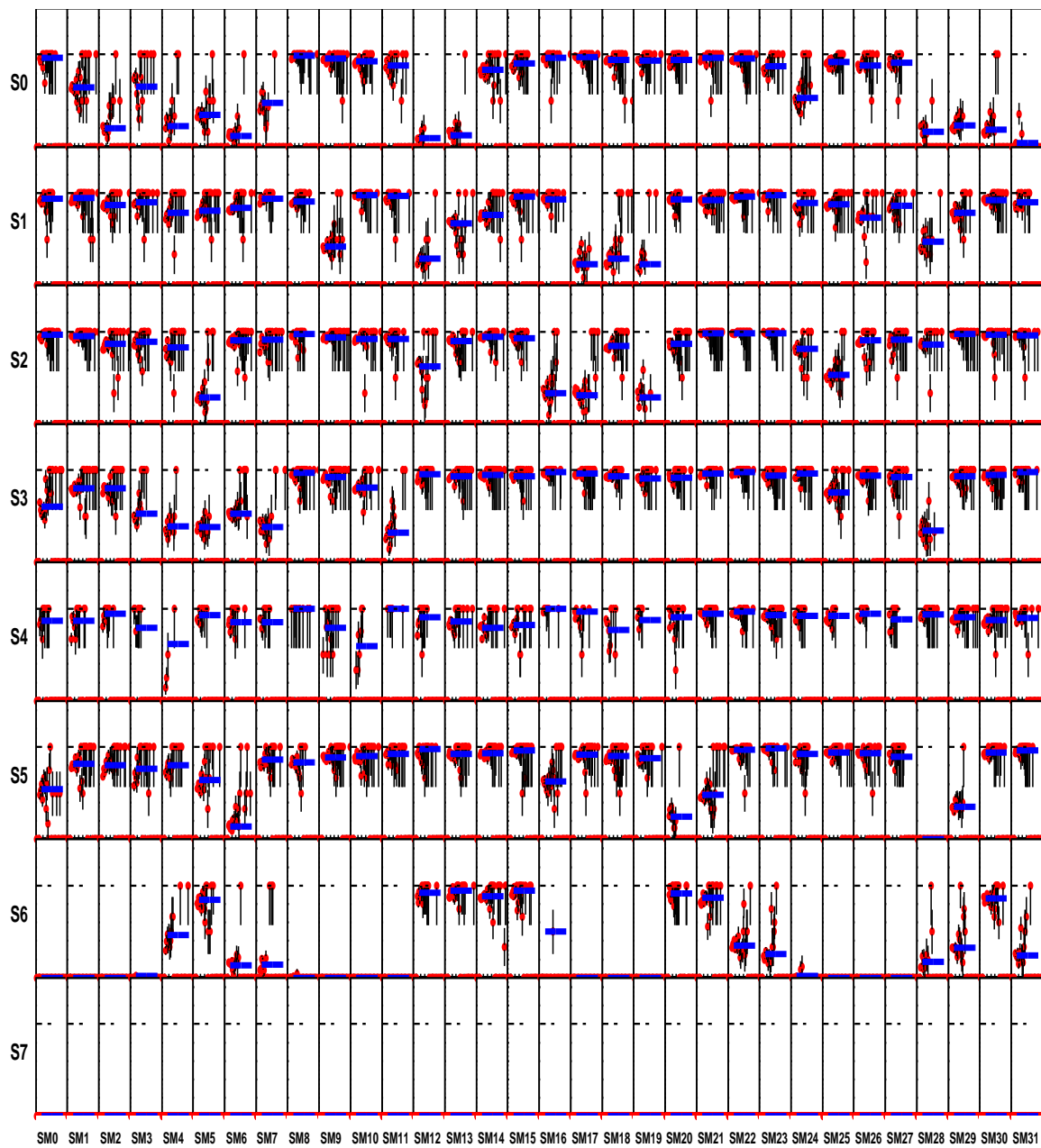


Figure F.8: (color online) RICH SM efficiencies for rungroup 3 where the bred points are the data and the blue lines the fit.

F.2 Invariant Mass Spectra in Different Centrality Bins

The invariant mass spectra for 0-20%, 20-40%, 40-60% and 60-88% central collisions are shown in Figures F.9, F.10, F.11 and F.12.

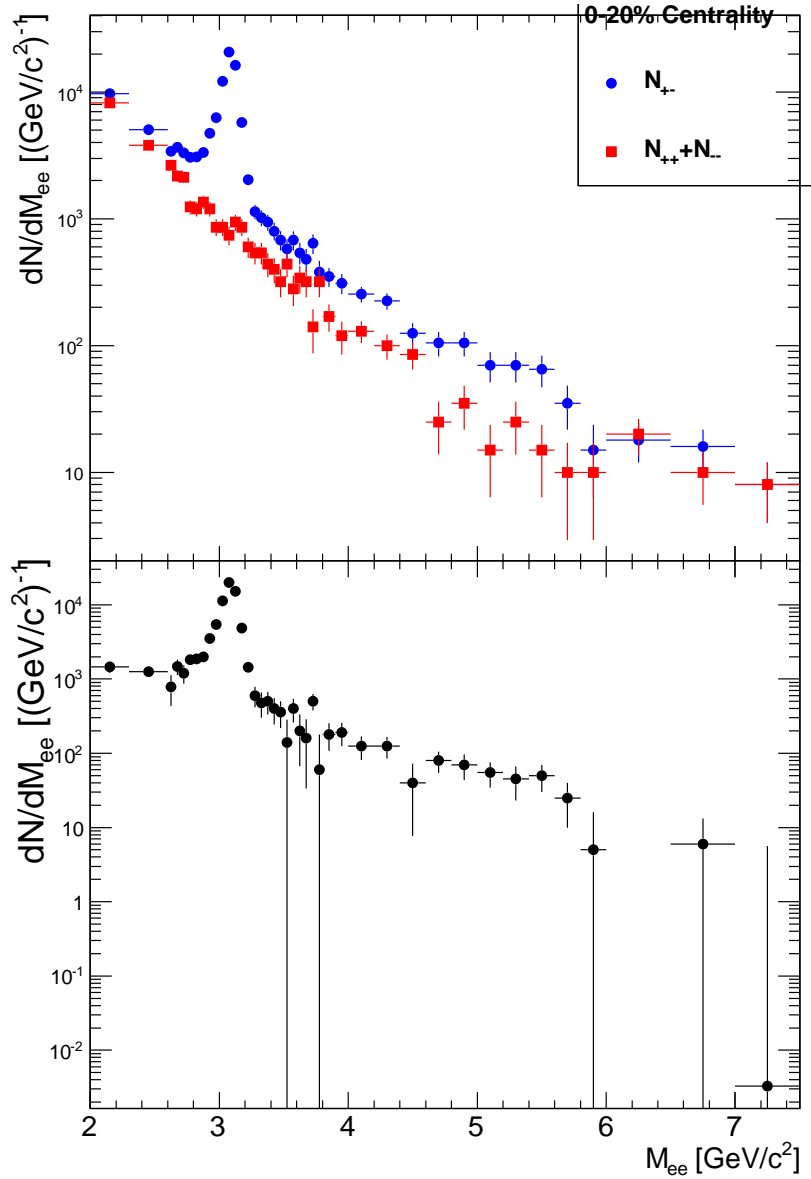


Figure F.9: Plot of the 0-20% invariant mass distributions for unlike-sign and like-sign (Top) and like-sign subtracted (Bottom).

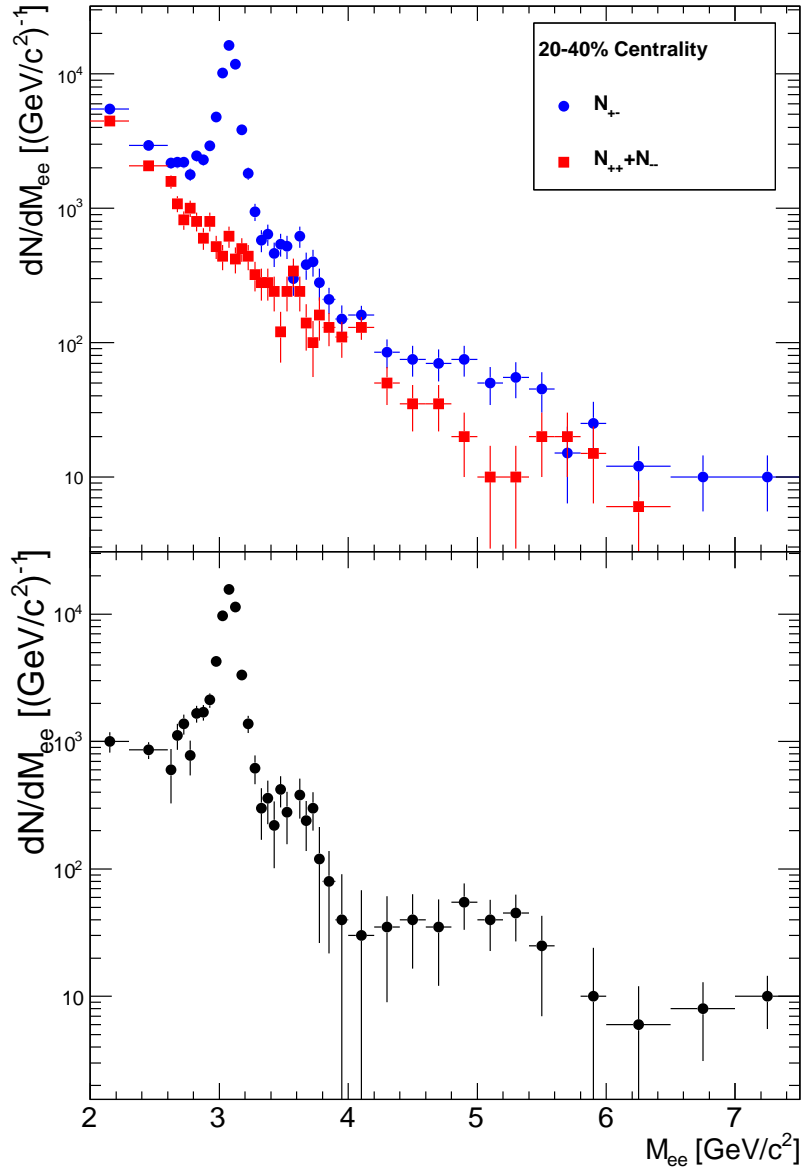


Figure F.10: Plot of the 20-40% invariant mass distributions for unlike-sign and like-sign (Top) and like-sign subtracted (Bottom).

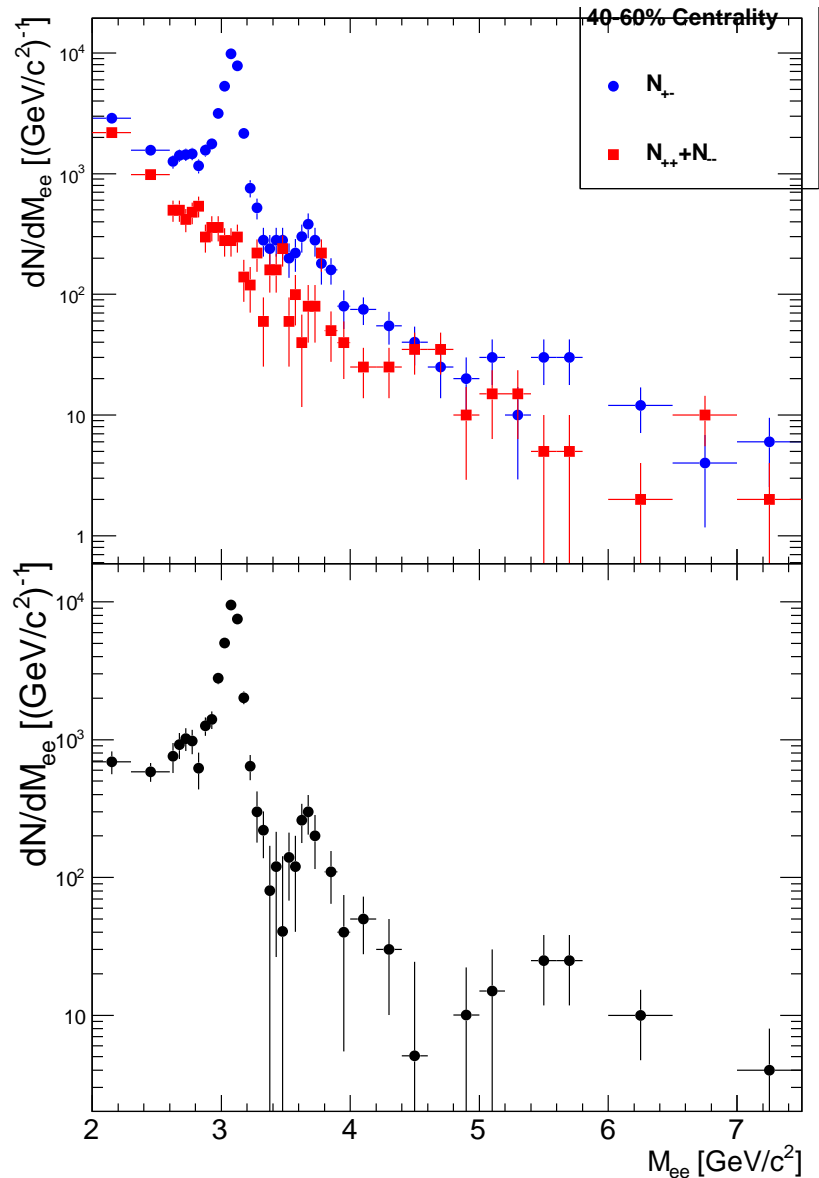


Figure F.11: Plot of the 40-60% invariant mass distributions for unlike-sign and like-sign (Top) and like-sign subtracted (Bottom).

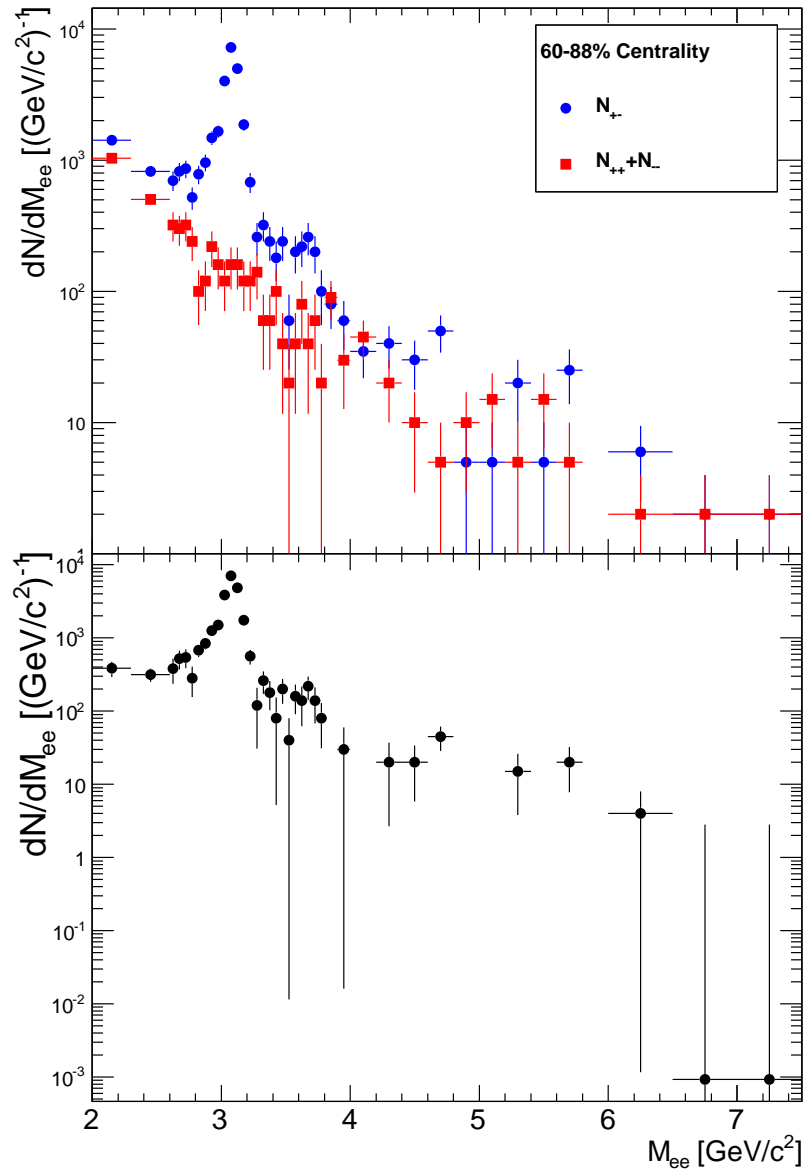


Figure F.12: Plot of the 60-88% invariant mass distributions for unlike-sign and like-sign (Top) and like-sign subtracted (Bottom).

APPENDIX G

TABLES

G.1 J/ψ Yield Values

The raw yields for each rungroup are summarized in Tab. G.1 for the first rapidity bin, Tab. G.2 for the second rapidity bin, and in Tab. G.3 third rapidity bin.

Table G.1: J/ψ counts for each rungroup and $-0.5 < y < -0.1$.

| Rapidity | p_T [GeV/c] | centrality | G0 | | G1 | | G2 | | G3 | | Total | |
|-----------|---------------|------------|----|----|----|----|-----|----|----|----|-------|----|
| | | | FG | BG | FG | BG | FG | BG | FG | BG | FG | BG |
| -0.5→-0.1 | 0→20% | 0→0.5 | 27 | 4 | 21 | 2 | 42 | 7 | 15 | 1 | 105 | 14 |
| -0.5→-0.1 | 0→20% | 0.5→1 | 63 | 13 | 34 | 6 | 99 | 10 | 51 | 2 | 247 | 31 |
| -0.5→-0.1 | 0→20% | 1→1.5 | 72 | 11 | 37 | 7 | 144 | 13 | 47 | 5 | 300 | 36 |
| -0.5→-0.1 | 0→20% | 1.5→2 | 46 | 4 | 31 | 4 | 102 | 13 | 43 | 4 | 222 | 25 |
| -0.5→-0.1 | 0→20% | 2→2.5 | 30 | 4 | 13 | 2 | 60 | 13 | 27 | 4 | 130 | 23 |
| -0.5→-0.1 | 0→20% | 2.5→3 | 19 | 2 | 13 | 2 | 38 | 5 | 14 | 2 | 84 | 11 |
| -0.5→-0.1 | 0→20% | 3→3.5 | 14 | 3 | 10 | 1 | 26 | 1 | 20 | 2 | 70 | 7 |
| -0.5→-0.1 | 0→20% | 3.5→4 | 10 | 1 | 4 | 1 | 12 | 1 | 4 | 0 | 30 | 3 |
| -0.5→-0.1 | 0→20% | 4→4.5 | 6 | 1 | 1 | 0 | 10 | 0 | 4 | 1 | 21 | 2 |
| -0.5→-0.1 | 0→20% | 4.5→5 | 4 | 0 | 1 | 0 | 6 | 0 | 3 | 0 | 14 | 0 |
| -0.5→-0.1 | 0→20% | 5→6 | 6 | 4 | 4 | 1 | 5 | 1 | 3 | 1 | 15 | 7 |
| -0.5→-0.1 | 0→20% | 6→7 | 1 | 0 | 1 | 0 | 2 | 3 | 0 | 1 | 4 | 4 |
| -0.5→-0.1 | 0→20% | 7→9 | 2 | 0 | 1 | 0 | 5 | 1 | 1 | 1 | 9 | 2 |
| -0.5→-0.1 | 0→20% | 9→12 | 0 | 0 | 0 | 0 | 2 | 1 | 0 | 0 | 2 | 1 |
| -0.5→-0.1 | 0→20% | 12→15 | 0 | 0 | 0 | 0 | 0 | 0 | 0 | 0 | 0 | 0 |
| -0.5→-0.1 | 20→40% | 0→0.5 | 19 | 4 | 7 | 0 | 43 | 2 | 18 | 0 | 87 | 6 |
| -0.5→-0.1 | 20→40% | 0.5→1 | 47 | 8 | 25 | 1 | 89 | 6 | 39 | 3 | 200 | 18 |
| -0.5→-0.1 | 20→40% | 1→1.5 | 44 | 5 | 30 | 7 | 82 | 11 | 35 | 6 | 191 | 29 |
| -0.5→-0.1 | 20→40% | 1.5→2 | 38 | 4 | 24 | 4 | 68 | 5 | 25 | 2 | 155 | 15 |
| -0.5→-0.1 | 20→40% | 2→2.5 | 20 | 3 | 12 | 1 | 34 | 3 | 16 | 2 | 82 | 9 |
| -0.5→-0.1 | 20→40% | 2.5→3 | 11 | 1 | 9 | 0 | 19 | 2 | 11 | 2 | 50 | 5 |
| -0.5→-0.1 | 20→40% | 3→3.5 | 5 | 1 | 5 | 1 | 21 | 1 | 9 | 2 | 40 | 5 |
| -0.5→-0.1 | 20→40% | 3.5→4 | 2 | 0 | 4 | 0 | 14 | 0 | 2 | 0 | 22 | 0 |
| -0.5→-0.1 | 20→40% | 4→4.5 | 2 | 0 | 2 | 0 | 4 | 1 | 3 | 1 | 11 | 2 |
| -0.5→-0.1 | 20→40% | 4.5→5 | 1 | 0 | 0 | 0 | 2 | 0 | 0 | 0 | 3 | 0 |
| -0.5→-0.1 | 20→40% | 5→6 | 3 | 1 | 3 | 0 | 7 | 0 | 0 | 0 | 13 | 1 |
| -0.5→-0.1 | 20→40% | 6→7 | 1 | 0 | 0 | 0 | 2 | 0 | 1 | 1 | 4 | 1 |
| -0.5→-0.1 | 20→40% | 7→9 | 2 | 0 | 0 | 0 | 1 | 1 | 0 | 0 | 3 | 1 |
| -0.5→-0.1 | 20→40% | 9→12 | 2 | 0 | 0 | 0 | 3 | 0 | 0 | 0 | 5 | 0 |
| -0.5→-0.1 | 20→40% | 12→15 | 0 | 0 | 0 | 0 | 1 | 0 | 0 | 0 | 1 | 0 |
| -0.5→-0.1 | 40→60% | 0→0.5 | 18 | 1 | 1 | 0 | 30 | 1 | 9 | 1 | 58 | 3 |
| -0.5→-0.1 | 40→60% | 0.5→1 | 21 | 1 | 14 | 1 | 62 | 5 | 22 | 2 | 119 | 9 |
| -0.5→-0.1 | 40→60% | 1→1.5 | 29 | 2 | 19 | 2 | 50 | 8 | 29 | 1 | 127 | 13 |
| -0.5→-0.1 | 40→60% | 1.5→2 | 28 | 1 | 13 | 1 | 41 | 1 | 18 | 0 | 100 | 3 |
| -0.5→-0.1 | 40→60% | 2→2.5 | 11 | 0 | 9 | 0 | 24 | 1 | 14 | 0 | 58 | 1 |
| -0.5→-0.1 | 40→60% | 2.5→3 | 12 | 5 | 10 | 1 | 11 | 0 | 5 | 0 | 38 | 6 |
| -0.5→-0.1 | 40→60% | 3→3.5 | 2 | 1 | 4 | 1 | 9 | 1 | 5 | 2 | 20 | 5 |
| -0.5→-0.1 | 40→60% | 3.5→4 | 3 | 1 | 3 | 0 | 6 | 1 | 0 | 1 | 12 | 3 |
| -0.5→-0.1 | 40→60% | 4→4.5 | 1 | 0 | 0 | 0 | 3 | 1 | 3 | 1 | 7 | 2 |
| -0.5→-0.1 | 40→60% | 4.5→5 | 0 | 1 | 0 | 0 | 5 | 0 | 0 | 0 | 5 | 1 |
| -0.5→-0.1 | 40→60% | 5→6 | 1 | 0 | 1 | 0 | 3 | 0 | 2 | 0 | 7 | 0 |
| -0.5→-0.1 | 40→60% | 6→7 | 0 | 0 | 1 | 0 | 2 | 1 | 1 | 0 | 4 | 1 |
| -0.5→-0.1 | 40→60% | 7→9 | 0 | 1 | 0 | 0 | 1 | 2 | 0 | 0 | 1 | 3 |
| -0.5→-0.1 | 40→60% | 9→12 | 0 | 1 | 0 | 0 | 0 | 0 | 0 | 0 | 0 | 1 |
| -0.5→-0.1 | 40→60% | 12→15 | 0 | 0 | 0 | 0 | 0 | 0 | 0 | 0 | 0 | 0 |
| -0.5→-0.1 | 60→88% | 0→0.5 | 9 | 0 | 6 | 2 | 15 | 0 | 3 | 0 | 33 | 2 |
| -0.5→-0.1 | 60→88% | 0.5→1 | 14 | 0 | 7 | 2 | 41 | 3 | 21 | 0 | 83 | 5 |
| -0.5→-0.1 | 60→88% | 1→1.5 | 22 | 1 | 13 | 1 | 33 | 4 | 17 | 0 | 85 | 6 |
| -0.5→-0.1 | 60→88% | 1.5→2 | 16 | 0 | 12 | 0 | 31 | 0 | 17 | 0 | 76 | 0 |
| -0.5→-0.1 | 60→88% | 2→2.5 | 8 | 0 | 3 | 0 | 12 | 1 | 6 | 0 | 29 | 1 |
| -0.5→-0.1 | 60→88% | 2.5→3 | 5 | 0 | 4 | 0 | 10 | 0 | 7 | 0 | 26 | 0 |
| -0.5→-0.1 | 60→88% | 3→3.5 | 4 | 0 | 2 | 1 | 6 | 0 | 4 | 0 | 16 | 1 |
| -0.5→-0.1 | 60→88% | 3.5→4 | 2 | 0 | 1 | 0 | 3 | 0 | 1 | 1 | 7 | 1 |
| -0.5→-0.1 | 60→88% | 4→4.5 | 2 | 0 | 2 | 0 | 0 | 1 | 0 | 0 | 4 | 1 |
| -0.5→-0.1 | 60→88% | 4.5→5 | 1 | 0 | 1 | 0 | 0 | 0 | 0 | 0 | 2 | 0 |
| -0.5→-0.1 | 60→88% | 5→6 | 2 | 0 | 1 | 0 | 1 | 0 | 1 | 0 | 5 | 0 |
| -0.5→-0.1 | 60→88% | 6→7 | 0 | 0 | 0 | 0 | 2 | 1 | 0 | 0 | 2 | 1 |
| -0.5→-0.1 | 60→88% | 7→9 | 1 | 0 | 1 | 0 | 1 | 0 | 0 | 0 | 3 | 0 |
| -0.5→-0.1 | 60→88% | 9→12 | 0 | 0 | 0 | 0 | 0 | 0 | 0 | 0 | 0 | 0 |
| -0.5→-0.1 | 60→88% | 12→15 | 0 | 0 | 0 | 0 | 0 | 0 | 0 | 0 | 0 | 0 |

Table G.2: J/ψ counts for each rungroup and $-0.1 < y < 0.1$.

| Rapidity | p_T [GeV/c] | centrality | G0 | | G1 | | G2 | | G3 | | Total | |
|----------|---------------|------------|-----|----|----|----|-----|----|----|----|-------|----|
| | | | FG | BG | FG | BG | FG | BG | FG | BG | FG | BG |
| -0.1→0.1 | 0→20% | 0→0.5 | 58 | 5 | 23 | 7 | 77 | 4 | 30 | 4 | 188 | 20 |
| -0.1→0.1 | 0→20% | 0.5→1 | 104 | 24 | 51 | 8 | 154 | 16 | 80 | 8 | 389 | 56 |
| -0.1→0.1 | 0→20% | 1→1.5 | 109 | 13 | 60 | 9 | 157 | 21 | 69 | 12 | 395 | 55 |
| -0.1→0.1 | 0→20% | 1.5→2 | 63 | 8 | 44 | 4 | 110 | 9 | 58 | 10 | 275 | 31 |
| -0.1→0.1 | 0→20% | 2→2.5 | 46 | 7 | 21 | 3 | 70 | 8 | 32 | 3 | 169 | 21 |
| -0.1→0.1 | 0→20% | 2.5→3 | 20 | 2 | 9 | 0 | 34 | 3 | 17 | 3 | 80 | 8 |
| -0.1→0.1 | 0→20% | 3→3.5 | 7 | 1 | 10 | 0 | 24 | 4 | 10 | 0 | 51 | 5 |
| -0.1→0.1 | 0→20% | 3.5→4 | 6 | 1 | 5 | 1 | 8 | 1 | 5 | 1 | 24 | 4 |
| -0.1→0.1 | 0→20% | 4→4.5 | 6 | 0 | 3 | 1 | 9 | 0 | 5 | 0 | 23 | 1 |
| -0.1→0.1 | 0→20% | 4.5→5 | 5 | 0 | 2 | 0 | 1 | 1 | 4 | 0 | 12 | 1 |
| -0.1→0.1 | 0→20% | 5→6 | 3 | 0 | 2 | 0 | 5 | 1 | 1 | 0 | 11 | 1 |
| -0.1→0.1 | 0→20% | 6→7 | 3 | 0 | 1 | 0 | 3 | 0 | 0 | 0 | 7 | 0 |
| -0.1→0.1 | 0→20% | 7→9 | 1 | 0 | 1 | 0 | 2 | 0 | 1 | 0 | 5 | 0 |
| -0.1→0.1 | 0→20% | 9→12 | 0 | 0 | 0 | 0 | 0 | 0 | 2 | 0 | 2 | 0 |
| -0.1→0.1 | 0→20% | 12→15 | 0 | 0 | 1 | 0 | 0 | 0 | 0 | 0 | 1 | 0 |
| -0.1→0.1 | 20→40% | 0→0.5 | 36 | 1 | 12 | 2 | 52 | 1 | 21 | 4 | 121 | 8 |
| -0.1→0.1 | 20→40% | 0.5→1 | 73 | 9 | 36 | 4 | 117 | 6 | 41 | 6 | 267 | 25 |
| -0.1→0.1 | 20→40% | 1→1.5 | 66 | 9 | 30 | 1 | 116 | 11 | 53 | 2 | 265 | 23 |
| -0.1→0.1 | 20→40% | 1.5→2 | 60 | 8 | 20 | 6 | 78 | 9 | 37 | 2 | 195 | 25 |
| -0.1→0.1 | 20→40% | 2→2.5 | 20 | 5 | 27 | 4 | 35 | 2 | 14 | 4 | 96 | 15 |
| -0.1→0.1 | 20→40% | 2.5→3 | 14 | 2 | 6 | 1 | 27 | 2 | 19 | 2 | 66 | 7 |
| -0.1→0.1 | 20→40% | 3→3.5 | 11 | 1 | 7 | 0 | 7 | 2 | 4 | 0 | 29 | 3 |
| -0.1→0.1 | 20→40% | 3.5→4 | 10 | 1 | 5 | 0 | 8 | 0 | 7 | 0 | 30 | 1 |
| -0.1→0.1 | 20→40% | 4→4.5 | 4 | 0 | 4 | 0 | 7 | 0 | 1 | 1 | 16 | 1 |
| -0.1→0.1 | 20→40% | 4.5→5 | 3 | 0 | 3 | 0 | 6 | 0 | 3 | 0 | 15 | 0 |
| -0.1→0.1 | 20→40% | 5→6 | 3 | 0 | 2 | 0 | 7 | 0 | 4 | 0 | 16 | 0 |
| -0.1→0.1 | 20→40% | 6→7 | 1 | 0 | 0 | 0 | 3 | 0 | 0 | 0 | 4 | 0 |
| -0.1→0.1 | 20→40% | 7→9 | 0 | 0 | 2 | 0 | 3 | 0 | 0 | 0 | 5 | 0 |
| -0.1→0.1 | 20→40% | 9→12 | 1 | 0 | 1 | 0 | 1 | 0 | 0 | 0 | 3 | 0 |
| -0.1→0.1 | 20→40% | 12→15 | 0 | 1 | 0 | 0 | 0 | 0 | 0 | 0 | 0 | 1 |
| -0.1→0.1 | 40→60% | 0→0.5 | 14 | 1 | 7 | 0 | 31 | 1 | 15 | 0 | 67 | 2 |
| -0.1→0.1 | 40→60% | 0.5→1 | 49 | 5 | 23 | 3 | 64 | 7 | 28 | 2 | 164 | 17 |
| -0.1→0.1 | 40→60% | 1→1.5 | 42 | 5 | 23 | 2 | 76 | 12 | 28 | 2 | 169 | 21 |
| -0.1→0.1 | 40→60% | 1.5→2 | 37 | 1 | 12 | 1 | 43 | 3 | 25 | 1 | 117 | 6 |
| -0.1→0.1 | 40→60% | 2→2.5 | 20 | 1 | 9 | 1 | 28 | 1 | 8 | 2 | 65 | 5 |
| -0.1→0.1 | 40→60% | 2.5→3 | 7 | 0 | 6 | 0 | 14 | 1 | 6 | 0 | 33 | 1 |
| -0.1→0.1 | 40→60% | 3→3.5 | 9 | 0 | 3 | 0 | 8 | 1 | 5 | 0 | 25 | 1 |
| -0.1→0.1 | 40→60% | 3.5→4 | 3 | 0 | 0 | 0 | 1 | 0 | 3 | 1 | 7 | 1 |
| -0.1→0.1 | 40→60% | 4→4.5 | 1 | 0 | 0 | 0 | 1 | 0 | 3 | 0 | 5 | 0 |
| -0.1→0.1 | 40→60% | 4.5→5 | 1 | 0 | 2 | 0 | 3 | 0 | 0 | 0 | 6 | 0 |
| -0.1→0.1 | 40→60% | 5→6 | 4 | 0 | 0 | 0 | 0 | 0 | 3 | 0 | 7 | 0 |
| -0.1→0.1 | 40→60% | 6→7 | 0 | 0 | 0 | 0 | 1 | 0 | 0 | 0 | 1 | 0 |
| -0.1→0.1 | 40→60% | 7→9 | 0 | 0 | 0 | 1 | 2 | 0 | 0 | 0 | 2 | 1 |
| -0.1→0.1 | 40→60% | 9→12 | 0 | 0 | 1 | 0 | 0 | 0 | 0 | 0 | 1 | 0 |
| -0.1→0.1 | 40→60% | 12→15 | 0 | 0 | 0 | 0 | 0 | 0 | 0 | 0 | 0 | 0 |
| -0.1→0.1 | 60→88% | 0→0.5 | 16 | 0 | 7 | 1 | 25 | 0 | 6 | 0 | 54 | 1 |
| -0.1→0.1 | 60→88% | 0.5→1 | 34 | 4 | 18 | 3 | 49 | 3 | 25 | 2 | 126 | 12 |
| -0.1→0.1 | 60→88% | 1→1.5 | 30 | 1 | 18 | 0 | 42 | 5 | 17 | 2 | 107 | 8 |
| -0.1→0.1 | 60→88% | 1.5→2 | 20 | 2 | 10 | 0 | 33 | 3 | 7 | 1 | 70 | 6 |
| -0.1→0.1 | 60→88% | 2→2.5 | 9 | 0 | 6 | 0 | 29 | 3 | 5 | 2 | 49 | 5 |
| -0.1→0.1 | 60→88% | 2.5→3 | 7 | 0 | 3 | 0 | 11 | 2 | 4 | 0 | 25 | 2 |
| -0.1→0.1 | 60→88% | 3→3.5 | 2 | 0 | 0 | 0 | 5 | 0 | 10 | 0 | 17 | 0 |
| -0.1→0.1 | 60→88% | 3.5→4 | 1 | 0 | 0 | 0 | 3 | 1 | 2 | 0 | 6 | 1 |
| -0.1→0.1 | 60→88% | 4→4.5 | 2 | 0 | 1 | 0 | 0 | 0 | 0 | 0 | 3 | 0 |
| -0.1→0.1 | 60→88% | 4.5→5 | 0 | 0 | 1 | 0 | 3 | 0 | 0 | 0 | 4 | 0 |
| -0.1→0.1 | 60→88% | 5→6 | 0 | 0 | 1 | 0 | 1 | 0 | 0 | 0 | 2 | 0 |
| -0.1→0.1 | 60→88% | 6→7 | 0 | 0 | 0 | 0 | 0 | 0 | 1 | 0 | 1 | 0 |
| -0.1→0.1 | 60→88% | 7→9 | 2 | 0 | 0 | 0 | 2 | 0 | 0 | 0 | 4 | 0 |
| -0.1→0.1 | 60→88% | 9→12 | 0 | 0 | 0 | 0 | 0 | 0 | 0 | 0 | 0 | 0 |
| -0.1→0.1 | 60→88% | 12→15 | 0 | 0 | 0 | 0 | 0 | 0 | 1 | 0 | 0 | 1 |

Table G.3: J/ψ counts for each rungroup and $0.1 < y < 0.5$.

| Rapidity | p_T [GeV/c] | centrality | G0 | | G1 | | G2 | | G3 | | Total | |
|----------|---------------|------------|----|----|----|----|----|----|----|----|-------|----|
| | | | FG | BG | FG | BG | FG | BG | FG | BG | FG | BG |
| 0.1→0.5 | 0→20% | 0→0.5 | 27 | 4 | 11 | 4 | 46 | 2 | 15 | 3 | 99 | 13 |
| 0.1→0.5 | 0→20% | 0.5→1 | 58 | 6 | 26 | 2 | 79 | 10 | 32 | 1 | 195 | 19 |
| 0.1→0.5 | 0→20% | 1→1.5 | 77 | 6 | 32 | 3 | 96 | 12 | 41 | 4 | 246 | 25 |
| 0.1→0.5 | 0→20% | 1.5→2 | 52 | 4 | 21 | 3 | 85 | 7 | 33 | 2 | 191 | 16 |
| 0.1→0.5 | 0→20% | 2→2.5 | 39 | 3 | 16 | 2 | 52 | 4 | 24 | 2 | 131 | 11 |
| 0.1→0.5 | 0→20% | 2.5→3 | 24 | 4 | 13 | 1 | 26 | 3 | 8 | 2 | 71 | 10 |
| 0.1→0.5 | 0→20% | 3→3.5 | 7 | 0 | 6 | 0 | 26 | 0 | 8 | 0 | 47 | 0 |
| 0.1→0.5 | 0→20% | 3.5→4 | 12 | 0 | 6 | 0 | 8 | 1 | 4 | 0 | 30 | 1 |
| 0.1→0.5 | 0→20% | 4→4.5 | 6 | 0 | 2 | 0 | 11 | 1 | 2 | 1 | 21 | 2 |
| 0.1→0.5 | 0→20% | 4.5→5 | 0 | 0 | 0 | 0 | 3 | 1 | 1 | 0 | 4 | 1 |
| 0.1→0.5 | 0→20% | 5→6 | 4 | 0 | 2 | 0 | 6 | 1 | 1 | 2 | 13 | 3 |
| 0.1→0.5 | 0→20% | 6→7 | 0 | 1 | 0 | 0 | 3 | 0 | 0 | 0 | 3 | 1 |
| 0.1→0.5 | 0→20% | 7→9 | 1 | 1 | 1 | 0 | 4 | 0 | 0 | 0 | 6 | 1 |
| 0.1→0.5 | 0→20% | 9→12 | 0 | 0 | 0 | 0 | 0 | 0 | 0 | 0 | 0 | 0 |
| 0.1→0.5 | 0→20% | 12→15 | 0 | 0 | 0 | 0 | 1 | 0 | 0 | 0 | 1 | 0 |
| 0.1→0.5 | 20→40% | 0→0.5 | 13 | 2 | 9 | 0 | 30 | 1 | 10 | 1 | 62 | 4 |
| 0.1→0.5 | 20→40% | 0.5→1 | 55 | 4 | 24 | 0 | 67 | 1 | 25 | 3 | 171 | 8 |
| 0.1→0.5 | 20→40% | 1→1.5 | 50 | 7 | 24 | 2 | 71 | 11 | 31 | 1 | 176 | 21 |
| 0.1→0.5 | 20→40% | 1.5→2 | 38 | 5 | 17 | 0 | 64 | 7 | 34 | 3 | 153 | 15 |
| 0.1→0.5 | 20→40% | 2→2.5 | 25 | 4 | 14 | 0 | 51 | 2 | 11 | 2 | 101 | 8 |
| 0.1→0.5 | 20→40% | 2.5→3 | 8 | 1 | 4 | 0 | 21 | 1 | 5 | 0 | 38 | 2 |
| 0.1→0.5 | 20→40% | 3→3.5 | 6 | 1 | 4 | 1 | 12 | 1 | 6 | 0 | 28 | 3 |
| 0.1→0.5 | 20→40% | 3.5→4 | 8 | 0 | 1 | 0 | 3 | 1 | 6 | 1 | 18 | 2 |
| 0.1→0.5 | 20→40% | 4→4.5 | 6 | 0 | 0 | 0 | 4 | 0 | 5 | 0 | 15 | 0 |
| 0.1→0.5 | 20→40% | 4.5→5 | 4 | 1 | 0 | 0 | 4 | 1 | 1 | 1 | 9 | 3 |
| 0.1→0.5 | 20→40% | 5→6 | 1 | 0 | 3 | 0 | 2 | 2 | 3 | 0 | 9 | 2 |
| 0.1→0.5 | 20→40% | 6→7 | 1 | 0 | 2 | 0 | 3 | 0 | 0 | 0 | 6 | 0 |
| 0.1→0.5 | 20→40% | 7→9 | 0 | 0 | 0 | 0 | 0 | 0 | 0 | 0 | 0 | 0 |
| 0.1→0.5 | 20→40% | 9→12 | 0 | 0 | 0 | 0 | 2 | 0 | 0 | 0 | 2 | 0 |
| 0.1→0.5 | 20→40% | 12→15 | 0 | 0 | 0 | 0 | 0 | 0 | 0 | 0 | 0 | 0 |
| 0.1→0.5 | 40→60% | 0→0.5 | 17 | 0 | 8 | 1 | 18 | 0 | 6 | 0 | 49 | 1 |
| 0.1→0.5 | 40→60% | 0.5→1 | 24 | 1 | 16 | 1 | 34 | 3 | 14 | 0 | 88 | 5 |
| 0.1→0.5 | 40→60% | 1→1.5 | 28 | 1 | 17 | 1 | 49 | 5 | 15 | 1 | 109 | 8 |
| 0.1→0.5 | 40→60% | 1.5→2 | 20 | 4 | 8 | 0 | 32 | 3 | 12 | 1 | 72 | 8 |
| 0.1→0.5 | 40→60% | 2→2.5 | 13 | 1 | 8 | 0 | 20 | 1 | 9 | 0 | 50 | 2 |
| 0.1→0.5 | 40→60% | 2.5→3 | 3 | 0 | 4 | 0 | 13 | 1 | 5 | 0 | 25 | 1 |
| 0.1→0.5 | 40→60% | 3→3.5 | 3 | 1 | 3 | 0 | 7 | 2 | 2 | 0 | 15 | 3 |
| 0.1→0.5 | 40→60% | 3.5→4 | 2 | 0 | 2 | 0 | 3 | 2 | 0 | 0 | 7 | 2 |
| 0.1→0.5 | 40→60% | 4→4.5 | 0 | 0 | 1 | 0 | 3 | 0 | 2 | 0 | 6 | 0 |
| 0.1→0.5 | 40→60% | 4.5→5 | 3 | 0 | 1 | 0 | 3 | 1 | 1 | 0 | 8 | 1 |
| 0.1→0.5 | 40→60% | 5→6 | 2 | 0 | 2 | 0 | 6 | 1 | 2 | 0 | 12 | 1 |
| 0.1→0.5 | 40→60% | 6→7 | 1 | 0 | 1 | 0 | 3 | 0 | 0 | 0 | 5 | 0 |
| 0.1→0.5 | 40→60% | 7→9 | 0 | 0 | 0 | 0 | 1 | 0 | 1 | 0 | 2 | 0 |
| 0.1→0.5 | 40→60% | 9→12 | 0 | 0 | 0 | 0 | 0 | 0 | 0 | 0 | 0 | 0 |
| 0.1→0.5 | 40→60% | 12→15 | 0 | 0 | 0 | 0 | 0 | 0 | 0 | 0 | 0 | 0 |
| 0.1→0.5 | 60→88% | 0→0.5 | 10 | 1 | 3 | 0 | 11 | 0 | 9 | 1 | 33 | 2 |
| 0.1→0.5 | 60→88% | 0.5→1 | 22 | 2 | 11 | 0 | 36 | 0 | 11 | 1 | 80 | 3 |
| 0.1→0.5 | 60→88% | 1→1.5 | 16 | 1 | 15 | 0 | 27 | 0 | 16 | 0 | 74 | 1 |
| 0.1→0.5 | 60→88% | 1.5→2 | 15 | 1 | 10 | 0 | 16 | 1 | 6 | 1 | 47 | 3 |
| 0.1→0.5 | 60→88% | 2→2.5 | 6 | 2 | 4 | 0 | 17 | 1 | 5 | 0 | 32 | 3 |
| 0.1→0.5 | 60→88% | 2.5→3 | 3 | 0 | 2 | 0 | 11 | 0 | 4 | 0 | 20 | 0 |
| 0.1→0.5 | 60→88% | 3→3.5 | 3 | 0 | 1 | 0 | 5 | 1 | 1 | 0 | 10 | 1 |
| 0.1→0.5 | 60→88% | 3.5→4 | 3 | 0 | 1 | 0 | 2 | 0 | 1 | 0 | 7 | 0 |
| 0.1→0.5 | 60→88% | 4→4.5 | 2 | 0 | 0 | 0 | 3 | 0 | 0 | 0 | 5 | 0 |
| 0.1→0.5 | 60→88% | 4.5→5 | 0 | 0 | 0 | 0 | 0 | 0 | 0 | 0 | 0 | 0 |
| 0.1→0.5 | 60→88% | 5→6 | 0 | 0 | 0 | 0 | 0 | 0 | 0 | 0 | 0 | 0 |
| 0.1→0.5 | 60→88% | 6→7 | 0 | 0 | 0 | 0 | 0 | 1 | 0 | 0 | 1 | 1 |
| 0.1→0.5 | 60→88% | 7→9 | 0 | 0 | 0 | 0 | 0 | 0 | 0 | 0 | 0 | 0 |
| 0.1→0.5 | 60→88% | 9→12 | 0 | 0 | 0 | 0 | 0 | 0 | 0 | 0 | 0 | 0 |
| 0.1→0.5 | 60→88% | 12→15 | 0 | 0 | 0 | 0 | 0 | 0 | 0 | 0 | 0 | 0 |

G.2 J/ψ Acceptance x Reconstruction Efficiency Values

The J/ψ acceptance x reconstruction efficiency vs. p_T is shown in Tab. G.5.

Table G.4: The J/ψ Acceptance x Reconstruction Efficiency for each rungroup.

| Rapidity | p_T | G0 | G1 | G2 | G3 |
|----------|-------|------------------|------------------|------------------|------------------|
| -0.5→0.1 | 0→0.5 | 0.0114 ± 0.0004 | 0.011 ± 0.0004 | 0.00901 ± 0.0004 | 0.00899 ± 0.0004 |
| -0.5→0.1 | 0.5→1 | 0.0114 ± 0.0004 | 0.0108 ± 0.0004 | 0.00943 ± 0.0004 | 0.00926 ± 0.0004 |
| -0.5→0.1 | 1→1.5 | 0.0108 ± 0.0004 | 0.0104 ± 0.0004 | 0.00899 ± 0.0004 | 0.00877 ± 0.0004 |
| -0.5→0.1 | 1.5→2 | 0.00895 ± 0.0004 | 0.00887 ± 0.0004 | 0.00797 ± 0.0004 | 0.00789 ± 0.0004 |
| -0.5→0.1 | 2→2.5 | 0.00809 ± 0.0004 | 0.00787 ± 0.0004 | 0.00699 ± 0.0003 | 0.00697 ± 0.0003 |
| -0.5→0.1 | 2.5→3 | 0.00593 ± 0.0003 | 0.00606 ± 0.0003 | 0.00559 ± 0.0003 | 0.00536 ± 0.0003 |
| -0.5→0.1 | 3→3.5 | 0.00684 ± 0.0003 | 0.00648 ± 0.0003 | 0.00569 ± 0.0003 | 0.00588 ± 0.0003 |
| -0.5→0.1 | 3.5→4 | 0.00548 ± 0.0003 | 0.00523 ± 0.0003 | 0.00458 ± 0.0003 | 0.00451 ± 0.0003 |
| -0.5→0.1 | 4→4.5 | 0.00576 ± 0.0003 | 0.00553 ± 0.0003 | 0.0047 ± 0.0003 | 0.0047 ± 0.0003 |
| -0.5→0.1 | 4.5→5 | 0.00633 ± 0.0003 | 0.00624 ± 0.0003 | 0.00531 ± 0.0003 | 0.0052 ± 0.0003 |
| -0.5→0.1 | 5→6 | 0.00782 ± 0.0003 | 0.00738 ± 0.0002 | 0.00621 ± 0.0002 | 0.00624 ± 0.0002 |
| -0.5→0.1 | 6→7 | 0.00994 ± 0.0003 | 0.0095 ± 0.0003 | 0.00795 ± 0.0003 | 0.00822 ± 0.0003 |
| -0.5→0.1 | 7→9 | 0.0134 ± 0.0002 | 0.013 ± 0.0002 | 0.0115 ± 0.0002 | 0.0116 ± 0.0002 |
| -0.5→0.1 | 9→12 | 0.0225 ± 0.0002 | 0.0215 ± 0.0002 | 0.0196 ± 0.0002 | 0.0196 ± 0.0002 |
| -0.5→0.1 | 12→15 | 0.033 ± 0.0003 | 0.0313 ± 0.0003 | 0.0289 ± 0.0003 | 0.029 ± 0.0003 |
| -0.1→0.1 | 0→0.5 | 0.0413 ± 0.001 | 0.0343 ± 0.001 | 0.0309 ± 0.001 | 0.0314 ± 0.001 |
| -0.1→0.1 | 0.5→1 | 0.0359 ± 0.001 | 0.0296 ± 0.001 | 0.0268 ± 0.0009 | 0.0264 ± 0.0009 |
| -0.1→0.1 | 1→1.5 | 0.032 ± 0.001 | 0.0281 ± 0.001 | 0.0253 ± 0.0009 | 0.0246 ± 0.0009 |
| -0.1→0.1 | 1.5→2 | 0.0251 ± 0.0009 | 0.0216 ± 0.0008 | 0.0202 ± 0.0008 | 0.0212 ± 0.0008 |
| -0.1→0.1 | 2→2.5 | 0.0197 ± 0.0008 | 0.0172 ± 0.0008 | 0.0161 ± 0.0007 | 0.016 ± 0.0007 |
| -0.1→0.1 | 2.5→3 | 0.017 ± 0.0007 | 0.0155 ± 0.0007 | 0.0143 ± 0.0007 | 0.0146 ± 0.0007 |
| -0.1→0.1 | 3→3.5 | 0.0135 ± 0.0007 | 0.0127 ± 0.0006 | 0.0115 ± 0.0006 | 0.0115 ± 0.0006 |
| -0.1→0.1 | 3.5→4 | 0.0133 ± 0.0007 | 0.0125 ± 0.0006 | 0.0117 ± 0.0006 | 0.0112 ± 0.0006 |
| -0.1→0.1 | 4→4.5 | 0.0149 ± 0.0007 | 0.0128 ± 0.0006 | 0.0111 ± 0.0006 | 0.0112 ± 0.0006 |
| -0.1→0.1 | 4.5→5 | 0.0156 ± 0.0007 | 0.0131 ± 0.0007 | 0.0118 ± 0.0006 | 0.0118 ± 0.0006 |
| -0.1→0.1 | 5→6 | 0.0213 ± 0.0006 | 0.0178 ± 0.0005 | 0.0157 ± 0.0005 | 0.0162 ± 0.0005 |
| -0.1→0.1 | 6→7 | 0.0278 ± 0.0007 | 0.0233 ± 0.0006 | 0.0216 ± 0.0006 | 0.0217 ± 0.0006 |
| -0.1→0.1 | 7→9 | 0.0402 ± 0.0006 | 0.0358 ± 0.0005 | 0.0332 ± 0.0005 | 0.0331 ± 0.0005 |
| -0.1→0.1 | 9→12 | 0.0688 ± 0.0006 | 0.0628 ± 0.0006 | 0.0597 ± 0.0006 | 0.0595 ± 0.0006 |
| -0.1→0.1 | 12→15 | 0.0972 ± 0.0007 | 0.0877 ± 0.0007 | 0.0846 ± 0.0007 | 0.0856 ± 0.0007 |
| 0.1→0.5 | 0→0.5 | 0.013 ± 0.0005 | 0.00908 ± 0.0004 | 0.00864 ± 0.0004 | 0.00876 ± 0.0004 |
| 0.1→0.5 | 0.5→1 | 0.0118 ± 0.0004 | 0.00854 ± 0.0004 | 0.00833 ± 0.0004 | 0.00833 ± 0.0004 |
| 0.1→0.5 | 1→1.5 | 0.0104 ± 0.0004 | 0.00755 ± 0.0004 | 0.00728 ± 0.0003 | 0.00733 ± 0.0003 |
| 0.1→0.5 | 1.5→2 | 0.00908 ± 0.0004 | 0.00731 ± 0.0003 | 0.00718 ± 0.0003 | 0.00731 ± 0.0003 |
| 0.1→0.5 | 2→2.5 | 0.0072 ± 0.0003 | 0.00598 ± 0.0003 | 0.00583 ± 0.0003 | 0.00575 ± 0.0003 |
| 0.1→0.5 | 2.5→3 | 0.00698 ± 0.0003 | 0.00583 ± 0.0003 | 0.0057 ± 0.0003 | 0.00576 ± 0.0003 |
| 0.1→0.5 | 3→3.5 | 0.00636 ± 0.0003 | 0.00509 ± 0.0003 | 0.00497 ± 0.0003 | 0.00492 ± 0.0003 |
| 0.1→0.5 | 3.5→4 | 0.00582 ± 0.0003 | 0.00417 ± 0.0003 | 0.00409 ± 0.0003 | 0.00389 ± 0.0003 |
| 0.1→0.5 | 4→4.5 | 0.00596 ± 0.0003 | 0.00474 ± 0.0003 | 0.00454 ± 0.0003 | 0.00437 ± 0.0003 |
| 0.1→0.5 | 4.5→5 | 0.00616 ± 0.0003 | 0.0047 ± 0.0003 | 0.00453 ± 0.0003 | 0.00482 ± 0.0003 |
| 0.1→0.5 | 5→6 | 0.00795 ± 0.0003 | 0.00614 ± 0.0002 | 0.00584 ± 0.0002 | 0.00591 ± 0.0002 |
| 0.1→0.5 | 6→7 | 0.00987 ± 0.0003 | 0.00757 ± 0.0003 | 0.00726 ± 0.0002 | 0.00709 ± 0.0002 |
| 0.1→0.5 | 7→9 | 0.0141 ± 0.0002 | 0.0113 ± 0.0002 | 0.0109 ± 0.0002 | 0.011 ± 0.0002 |
| 0.1→0.5 | 9→12 | 0.0227 ± 0.0002 | 0.0194 ± 0.0002 | 0.0189 ± 0.0002 | 0.0188 ± 0.0002 |
| 0.1→0.5 | 12→15 | 0.0337 ± 0.0003 | 0.0288 ± 0.0003 | 0.0284 ± 0.0003 | 0.0287 ± 0.0003 |

Table G.5: J/ψ Acceptance x Reconstruction Efficiency for each rungroup.

G.3 J/ψ Trigger Efficiencies

The J/ψ trigger efficiencies vs. p_T are given in Tab. G.6.

Table G.6: J/ψ Trigger Efficiency for each rungroup.

| Rapidity | p_T [GeV/c] | G0 | G1 | G2 | G3 |
|-----------|---------------|-----------------|-----------------|-----------------|-----------------|
| -0.5→-0.1 | 0→0.5 | 0.85 ± 0.0137 | 0.873 ± 0.013 | 0.771 ± 0.0182 | 0.813 ± 0.0169 |
| -0.5→-0.1 | 0.5→1 | 0.865 ± 0.0131 | 0.888 ± 0.0124 | 0.794 ± 0.017 | 0.797 ± 0.017 |
| -0.5→-0.1 | 1→1.5 | 0.845 ± 0.0142 | 0.862 ± 0.0139 | 0.779 ± 0.0179 | 0.762 ± 0.0186 |
| -0.5→-0.1 | 1.5→2 | 0.825 ± 0.0164 | 0.795 ± 0.0175 | 0.72 ± 0.0205 | 0.749 ± 0.0199 |
| -0.5→-0.1 | 2→2.5 | 0.781 ± 0.0188 | 0.752 ± 0.0199 | 0.624 ± 0.0237 | 0.687 ± 0.0227 |
| -0.5→-0.1 | 2.5→3 | 0.746 ± 0.0231 | 0.796 ± 0.0211 | 0.663 ± 0.0258 | 0.707 ± 0.0254 |
| -0.5→-0.1 | 3→3.5 | 0.72 ± 0.0221 | 0.708 ± 0.023 | 0.598 ± 0.0265 | 0.644 ± 0.0254 |
| -0.5→-0.1 | 3.5→4 | 0.716 ± 0.0249 | 0.767 ± 0.0239 | 0.624 ± 0.0293 | 0.693 ± 0.0281 |
| -0.5→-0.1 | 4→4.5 | 0.756 ± 0.023 | 0.773 ± 0.0229 | 0.775 ± 0.0247 | 0.775 ± 0.0247 |
| -0.5→-0.1 | 4.5→5 | 0.688 ± 0.0237 | 0.761 ± 0.022 | 0.709 ± 0.0254 | 0.76 ± 0.0241 |
| -0.5→-0.1 | 5→6 | 0.803 ± 0.0129 | 0.824 ± 0.0128 | 0.784 ± 0.015 | 0.821 ± 0.014 |
| -0.5→-0.1 | 6→7 | 0.83 ± 0.0109 | 0.826 ± 0.0112 | 0.803 ± 0.0129 | 0.81 ± 0.0125 |
| -0.5→-0.1 | 7→9 | 0.837 ± 0.00652 | 0.842 ± 0.00653 | 0.825 ± 0.00722 | 0.849 ± 0.00678 |
| -0.5→-0.1 | 9→12 | 0.825 ± 0.00422 | 0.838 ± 0.00418 | 0.826 ± 0.00452 | 0.835 ± 0.00442 |
| -0.5→-0.1 | 12→15 | 0.816 ± 0.00354 | 0.828 ± 0.00355 | 0.805 ± 0.00387 | 0.826 ± 0.00371 |
| -0.1→0.1 | 0→0.5 | 0.838 ± 0.0104 | 0.8 ± 0.0124 | 0.745 ± 0.0143 | 0.789 ± 0.0132 |
| -0.1→0.1 | 0.5→1 | 0.828 ± 0.0114 | 0.816 ± 0.0129 | 0.762 ± 0.0149 | 0.762 ± 0.0151 |
| -0.1→0.1 | 1→1.5 | 0.856 ± 0.0114 | 0.822 ± 0.0132 | 0.751 ± 0.0158 | 0.755 ± 0.0159 |
| -0.1→0.1 | 1.5→2 | 0.82 ± 0.014 | 0.796 ± 0.0158 | 0.704 ± 0.0185 | 0.725 ± 0.0177 |
| -0.1→0.1 | 2→2.5 | 0.786 ± 0.0168 | 0.805 ± 0.0174 | 0.716 ± 0.0205 | 0.724 ± 0.0204 |
| -0.1→0.1 | 2.5→3 | 0.799 ± 0.0178 | 0.765 ± 0.0197 | 0.707 ± 0.022 | 0.715 ± 0.0216 |
| -0.1→0.1 | 3→3.5 | 0.73 ± 0.022 | 0.736 ± 0.0226 | 0.644 ± 0.0257 | 0.714 ± 0.0243 |
| -0.1→0.1 | 3.5→4 | 0.787 ± 0.0205 | 0.728 ± 0.023 | 0.696 ± 0.0246 | 0.746 ± 0.0238 |
| -0.1→0.1 | 4→4.5 | 0.805 ± 0.0187 | 0.756 ± 0.0219 | 0.738 ± 0.0241 | 0.764 ± 0.0232 |
| -0.1→0.1 | 4.5→5 | 0.795 ± 0.0187 | 0.793 ± 0.0205 | 0.789 ± 0.0218 | 0.832 ± 0.0199 |
| -0.1→0.1 | 5→6 | 0.814 ± 0.0109 | 0.799 ± 0.0123 | 0.775 ± 0.0136 | 0.831 ± 0.0121 |
| -0.1→0.1 | 6→7 | 0.815 ± 0.00946 | 0.777 ± 0.0111 | 0.801 ± 0.011 | 0.842 ± 0.0101 |
| -0.1→0.1 | 7→9 | 0.818 ± 0.00555 | 0.792 ± 0.00619 | 0.815 ± 0.00614 | 0.84 ± 0.0058 |
| -0.1→0.1 | 9→12 | 0.809 ± 0.00353 | 0.788 ± 0.00384 | 0.809 ± 0.00379 | 0.83 ± 0.00362 |
| -0.1→0.1 | 12→15 | 0.8 ± 0.00302 | 0.79 ± 0.00324 | 0.805 ± 0.0032 | 0.814 ± 0.00313 |
| 0.1→0.5 | 0→0.5 | 0.825 ± 0.0136 | 0.772 ± 0.018 | 0.751 ± 0.019 | 0.781 ± 0.018 |
| 0.1→0.5 | 0.5→1 | 0.862 ± 0.013 | 0.793 ± 0.0179 | 0.758 ± 0.0192 | 0.776 ± 0.0186 |
| 0.1→0.5 | 1→1.5 | 0.833 ± 0.0149 | 0.81 ± 0.0184 | 0.755 ± 0.0206 | 0.812 ± 0.0186 |
| 0.1→0.5 | 1.5→2 | 0.849 ± 0.0153 | 0.81 ± 0.0187 | 0.753 ± 0.0207 | 0.778 ± 0.0198 |
| 0.1→0.5 | 2→2.5 | 0.824 ± 0.0183 | 0.744 ± 0.023 | 0.691 ± 0.0247 | 0.725 ± 0.024 |
| 0.1→0.5 | 2.5→3 | 0.764 ± 0.0208 | 0.737 ± 0.0235 | 0.713 ± 0.0244 | 0.72 ± 0.0241 |
| 0.1→0.5 | 3→3.5 | 0.778 ± 0.0212 | 0.765 ± 0.0242 | 0.712 ± 0.0262 | 0.753 ± 0.0251 |
| 0.1→0.5 | 3.5→4 | 0.711 ± 0.0243 | 0.74 ± 0.0277 | 0.714 ± 0.0289 | 0.665 ± 0.0309 |
| 0.1→0.5 | 4→4.5 | 0.751 ± 0.0228 | 0.695 ± 0.0273 | 0.685 ± 0.0281 | 0.71 ± 0.028 |
| 0.1→0.5 | 4.5→5 | 0.747 ± 0.0226 | 0.724 ± 0.0266 | 0.7 ± 0.0277 | 0.739 ± 0.0258 |
| 0.1→0.5 | 5→6 | 0.77 ± 0.0137 | 0.745 ± 0.0161 | 0.817 ± 0.0146 | 0.823 ± 0.0144 |
| 0.1→0.5 | 6→7 | 0.799 ± 0.0116 | 0.702 ± 0.0152 | 0.789 ± 0.0138 | 0.836 ± 0.0127 |
| 0.1→0.5 | 7→9 | 0.799 ± 0.00689 | 0.718 ± 0.00865 | 0.815 ± 0.00759 | 0.831 ± 0.00729 |
| 0.1→0.5 | 9→12 | 0.807 ± 0.00435 | 0.731 ± 0.0053 | 0.813 ± 0.00472 | 0.83 ± 0.00455 |
| 0.1→0.5 | 12→15 | 0.791 ± 0.00368 | 0.741 ± 0.00429 | 0.802 ± 0.00393 | 0.816 ± 0.00381 |

G.4 J/ψ Inv. Yield Values

The yield summed over all rungroups along with the corresponding invariant yield is given in Tab. G.7 for the first rapidity range, Tab. G.8 for the second rapidity range, and Tab. G.9 for the final rapidity range.

Table G.7: J/ψ yield values summed over rungroups for $-0.5 < y < -0.1$.

| y | centrality | p_T | FG | BG | yield | inv. yield |
|-----------|------------|-------|-----|----|-------------------|--------------------------------|
| -0.5→-0.1 | 0-20 | 0→0.5 | 105 | 14 | 91 ± 10.9087 | $1.75935e-06 \pm 2.29995e-07$ |
| -0.5→-0.1 | 0-20 | 0.5→1 | 247 | 31 | 216 ± 16.6733 | $4.02834e-06 \pm 3.47157e-07$ |
| -0.5→-0.1 | 0-20 | 1→1.5 | 300 | 36 | 264 ± 18.3303 | $5.31155e-06 \pm 4.17403e-07$ |
| -0.5→-0.1 | 0-20 | 1.5→2 | 222 | 25 | 197 ± 15.7162 | $4.81163e-06 \pm 4.32615e-07$ |
| -0.5→-0.1 | 0-20 | 2→2.5 | 130 | 23 | 107 ± 12.3693 | $3.24885e-06 \pm 4.14555e-07$ |
| -0.5→-0.1 | 0-20 | 2.5→3 | 84 | 11 | 73 ± 9.74679 | $2.789e-06 \pm 4.10599e-07$ |
| -0.5→-0.1 | 0-20 | 3→3.5 | 70 | 7 | 63 ± 8.77496 | $2.44936e-06 \pm 3.75217e-07$ |
| -0.5→-0.1 | 0-20 | 3.5→4 | 30 | 3 | 27 ± 6 | $1.2621e-06 \pm 3.04202e-07$ |
| -0.5→-0.1 | 0-20 | 4→4.5 | 21 | 2 | 19 ± 5.8 | $7.52747e-07 \pm 2.94356e-07$ |
| -0.5→-0.1 | 0-20 | 4.5→5 | 14 | 0 | 14 ± 4.05 | $5.29991e-07 \pm 1.59158e-07$ |
| -0.5→-0.1 | 0-20 | 5→6 | 15 | 7 | 8 ± 5.1 | $1.14394e-07 \pm 7.81179e-08$ |
| -0.5→-0.1 | 0-20 | 6→7 | 4 | 4 | 0 ± 2.82843 | $0 \pm 3.31332e-08$ |
| -0.5→-0.1 | 0-20 | 7→9 | 9 | 2 | 7 ± 3.65 | $2.66391e-08 \pm 1.48749e-08$ |
| -0.5→-0.1 | 0-20 | 9→12 | 2 | 1 | 1 ± 2.7 | $1.5108e-09 \pm 4.36742e-09$ |
| -0.5→-0.1 | 0-20 | 12→15 | 0 | 0 | 0 ± 0 | 0 ± 0 |
| -0.5→-0.1 | 20-40 | 0→0.5 | 87 | 6 | 81 ± 9.64365 | $1.56602e-06 \pm 2.03374e-07$ |
| -0.5→-0.1 | 20-40 | 0.5→1 | 200 | 18 | 182 ± 14.7648 | $3.39425e-06 \pm 3.06250e-07$ |
| -0.5→-0.1 | 20-40 | 1→1.5 | 191 | 29 | 162 ± 14.8324 | $3.25936e-06 \pm 3.30123e-07$ |
| -0.5→-0.1 | 20-40 | 1.5→2 | 155 | 15 | 140 ± 13.0384 | $3.41943e-06 \pm 3.54216e-07$ |
| -0.5→-0.1 | 20-40 | 2→2.5 | 82 | 9 | 73 ± 9.53939 | $2.21651e-06 \pm 3.17648e-07$ |
| -0.5→-0.1 | 20-40 | 2.5→3 | 50 | 5 | 45 ± 7.7 | $1.71925e-06 \pm 3.20729e-07$ |
| -0.5→-0.1 | 20-40 | 3→3.5 | 40 | 5 | 35 ± 6.95 | $1.36076e-06 \pm 3.08590e-07$ |
| -0.5→-0.1 | 20-40 | 3.5→4 | 22 | 0 | 22 ± 4.95 | $1.02838e-06 \pm 2.50888e-07$ |
| -0.5→-0.1 | 20-40 | 4→4.5 | 11 | 2 | 9 ± 3.9 | $3.56564e-07 \pm 1.65923e-07$ |
| -0.5→-0.1 | 20-40 | 4.5→5 | 3 | 0 | 3 ± 2.25 | $1.1357e-07 \pm 1.55353e-07$ |
| -0.5→-0.1 | 20-40 | 5→6 | 13 | 1 | 12 ± 3.85 | $1.71591e-07 \pm 6.13488e-08$ |
| -0.5→-0.1 | 20-40 | 6→7 | 4 | 1 | 3 ± 3.8 | $3.28236e-08 \pm 3.28060e-08$ |
| -0.5→-0.1 | 20-40 | 7→9 | 3 | 1 | 2 ± 2.75 | $7.61116e-09 \pm 1.12052e-08$ |
| -0.5→-0.1 | 20-40 | 9→12 | 5 | 0 | 5 ± 2.65 | $7.554e-09 \pm 4.28686e-09$ |
| -0.5→-0.1 | 20-40 | 12→15 | 1 | 0 | 1 ± 1.55 | $1.04441e-09 \pm 1.73324e-09$ |
| -0.5→-0.1 | 40-60 | 0→0.5 | 58 | 3 | 55 ± 7.81025 | $1.06334e-06 \pm 1.63812e-07$ |
| -0.5→-0.1 | 40-60 | 0.5→1 | 119 | 9 | 110 ± 11.3137 | $2.05147e-06 \pm 2.31396e-07$ |
| -0.5→-0.1 | 40-60 | 1→1.5 | 127 | 13 | 114 ± 11.8322 | $2.29362e-06 \pm 2.61492e-07$ |
| -0.5→-0.1 | 40-60 | 1.5→2 | 100 | 3 | 97 ± 10.1489 | $2.36918e-06 \pm 2.73605e-07$ |
| -0.5→-0.1 | 40-60 | 2→2.5 | 58 | 1 | 57 ± 7.68115 | $1.7307e-06 \pm 2.55414e-07$ |
| -0.5→-0.1 | 40-60 | 2.5→3 | 38 | 6 | 32 ± 6.9 | $1.22257e-06 \pm 2.85506e-07$ |
| -0.5→-0.1 | 40-60 | 3→3.5 | 20 | 5 | 15 ± 5.25 | $5.83182e-07 \pm 2.19491e-07$ |
| -0.5→-0.1 | 40-60 | 3.5→4 | 12 | 3 | 9 ± 4.15 | $4.207e-07 \pm 2.0833e-07$ |
| -0.5→-0.1 | 40-60 | 4→4.5 | 7 | 2 | 5 ± 3.45 | $1.98091e-07 \pm 1.93364e-07$ |
| -0.5→-0.1 | 40-60 | 4.5→5 | 5 | 1 | 4 ± 2.65 | $1.51426e-07 \pm 1.76622e-07$ |
| -0.5→-0.1 | 40-60 | 5→6 | 7 | 0 | 7 ± 2.15 | $1.00095e-07 \pm 8.73046e-08$ |
| -0.5→-0.1 | 40-60 | 6→7 | 4 | 1 | 3 ± 2.8 | $3.28236e-08 \pm 3.28060e-08$ |
| -0.5→-0.1 | 40-60 | 7→9 | 1 | 3 | -2 ± 2 | $-7.61116e-09 \pm 8.14943e-09$ |
| -0.5→-0.1 | 40-60 | 9→12 | 0 | 1 | -1 ± 1 | $-1.5108e-09 \pm 1.61759e-09$ |
| -0.5→-0.1 | 40-60 | 12→15 | 0 | 0 | 0 ± 0 | 0 ± 0 |
| -0.5→-0.1 | 60-88 | 0→0.5 | 33 | 2 | 31 ± 6.2 | $4.28099e-07 \pm 9.22845e-08$ |
| -0.5→-0.1 | 60-88 | 0.5→1 | 83 | 5 | 78 ± 9.38083 | $1.03906e-06 \pm 1.3618e-07$ |
| -0.5→-0.1 | 60-88 | 1→1.5 | 85 | 6 | 79 ± 9.53939 | $1.13532e-06 \pm 1.49602e-07$ |
| -0.5→-0.1 | 60-88 | 1.5→2 | 76 | 0 | 76 ± 8.7178 | $1.3259e-06 \pm 1.67039e-07$ |
| -0.5→-0.1 | 60-88 | 2→2.5 | 29 | 1 | 28 ± 5.75 | $6.07262e-07 \pm 1.30244e-07$ |
| -0.5→-0.1 | 60-88 | 2.5→3 | 26 | 0 | 26 ± 5.55 | $7.0953e-07 \pm 1.58298e-07$ |
| -0.5→-0.1 | 60-88 | 3→3.5 | 16 | 1 | 15 ± 4.4 | $1.416559e-07 \pm 1.53972e-07$ |
| -0.5→-0.1 | 60-88 | 3.5→4 | 7 | 1 | 6 ± 3.2 | $2.00333e-07 \pm 1.14655e-07$ |
| -0.5→-0.1 | 60-88 | 4→4.5 | 4 | 1 | 3 ± 2.8 | $8.48963e-08 \pm 8.48903e-08$ |
| -0.5→-0.1 | 60-88 | 4.5→5 | 2 | 0 | 2 ± 2.05 | $5.40807e-08 \pm 5.938e-08$ |
| -0.5→-0.1 | 60-88 | 5→6 | 5 | 0 | 5 ± 2.65 | $5.10688e-08 \pm 5.8997e-08$ |
| -0.5→-0.1 | 60-88 | 6→7 | 2 | 1 | 1 ± 2.7 | $7.81514e-09 \pm 2.5924e-08$ |
| -0.5→-0.1 | 60-88 | 7→9 | 3 | 0 | 3 ± 2.25 | $8.15481e-09 \pm 6.54892e-09$ |
| -0.5→-0.1 | 60-88 | 9→12 | 0 | 0 | 0 ± 0 | 0 ± 0 |
| -0.5→-0.1 | 60-88 | 12→15 | 0 | 0 | 0 ± 0 | 0 ± 0 |

Table G.8: J/ψ yield values summed over rungroups for $-0.1 < y < 0.1$.

| y | centrality | p_T | FG | BG | yield | inv. yield |
|----------|------------|-------|-----|----|-------------------|---|
| -0.1→0.1 | 0-20 | 0→0.5 | 188 | 20 | 168 ± 14.4222 | $1.95856e-06 \pm 1.8383e-07$ |
| -0.1→0.1 | 0-20 | 0.5→1 | 389 | 56 | 333 ± 21.095 | $4.49221e-06 \pm 3.18337e-07$ |
| -0.1→0.1 | 0-20 | 1→1.5 | 395 | 55 | 340 ± 21.2132 | $4.93385e-06 \pm 3.46207e-07$ |
| -0.1→0.1 | 0-20 | 1.5→2 | 275 | 31 | 244 ± 17.4929 | $4.64112e-06 \pm 3.73916e-07$ |
| -0.1→0.1 | 0-20 | 2→2.5 | 169 | 21 | 148 ± 13.784 | $3.58906e-06 \pm 3.71606e-07$ |
| -0.1→0.1 | 0-20 | 2.5→3 | 80 | 8 | 72 ± 9.38083 | $1.98873e-06 \pm 2.83702e-07$ |
| -0.1→0.1 | 0-20 | 3→3.5 | 51 | 5 | 46 ± 7.75 | $1.69545e - 06^{+3.11293e-07}_{-2.9967e-07}$ |
| -0.1→0.1 | 0-20 | 3.5→4 | 24 | 4 | 20 ± 5.55 | $6.99588e - 07^{+2.09192e-07}_{-2.85051e-07}$ |
| -0.1→0.1 | 0-20 | 4→4.5 | 23 | 1 | 22 ± 5.15 | $7.32344e - 07^{+1.79794e-07}_{-1.26676e-07}$ |
| -0.1→0.1 | 0-20 | 4.5→5 | 12 | 1 | 11 ± 3.9 | $3.32579e - 07^{+1.21838e-07}_{-1.48297e-08}$ |
| -0.1→0.1 | 0-20 | 5→6 | 11 | 1 | 10 ± 3.75 | $1.11533e - 07^{+4.30405e-08}_{-4.30405e-08}$ |
| -0.1→0.1 | 0-20 | 6→7 | 7 | 0 | 7 ± 3 | $5.7561e - 08^{+2.64286e-08}_{-2.51089e-08}$ |
| -0.1→0.1 | 0-20 | 7→9 | 5 | 0 | 5 ± 2.65 | $1.34427e - 08^{+7.62911e-09}_{-6.76568e-09}$ |
| -0.1→0.1 | 0-20 | 9→12 | 2 | 0 | 2 ± 2.35 | $2.04152e - 09^{+2.24045e-09}_{-1.31152e-09}$ |
| -0.1→0.1 | 0-20 | 12→15 | 1 | 0 | 1 ± 1.55 | $7.26166e - 10^{+1.2051e-09}_{-4.665e-10}$ |
| -0.1→0.1 | 20-40 | 0→0.5 | 121 | 8 | 113 ± 11.3578 | $3.17373e-06 \pm 1.43964e-07$ |
| -0.1→0.1 | 20-40 | 0.5→1 | 267 | 25 | 242 ± 17.088 | $3.26461e-06 \pm 2.55748e-07$ |
| -0.1→0.1 | 20-40 | 1→1.5 | 265 | 23 | 242 ± 16.9706 | $3.51174e-06 \pm 2.74247e-07$ |
| -0.1→0.1 | 20-40 | 1.5→2 | 195 | 25 | 170 ± 14.8324 | $3.23357e-06 \pm 3.1226e-07$ |
| -0.1→0.1 | 20-40 | 2→2.5 | 96 | 15 | 81 ± 10.5357 | $1.96428e-06 \pm 2.78973e-07$ |
| -0.1→0.1 | 20-40 | 2.5→3 | 66 | 7 | 59 ± 8.544 | $1.62965e-06 \pm 2.57313e-07$ |
| -0.1→0.1 | 20-40 | 3→3.5 | 29 | 3 | 26 ± 5.9 | $9.58296e - 07^{+2.35127e-07}_{-2.27315e-07}$ |
| -0.1→0.1 | 20-40 | 3.5→4 | 30 | 1 | 29 ± 5.85 | $0.0144e - 06^{+2.2175e-07}_{-2.14353e-07}$ |
| -0.1→0.1 | 20-40 | 4→4.5 | 16 | 1 | 15 ± 4.4 | $4.99326e - 07^{+1.76731e-07}_{-1.59449e-07}$ |
| -0.1→0.1 | 20-40 | 4.5→5 | 15 | 0 | 15 ± 4.15 | $4.53517e - 07^{+1.30261e-07}_{-1.35089e-07}$ |
| -0.1→0.1 | 20-40 | 5→6 | 16 | 0 | 16 ± 4.3 | $1.78452e - 07^{+5.14583e-08}_{-4.96711e-08}$ |
| -0.1→0.1 | 20-40 | 6→7 | 4 | 0 | 4 ± 2.45 | $3.2892e - 08^{+2.15765e-08}_{-1.80562e-08}$ |
| -0.1→0.1 | 20-40 | 7→9 | 5 | 0 | 5 ± 2.65 | $1.34427e - 08^{+7.62911e-09}_{-6.76568e-09}$ |
| -0.1→0.1 | 20-40 | 9→12 | 3 | 0 | 3 ± 2.25 | $3.06227e - 09^{+2.45906e-09}_{-1.85799e-09}$ |
| -0.1→0.1 | 20-40 | 12→15 | 0 | 1 | 1 ± 1 | $-7.26166e-10 \pm 7.77487e-10$ |
| -0.1→0.1 | 40-60 | 0→0.5 | 67 | 2 | 65 ± 8.30662 | $7.57777e-07 \pm 1.04679e-07$ |
| -0.1→0.1 | 40-60 | 0.5→1 | 164 | 17 | 147 ± 13.4536 | $1.98305e-06 \pm 1.98535e-07$ |
| -0.1→0.1 | 40-60 | 1→1.5 | 169 | 21 | 148 ± 13.784 | $2.14768e-06 \pm 2.19073e-07$ |
| -0.1→0.1 | 40-60 | 1.5→2 | 117 | 6 | 111 ± 11.0905 | $2.11133e-06 \pm 2.31696e-07$ |
| -0.1→0.1 | 40-60 | 2→2.5 | 65 | 5 | 60 ± 8.3666 | $1.45502e-06 \pm 2.20984e-07$ |
| -0.1→0.1 | 40-60 | 2.5→3 | 33 | 1 | 32 ± 6.1 | $8.83879e - 07^{+1.82315e-07}_{-1.76465e-07}$ |
| -0.1→0.1 | 40-60 | 3→3.5 | 25 | 1 | 24 ± 5.35 | $8.84581e - 07^{+2.13284e-07}_{-2.07426e-07}$ |
| -0.1→0.1 | 40-60 | 3.5→4 | 7 | 1 | 6 ± 3.2 | $2.09876e - 07^{+1.20053e-07}_{-0.05102e-07}$ |
| -0.1→0.1 | 40-60 | 4→4.5 | 5 | 0 | 5 ± 2.65 | $1.66442e - 07^{+9.16033e-08}_{-8.32169e-08}$ |
| -0.1→0.1 | 40-60 | 4.5→5 | 6 | 0 | 6 ± 2.35 | $1.81407e - 07^{+8.43562e-08}_{-8.08168e-08}$ |
| -0.1→0.1 | 40-60 | 5→6 | 7 | 0 | 7 ± 2.6 | $7.80729e - 08^{+3.58545e-08}_{-3.40649e-08}$ |
| -0.1→0.1 | 40-60 | 6→7 | 1 | 0 | 1 ± 1.55 | $8.2223e - 09^{+1.3647e-08}_{-5.28412e-09}$ |
| -0.1→0.1 | 40-60 | 7→9 | 2 | 1 | 1 ± 2.7 | $2.68854e - 09^{+7.77205e-09}_{-1.29558e-09}$ |
| -0.1→0.1 | 40-60 | 9→12 | 1 | 0 | 1 ± 1.55 | $1.02076e - 09^{+1.69399e-09}_{-6.55759e-10}$ |
| -0.1→0.1 | 40-60 | 12→15 | 0 | 0 | 0 ± 0 | 0 ± 0 |
| -0.1→0.1 | 60-88 | 0→0.5 | 54 | 1 | 53 ± 7.4162 | $4.41343e-07 \pm 6.66508e-08$ |
| -0.1→0.1 | 60-88 | 0.5→1 | 126 | 12 | 114 ± 11.7473 | $1.09848e-06 \pm 1.23274e-07$ |
| -0.1→0.1 | 60-88 | 1→1.5 | 107 | 8 | 99 ± 10.7238 | $1.02616e-06 \pm 1.21034e-07$ |
| -0.1→0.1 | 60-88 | 1.5→2 | 70 | 6 | 64 ± 8.7178 | $8.69532e-07 \pm 1.28587e-07$ |
| -0.1→0.1 | 60-88 | 2→2.5 | 49 | 5 | 44 ± 7.6 | $7.62156e - 07^{+1.42539e-07}_{-1.37956e-07}$ |
| -0.1→0.1 | 60-88 | 2.5→3 | 25 | 2 | 23 ± 5.45 | $4.53777e - 07^{+1.15918e-07}_{-1.17232e-07}$ |
| -0.1→0.1 | 60-88 | 3→3.5 | 17 | 0 | 17 ± 4.4 | $4.47556e - 07^{+1.24777e-07}_{-1.20772e-07}$ |
| -0.1→0.1 | 60-88 | 3.5→4 | 6 | 1 | 5 ± 3.05 | $1.24926e - 07^{+8.16994e-08}_{-6.83449e-08}$ |
| -0.1→0.1 | 60-88 | 4→4.5 | 3 | 0 | 3 ± 2.55 | $7.13322e - 08^{+5.73268e-08}_{-4.33403e-08}$ |
| -0.1→0.1 | 60-88 | 4.5→5 | 4 | 0 | 4 ± 2.45 | $8.63843e - 08^{+5.67138e-08}_{-4.74776e-08}$ |
| -0.1→0.1 | 60-88 | 5→6 | 2 | 0 | 2 ± 2.05 | $1.59332e - 08^{+1.74882e-08}_{-0.02399e-08}$ |
| -0.1→0.1 | 60-88 | 6→7 | 1 | 0 | 1 ± 1.55 | $5.87357e - 09^{+9.77432e-09}_{-3.77432e-09}$ |
| -0.1→0.1 | 60-88 | 7→9 | 4 | 0 | 4 ± 2.45 | $7.68154e - 09^{+5.03792e-09}_{-4.21558e-09}$ |
| -0.1→0.1 | 60-88 | 9→12 | 0 | 0 | 0 ± 0 | 0 ± 0 |
| -0.1→0.1 | 60-88 | 12→15 | 0 | 1 | -1 ± 1 | $-5.1869e-10 \pm 5.55348e-10$ |

Table G.9: J/ψ yield values summed over rungroups for $0.1 < y < 0.5$.

| y | centrality | p_T | FG | BG | yield | inv. yield |
|---------|------------|-------|-----|----|----------------------|--|
| 0.1→0.5 | 0-20 | 0→0.5 | 99 | 13 | 86 ± 10.583 | $1.76403e-06 \pm 2.36746e-07$ |
| 0.1→0.5 | 0-20 | 0.5→1 | 195 | 19 | 176 ± 14.6287 | $3.75938e-06 \pm 3.48733e-07$ |
| 0.1→0.5 | 0-20 | 1→1.5 | 246 | 25 | 221 ± 16.4621 | $5.37278e-06 \pm 4.53839e-07$ |
| 0.1→0.5 | 0-20 | 1.5→2 | 191 | 16 | 175 ± 14.3875 | $4.48288e-06 \pm 4.14996e-07$ |
| 0.1→0.5 | 0-20 | 2→2.5 | 131 | 11 | 120 ± 11.9164 | $4.09325e-06 \pm 4.55875e-07$ |
| 0.1→0.5 | 0-20 | 2.5→3 | 71 | 10 | 61 ± 9 | $2.14431e-06 \pm 3.46452e-07$ |
| 0.1→0.5 | 0-20 | 3→3.5 | 47 | 0 | $47^{+7.15}_{-6.85}$ | $1.84801e-06^{+3.08137e-07}_{-2.95813e-07}$ |
| 0.1→0.5 | 0-20 | 3.5→4 | 30 | 1 | $29^{+5.85}_{-5.65}$ | $1.42578e-06^{+3.1322e-07}_{-3.02876e-07}$ |
| 0.1→0.5 | 0-20 | 4→4.5 | 21 | 2 | $19^{+5.05}_{-4.9}$ | $8.55657e-07^{+2.45686e-07}_{-2.3852e-07}$ |
| 0.1→0.5 | 0-20 | 4.5→5 | 4 | 1 | $3^{+2.8}_{-1.7}$ | $1.29068e-07^{+1.29065e-07}_{-7.1535e-08}$ |
| 0.1→0.5 | 0-20 | 5→6 | 13 | 3 | $10^{+4.25}_{-4.15}$ | $1.52526e-07^{+6.91e-08}_{-6.6227e-08}$ |
| 0.1→0.5 | 0-20 | 6→7 | 3 | 1 | $2^{+2.75}_{-1.1}$ | $2.49825e-08^{+3.67818e-08}_{-1.472e-08}$ |
| 0.1→0.5 | 0-20 | 7→9 | 6 | 1 | $5^{+3.05}_{-2.55}$ | $2.06277e-08^{+1.34742e-08}_{-1.12661e-08}$ |
| 0.1→0.5 | 0-20 | 9→12 | 0 | 0 | 0 ± 0 | 0 ± 0 |
| 0.1→0.5 | 0-20 | 12→15 | 1 | 0 | $1^{+1.55}_{-0.6}$ | $1.09018e-09^{+1.8092e-09}_{-7.00361e-10}$ |
| 0.1→0.5 | 20-40 | 0→0.5 | 62 | 4 | 58 ± 8.12404 | $1.18969e-06 \pm 1.80985e-07$ |
| 0.1→0.5 | 20-40 | 0.5→1 | 171 | 8 | 163 ± 13.3791 | $3.4817e-06 \pm 3.19266e-07$ |
| 0.1→0.5 | 20-40 | 1→1.5 | 176 | 21 | 155 ± 14.0357 | $3.76824e-06 \pm 3.80094e-07$ |
| 0.1→0.5 | 20-40 | 1.5→2 | 153 | 15 | 138 ± 12.9615 | $3.53507e-06 \pm 3.69656e-07$ |
| 0.1→0.5 | 20-40 | 2→2.5 | 101 | 8 | 93 ± 10.4403 | $3.17227e-06 \pm 3.95536e-07$ |
| 0.1→0.5 | 20-40 | 2.5→3 | 38 | 2 | $36^{+6.6}_{-6.35}$ | $1.2655e-06^{+2.52084e-07}_{-2.46673e-07}$ |
| 0.1→0.5 | 20-40 | 3→3.5 | 28 | 3 | $25^{+5.85}_{-5.55}$ | $9.82984e-07^{+2.40425e-07}_{-2.49413e-07}$ |
| 0.1→0.5 | 20-40 | 3.5→4 | 18 | 2 | $16^{+4.7}_{-4.55}$ | $7.86636e-07^{+2.41583e-07}_{-2.01762e-07}$ |
| 0.1→0.5 | 20-40 | 4→4.5 | 15 | 0 | $15^{+4.15}_{-4}$ | $6.75519e-07^{+1.94591e-07}_{-1.43116e-07}$ |
| 0.1→0.5 | 20-40 | 4.5→5 | 9 | 3 | $6^{+3.85}_{-3.1}$ | $2.58136e-07^{+1.77601e-07}_{-1.43116e-07}$ |
| 0.1→0.5 | 20-40 | 5→6 | 9 | 2 | $7^{+3.55}_{-3.25}$ | $1.06768e-07^{+5.96544e-08}_{-5.31281e-08}$ |
| 0.1→0.5 | 20-40 | 6→7 | 6 | 0 | $6^{+2.8}_{-2.6}$ | $7.49476e-08^{+3.747478e-08}_{-3.48054e-08}$ |
| 0.1→0.5 | 20-40 | 7→9 | 0 | 0 | 0 ± 0 | 0 ± 0 |
| 0.1→0.5 | 20-40 | 9→12 | 2 | 0 | $2^{+2.05}_{-1.2}$ | $3.2321e-09^{+3.54709e-09}_{-2.07643e-09}$ |
| 0.1→0.5 | 20-40 | 12→15 | 0 | 0 | 0^{+0}_{-0} | 0 ± 0 |
| 0.1→0.5 | 40-60 | 0→0.5 | 49 | 1 | $48^{+7.35}_{-7.05}$ | $9.84574e-07^{+1.63364e-07}_{-1.56858e-07}$ |
| 0.1→0.5 | 40-60 | 0.5→1 | 88 | 5 | 83 ± 9.64365 | $1.77289e-06 \pm 2.25378e-07$ |
| 0.1→0.5 | 40-60 | 1→1.5 | 109 | 8 | 101 ± 10.8167 | $2.45543e-06 \pm 2.89724e-07$ |
| 0.1→0.5 | 40-60 | 1.5→2 | 72 | 8 | 64 ± 8.94427 | $1.63945e-06 \pm 2.49772e-07$ |
| 0.1→0.5 | 40-60 | 2→2.5 | 50 | 2 | $48^{+7.5}_{-7.2}$ | $1.6373e-06^{+2.79236e-07}_{-2.68497e-07}$ |
| 0.1→0.5 | 40-60 | 2.5→3 | 25 | 1 | $24^{+5.35}_{-5.2}$ | $8.43665e-07^{+2.0338e-07}_{-1.97792e-07}$ |
| 0.1→0.5 | 40-60 | 3→3.5 | 15 | 3 | $12^{+4.5}_{-4.3}$ | $4.71832e-07^{+1.90187e-07}_{-1.81802e-07}$ |
| 0.1→0.5 | 40-60 | 3.5→4 | 7 | 2 | $5^{+3.45}_{-2.65}$ | $2.45824e-07^{+1.81873e-07}_{-1.39842e-07}$ |
| 0.1→0.5 | 40-60 | 4→4.5 | 6 | 0 | $6^{+2.8}_{-2.6}$ | $2.70208e-07^{+1.33782e-07}_{-1.57789e-07}$ |
| 0.1→0.5 | 40-60 | 4.5→5 | 8 | 1 | $7^{+3.3}_{-3.05}$ | $3.01159e-07^{+1.40936e-07}_{-1.52419e-07}$ |
| 0.1→0.5 | 40-60 | 5→6 | 12 | 1 | $11^{+3.9}_{-3.75}$ | $1.67779e-07^{+6.38002e-08}_{-6.13551e-08}$ |
| 0.1→0.5 | 40-60 | 6→7 | 5 | 0 | $5^{+2.65}_{-2.35}$ | $6.24563e-08^{+3.54635e-08}_{-3.14542e-08}$ |
| 0.1→0.5 | 40-60 | 7→9 | 2 | 0 | $2^{+2.05}_{-1.2}$ | $8.25109e-09^{+9.0556e-09}_{-5.30136e-09}$ |
| 0.1→0.5 | 40-60 | 9→12 | 0 | 0 | 0 ± 0 | 0 ± 0 |
| 0.1→0.5 | 40-60 | 12→15 | 0 | 0 | 0 ± 0 | 0 ± 0 |
| 0.1→0.5 | 60-88 | 0→0.5 | 33 | 2 | $31^{+6.2}_{-5.95}$ | $4.54193e-07^{+9.79473e-08}_{-9.40544e-08}$ |
| 0.1→0.5 | 60-88 | 0.5→1 | 80 | 3 | 77 ± 9.11043 | $1.17481e-06 \pm 1.51968e-07$ |
| 0.1→0.5 | 60-88 | 1→1.5 | 74 | 1 | 73 ± 8.66025 | $1.26766e-06 \pm 1.64834e-07$ |
| 0.1→0.5 | 60-88 | 1.5→2 | 47 | 3 | $44^{+7.35}_{-7.05}$ | $8.05089e-07^{+1.45827e-07}_{-1.40019e-07}$ |
| 0.1→0.5 | 60-88 | 2→2.5 | 32 | 3 | $29^{+6.5}_{-5.95}$ | $7.06573e-07^{+1.62133e-07}_{-1.56972e-07}$ |
| 0.1→0.5 | 60-88 | 2.5→3 | 20 | 0 | $20^{+4.75}_{-4.6}$ | $5.02181e-07^{+1.28827e-07}_{-1.24831e-07}$ |
| 0.1→0.5 | 60-88 | 3→3.5 | 10 | 1 | $9^{+3.6}_{-3.45}$ | $2.52767e-07^{+1.08627e-07}_{-1.04132e-07}$ |
| 0.1→0.5 | 60-88 | 3.5→4 | 7 | 0 | $7^{+3}_{-2.85}$ | $2.45824e-07^{+1.13229e-07}_{-1.07612e-07}$ |
| 0.1→0.5 | 60-88 | 4→4.5 | 5 | 0 | $5^{+2.65}_{-2.35}$ | $1.60838e-07^{+9.14749e-08}_{-8.11691e-08}$ |
| 0.1→0.5 | 60-88 | 4.5→5 | 0 | 0 | 0 ± 0 | 0 ± 0 |
| 0.1→0.5 | 60-88 | 5→6 | 0 | 0 | 0 ± 0 | 0 ± 0 |
| 0.1→0.5 | 60-88 | 6→7 | 1 | 1 | 0 ± 1.41421 | $0 \pm 1.35097e-08$ |
| 0.1→0.5 | 60-88 | 7→9 | 0 | 0 | 0 ± 0 | 0 ± 0 |
| 0.1→0.5 | 60-88 | 9→12 | 0 | 0 | 0 ± 0 | 0 ± 0 |
| 0.1→0.5 | 60-88 | 12→15 | 0 | 0 | 0 ± 0 | 0 ± 0 |

G.5 $R_{\text{AA}}(CNM)$ Values

The J/ψ $R_{\text{AA}}(CNM)$ as a function of N_{part} at both mid and forward rapidity, as described in Section 9.1 is given in Table G.10. The ratio $R_{\text{AA}}/R_{\text{AA}}(CNM)$ as a function of N_{part} at both mid and forward rapidity, as described in Section G.11, is given in Table G.11

Table G.10: J/ψ $R_{\text{AA}}(CNM)$ values as a function of N_{part} calculated based on a step function nuclear shadowing given by Equation 8.14 using globally fit values of $R = 2.40$ fm and $d = 0.12$ fm and σ_{abs} values shown in Figure 8.6.

| y | N_{part} | $R_{\text{AA}}(CNM)$ | Type A | Type B |
|-------------------|-------------------|----------------------|--------|----------------------|
| $ y < 0.35$ | 351 | 0.636 | 0.005 | $+0.109$ -0.082 |
| $ y < 0.35$ | 299 | 0.636 | 0.005 | $+0.100$ -0.083 |
| $ y < 0.35$ | 253 | 0.653 | 0.005 | $+0.103$ -0.080 |
| $ y < 0.35$ | 215 | 0.678 | 0.005 | $+0.102$ -0.080 |
| $ y < 0.35$ | 167 | 0.722 | 0.004 | $+0.104$ -0.077 |
| $ y < 0.35$ | 114 | 0.777 | 0.004 | $+0.100$ -0.075 |
| $ y < 0.35$ | 58.4 | 0.829 | 0.003 | $+0.086$ -0.067 |
| $ y < 0.35$ | 14.5 | 0.890 | 0.003 | $+0.051$ -0.044 |
| $1.2 < y < 2.2$ | 351 | 0.478 | 0.004 | $+0.049$ -0.045 |
| $1.2 < y < 2.2$ | 299 | 0.513 | 0.004 | $+0.051$ -0.047 |
| $1.2 < y < 2.2$ | 253 | 0.532 | 0.004 | $+0.052$ -0.048 |
| $1.2 < y < 2.2$ | 215 | 0.544 | 0.004 | $+0.051$ -0.049 |
| $1.2 < y < 2.2$ | 167 | 0.558 | 0.003 | $+0.051$ -0.047 |
| $1.2 < y < 2.2$ | 114 | 0.585 | 0.003 | $+0.046$ -0.044 |
| $1.2 < y < 2.2$ | 58.4 | 0.637 | 0.003 | $+0.042$ -0.040 |
| $1.2 < y < 2.2$ | 14.5 | 0.743 | 0.002 | $+0.030$ -0.032 |

Table G.11: J/ψ $R_{\text{AA}}/R_{\text{AA}}(\text{CNM})$ values as a function of N_{part} as described in Section 9.2.

| y | N_{part} | $R_{\text{AA}}/R_{\text{AA}}(\text{CNM})$ | Type A | Type B | Type C |
|-------------------|-------------------|---|--------|----------------------|--------|
| $ y < 0.35$ | 351 | 0.408 | 0.079 | $+0.094$ -0.082 | 0.047 |
| $ y < 0.35$ | 299 | 0.534 | 0.094 | $+0.115$ -0.105 | 0.063 |
| $ y < 0.35$ | 253 | 0.551 | 0.092 | $+0.116$ -0.101 | 0.061 |
| $ y < 0.35$ | 215 | 0.663 | 0.103 | $+0.142$ -0.129 | 0.074 |
| $ y < 0.35$ | 167 | 0.803 | 0.097 | $+0.158$ -0.138 | 0.097 |
| $ y < 0.35$ | 114 | 0.746 | 0.103 | $+0.138$ -0.122 | 0.090 |
| $ y < 0.35$ | 58.4 | 0.784 | 0.084 | $+0.135$ -0.125 | 0.096 |
| $ y < 0.35$ | 14.5 | 0.832 | 0.135 | $+0.193$ -0.192 | 0.101 |
| $1.2 < y < 2.2$ | 351 | 0.362 | 0.084 | $+0.086$ -0.060 | 0.043 |
| $1.2 < y < 2.2$ | 299 | 0.304 | 0.082 | $+0.057$ -0.049 | 0.036 |
| $1.2 < y < 2.2$ | 253 | 0.382 | 0.073 | $+0.068$ -0.065 | 0.045 |
| $1.2 < y < 2.2$ | 215 | 0.460 | 0.066 | $+0.082$ -0.081 | 0.055 |
| $1.2 < y < 2.2$ | 167 | 0.527 | 0.047 | $+0.085$ -0.080 | 0.063 |
| $1.2 < y < 2.2$ | 114 | 0.637 | 0.045 | 0.098 | 0.076 |
| $1.2 < y < 2.2$ | 58.4 | 0.864 | 0.038 | 0.140 | 0.103 |
| $1.2 < y < 2.2$ | 14.5 | 1.110 | 0.047 | 0.231 | 0.132 |

REFERENCES

- [1] GEANT 3.2.1 Manual (CERN, Geneva, 1993); available at <http://wwwasdoc.web.cern.ch/wwwasdoc/pdfdir/geant.pdf>.
- [2] J/psi results from cms in pbpb collisions, with 150mub-1 data. 2012.
- [3] Georges Aad et al. Observation of a new particle in the search for the Standard Model Higgs boson with the ATLAS detector at the LHC. *Phys.Lett.B*, 2012.
- [4] G.S. Abrams, D. Briggs, William Chinowsky, C.E. Friedberg, G. Goldhaber, et al. The Discovery of a Second Narrow Resonance in e+ e- Annihilation. *Phys.Rev.Lett.*, 33:1453–1455, 1974.
- [5] M.C. Abreu et al. Charmonia production in 450-GeV/c proton induced reactions. *Phys. Lett. B*, 444:516–522, 1998.
- [6] M.C. Abreu et al. J / psi, psi-prime and Drell-Yan production in S U interactions at 200-GeV per nucleon. *Phys.Lett.*, B449:128–136, 1999.
- [7] M.C. Abreu et al. Evidence for deconfinement of quarks and gluons from the J / psi suppression pattern measured in Pb + Pb collisions at the CERN SPS. *Phys.Lett.*, B477:28–36, 2000.
- [8] I. Abt et al. Kinematic distributions and nuclear effects of J/psi production in 920-GeV fixed-target proton-nucleus collisions. *Eur. Phys. J. C*, 60:525–542, 2009.
- [9] J. Adams et al. Evidence from d + Au measurements for final state suppression of high p(T) hadrons in Au+Au collisions at RHIC. *Phys.Rev.Lett.*, 91:072304, 2003.
- [10] A. Adare, S. Afanasiev, C. Aidala, N.N. Ajitanand, Y. Akiba, et al. Transverse-Momentum Dependence of the J/psi Nuclear Modification in d+Au Collisions at $\sqrt{s_{NN}} = 200$ GeV. 2012.
- [11] A. Adare et al. J/psi production vs centrality, transverse momentum, and rapidity in Au + Au collisions at $s(\text{NN})^{**}(1/2) = 200$ - GeV. *Phys. Rev. Lett.*, 98:232301, 2007.
- [12] A. Adare et al. Scaling properties of azimuthal anisotropy in Au+Au and Cu+Cu collisions at $s(\text{NN}) = 200$ -GeV. *Phys.Rev.Lett.*, 98:162301, 2007.
- [13] A. Adare et al. Cold Nuclear Matter Effects on J/Psi as Constrained by Deuteron-Gold Measurements at $\sqrt{s_{NN}} = 200$ GeV. *Phys. Rev. C*, 77:024912, 2008.

- [14] A. Adare et al. J/psi Production in $\sqrt{s_{NN}} = 200$ GeV Cu+Cu Collisions. *Phys. Rev. Lett.*, 101:122301, 2008.
- [15] A. Adare et al. Quantitative Constraints on the Opacity of Hot Partonic Matter from Semi-Inclusive Single High Transverse Momentum Pion Suppression in Au+Au collisions at $s(\text{NN})^{**}(1/2) = 200\text{-GeV}$. *Phys. Rev.*, C77:064907, 2008.
- [16] A. Adare et al. Dilepton mass spectra in p+p collisions at $s^{**}(1/2) = 200\text{-GeV}$ and the contribution from open charm. *Phys.Lett.*, B670:313–320, 2009.
- [17] A. Adare et al. Enhanced production of direct photons in Au+Au collisions at $\sqrt{s_{NN}} = 200$ GeV and implications for the initial temperature. *Phys.Rev.Lett.*, 104:132301, 2010.
- [18] A. Adare et al. Transverse momentum dependence of J/psi polarization at midrapidity in p+p collisions at $s^{**}(1/2) = 200\text{-GeV}$. *Phys.Rev.*, D82:012001, 2010.
- [19] A. Adare et al. Cold Nuclear Matter Effects on J/ψ Yields as a Function of Rapidity and Nuclear Geometry in Deuteron-Gold Collisions at $\sqrt{s_{NN}} = 200$ GeV. *Phys.Rev.Lett.*, 107:142301, 2011.
- [20] A. Adare et al. Ground and excited charmonium state production in $p + p$ collisions at $\sqrt{s} = 200$ GeV. 2011.
- [21] A. Adare et al. J/ψ suppression at forward rapidity in Au+Au collisions at $\sqrt{s_{NN}} = 200$ GeV. *Phys.Rev.*, C84:054912, 2011.
- [22] A. Adare et al. Measurements of Higher-Order Flow Harmonics in Au+Au Collisions at $\sqrt{s_{NN}} = 200$ GeV. *Phys.Rev.Lett.*, 107:252301, 2011.
- [23] A. Adare et al. J/ψ suppression at forward rapidity in Au+Au collisions at $\sqrt{s_{NN}} = 39$ and 62.4 GeV. 2012.
- [24] K. Adcox et al. PHENIX central arm tracking detectors. *Nucl.Instrum.Meth.*, A499:489–507, 2003.
- [25] K. Adcox et al. PHENIX detector overview. *Nucl. Instrum. Meth.*, A499:469–479, 2003.
- [26] S.S. Adler et al. Dense-Medium Modifications to Jet-Induced Hadron Pair Distributions in Au+Au Collisions at $s(\text{NN})^{**}(1/2) = 200\text{-GeV}$. *Phys.Rev.Lett.*, 97:052301, 2006.
- [27] S.S. Adler et al. Jet properties from dihadron correlations in p^+p collisions at $\sqrt{s} = 200\text{-GeV}$. *Phys.Rev.*, D74:072002, 2006.
- [28] S.S. Adler et al. Jet structure from dihadron correlations in d+Au collisions at $s(\text{NN})^{**}(1/2) = 200\text{-GeV}$. *Phys.Rev.*, C73:054903, 2006.
- [29] Stephen Scott Adler et al. PHENIX on-line systems. *Nucl.Instrum.Meth.*, A499:560–592, 2003.

- [30] M. Aizawa et al. PHENIX central arm particle ID detectors. *Nucl.Instrum.Meth.*, A499:508–520, 2003.
- [31] H. Akikawa et al. PHENIX muon arms. *Nucl.Instrum.Meth.*, A499:537–548, 2003.
- [32] B. Alessandro et al. Charmonia and Drell-Yan production in proton-nucleus collisions at the CERN SPS. *Phys. Lett. B*, 553:167–178, 2003.
- [33] B. Alessandro et al. Charmonium production and nuclear absorption in p A interactions at 450-GeV. *Eur. Phys. J. C*, 33:31–40, 2004.
- [34] B. Alessandro et al. A New measurement of J/psi suppression in Pb-Pb collisions at 158-GeV per nucleon. *Eur.Phys.J.*, C39:335–345, 2005.
- [35] B. Alessandro et al. J/psi and psi-prime production and their normal nuclear absorption in proton-nucleus collisions at 400-GeV. *Eur. Phys. J. C*, 48:329, 2006.
- [36] M. Allen et al. PHENIX inner detectors. *Nucl.Instrum.Meth.*, A499:549–559, 2003.
- [37] L. Aphecetche et al. PHENIX calorimeter. *Nucl.Instrum.Meth.*, A499:521–536, 2003.
- [38] F. Arleo, P.B. Gossiaux, T. Gousset, and J. Aichelin. Charmonium suppression in p-A collisions. *Phys.Rev.*, C61:054906, 2000.
- [39] Francois Arleo and Stephane Peigne. J/ ψ suppression in p-A collisions from parton energy loss in cold QCD matter. 2012.
- [40] Nestor Armesto, Brian Cole, Charles Gale, William A. Horowitz, Peter Jacobs, et al. Comparison of Jet Quenching Formalisms for a Quark-Gluon Plasma 'Brick'. 2011.
- [41] T.A. Armstrong et al. Observation of the radiative decay J / psi $\rightarrow e^+e^-\gamma$. *Phys.Rev.*, D54:7067–7070, 1996.
- [42] R. Arnaldi et al. J/psi production in indium-indium collisions at 158- GeV/nucleon. *Phys. Rev. Lett.*, 99:132302, 2007.
- [43] R Arnaldi et al. J/psi production in proton-nucleus collisions at 158 and 400 GeV. *Phys. Lett. B*, 706:263–267, 2012.
- [44] J.J. Aubert et al. Experimental Observation of a Heavy Particle J. *Phys.Rev.Lett.*, 33:1404–1406, 1974.
- [45] J.J. Aubert et al. The ratio of the nucleon structure functions F_{2n} for iron and deuterium. *Phys. Lett. B*, 123:275, 1983.
- [46] J.E. Augustin et al. Discovery of a Narrow Resonance in e+ e- Annihilation. *Phys.Rev.Lett.*, 33:1406–1408, 1974.
- [47] A. Bazavov, T. Bhattacharya, M. Cheng, N.H. Christ, C. DeTar, et al. Equation of state and QCD transition at finite temperature. *Phys.Rev.*, D80:014504, 2009.

- [48] J. Beringer et al. Review of Particle Physics (RPP). *Phys.Rev.*, D86:010001, 2012.
- [49] Siegfried Bethke. The 2009 World Average of alpha(s). *Eur.Phys.J.*, C64:689–703, 2009.
- [50] Geoffrey T. Bodwin, Eric Braaten, and G. Peter Lepage. Rigorous QCD analysis of inclusive annihilation and production of heavy quarkonium. *Phys.Rev.*, D51:1125–1171, 1995.
- [51] N. Brambilla, S. Eidelman, B.K. Heltsley, R. Vogt, G.T. Bodwin, et al. Heavy quarkonium: progress, puzzles, and opportunities. *Eur.Phys.J.*, C71:1534, 2011.
- [52] R. Brun and F. Rademakers. ROOT: An object oriented data analysis framework. *Nucl.Instrum.Meth.*, A389:81–86, 1997.
- [53] Mathias Butenschoen and Bernd A. Kniehl. Reconciling J/ψ production at HERA, RHIC, Tevatron, and LHC with NRQCD factorization at next-to-leading order. *Phys.Rev.Lett.*, 106:022003, 2011.
- [54] Matteo Cacciari, Paolo Nason, and Ramona Vogt. QCD predictions for charm and bottom production at RHIC. *Phys.Rev.Lett.*, 95:122001, 2005.
- [55] Serguei Chatrchyan et al. Observation of a new boson at a mass of 125 GeV with the CMS experiment at the LHC. *Phys.Lett.B*, 2012.
- [56] J.W. Cronin, Henry J. Frisch, M.J. Shochet, J.P. Boymond, R. Mermod, et al. Production of Hadrons with Large Transverse Momentum at 200-GeV, 300-GeV, and 400-GeV. *Phys. Rev. D*, 11:3105, 1975.
- [57] Cesar Luiz da Silva. Υ , χ_c , and ψ' production and nuclear modifications from PHENIX, 2012. Proceedings from WWND2012, to be published in JPCS.
- [58] D. de Florian and R. Sassot. Nuclear parton distributions at next to leading order. *Phys. Rev. D*, 69:074028, 2004.
- [59] F. Dominguez, D.E. Kharzeev, E.M. Levin, A.H. Mueller, and K. Tuchin. Gluon saturation effects on the color singlet J/Ψ production in high energy dA and AA collisions. *Phys.Lett.*, B710:182–187, 2012.
- [60] E. Eichten, K. Gottfried, T. Kinoshita, K.D. Lane, and Tung-Mow Yan. Charmonium: The Model. *Phys.Rev.*, D17:3090, 1978.
- [61] E. Eichten, K. Gottfried, T. Kinoshita, K.D. Lane, and Tung-Mow Yan. Charmonium: Comparison with Experiment. *Phys.Rev.*, D21:203, 1980.
- [62] M.B. Einhorn and S.D. Ellis. Hadronic Production of the New Resonances: Probing Gluon Distributions. *Phys.Rev.*, D12:2007, 1975.
- [63] K. J. Eskola, H. Paukkunen, and C. A. Salgado. EPS09 - a New Generation of NLO and LO Nuclear Parton Distribution Functions. *JHEP*, 04:065, 2009.

- [64] Kari J. Eskola, Hannu Paukkunen, and Carlos A. Salgado. An Improved global analysis of nuclear parton distribution functions including RHIC data. *JHEP*, 0807:102, 2008.
- [65] K.J. Eskola, V.J. Kolhinen, and C.A. Salgado. The Scale dependent nuclear effects in parton distributions for practical applications. *Eur. Phys. J. C*, 9:61–68, 1999.
- [66] P. Faccioli, C. Lourenco, J. Seixas, and H.K. Woehri. Study of ψ' and χ_c decays as feed-down sources of J/ψ hadro-production. *JHEP*, 0810:004, 2008.
- [67] E.G. Ferreiro, F. Fleuret, J.P. Lansberg, N. Matagne, and A. Rakotozafindrabe. arXiv:1201.5574 (2012).
- [68] E.G. Ferreiro, F. Fleuret, J.P. Lansberg, and A. Rakotozafindrabe. Cold nuclear matter effects on J/ψ production: Intrinsic and extrinsic transverse momentum effects. *Phys. Lett. B*, 680:50–55, 2009.
- [69] Anthony D. Frawley, T. Ullrich, and R. Vogt. Heavy flavor in heavy-ion collisions at RHIC and RHIC II. *Phys.Rept.*, 462:125–175, 2008.
- [70] Harald Fritzsch. Producing Heavy Quark Flavors in Hadronic Collisions: A Test of Quantum Chromodynamics. *Phys.Lett.*, B67:217, 1977.
- [71] Krzysztof J. Golec-Biernat and M. Wusthoff. Saturation in diffractive deep inelastic scattering. *Phys. Rev. D*, 60:114023, 1999.
- [72] L.V. Gribov, E.M. Levin, and M.G. Ryskin. Semihard Processes in QCD. *Phys.Rept.*, 100:1–150, 1983.
- [73] Rajan Gupta. Introduction to lattice QCD: Course. pages 83–219, 1997.
- [74] Ilkka Helenius, Kari J. Eskola, Heli Honkanen, and Carlos A. Salgado. Impact-parameter dependent nuclear parton distribution functions: EPS09s and EKS98s and their applications in nuclear hard processes. *JHEP*, 1207:073, 2012.
- [75] Peter W. Higgs. Broken symmetries, massless particles and gauge fields. *Phys.Lett.*, 12:132–133, 1964.
- [76] P.E. Hodgson. *Nuclear Reactions and Nuclear Structure*. Clarendon Press, 1971.
- [77] J. Kamin. *A Search for Charm and Beauty in a Very Strange World*. PhD thesis, Stony Brook University, 2012.
- [78] D. Kharzeev and K. Tuchin. Open charm production in heavy ion collisions and the color glass condensate. *Nucl.Phys.*, A735:248–266, 2004.
- [79] D.E. Kharzeev, E.M. Levin, and K. Tuchin. Nuclear modification of the J/Ψ transverse momentum distributions in high energy pA and AA collisions. 2012.
- [80] Dmitri Kharzeev, Eugene Levin, Marzia Nardi, and Kirill Tuchin. Gluon saturation effects on J/Ψ production in heavy ion collisions. *Phys.Rev.Lett.*, 102:152301, 2009.

- [81] Dmitri Kharzeev and Kirill Tuchin. Signatures of the color glass condensate in J/psi production off nuclear targets. *Nucl.Phys.*, A770:40–56, 2006.
- [82] B.Z. Kopeliovich, I.K. Potashnikova, and Ivan Schmidt. J/Ψ production in nuclear collisions: Theoretical approach to measuring the transport coefficient. *Phys. Rev. C*, 82:024901, 2010.
- [83] B.Z. Kopeliovich, I.K. Potashnikova, and Ivan Schmidt. Measuring the saturation scale in nuclei. *Phys.Rev.*, C81:035204, 2010.
- [84] B.Z. Kopeliovich, I.K. Potashnikova, and Ivan Schmidt. Nuclear suppression of J/Psi: from RHIC to the LHC. *Nucl. Phys. A*, 864:203–212, 2011.
- [85] J.P. Lansberg. QCD corrections to J/psi polarisation in pp collisions at RHIC. *Phys.Lett.*, B695:149–156, 2011.
- [86] M. J. Leitch et al. Measurement of J/psi and psi' suppression in p A collisions at 800-GeV/c. *Phys. Rev. Lett.*, 84:3256–3260, 2000.
- [87] Carlos Lourenco, Ramona Vogt, and Hermine K. Woehri. Energy dependence of J/psi absorption in proton-nucleus collisions. *JHEP*, 0902:014, 2009.
- [88] Matthew Luzum and Paul Romatschke. Conformal Relativistic Viscous Hydrodynamics: Applications to RHIC results at $s(\text{NN})^{**}(1/2) = 200\text{-GeV}$. *Phys.Rev.*, C78:034915, 2008.
- [89] T. Matsui and H. Satz. J/psi Suppression by Quark-Gluon Plasma Formation. *Phys.Lett.*, B178:416, 1986.
- [90] D.C. McGlinchey, A.D. Frawley, and R. Vogt. Impact parameter dependence of the nuclear modification of J/ψ production in d+Au collisions at $\sqrt{s_{NN}} = 200 \text{ GeV}$. 2012.
- [91] Michael L. Miller, Klaus Reygers, Stephen J. Sanders, and Peter Steinberg. Glauber modeling in high energy nuclear collisions. *Ann. Rev. Nucl. Part. Sci.*, 57:205–243, 2007.
- [92] Alfred H. Mueller and Jian-wei Qiu. Gluon Recombination and Shadowing at Small Values of x. *Nucl.Phys.*, B268:427, 1986.
- [93] Berndt Muller, Jurgen Schukraft, and Boleslaw Wyslouch. First Results from Pb+Pb collisions at the LHC. 2012.
- [94] J.L. Nagle, A.D. Frawley, L.A. Linden Levy, and M.G. Wysocki. Theoretical Modeling of J/psi Yield Modifications in Proton (Deuteron) - Nucleus Collisions at High Energy. *Phys.Rev.*, C84:044911, 2011.
- [95] P.R. Norton. The EMC effect. *Rept.Prog.Phys.*, 66:1253–1297, 2003.
- [96] W. H. Press, S. A. Teukolsky, W.T. Vetterling, and B. P. Flannery. *Numerical Recipes in C: The Art of Scientific Computing*. Cambridge University Press, 1993.

- [97] J. Pumplin, D.R. Stump, J. Huston, H.L. Lai, Pavel M. Nadolsky, et al. New generation of parton distributions with uncertainties from global QCD analysis. *JHEP*, 0207:012, 2002.
- [98] Helmut Satz. Colour deconfinement and quarkonium binding. *J.Phys.G*, G32:R25, 2006.
- [99] Bjorn Schenke, Sangyong Jeon, and Charles Gale. Higher flow harmonics from (3+1)D event-by-event viscous hydrodynamics. *Phys.Rev.*, C85:024901, 2012.
- [100] Gerhard A. Schuler. Quarkonium production and decays. *Phys.Rept.*, 1994.
- [101] Richard Seto. The sPHENIX Forward Angle Spectrometer. 2012.
- [102] Rishi Sharma and Ivan Vitev. arXiv:1203.0329 (2012).
- [103] Torbjorn Sjostrand, Stephen Mrenna, and Peter Z. Skands. PYTHIA 6.4 Physics and Manual. *JHEP*, 05:026, 2006.
- [104] Alexander Spiridonov. Bremsstrahlung in leptonic onia decays: Effects on mass spectra. 2004.
- [105] I. Vitev, J. Terrance Goldman, M. B. Johnson, and J. W. Qiu. Open charm tomography of cold nuclear matter. *Phys. Rev. D*, 74:054010, 2006.
- [106] W. Vogelsang. private communication, 2007.
- [107] R. Vogt. Shadowing and absorption effects on J/psi production in dA collisions. *Phys.Rev.*, C71:054902, 2005.
- [108] R. Vogt. private communication, 2012.
- [109] Sebastian N. White. Diffraction dissociation - 50 years later. *AIP Conf. Proc.*, 792:527–531, 2005.
- [110] Jens Wiechula. Nuclear modification of J/psi production in Pb-Pb collisions at $\sqrt{s_{NN}} = 2.76$ TeV. 2012.
- [111] C. Wong. *Introduction to High-Energy Heavy-Ion Collisions*. World Scientific, 1994.
- [112] Xingbo Zhao and Ralf Rapp. Forward and midrapidity charmonium production at RHIC. *Eur.Phys.J.*, C62:109–117, 2009.
- [113] Xingbo Zhao and Ralf Rapp. Charmonium in Medium: From Correlators to Experiment. *Phys.Rev.*, C82:064905, 2010.

BIOGRAPHICAL SKETCH

Education

- M.S. Physics, Florida State University, 2009
- B.S. Physics, Ursinus College, 2007
 - *Minors:* Mathematics
 - *Honors:* Distinguished Departmental Honors in Physics, Cum Laude

Academic Experience

Florida State University, Department of Physics

- Graduate Research Assistant, *Advisor:* Anthony D. Frawley, Summer 2009-Fall 2012
- Teaching Assistant, *General Physics Lab*, Fall 2007-Spring 2009

Ursinus College, Department of Physics & Astronomy

- Distinguished Honors Research, *Advisor:* Lewis Riley, Fall 2006-Spring 2007
- Summer Fellow, *Advisor:* Lewis Riley, Summer 2005, Summer 2006
- Physics Tutor, Fall 2005-Fall 2006

Research

Publications

- Impact Parameter Dependence of the Nuclear Modification of J/ψ Production in $d+Au$ Collisions at $\sqrt{s_{NN}} = 200$ GeV, **D. McGlinchey**, A.D. Frawley, R. Vogt, (submitted to PRL) arXiv:1208.2667
- Transverse-Momentum Dependence of the J/ψ Nuclear Modification in $d+Au$ Collisions at $\sqrt{s_{NN}} = 200$ GeV, PHENIX Collaboration (A. Adare *et al.*), (submitted to PRC) arXiv:1204.0777
- Cold Nuclear Matter Effects on J/ψ Yields as a Function of Rapidity and Nuclear Geometry in Deuteron-Gold Collisions at $\sqrt{s_{NN}} = 200$ GeV, PHENIX Collaboration (A. Adare *et al.*), Phys. Rev. Lett. 107 (2011) 142301

Presentations

- Quark Matter 2012, Washington D.C., August 12-18, 2012, Recent Heavy Quarkonia Results from PHENIX. (oral presentation)
- 28th Winter Workshop on Nuclear Dynamics, Dorado del Mar, Puerto Rico, April 7-14 2012, Cold Nuclear Matter Effects on J/ψ production from PHENIX. (oral presentation)
- 8th International Workshop on Heavy Quarkonium 2011, GSI, Germany, October 4-7, 2011, Parametrizing Cold Nuclear Matter Effects at RHIC. (oral presentation)
- 19th Particles & Nuclei International Conference, Cambridge, Massachusetts, July 24-29, 2011, Heavy Flavor Measurements in Heavy Ion Collisions by PHENIX at RHIC. (oral presentation)
- Quark Matter 2011, Annecy, France, May 23-28, 2011, Constraining Cold Nuclear Matter Effects on J/ψ Production in Au+Au Collisions.(poster presentation)
- Lake Louise Winter Institute, Lake Louise, Alberta, Canada, February 20-26, 2011, Cold Nuclear Matter Effects on J/ψ Production in $d + Au$ Collisions by PHENIX at RHIC. (oral presentation)
- Quark Matter 2009, Knoxville, TN, March 30-April 4, 2009, Measurement of $J/\psi \rightarrow e^+e^-$ at $\sqrt{s} = 200$ GeV and $|y| < 0.35$ in $d + Au$ Collisions. (poster presentation)
- The Annual Meeting of the Division of Nuclear Physics of the American Physical Society, Nashville, TN, October 25-28, 2006, GEANT4 Simulations of Gamma Ray Detectors. (undergraduate poster presentation)
- 2nd Joint Meeting of the Nuclear Physics Divisions of the APS and The Physical Society of Japan, Maui, Hawaii, September 18-22, 2005, Coulomb Excitation of ^{50}Mn and Isospin Symmetry in the $A = 50$, $T = 1$ Multiplet. (undergraduate poster presentation)

Schools and Workshops Attended

- INT 10-2A, Quantifying the Properties of Hot QCD Matter, Week 7 - Quarkonia and Heavy Flavor, Seattle, WA, July 5-9, 2010.

Awards

- John D. Fox Award, FSU, April 2012.
- The Professor Evan S. Snyder Prize, Ursinus College, May 2007.